To Be Or Not To B

Meteoritic Implications for the Galactic Environment of Solar System Formation

by

Emilie T. Dunham

A Dissertation Presented in Partial Fulfillment
of the Requirements for the Degree
Doctor of Philosophy

Approved September 2019 by the
Graduate Supervisory Committee:

Meenakshi Wadhwa, Chair
Steven Desch
Richard Hervig
Maitrayee Bose
Devin Schrader

ARIZONA STATE UNIVERSITY

May 2020

ABSTRACT

Short-lived radionuclides (SLRs) once present in the solar nebula can be used to probe the Solar System's galactic formation environment. Isotopic analyses reveal that the first solids formed in the Solar System, calcium- and aluminum-rich inclusions (CAIs) in chondritic meteorites, formed with the live SLRs ^{10}Be ($t_{1/2}$ = 1.4 Ma) and ^{26}Al ($t_{1/2}$ = 0.7 Ma). Beryllium-10 is produced when high-energy ions, solar energetic particles or galactic cosmic rays (GCRs), spall nuclei in gas or dust. The most likely source of Solar System ^{10}Be is inheritance of GCR-irradiated protosolar molecular cloud material, but only if all CAIs recorded the same initial ^{10}Be abundance. The goal of this dissertation is to assess the homogeneity of ^{10}Be by measuring CAIs for ^{10}Be–^{10}B isotope systematics, correlated to ^{26}Al–^{26}Mg and oxygen isotopes.

I synthesized appropriate standards for secondary ion mass spectrometry (SIMS) measurements of ^{10}Be–^{10}B, necessary for accurate determination of the ^{10}Be/^{9}Be ratio. I then analyzed 32 CAIs for ^{10}Be–^{10}B as well as 6 CAIs for ^{26}Al–^{26}Mg and 5 CAIs for oxygen isotopes within this sample set using SIMS. Previous studies analyzed CAIs primarily from CV3 chondrites, which are known to have experienced thermal metamorphism and aqueous alteration. My work included a variety of CAIs (Type A, B, fine-grained, igneous) from $CV3_{oxidized}$, $CV3_{reduced}$, CO3, CR2, and CH/CB chondrites. Finally, after evaluating my data and literature data consistently, I statistically tested whether all CAIs belong to a single ^{10}Be population. I find that the majority (~85%) of the normal (i.e., without large isotopic fractionations or anomalies), ^{26}Al-bearing CAIs recorded a single value, ^{10}Be/^{9}Be = (7.0 ± 0.2) × 10^{-4}. Although 6 CAIs recorded higher or lower values, these are plausibly explained by secondary alteration processes.

The galaxy-wide average value of $^{10}Be/^{9}Be$ from GCR interactions 4.56 billion years ago is predicted to be $<2 \times 10^{-4}$; the value I measured is more than 3 times higher. Because GCRs trace supernovae and star formation, my results suggest a similarly enhanced star formation rate in the molecular cloud within ~1 kpc of the Sun, in the ~15 Ma prior to the Sun's birth.

DEDICATION

I dedicate this dissertation to my grandparents who were invested in my education and happiness above anything else. Their unwavering support meant everything to me.

ACKNOWLEDGMENTS

This dissertation would not have been possible without the guidance, support, and mentorship from a number of individuals. First, I would like to thank my PhD committee members: my advisor Meenakshi Wadhwa for taking a risk on me and giving me the opportunity to become part of and navigate cutting-edge cosmochemistry research, Steve Desch for making me a more well-rounded scientist by supplementing my analytical cosmochemistry research with a wide array of other topics in planetary science, Rick Hervig for introducing me to and teaching me SIMS; I always learn a lot from Rick even when I ask quick questions, Devin Schrader for your infinite knowledge of CR2 chondrites and your ability to help me at a moment's notice, and Maitrayee Bose for fun discussions and taking the time to provide me with career advice. I am grateful for the warm support of other faculty and staff in SESE: Jemma Davidson, Rebekah Hines, Vinai Rai, Laurence Garvie, Axel Wittmann, Kurt Roggensack, Kurt Leinenweber, Rebecca Davis, Becca Dial, Becky Polley, and Alicia Mangosing.

I was fortunate during my graduate career to work with exceptional external collaborators. At University of Wisconsin, Madison, WiscSIMS lab manager Noriko Kita and postdocs Kohei Fukuda and Celine Defouilloy taught me about Al-Mg and oxygen isotope analyses and helped me obtain results presented in this dissertation. At University of California, Los Angeles, IMS-1290 lab manager Ming-Chang Liu and postdoc Andreas Hertwig welcomed me many times and provided me with everything I needed, including many discussions, to obtain precise data and make interpretations.

I am extremely grateful to have a network of very supportive friends who never let me down. Thank you to members of my SESE cohort including Jessica Noviello, Kara

Brugman, Alyssa Anderson, Aleisha Johnson, Hannah Shamloo, Crystyl Fudge, Anna Brunner, and Meghan Guild for many brunches, hikes, and compassionate company. Thank you to Boom Kittiwisit, Sam Gordon, Nari Miller, Kristin Whitney, and Rubble, for scintillating conversation, froyo runs, and companionship. Thank you to my present and past lab mates: Soumya Ray, Zack Torrano, Daniel Dunlap, Prajkta Mane, and Alice Stephant. You truly made working more fun and eased the PhD struggle. Thank you all for letting me drag you on adventures and embracing life with me.

Encouragement and comfort from my family, Bruce Dunham, Diane Dunham, and Audrey Dunham, over the past 5 years has provided me with much needed strength. Finally, I would like to thank my future husband, Zach Porter, for his unwavering support throughout my entire graduate career. Through the ups and downs, he never fails to boost my confidence and make me laugh.

TABLE OF CONTENTS

Page

LIST OF TABLES xi

LIST OF FIGURES xii

CHAPTER

1 INTRODUCTION 1

1.1 Background 1

1.2 Motivation 6

1.3 Abstract for Chapter 2 7

1.4 Abstract for Chapter 3 8

1.5 Abstract for Chapter 4 9

1.6 Abstract for Chapter 5 10

2 BEST PRACTICES FOR DETERMINATION OF INITIAL $^{10}Be/^{9}Be$ IN EARLY SOLAR SYSTEM MATERIALS BY SIMS 11

2.1 Introduction 11

2.2 Melilite Glasses Developed to Standardize Relative Sensitivity Factor 17

2.2.1 Synthesizing Melilite-Composition Glasses 20

2.2.2 Melilite-Composition Glass Elemental Concentrations 20

2.2.3 Melilite-Composition Glass Isotope Composition 22

2.2.3.1 Cameca ims-6f SIMS 22

2.2.3.2 Cameca ims-1290 SIMS 23

2.2.4 Matrix-matched SIMS RSF 25

2.3 Re-Evaluation of Literature Data 29

CHAPTER Page

2.3.1 York Regression Calculation and Isochron Validity 29

2.3.2 Correlated Errors 32

2.3.3 Re-Evaluated Dataset Table 33

2.3.4 Examining the New Dataset 33

2.4 Evidence for Irradiation 36

2.5 Evidence for Aqueous Alteration 43

2.6 Method for Reporting of ^{10}Be–^{10}B Isotope Systematics 45

2.7 Conclusions 46

3 UNIFORM LEVEL OF ^{10}Be IN CR2 CAIs SUGGESTS IT WAS INHERITED DURING SOLAR SYSTEM FORMATION 48

3.1 Introduction 48

3.2 CR2 CAI Petrologic Characterization 51

3.3 Isotope Characteristics 52

3.4 CR2 CAIs Record Uniform ^{10}Be Distribution 59

3.5 Implications for the Origin of ^{10}Be 62

3.6 Methods 65

3.6.1 Sample Preparation and Characterization 65

3.6.2 Secondary Ion Mass Spectrometry: ^{10}Be–^{10}B 65

3.6.3 Secondary Ion Mass Spectrometry ^{26}Al–^{26}Mg 66

3.7 Sample Characterization 67

CHAPTER Page

4 CAIs RECORD UNIFORM $^{10}Be/^{9}Be$: EVIDENCE THAT ^{10}Be WAS PRODUCED IN THE MOLECULAR CLOUD 75

4.1 Introduction 75

4.2 Results and Discussion 79

4.2.1 ^{10}Be–^{10}B Isotope Systematics 79

4.2.2 ^{26}Al–^{26}Mg Isotope Systematics 84

4.2.3 Integrating Results with Literature Data 86

4.2.4 Statistically Examining the Dataset 88

4.2.5 FUN CAIs and PLACs 91

4.2.6 Astrophysical Modeling 95

4.3 Conclusions 99

4.4 Methods Summary 104

4.5 Detailed Results 105

4.6 CAI Characterization Methods 121

4.7 IMS-6f (ASU) Measurements of Be-B Systematics 122

4.8 IMS-1290 (UCLA) Measurements of Be-B Systematics 123

4.8.1 First Session with Monocollection Spot Analysis 123

4.8.2 Second Session with Multicollection Spot Analysis 123

4.8.3 Third Session with Multicollection Using O_2^- Raster Analysis 124

CHAPTER Page

4.9 IMS-1280 (UW-Madison) Measurements of Al-Mg Systematics 124

4.10 Statistical Analysis 126

4.11 The Reclassification of Northwest Africa 5028 126

4.11.1 Analytical Methods 127

4.11.2 Results 127

4.11.3 Discussion 128

4.11.4 Conclusions 130

5 OXYGEN ISOTOPE VARIATIONS IN CV3 CAIs CORRELATED TO ^{26}Al AND ^{10}Be: IMPLICATIONS FOR SOLAR SYSTEM OXYGEN ISOTOPE RESERVOIRS.....132

5.1 Introduction 132

5.2 Samples..... 134

5.3 Methods 135

5.3.1 Petrography and Mineralogy..... 135

5.3.2 Oxygen Isotopes 136

5.4 Results 137

5.4.1 NWA 5028 CAI Agave..... 137

5.4.2 NWA 5028 CAI Cholla..... 138

5.4.3 NWA 5508 CAI Saguaro 138

5.4.4 NWA 6991 CAI B4..... 139

CHAPTER Page

5.4.5 Allende CAI TS23 139

5.5 Discussion 140

5.5.1 Distinct Oxygen Isotope Distributions in CAI minerals 141

5.5.2 Comparing Oxygen Isotopes of Adjacent CAIs 143

5.5.3 Implications for Combined ^{10}Be, ^{26}Al and oxygen isotopes 145

5.6 Conclusions 148

6 SUMMARY AND FUTURE DIRECTIONS 151

6.1 Summary 151

6.2 Future Directions and Implications 157

6.2.1 Expanding the Sample Set 157

6.2.2 Improving Analytical Uncertainties 159

6.2.3 Experimental Studies to Test Be and B Behavior 161

6.2.4 Modeling 162

REFERENCES 163

APPENDIX

A LONG TABLES 179

B PREVIOUS PUBLICATIONS/STATEMENT OF CO-AUTHORS 199

LIST OF TABLES

Table		Page
2.1	Standards for ^{10}Be–^{10}B Measurements	24
2.2	Elemental and Isotopic Composition of Relevant Standards	29
2.3	Compiled ^{10}Be–^{10}B Dataset from Previous Studies	35
2.4	^{10}Be–^{10}B Isotope Systematics of NWA 6991 CAI Lisa	38
3.1	CR2 CAI ^{10}Be–^{10}B and ^{26}Al–^{26}Mg Isotope Systematics	55
4.1	^{10}Be–^{10}B Isotope Systematics for 25 CAIs	84
5.1	Summary of Oxygen Isotope Measurements, ^{10}Be, and ^{26}Al	149
S1	Chapter 3: ^{10}Be–^{10}B Data for 8 CR2 CAIs	180
S2	Chapter 3: ^{26}Al–^{26}Mg Data for 4 CR2 CAIs	181
S3	Chapter 3: Representative CR2 CAI Mineralogy	182
S4	Chapter 4: Classification of NWA 5028, Olivine and Metal Data	184
S5	Chapter 4: Summary of CAI Classifications	185
S6	Chapter 4: Calibration Details of SIMS Sessions	187
S7	Chapter 4: ^{10}Be–^{10}B Data for 25 CAIs	189
S8	Chapter 4: ^{10}Be–^{10}B Extra Results for 4 CO3 CAIs	194
S9	Chapter 4: ^{26}Al–^{26}Mg Results for 2 CAIs from NWA 5028	195
S10	Chapter 5: Oxygen Isotope Data for 5 CAIs	197

LIST OF FIGURES

Figure		Page
2.1	Example ^{10}Be–^{10}B Isochron	25
2.2	Comparing Relative Sensitivity Factors	28
2.3	CAI Lisa Measured and Modeled Data - Isochron	41
2.4	CAI Lisa Measured and Modeled Data – [B] and MSWD	42
3.1	^{10}Be–^{10}B Isotope Systematics for 5 CR2 CAIs	56
3.2	^{26}Al–^{26}Mg Isotope Systematics for 3 CR2 CAIs	57
3.3	CR2 CAI Correlated ^{10}Be–^{10}B and ^{26}Al–^{26}Mg	58
3.4	Characterization of CAIs Yucca and Creosote from MIL 090657	68
3.5	Compositional Maps of CAI Creosote	70
3.6	Characterization of CAIs Dalea and Dalea2 from Shişr 033	71
3.7	Characterization of CAI Cereus from LAP 02342	72
3.8	Characterization of CAI Palo Verde from NWA 801	73
3.9	CR2 CAIs [B] ppm versus $^{10}B/^{11}B$	74
4.1	^{10}Be–^{10}B Isotope Regressions for 25 CAIs	83
4.2	Correlated ^{10}Be versus ^{26}Al	85
4.3	Compiled $^{10}Be/^{9}Be$ Results and Interpretation	102
4.4	Modeling – Distribution of Star Formation Rates	103
4.5	Characterization and Results: CAI Bascom (DaG 005)	106

Figure Page

4.6 Characterization and Results: CAI Mitchell (DaG 005) 107

4.7 Characterization and Results: CAI Krafft (DaG 027) 107

4.8 Characterization and Results: CAI Anning (DaG 027) 108

4.9 Characterization and Results: CAI Jemmison (DaG 027) 108

4.10 Characterization and Results: CAI Goeppert (DaG 027) 109

4.11 Characterization and Results: CAI Mesquite (NWA 7892) 110

4.12 Characterization and Results: CAI 31-2 (DOM 08006) 111

4.13 Characterization and Results: Isheyevo CAIs 113

4.14 Characterization and Results: CAI CMS-1 (Allende) 114

4.15 Characterization and Results: CAI B4 (NWA 6991) 114

4.16 Characterization and Results: CAI Lisa (NWA 6991) 115

4.17 Characterization and Results: CAI TS68 (Allende) 116

4.18 Characterization and Results: CAI TS23 (Allende) 114

4.19 Characterization and Results: CAI FoB 3137-2 (Vigarano) 117

4.20 Characterization and Results: CAI TS23 (Allende) 118

4.21 Characterization and Results: CAI Cholla (NWA 5028) 118

4.22 Characterization and Results: CAI ZT1 (Leoville) 119

4.23 Characterization and Results: CAI Agave (NWA 5028) 119

4.24 Characterization and Results: CAI Saguaro (NWA 5508) 120

4.25 Characterization and Results: CAI ZT7 (NWA 7891) 120

4.26 ^{26}Al–^{26}Mg Isotope Regressions for 2 CV3 CAIs 121

Figure Page

4.27 BSE Image of NWA 5028 CAI 130

4.28 BSE Image of NWA 5028 Representative Chondrules 130

4.29 NWA 5028 Representative Chondrules, Ni versus Co 131

5.1 Oxygen Isotope Composition of 5 CAIs 139

5.2 $\Delta^{17}O$ of 5 CAIs 140

5.3 $\Delta^{17}O$ versus Åkermanite Content 148

5.4 $\Delta^{17}O$ versus $^{10}Be/^{9}Be$ in Spinel and Melilite 148

5.5 $\Delta^{17}O$ versus $^{26}Al/^{27}Al$ in Spinel and Melilite 149

CHAPTER 1

INTRODUCTION

1.1 Background

The initial conditions of Solar System formation are important to constrain in order to better understand our place in the Milky Way galaxy and the universe. Our current knowledge of the astrophysical environment of the Solar System primarily comes from astronomical observations and theoretical models. Observations of protoplanetary disks show us the molecular cloud environments in which solar systems preferentially form and evolve and show how exploding active young stars change the material around them. Observations of specific stars in our Milky Way galaxy give evidence of the star formation rate (SFR) 4.56 billion years ago when our Sun was just forming (Rocha-Pinto et al., 2000a). Models can provide explanations for these observations. However, SFRs, based on mean ages of stars, tend to be low precision and low resolution due to the difficulty of the observations (Rocha-Pinto et al., 2000b). Meteoritic materials recorded conditions in the solar nebula ~4.56 billion years ago and can be used as higher precision spatial and chronologic probes to constrain the environment of Solar System formation.

This dissertation aims to place additional constraints on the astrophysical environment of Solar System formation by determining the initial abundances of specific short-lived radionuclides (SLR) in the Solar System's first-formed solids (calcium- and aluminum- rich inclusions, or CAIs). Stable and very long-lived nuclides are produced by stellar nucleosynthesis before being incorporated into the Solar System, and their

abundances in the early Solar System can be estimated by galactic chemical evolution (GCE) models. Short-lived radionuclides (SLRs), on the other hand, have half-lives much less than the lifetime of the Solar System ($t_{1/2}$ < ~100 Ma) and can be products of stellar nucleosynthesis and irradiation processes. Determining the initial abundances and distributions of SLRs (such as ^{10}Be, ^{26}Al, ^{36}Cl, ^{41}Ca, ^{53}Mn, ^{60}Fe, ^{129}I, ^{146}Sm, and ^{182}Hf) can help us to better understand astrophysical events which occurred either shortly before or during the formation of the Solar System (Davis & McKeegan, 2014). Thus, we can gather information about the types of stars that contributed material to the Solar System, to constrain the astrophysical setting in which the Sun formed (e.g., Huss et al. 2009).

Evidence of the prior existence of SLRs in the early Solar System is recorded in CAIs because they are the earliest-forming solids in the Solar System, having formed around 4.56 billion years ago, before the SLRs decayed away (Davis & McKeegan, 2014). The CAIs are small inclusions (~10 μm–20 mm) composed of Ca- and Al-rich minerals which condensed and crystallized at high temperatures (~1300–1700 ºC), such as corundum (Al_2O_3), hibonite ($Ca(Al,Ti,Mg)_{12}O_{19}$), spinel ($MgAl_2O_4$), melilite (solid solution between $Ca_2Al_2SiO_7$ and $Ca_2MgSi_2O_7$), Ti-rich pyroxene ($Ca(Mg,Fe,Al,Ti)(Si,Al)_2O_6$), and anorthite ($CaAl_2Si_2O_8$) (Macpherson, 2003; Scott & Krot, 2013).

The CAIs are thought to have formed in the hot inner Solar System (~0.1–1 AU) and were then accreted into the parent bodies of carbonaceous chondrite meteorites (Dauphas & Chaussidon, 2011; MacPherson, 2013). The abundances and sizes of CAIs in chondritic meteorites are quite variable. For example, while CAIs in the CV3

carbonaceous chondrites are quite abundant (up to ~5 vol.%) and relatively large (up to several mm), those in CO3 chondrites are significantly less abundant (< 1 vol.%) and are much smaller (<500 μm) (Weisberg et al., 2006). CAIs are complex objects and are not just simple aggregates of high-temperature nebular grains. They record prolonged histories of reactions with nebular gas, reheating that led to melting episodes, impact-induced shock, and secondary mineralization in the nebula and/or on their host asteroidal parent body (MacPherson, 2013; Ivanova, 2016). To constrain the initial abundances of SLRs based on analyses of CAIs, it is important to understand their primary formation histories, as well as any secondary alteration they may have experienced. In this work, to estimate the initial abundances of SLRs such as ^{10}Be and ^{26}Al in the early Solar System, I selected only those CAIs that contained minimal, if any, alteration effects , even in CV3 chondrites. These relatively pristine CAIs exhibited few secondary minerals formed by aqueous alteration have isotope systematics less likely disturbed by secondary processes.

The primary formation histories of CAIs are recorded in their mineralogy and texture. Type A CAIs are melilite-rich, and texturally can be either fluffy and fine-grained (interpreted to be direct condensates from the solar nebula) or compact (which underwent some degree of reheating and recrystallization). Type B CAIs, on the other hand, are composed of melilite, spinel, pyroxene, and anorthite; they are typically spherical and have igneous textures indicating that they were produced by melting of precursor solids. It is interesting that type B CAIs only occur in CV3 chondrites (MacPherson, 2013). It is important to place the isotopic results in the context of the texture of these CAIs.

In this dissertation, I focus on determining the initial abundances of SLRs ^{10}Be and ^{26}Al, along with oxygen isotopes, in pristine CAIs; if any correlations exist between these isotope systems, these can inform us of the irradiation histories and the timing of CAI formation. Beryllium-10 is unique because it can only be produced by spallation of gas and/or solids by energetic charged particles; ^{10}Be is destroyed during stellar nucleosynthesis. Currently, over 30 CAIs, primarily from CV3 chondrites, have been measured for ^{10}Be–^{10}B isotopic systematics; the linear correlation between ^{10}B/^{11}B and ^{9}Be/^{11}B is considered to be evidence of the prior existence of ^{10}Be in these CAIs (McKeegan et al., 2000).

While many of the CAIs yield a ^{10}Be/^{9}Be ~7×10^{-4} (McKeegan et al., 2000; Sugiura et al., 2001; Marhas et al., 2002; MacPherson et al., 2003; Chaussidon, 2006; Liu et al., 2009, 2010; Wielandt et al., 2012; Srinivasan & Chaussidon, 2013; Sossi et al., 2017; Mishra & Marhas, 2019), there are several others that have quite different values (Gounelle et al., 2013; Sossi et al., 2017). Two main astrophysical models have been proposed to account for the presence of live ^{10}Be in the early Solar System: (1) spallation reactions by galactic cosmic ray reactions in the molecular cloud just before the Sun's formation (McKeegan et al., 2000; Gounelle et al., 2001; Tatischeff et al., 2014) and (2) spallation reactions in the protoplanetary disk by solar energetic particles accelerated by flares from the young Sun (McKeegan et al., 2000; MacPherson et al., 2003; Bricker & Caffee, 2010; Jacquet, 2019). Because previously published measurements show a range of ^{10}Be/^{9}Be values, they suggest a heterogeneous distribution of ^{10}Be, favoring a solar

nebula irradiation origin. But before rejecting the inheritance origin, more evidence from a wider variety of pristine CAIs is needed.

Another SLR, ^{26}Al, was likely produced during stellar nucleosynthesis and then expelled, into the formation environment of the Solar System by Wolf-Rayet winds or supernova ejecta (Davis & McKeegan, 2014; Dwarkadas et al., 2017). This SLR can also be produced by irradiation, but the reaction is inefficient; models that do not overproduce ^{10}Be will yield ^{26}Al/^{27}Al much smaller than 5×10^{-5} (MacPherson et al., 2003). There is a long history of ^{26}Al isotopic measurements in CAIs; most authors have argued that ^{26}Al was uniformly distributed in the early Solar System and can be used as a chronometer to date the formation of objects in the first few million years, including CAIs (Davis & McKeegan, 2014). If the estimated abundances of ^{10}Be and ^{26}Al in CAIs are correlated, that would indicate that both SLRs were probably produced by the same astrophysical source. Finally, I measure oxygen isotope composition of several CAIs for the purposes of constraining the nebular reservoir(s) in which the CAIs formed and evolved.

Isotopic analyses to determine initial abundances of SLRs in CAIs can be performed by a variety of mass spectrometry techniques, we employed in situ secondary ion mass spectrometry (SIMS) as this technique is particularly suited for measuring ^{10}Be–^{10}B isotope systematics in CAIs. This *in situ* technique is required, as opposed to a whole-rock, solution-based technique, for to the following reasons. Melilite, hibonite, and grossite are the only CAI minerals that have sufficiently high Be/B ratios to calculate resolved excesses in ^{10}B/^{11}B, that then allow us to calculate the initial ratio of ^{10}Be/^{9}Be; with SIMS we can analyze individual selected grains of these minerals. The

concentration of B in these CAI minerals is typically low (down to 1 ppb) and SIMS allows utilization of a high primary beam current for increased secondary ion counts and the ability to count secondary ions for extended periods of time with minimal drift. The high spatial resolution of this technique is additionally important given the typically small grain sizes in many CAIs; this spatial resolution also allows us to avoid any minor secondary phases that may be present. For this SIMS technique, we bombard a specific area of the polished section of the meteorite sample with primary oxygen ions; this sputtering produces secondary ions and the isotopes of interest are detected and counted (McKeegan et al., 2000). This method is detailed extensively in subsequent chapters. SIMS was the chosen technique to measure ^{26}Al–^{26}Mg and oxygen isotope systematics for similar reasons.

1.2 Motivation

The motivating question of this dissertation is: what astrophysical setting produced the short-lived radionuclide ^{10}Be and what does this imply about the environment of Solar System formation? Through the analysis of ^{10}Be–^{10}B, ^{26}Al–^{26}Mg, and oxygen isotope systematics via *in situ* SIMS techniques in a wide variety of CAIs (particularly non-CV3 CAIs belonging to different petrologic types), we find that ^{10}Be was likely produced in the protosolar molecular cloud and was inherited into the solar nebula. This implies that the Solar System formed in a region (~1 kpc, within 15 Ma of Solar System formation) of the Milky Way galaxy undergoing a high rate of star formation, when compared to spatially averaged galactic star formation rates. We

summarize below the main findings reported in the subsequent chapters, which were crucial in coming to this conclusion.

1.3 Chapter 2: Best Practices for the Determination of Initial $^{10}Be/^{9}Be$ in CAIs By SIMS

With the goal of determining the origin of ^{10}Be, in this chapter we examine the secondary ion mass spectrometry (SIMS) methods used to determine the initial Solar System $^{10}Be/^{9}Be$ ratio. Combining previously published SIMS analyses and new measurements, we conclude that the effect of chemistry on the secondary ion yields of Be and B is minor. It is important to perform regressions including correlated errors, and to determine and report mean square weighted deviation (MSWD), without which one cannot evaluate the validity of an isochron. We recalculated published data for 32 CAI regressions and find that several have high MSWD. We consider possible sources of isotopic disturbance. We find that irradiation of CAIs on the parent body, producing just ~ppb levels of spallogenic B, can increase the inferred initial $^{10}Be/^{9}Be$, without worsening the MSWD. We discuss how to determine if a CAI has been irradiated on the parent asteroid. We show that some CAIs appear disturbed by aqueous alteration, especially in $CV3_{ox}$ chondrites, and that this effect leads to both higher and lower inferred $^{10}Be/^{9}Be$, but usually results in high MSWD. We discuss the signatures of aqueous alteration. Finally, we outline best practices for reporting ^{10}Be–^{10}B data to allow for comparisons between datasets, so as to allow a more rigorous assessment of the abundance and distribution of ^{10}Be in the early Solar System.

1.4 Chapter 3: A Uniform Level of Beryllium-10 in CAIs from CR Chondrites Favors an Inherited Origin Over Local Production

Isotopic analyses of calcium- and aluminum-rich inclusions (CAIs) in meteorites have established that the early Solar System contained live ^{10}Be, a short-lived ($t_{1/2}$ = 1.4 Ma) radionuclide. The origin of this radionuclide is debated, and various models have been proposed. In one model, ^{10}Be is produced by spallation of nuclei in the molecular cloud by GCRs; ^{10}Be would be uniformly distributed in the solar nebula and its abundance would decrease with time. In another model, ^{10}Be was produced by spallation of nuclei in the solar nebula by solar energetic particles; ^{10}Be would be non-uniformly distributed and is predicted to increase with time. Current measurements cannot constrain whether ^{10}Be was uniform in the solar nebula, in part because it is difficult to correct for secondary effects such as parent-body irradiation and aqueous alteration. In this chapter, we determine the correlated ^{10}Be–^{10}B and ^{26}Al–^{26}Mg systematics in CAIs from CR2 (Renazzo-type) carbonaceous chondrites. CR2 (i.e., petrologic type 2) chondrites are among the least metamorphosed chondrites, so the effects of parent-body alteration on CAI isotopic compositions are minimized. We find that three CR2 CAIs recorded weighted mean initial ^{10}Be/^{9}Be = (7.5 ± 1.2) × 10^{-4} (2SE) and initial ^{26}Al/^{27}Al ratios range (4.4 − 4.7) × 10^{-5}. These results suggest that ^{10}Be was homogeneously distributed in the solar nebula with its uniform value by ~ 10^{5} years after the first CAIs formed. Because we do not find evidence for spatial or temporal heterogeneities in ^{10}Be/^{9}Be in CAIs this strongly suggest an inherited origin for ^{10}Be, and not one due to spallation in the solar nebula. We discuss the astrophysical consequences.

1.5 Chapter 4: CAIs Record Uniform $^{10}Be/^{9}Be$: Evidence that ^{10}Be was Produced in the Molecular Cloud

We measured ^{10}Be–^{10}B isotope systematics in CAIs from CV3, CO3, and CH/CB chondrites and combined these data with previous studies to show that the SLR ^{10}Be has a single value, $^{10}Be/^{9}Be = 7 \times 10^{-4}$, in the majority of CAIs. The existence of a uniform value suggests that ^{10}Be was inherited from the molecular cloud into the Solar System. A spiral galaxy like our Milky Way has regions of high star formation rate (i.e., spiral arms) as well as regions of lower star forming activity. We model that the region near (< 1 kpc) a newborn star experiences a galactic cosmic ray (GCR) flux about 3.7 times higher than a random point in the galaxy. Based on this factor as well as estimates of the higher star formation rate and GCR flux in the galaxy overall 4.56 billion years ago, we calculate a high probability (≈ 20–40%) of the Sun's molecular cloud forming with $^{10}Be/^{9}Be \geq 7 \times 10^{-4}$. The enrichment in ^{10}Be is similar to the enhanced abundances of other SLRs in self-enrichment scenarios. Thus, the meteoritic data provide a unique probe of the GCR flux and astrophysical environment at the Sun's birth.

1.6 Chapter 5: Oxygen Isotope Variations in CV3 CAIs Correlated To ^{26}Al and ^{10}Be: Implications for the Solar System Oxygen Isotope Composition

Correlating oxygen isotopes distribution to short-lived radionuclides ^{26}Al and ^{10}Be in a variety of types of CV3 CAIs allows us to make inferences about the origin of oxygen isotope distributions in CAI minerals. We measured 5 CV3 CAIs of different types (fine-grained fluffy type A, compact type A, type B1, and type B2) for oxygen

isotope systematics. We find that all CAI spinels recorded a ^{16}O-rich signature, but other minerals have variable oxygen isotope ratios. The fine-grained fluffy-type A (FTA) CAI composed of melilite, spinel, and pyroxene is predominantly ^{16}O-rich. The Type B1 CAIs have ^{16}O-rich pyroxene and anorthite varying in Δ^{17}O, the CTA has ^{16}O-rich pyroxene but ^{16}O-poor anorthite. We conclude that the initial reservoir in which CAIs formed was uniform with respect to oxygen isotopes (^{16}O-rich CAI spinel), ^{10}Be, and ^{26}Al. Oxygen isotope variations in melilite, pyroxene, and anorthite likely resulted from CAI re-processing in distinct oxygen isotope reservoirs within the solar nebula.

CHAPTER 2

BEST PRACTICES FOR DETERMINATION OF INITIAL $^{10}Be/^{9}Be$ IN EARLY SOLAR SYSTEM MATERIALS BY SIMS

2.1. Introduction

Beryllium-10, which decays to ^{10}B with a half-life of 1.4 Ma (Korschinek et al., 2010), is produced by spallation reactions induced by galactic and/or stellar cosmic rays (McKeegan et al., 2000; Desch et al., 2004; Liu et al., 2010; Tatischeff et al., 2014; Jacquet, 2019). The former presence of ^{10}Be is inferred by anomalous $^{10}B/^{11}B$ ratios (relative to the chondritic value of 0.25) in phases with high Be/B ratios (such as melilite) in calcium- and aluminum-rich inclusions (CAIs), the first solids formed in the Solar System. Previous studies over the past two decades have reported ^{10}Be–^{10}B isotope systematics in many CAIs and have amply demonstrated that live ^{10}Be was present in the early Solar System. However, the inferred initial $^{10}Be/^{9}Be$ ratios range from 3×10^{-4} to 1×10^{-2}, even though ~85% of CAIs record initial $^{10}Be/^{9}Be\sim(6–9)\times10^{-4}$ (McKeegan et al., 2000; Sugiura et al., 2001; Marhas et al., 2002; MacPherson et al., 2003; Chaussidon, 2006; Liu et al., 2010; Wielandt et al., 2012; Srinivasan & Chaussidon, 2013; Sossi et al., 2017; Mishra & Marhas, 2019). It is critical to determine whether the distribution of ^{10}Be in the early Solar System was homogeneous or heterogeneous, because that allows us to infer how it was produced. If ^{10}Be was homogeneously distributed (i.e., CAIs, which likely formed within a narrow time interval, record a single $^{10}Be/^{9}Be$ value), it was likely produced by galactic cosmic rays interacting with the molecular cloud core that collapsed

to form our Solar System (Desch et al., 2004; Tatischeff et al., 2014). On the other hand, if ^{10}Be was distributed heterogeneously (i.e., CAIs display a range of ^{10}Be/^{9}Be values), ^{10}Be was likely produced by solar particles interacting with gas and solids in the solar nebula (McKeegan et al., 2000; Gounelle et al., 2001; MacPherson et al., 2003; Jacquet, 2019). The origin of ^{10}Be is currently ambiguous partly because of the difficulty of interpreting the results to date.

In order to determine the initial ^{10}Be/^{9}Be ratios of CAIs, cosmochemists collect Be and B isotopic data via secondary ion mass spectrometry (SIMS) and then perform a York regression on the data to obtain the slopes of the ^{10}Be–^{10}B isochrons. The ^{10}Be–^{10}B isotope system is measured by the *in situ* SIMS technique; a primary beam of mass-filtered $^{16}O^-$ ions with high energies (typically 21-23 keV) is directed at a carefully-selected and documented, crack-free, mineral. The cascade of collisions produced by the primary beam in the atoms in the sample results in the ejection of atoms and molecules in a process known as "sputtering"; some sputtered material is ionized in the process. A positive potential (typically 5-10 kV) is applied to the sample to accelerate positive secondary ions into a double-focusing mass spectrometer where they are selected for energy and mass. The mass-analyzed ion beam is directed to an electron multiplier to record the signal. Because the ionization probabilities of Be and B are different, the number of counts/second produced for each μg/g of these elements in a sample is not the same, and comparison with a reference material is needed to calibrate the Be/B ratio.

In the case of a short-lived nuclide such as ^{10}Be, the amount of the daughter isotope (^{10}B) in a sample at the present time that originally contained live ^{10}Be can be

expressed as $^{10}B = {}^{10}B_0 + {}^{10}Be$, where $^{10}B_0$ and ^{10}Be are the original amounts present in the sample in the early Solar System. Normalization to a stable isotope of the daughter (^{11}B), then yields the following equation: $^{10}B/^{11}B = (^{10}B/^{11}B)_0 + (^{10}Be/^{11}B)$. This equation can be re-written as: $^{10}B/^{11}B = (^{10}B/^{11}B)_0 + (^{10}Be/^{9}Be)\times(^{9}Be/^{11}B)$. This is the equation for a straight line where the slope and intercept correspond to the initial radioactive parent-to-stable parent ratio ($^{10}Be/^{9}Be$) and the non-radiogenic daughter composition $(^{10}B/^{11}B)_0$, respectively. Thus, a ^{10}Be–^{10}B isochron for a CAI is made by plotting the measured $^{10}B/^{11}B$ versus $^{9}Be/^{11}B$ ratios for phases in that CAI with varying Be/B ratios, and fitting a straight line through these data points by a least squares regression (Ludwig, 1988; Vermeesch, 2018). To determine the least squares fit, the York regression method (York 1966; York et al. 2004) takes into account independent uncertainties in both the *x* and *y* variables, and allows for correlations between these uncertainties, to determine the least-squares fit.

Therefore, in a ^{10}Be–^{10}B isochron plot of $^{10}B/^{11}B$ versus $^{9}Be/^{11}B$, an age cannot be directly determined, unlike the case for isochron plots for long-lived radioisotope systems; but the slope of the fit represents the inferred initial $^{10}Be/^{9}Be$ ratio, and the intercept is the initial $(^{10}B/^{11}B)_0$ for that sample. Each of these ratios is associated with a standard error, which is typically quoted as two sigma (2σ). Statistically, a valid isochron is one that has scatter that can be attributed solely to the measurement errors, such that the reduced chi-squared or mean square weighted deviation (MSWD) is ~1.

When compared to other isotope measurements, there are a number of additional concerns when it comes to determining ^{10}Be–^{10}B isotopic systematics. One of the main

issues is the typically low concentrations of Be and B in CAIs. The ^{10}Be–^{10}B isotope measurements by SIMS are predominantly performed on melilite because when considering the phases commonly found in CAIs, the mineral structure for this phase is best suited to accommodating the small divalent beryllium ion. Moreover, previous studies show a large spread of $^{9}Be/^{11}B$ ratios in this phase. Melilite is a solid solution between $Ca_2Al_2SiO_7$ (gehlenite) and $Ca_2MgSi_2O_7$ (åkermanite). Condensation calculations predict that Be condenses in solid solution with melilite and most likely condenses into Mg and/or Ca sites (Lauretta & Lodders, 1997). The Be concentration in melilite is usually about 500 ng/g, while the B concentration in melilite varies drastically on ~5 μm scales from ~1 ng/g to 1 μg/g, depending on the sample (MacPherson et al., 2003). As described below, uncertainty in the isotope ratios measured by SIMS is particularly sensitive to the denominator species, $^{11}B^+$. In order to obtain appropriately high intensities of this isotope, it is necessary to increase the amount of the phase being sampled. For example, one sputters the melilite with a large primary ion current (typically 10–30 nA in most IMS-6f and IMS-1270/80 SIMS instruments). This, though, creates a large SIMS pit (>20 μm diameter), so measuring single grains in fine-grained or small samples is nearly impossible; intersecting multiple melilite crystals and possibly encountering a crack can bias the isotope ratios. Advances in micro-analytical mass spectrometry now allow smaller samples to be analyzed, such as with a bright oxygen ion source attached to a SIMS (Liu et al. 2018). However, even with a high sputtering rate on a small-diameter crater, $^{11}B^+$ intensities can be significantly less than 1 count/second. Small counts must be treated mathematically with care, to avoid introducing ratio

calculation bias, as in the case of ^{60}Fe–^{60}Ni systematics (Ogliore et al. 2011). To avoid such a bias, we use the integrated counts of the two boron isotopes throughout the analysis because the least biased ratio estimation for low count measurements is the Beale's estimator (Telus et al., 2013). Other methods to avoid statistical bias when using such low count rates include the Coath method (Coath et al., 2013). Regardless of the selected approach, different ratio estimation techniques change the final ^{10}Be/^{9}Be value by less than a few percent. Given the large range in boron isotope ratios and associated high uncertainties observed in CAIs in particular, we suggest the ratio estimation technique approaches are equivalent here.

In addition to these challenges, the ^{10}Be–^{10}B isotopic system is subject to disturbance. Isotopes of B and Be are otherwise rare and are efficiently produced by irradiation, especially by spallation of O nuclei, which can occur when cosmic rays interact with a meteorite parent body. Adding plausible amounts of extra spallogenic B to CAI melilite can drastically alter the original ^{10}Be/^{9}Be signature. Parent body aqueous alteration can also disturb the ^{10}Be–^{10}B system by mobilizing B; this alteration would likely increase the scatter in a ^{10}Be–^{10}B isochron for a CAI. These factors intrinsic to the ^{10}Be–^{10}B isotopic system make it difficult to determine the distribution of ^{10}Be in the early Solar System.

Interpreting the ^{10}Be–^{10}B data for CAIs in the existing literature is difficult because not all published datasets are complete. Previous ^{10}Be–^{10}B studies do not always report the necessary information, such as standardization details and raw data, required to reproduce or interpret the results. Reference materials are necessary to correct for

analytical artifacts in SIMS measurement. As an example, matrix-matched reference materials are used to determine the relative sensitivity factor (RSF), which is used to account for the difference in the ionization of Be with respect to B from a particular matrix. Previous studies have not always reported their RSF, and those that do use a variety of reference materials (most of which do not match the sample matrix), resulting in a range of RSF values (Table 2.1). For the ^{10}Be–^{10}B system, suitable matrix-matched reference materials have not been fully developed for phases such as melilite, hibonite ($Ca(Al,Ti,Mg)_{12}O_{19}$), or grossite ($CaAl_4O_7$) with trace concentrations of Be and B. Moreover, how the major element composition (matrix) of a reference material affects the RSF values for this isotope system is not well-understood. Other quantities that tend to not be reported include all the errors needed to reproduce a regression, correlation coefficients, and mean square weighted deviations (MSWD, or reduced chi-squared) associated with the isochron regressions. Because of the typically low concentrations of B found in CAI phases, errors in the ^{9}Be/^{11}B and ^{10}B/^{11}B ratios are correlated; taking the correlation coefficient into account can alter the regression. The MSWD of regressions is necessary to report because this quantity is needed to judge the validity of an isochron.

The purpose of this paper is to establish consistent best practices for measuring and reporting ^{10}Be–^{10}B data. In doing so, we hope that previous and future studies can be more easily integrated, to elucidate the distribution and origin of ^{10}Be in the early Solar System. We report on melilite glasses we developed to standardize the RSF. We re-evaluate previous ^{10}Be–^{10}B data to create a unified dataset by uniformly constructing the regressions. We discuss factors that can disturb the ^{10}Be–^{10}B system, such as how

irradiation that produces spallogenic B can change the slope of the isochron without affecting the MSWD, and how to assess the effects of irradiation (e.g., using a ^{149}Sm dosimeter). We discuss how aqueous alteration can produce more scatter in the regression, and how to recognize when a CAI has been disturbed by aqueous alteration. Finally, we discuss best practices for reporting regressions, to facilitate comparisons across datasets. The compiled dataset from previous literature, in addition to consistent reporting of ^{10}Be–^{10}B data in future studies, will allow us to constrain the origin of ^{10}Be in the early Solar System.

2.2. Melilite Glasses Developed to Standardize Relative Sensitivity Factor

Beryllium is ionized more efficiently than B during SIMS analyses (e.g., Hervig et al. 2006), so the Be^+/B^+ ion ratio needs to be corrected for fractionation caused during the sputtering process. To do this, we need to measure reference materials with known Be and B concentrations (i.e., [Be] and [B], respectively). SIMS measurements of reference materials allow us to calculate a relative sensitivity factor (RSF) which is defined as:

$$\mathrm{RSF} = \left(\frac{^{9}\mathrm{Be}^{+}}{^{11}\mathrm{B}^{+}}\right)_{\mathrm{SIMS}} / \left(\frac{^{9}\mathrm{Be}}{^{11}\mathrm{B}}\right)_{\mathrm{true}}$$

where $(^{9}Be+/^{11}B+)_{SIMS}$ is the apparent $^{9}Be/^{11}B$ ion ratio measured via SIMS and $(^{9}Be/^{11}B)_{true}$ is the actual atomic $^{9}Be/^{11}B$ ratio in a reference material. We then use this RSF to calculate the correct $^{9}Be/^{11}B$ ratio in the sample as follows:

$$\left(\frac{^{9}\mathrm{Be}}{^{11}\mathrm{B}}\right)_{\mathrm{corrected}} = \left(\frac{^{9}\mathrm{Be}^{+}}{^{11}\mathrm{B}^{+}}\right)_{\mathrm{uncorrected}} / \mathrm{RSF}$$

In previous studies, the CAI phase most commonly measured for ^{10}Be–^{10}B isotope systematics is melilite. The RSF for melilite was assumed to be the same as that of the commonly available silicate glasses (Table 2.1), which have RSF values of ~2.5–3.2 depending on the study and the specific reference material measured. Changes in ionization probabilities as a function of major element concentration have often been observed in SIMS analyses (Ihinger et al., 1994; Ottolini et al., 2002), so it is preferable that reference materials have a bulk composition similar to the unknown sample (i.e., are matrix-matched). However, the chemical compositions of these glass reference materials are very different from melilite (Table 2.2).

The consequence of using an RSF from an inappropriate reference material is that the resulting inferred $^{10}Be/^{9}Be$ ratios for CAIs could be underestimated or overestimated. Fukuda et al. (2018) synthesized melilite-composition glasses containing trace amounts of Be and B to test if the RSF was different than silica-rich glasses. They used the University of Tokyo NanoSIMS to determine that the RSF is the same between melilite-composition glass and the reference material NIST SRM 610. As described in section 2.1, we have also synthesized melilite-composition glasses and determined the RSF on two other SIMS instruments: SIMS IMS-6f at Arizona State University (ASU) and IMS-1290 at University of California, Los Angeles (UCLA).

The $^{10}B/^{11}B$ ion ratio determined on the sample must also be corrected for instrumental mass fractionation (IMF) which occurs during the process of sputtering, transmission through the mass spectrometer, and detection. In general, the $^{10}B/^{11}B$ ratio is higher than bulk-analyzed (“true”) values because all boron ions have the same kinetic

energy, but the lighter isotope has higher velocity, possibly allowing it to avoid neutralizing collisions as it leaves the sample surface. The velocity effect has been studied in detail for B and other isotopic systems (Gnaser & Hutcheon, 1987). This will only play a role in the measured isotope ratio if: a) the energy bandpass is small (unlikely for most SIMS analyses); and b) sample charging is not controlled. Another cause of uncertainty in correcting the raw $^{10}B^{+}/^{11}B^{+}$ ion ratio to true atomic ratios is the effect of changing bulk chemistry. While some studies (e.g., Sugiura et al. 2001; Marschall and Monteleone 2014) suggest that bulk chemistry does not have a significant effect on fractionation of boron isotopes during sputtering, Rosner et al. (2008) found a ~3‰ effect between NIST SRM 610 and NIST SRM 612 synthetic glasses relative to natural silicate glasses with a wide range of chemistry. In a follow-up study, De Hoog et al. (2017) found that hydrous minerals showed different IMF for boron isotopes than natural glasses by a few permil. However, because the boron isotope ratios measured in CAI phases typically vary by a factor of nearly 2, any matrix effects on the IMF correction for their boron isotope compositions are relatively minor compared to the typical analytical errors and we can safely use the synthetic NIST SRM glass reference materials to correct for this fractionation. The IMF is calculated as follows:

$$\mathrm{IMF} = \left(\frac{^{10}\mathrm{B}^{+}}{^{11}\mathrm{B}^{+}}\right)_{\mathrm{SIMS}} \Big/ \left(\frac{^{10}\mathrm{B}}{^{11}\mathrm{B}}\right)_{\mathrm{true}}$$

The measured B isotope ion ratio is normalized to the value of the IMF to generate the corrected B isotope ratio. Typical values of IMF for our analyses vary from ~1.02 to 1.04.

2.2.1. Synthesizing Melilite-Composition Glasses

Glasses of melilite composition doped with Be and B were synthesized at ASU. In ASU's Isotope Cosmochemistry and Geochronology Lab (a class 1000 clean laboratory), 99.9% or higher purity Alfa Aesar oxide powders of MgO, $CaCO_3$, SiO_2, Al_2O_3 were weighed in different proportions (total ~ 4 grams for each glass) to produce three melilite-composition powders with varying åkermanite content, and each of these powders were doped with different amounts of BeO (American Beryllia) and $B(OH)_3$ (NIST SRM 951 boric acid) using a microbalance. Each powder was then mixed in a mortar and pestle with methanol for at least 10 minutes. These mixtures were subsequently converted to glasses in the Depths of the Earth lab at ASU. A 50 ml volume Pt crucible was filled with the powder mixture and lowered into a DelTech furnace, the temperature raised to 1050°C at 3°C/min in order to allow the CO_2 to release slowly, and then to 1600°C at 10°C/min. After 3 hours at this liquidus temperature, the crucible was dropped into water for rapid quenching. This glass was removed from the crucible, ground to a powder by mortar and pestle, and the melting process repeated at least 2 times to ensure homogenization.

2.2.2. Melilite-Composition Glass Elemental Concentration

Glass fragments from the synthesized melilite-composition glasses (section 2.1) were co-mounted in epoxy (EpoxySet resin and hardener from Allied) and polished. Major elements were determined using the JEOL JXA-8530F electron probe microanalyzer (EPMA). For the EPMA, we used 15kV accelerating voltage and an

electron current of 15 nA and obtained 13 or more energy dispersive spectra (EDS) of MgO, Al_2O_3, SiO_2, and CaO abundances per sample.

The Be and B contents of the three synthesized glasses (GN, G2, and GX) were measured using the iCAP-Q quadrupole inductively coupled plasma mass spectrometer (ICPMS) at ASU. For each of the three synthetic glasses, we started with four powdered 15-50 mg aliquots. To measure the B content, following the procedure of Gangjian et al. (2013), two of the four powdered aliquots for each glass were mixed in a Teflon container with 1 mL concentrated HF, 100 µL H_2O_2, and 100 µL 1% mannitol solution and were digested by heating on a hot plate at 60°C for 3 days. These aliquots were ultimately brought into 3% nitric solution, and their B concentrations were measured using the standard addition technique on the iCAP-Q ICPMS. To measure Be, we digested the other two powdered aliquots for each glass in 2 mL concentrated nitric and 0.4 mL concentrated HF at 80°C for a day. Following digestion and drying down, each residue was brought into solution with 5 mL 6M HCl. The dry down and treatment with HCl was repeated to ensure complete dissolution. After drying down a final time, each residue was brought into final solution with 1.2 mL of 3% nitric prior to analyses with the iCAP-Q ICPMS. The GN, G2, and GX solutions were measured against six standard solutions with a range of B and Be contents from 0-155 µg/g. The elemental compositions of the melilite-composition synthetic glasses are shown in Table 2.2.

2.2.3. Melilite-Composition Glass Isotope Composition

We conducted measurements of Be/B ratios on the synthesized melilite-composition glasses (GN, G2, and GX) using the Cameca IMS-6f SIMS at ASU and the Cameca IMS-1290 SIMS at the UCLA. We measured the glasses on both instruments to test for any variation in RSF on different instruments (Tables 2.1 and 2.2). The results shown in Table 2.1 and 2.2 for these glasses are based on averages of three or more analyses for each glass composition. These tables also show data based on reference materials analyzed by previous studies. We note that some previous studies do not report the RSF value but do report the reference material(s) that they used. For example, McKeegan (2000) used GB4, a high-silica natural sample melted and quenched to a glass; Srinivasan and Chaussidon (2013) used a set of in-house and well-known reference glasses (basaltic, pyroxene, and melilite composition, as well as BHVO and NBS); Liu et al. (2010) used NIST SRM 612.

2.2.3.1. Cameca ims-6f SIMS (Arizona State University)

The Cameca duoplasmatron was used to generate the primary ion beam and samples were held at a potential of 12.5 kV. Using a current of ~10 nA, the $^{16}O^-$ primary beam was focused to a spot ~20 μm in diameter. No energy filtering was applied. We operated the mass spectrometer at a mass resolving power (MRP) of ~1500 to resolve and avoid interferences on ^{9}Be (from $^{27}Al^{+++}$) as well as ^{10}B and ^{11}B from ^{9}BeH and ^{10}BH interferences (other interferences such as $^{30}Si^{+++}$) are also separated at these conditions. We caution that calibrating the SIMS with MRP greater than ~1200 is necessary to

resolve ^{9}BeH from ^{10}B to obtain accurate results, and high-resolution mass scans should be conducted to ensure that the interference is resolved. For the melilite-composition glasses, we measured ^{9}Be (8s), ^{10}B (16s) and ^{11}B (4s) during 30 cycles for each measurement. At the end of each analysis, ^{28}Si was additionally measured as a reference. The $M^{+}/^{28}Si^{+}$ ion ratios (after normalizing to the known SiO_2 content of the reference materials) were used to determine calibration factors for calculating the Be and B contents of the unknown materials. The RSF values from this study are reported in Table 2.1 as weighted means of the analyses of different reference materials ("NIST" is a weighted mean of analyses of NIST SRM 610, 612, and 614 glasses; "GSC, GSD, GSE" is a weighted mean of analyses of USGS GSC-1G, USGS GSD-1G and USGS GSE-1G glasses; "Melilite glass" is a weighted mean of the analyses of the three synthesized glasses). Table 2.2 provides the individually determined RSF values for the different glass reference materials (the three synthesized melilite-composition glasses, the NIST SRM 610, 612, and 614 glasses, and the USGS GSC-1G, USGS GSD-1G and USGS GSE-1G glasses).

2.2.3.2. Cameca ims-1290 SIMS (University of California, LA)

A 5−10 nA $^{16}O^{-}$ primary beam resulting in a beam diameter ~5−10 μm was generated by a *Hyperion-II* RF source (Liu et al., 2018). The mass resolving power was ~2500, the entrance and exit slits were fully open, the aperture was 750 μm and the image field was 80 μm. Secondary ion intensities were measured in peak jumping mode with three electron multipliers (EM). The first mass jump with a 5 second count time

measured $^{27}Al^{+++}$ and $^{28}Si^{+++}$, the second mass jump with a 10 second count time measured $^{9}Be^{+}$, and the third mass jump with a 40 second count time measured $^{10}B^{+}$ and $^{11}B^{+}$. Pre-sputtering (without raster) for 3 minutes was used to remove surface B contamination. The RSF values from this study are reported in Table 2.1 as weighted means of the analyses of different reference materials ("NIST" is a weighted mean of analyses of NIST SRM 610 and 614 glasses; "Melilite glass" is a weighted mean of the analyses the three synthesized glasses). Table 2.2 provides the individually determined RSF values for the different glass reference materials (the three synthesized melilite-composition glasses, and the NIST SRM 610 and 614 glasses).

Table 2.1

Standards for ^{10}Be–^{10}B Measurements

Study	**SIMS model**	**Reference Material**	**RSF**
Sugiura et al. 2001	IMS-6f	JB, JA, JG	2.7
MacPherson et al. 2003	IMS-6f	NIST SRM 612	2.4–2.7
Chaussidon 2006	IMS-1270	GB4, BHVO-1, UTR-2	2.5-2.6
Wielandt et al. 2012	IMS-1280	NIST SRM 612 GSC, GSD	2.6 1.8
Fukuda et al. 2018	NanoSIMS	Melilite glass NIST SRM 610	2.55±0.11 2.44±0.12
Sossi et al. 2017	IMS-1280	GB4	3.17±0.13
Mishra and Marhas 2019	IMS-4f	GB4	2.62–2.95
This study	**IMS-6f**	**NIST SRM** **USGS GSC-1G, GSD-1G, GSE-1G** **Melilite glass**	**2.36±0.13** **2.03±0.18** **2.21±0.18**
This study	**IMS-1290**	**NIST SRM** **Melilite glass**	**2.45±0.28** **1.91±0.15**

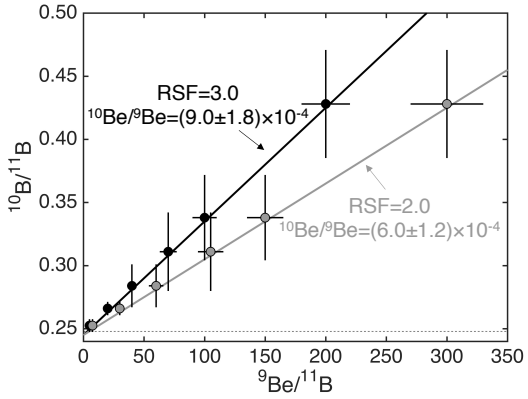


Figure 2.1. An example of a ^{10}Be–^{10}B isochron (based on hypothetical data, with 2σ errors, comparable to those reported in the previous literature for CAIs), demonstrating the effect of RSF on the ^{10}Be/^{9}Be slope. Using different RSF values changes the slope without altering the MSWD. The horizontal dashed line is the chondritic B isotope ratio (^{10}B/^{11}B=0.2481; Zhai et al., 1998). Because the regressions are hypothetical, they both have MSWD=1.

2.2.4. Determining RSF with Matrix-Matched SIMS Reference Materials

In SIMS analyses, the correct value of the RSF based on the measurement of appropriate reference materials must be used for determining accurate ^{10}Be–^{10}B isotope systematics. To illustrate this, we created two example isochrons with data and associated (2SE) errors comparable to a real CAI isochron (Figure 2.1). When RSF = 2, initial ^{10}Be/^{9}Be = (6.0 ± 1.2) × 10^{-4}, while when RSF=3, initial ^{10}Be/^{9}Be = (9.0 ± 1.8) × 10^{-4}. In both cases MSWD=1. Importantly, the ^{9}Be/^{11}B ratio and the uncertainties in this ratio are both inversely proportional to the RSF multiplied by the ^{9}Be counts and divided by the ^{11}B counts, so that MSWD is not affected by the RSF. As can be seen here, when the RSF

is increased by ~50%, the inferred initial $^{10}Be/^{9}Be$ ratio correspondingly increases by ~50%. However, given the relatively large uncertainties, the $^{10}Be/^{9}Be$ values are just within uncertainty of each other. This exercise shows that it is important to evaluate matrix effects and determine the best reference material(s) to obtain the most accurate SIMS data for constraining ^{10}Be–^{10}B isotope systematics. Nevertheless, because of the typically large uncertainties involved in such measurements, using an imperfect reference material may not significantly alter the results.

Indeed, due to the intrinsically large uncertainties when measuring trace amounts of Be and B in CAIs, we show here that the use of a matrix-matched reference material (i.e., composition of the reference material is similar to the composition of the unknown sample) may not be critical. Like Fukuda et al. (2018), we synthesized and measured matrix-matched melilite-composition glass. However, we used different synthesis techniques and determined the RSF using an IMS-6f and an IMS-1290 SIMS to validate the results from the Fukuda et al. (2018) NanoSIMS study. We find that, in general, matrix-matched reference materials may not be critical for accurate ^{10}Be–^{10}B isotopic measurements. This is broadly in agreement with the results reported by Fukuda et al. (2018). Our IMS-6f SIMS data (Table 2.1, 2.2, Figure 2.2a) show that the NIST SRM glasses 610, 612, and 614 (SiO_2=70 wt.%, [B]=0.8–476.0 μg/g) define a weighted mean RSF=2.36±0.13 while our melilite-composition glasses (SiO_2~25–38 wt.%, [B]=16–85 μg/g, [Be]~600 μg/g) with varying Åk content ($Åk_{20–75}$), GX, G2, and GN, define a weighted mean RSF=2.21±0.18. However, our IMS-1290 SIMS data (Table 2.1, 2.2, Figure 2.2b) are a bit more complex. While one of the NIST SRM glasses (610) defines

the same RSF (2.14±0.37) as the melilite-composition glasses (1.91±0.15) within the uncertainties, the other NIST SRM glass (614) defines a resolvably higher RSF (2.89±0.43) than the melilite-composition glasses. The reason for the slight difference noted here between the RSFs determined using the IMS-6f and IMS-1290 SIMS instruments is not well understood, but could potentially be related to different instrument characteristics, such as monocollection versus multicollection, respectively, or differences in electron multiplier gain settings.

Because at present it is not clear why some reference materials yield somewhat different RSF values than the melilite-composition glasses, it is suggested that homogeneous matrix-matched reference materials (containing Be and B concentrations comparable to those in CAIs) should be utilized where possible in determining ^{10}Be–^{10}B isotope systematics of CAIs. It would be beneficial to measure the true Be and B concentrations of the melilite composition glasses with higher precision to better understand the intricacies of standardization for determining ^{10}Be–^{10}B isotope systematics.

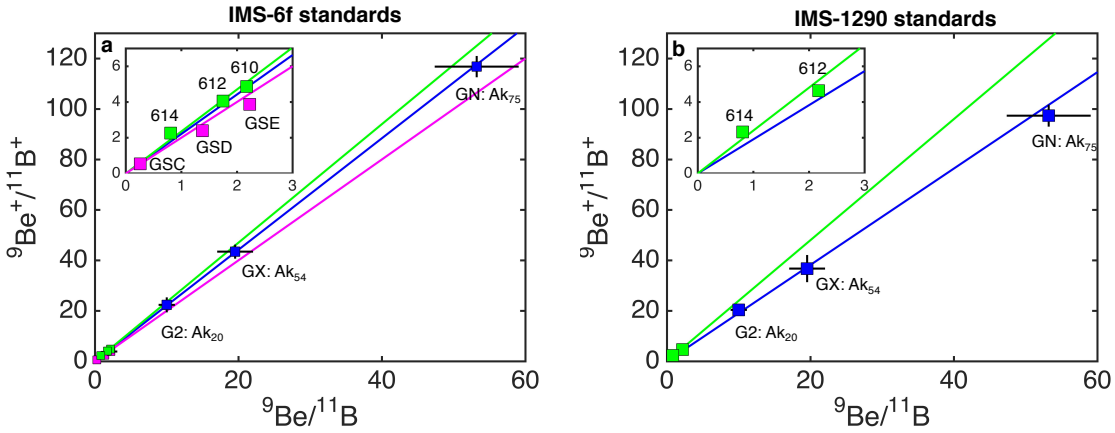


Figure 2.2. Relative sensitivity factors (RSF) of NIST SRM 610, 612, and 614 (green symbols; Jochum et al. 2011), USGS GSC-1G, USGS GSD-1G, and USGS GSE-1G (magenta symbols; Jochum et al. 2005), and melilite-composition glasses G2, GX, and GN (blue symbols; this study) utilizing the IMS-6f (a) and the IMS-1290 (b). The RSFs are based on the slopes of $^{9}Be^{+}/^{11}B^{+}$ (measured by SIMS) vs $^{9}Be/^{11}B$ (true atomic ratios, literature values for the reference materials and values for the melilite glasses measured independently in this study by ICPMS) for these reference materials. Uncertainties are 2σ.

Table 2.2

Elemental and Isotopic Compositions of Relevant Standards

	GN	G2	GX	NIST SRM 610	NIST SRM 612	NIST SRM 614	USGS GSC-1G	USGS GSD-1G	USGS GSE-1G	GB4
Åk mol%	75	54	20							
SiO_2 wt.%	37.1±0.4	37.2±1.1	25.5±0.6	69.7±0.5	72.1±0.6	72.1±0.9	52.6± 0.6	53.2±0.8	53.7±1.5	72.9
MgO wt.%	10.7±0.3	7.9±0.3	2.6±0.4				3.6± 0.0	3.6±0.0	3.5±0.0	
Al_2O_3 wt.%	7.3±0.1	20.6±0.7	27.2±0.5	2.0±0.1	2.0±0.1	2.0±0.1	13.5±0.4	13.4±0.3	13.0±0.4	15.6
CaO wt.%	44.7±0.3	34.1±1.0	44.5±0.8	11.4±0.2	11.9±0.1	11.9±0.2	7.1±0.1	7.2±0.1	7.4±0.3	0.6
Na_2O wt.%	0.1±0.1	0.2±0.1	0.1±0.1	13.4±0.3	13.7±0.3	13.7±0.3	3.6±0.2	3.6±0.3	3.9±0.2	4.6
Be (µg/g)	554.8±25.5	567.7±26.1	630.9±29.0	476±31	37.5±1.5	0.8±0.1	4.5±0.4	46±5	490±80	11.3
B (µg/g)	15.6±1.6	48.3±5.8	85.0±8.8	350±56	34.3±1.7	1.5±0.2	26.0±7.0	50±20	330±120	970
$^{9}Be/^{11}B$	53.2±5.9	19.5±2.5	10.0±1.1	2.17±0.37	1.7±0.1	0.8±0.1	0.26±0.07	1.38±0.57	2.23±0.89	
IMS-6f										
$^{9}Be^{+}/^{11}B^{+}$	116.78±4.22	43.36±2.79	22.37±2.97	4.87±0.07	4.05±0.07	2.26±0.17	0.54±0.01	2.39±0.02	3.87±0.02	
6f RSF	2.19±0.25	2.22±0.32	2.24±0.39	2.25±0.39	2.32±0.15	2.80±0.45	2.09±0.59	1.73±0.72	1.74±0.69	
IMS-1290										
$^{9}Be^{+}/^{11}B^{+}$	97.34±4.34	36.73±5.38	20.37±1.29	4.63±0.02		2.32±0.04				
1290 RSF	1.82±0.22	1.88±0.37	2.04±0.26	2.14±0.37		2.89±0.43				

Note: The melilite composition glasses synthesized here, GN, G2, and GX, are representative of the range of Åk composition found in CAIs. The elemental data for the other reference materials are from the literature (NIST SRM 610, 612, 614: Jochum et al. 2011; USGS GSC-1G, USGS GSD-1G, USGS GSE-1G: Jochum et al. 2005, GB4: Chaussidon 2006). Uncertainties are 2σ.

2.3. Re-Evaluation of Literature Data

2.3.1. York Regression Calculation and Isochron Validity

To calculate a York regression (implemented using IsoplotR; Vermeesch 2018) to determine the $^{10}Be/^{9}Be$ ratio, the required inputs are: $x = {}^{9}Be/^{11}B$; σ_x, the ±2SE uncertainty in x; $y={}^{10}B/^{11}B$; σ_y, the ±2SE uncertainty in y; and r, the correlation coefficient of the x and y uncertainties. These inputs are supplied for multiple datapoints indexed by *i*, from 1 to N. The outputs of the York regression are the slope (i.e., the $^{10}Be/^{9}Be$ ratio), the ±2SE uncertainty in this slope, the intercept (the initial $^{10}B/^{11}B$ ratio), the ±2SE uncertainty in this intercept, and MSWD.

The correlation coefficient, *r*, is a common way to measure the credibility of a linear relationship between two variables. Values lie between -1 and 1, with a 1 indicating a perfect positive correlation, -1 indicating a perfect anticorrelation, and 0 indicating no correlation. In this context, however, the correlation coefficient is an input provided at each datapoint *i*. It is given by:

$$r_i = \frac{\sigma_{xy}^2}{\sigma_x \sigma_y},$$

where σ_x and σ_y are the standard deviations in x and y, and σ_{xy} is the covariance. This is not formally defined if the datapoint *i* corresponds to a single measurement, but in the case of ^{10}Be–^{10}B isotope systematics, multiple cycle counts are combined to provide x, σ_x, y, σ_y, and r. If x and y are measured in N_{cycle} cycles corresponding to a single analysis spot (or data point), then

$$\sigma_x^2 = \frac{1}{N_{cycles}} \sum |x - \mu_x|^2 ,$$

$$\sigma_y^2 = \frac{1}{N_{cycles}} \sum \left|y - \mu_y\right|^2,$$

$$\text{and } \sigma_{xy}^2 = \frac{1}{N_{cycles}} \sum (x - \mu_x)(y - \mu_y),$$

where $\mu_x = (1/N_{cycles}) \Sigma\, x$ and μ_y a= $(1/N_{cycles}) \Sigma\, y$ are the mean values, which are reported as x_i and y_i. Because both x_i=(^{9}Be)/(^{11}B) and y_i=(^{10}B)/(^{11}B) have ^{11}B in the denominator, the uncertainties in x and y are correlated. The low concentration of ^{11}B often means it is the dominant source of measurement error, which can make the correlation stronger (i.e., the high ^{9}Be/^{11}B analyses often have r values closer to 1). The assumption that x_i and y_i are uncorrelated overestimates the inherent uncertainty in the data and allows a broader

range of slopes within the uncertainty envelope for the regression; as such, r should be used for the most accurate and precise determination of ^{10}Be–^{10}B isotope systematics. The MSWD value is used to assess the degree of over- or under-dispersion of the data and is particularly important when an isochron has few data points. This value is calculated using the equation:

$$\mathrm{MSWD} = \frac{1}{N-2}\sum_{i=1}^{N}\frac{(y_i - a - bx_i)^2}{\sigma_{y_i}^2 + b^2\sigma_{x_i}^2}$$

where a is the inferred intercept of the fit and b is the inferred slope, N is the number of data points in the fit and x_i and y_i are $^{9}Be/^{11}B$ and $^{10}B/^{11}B$ values in our case. To determine the significance of the linear fit, we also calculate the uncertainty of the MSWD. For a dataset with two terms (in this case, $^{9}Be/^{11}B$ and $^{10}B/^{11}B$), the expected value of the MSWD is $1 \pm 2\sigma_{MSWD}$, where:

$$\sigma_{\mathrm{MSWD}} = \sqrt{\frac{2}{(N-2)}}$$

For example, in a ^{10}Be–^{10}B isotope dataset with 20 x-y pairs that defines a good isochron, the MSWD should be 1.0 within ± 0.67 (at $2\sigma_{\mathrm{MSWD}}$), i.e., MSWD should not exceed 1.67. If the fit yields an MSWD higher than this 2-sigma limit, there is a less than ~5% probability that the data conform to a simple linear model, and scientific inferences based on that model are statistically inappropriate. In other words, the linear regression to the data with too-high MSWD has < 5% probability of being a line and should not be considered an isochron (Wendt & Carl, 1991). In such cases for the ^{10}Be–^{10}B system, the

SLR ^{10}Be may have been present in that CAI, but the slope of the isochron, i.e., the inferred initial ^{10}Be/^{9}Be ratio, is too uncertain to report.

2.3.2. Correlation Coefficient of the Uncertainties in ^{9}Be/^{11}B and ^{10}B/^{11}B

Few previous studies (MacPherson et al., 2003; Wielandt et al., 2012) have taken into account the correlation coefficient of the uncertainties in ^{9}Be/^{11}B and ^{10}B/^{11}B on the inferred ^{10}Be/^{9}Be ratios. Because raw cycle-by-cycle data are necessary to calculate this correlation coefficient, r, we cannot determine this for previously reported analyses where such data are not provided. This correlated component of the uncertainties in the measured data should be reported in future ^{10}Be–^{10}B studies.

In estimating this correlation coefficient for previously published data, we find that the data points with higher ^{9}Be/^{11}B and ^{10}B/^{11}B ratios tend to have a higher correlation coefficient. Overall, the inferred initial ^{10}Be/^{9}Be and initial ^{10}B/^{11}B ratios do not change significantly. However, the uncertainty associated with the inferred ^{10}Be/^{9}Be ratio generally decreases when the correlation in the uncertainties in ^{9}Be/^{11}B and ^{10}B/^{11}B are taken into account, in agreement with MacPherson et al. (2003). For example, we found a CAI (Dunham et al., 2017) to have initial ^{10}Be/^{9}Be=(6.8±2.8)×10^{-4} (MSWD=0.5) when correlated errors were not taken into account and ^{10}Be/^{9}Be=(6.7±2.2)×10^{-4} (MSWD=0.6) when correlated errors were included in the York regression. As can be seen in this case, the uncertainty in the inferred initial ^{10}Be/^{9}Be changes more significantly than the ^{10}Be/^{9}Be value itself; the MSWD can also change slightly when correlated errors are taken into account. Although the correlation coefficient in the

uncertainties in $^{9}Be/^{11}B$ and $^{10}B/^{11}B$ is not the most important factor in determining the robustness and accuracy of an inferred initial $^{10}Be/^{9}Be$ ratio, this parameter should be considered and reported to produce the most complete $^{10}Be–^{10}B$ dataset.

2.3.3. Re-calculating $^{10}Be–^{10}B$ Isotope Systematics From Previous Studies

Previous $^{10}Be–^{10}B$ studies present data in different ways, and sometimes do not include key components, such as MSWD, so an important goal in this study was to re-calculate all previously reported data using a consistent method to create a single combined dataset. We did this by first gathering the reported SIMS data (i.e., $^{9}Be/^{11}B$ and $^{10}B/^{11}B$ ratios) for 32 CAI samples from the previous literature (McKeegan et al., 2000; Sugiura et al., 2001; Marhas et al., 2002; MacPherson et al., 2003; Chaussidon, 2006; Liu et al., 2010; Wielandt et al., 2012; Srinivasan & Chaussidon, 2013; Sossi et al., 2017). The $^{9}Be/^{11}B$ ratios that we extracted from literature were calculated by the authors using comparable RSF values. We entered these data into IsoplotR (Vermeesch, 2018) for each CAI to produce an isochron and recorded the results (Table 2.3). In each case, we evaluated the robustness of the isochron by reporting the MSWD as well as the $1+2\sigma_{MSWD}$; if the MSWD $>1+2\sigma_{MSWD}$, the regression must be considered in detail to evaluate its validity.

2.3.4. Examining the Re-calculated Dataset

Our re-calculated dataset (Table 2.3) shows that seven out of 32 regressions have MSWD $> 1+2\sigma_{MSWD}$. We will not discuss the individual regressions in detail but note

that regressions with high MSWD tend to come from CAIs in CH/CB chondrites, or from fine-grained CAIs (Gounelle et al., 2013; Sossi et al., 2017).

Two CAI regressions have exceptionally high inferred initial $^{10}Be/^{9}Be$ ratios when compared to other CAIs (Gounelle et al., 2013; Sossi et al., 2017), and both are associated with high MSWD. This indicates that the high $^{10}Be/^{9}Be$ ratios are inferred from invalid isochrons; the CAIs likely contained live ^{10}Be, but the inferred $^{10}Be/^{9}Be$ ratios are unreliable. One of these regressions with high inferred $^{10}Be/^{9}Be$ and high MSWD includes a multi-CAI regression (three fine-grained CAIs; Sossi et al. 2017). We argue that fine-grained CAIs should be treated with caution when determining ^{10}Be–^{10}B systematics. If a SIMS spot covers more than a single, crack-free, melilite grain, it is probable that the isotope analyses will be inaccurate.

Table 2.3

Compiled ^{10}Be–^{10}B Dataset from Previous Studies.

Published study	Meteorite	Chondrite -type	CAI sample	CAI-type	[B] range[2]	[Be] range[2]	$^{10}Be/^{9}Be$[3]	2SE	$^{10}Be/^{9}Be$[4]	2SE	$^{10}B/^{11}B$	2SE	n	MSWD	$1+2\sigma_{MSWD}$[5]	regression?[6]
Gounelle et al. 2013	Isheyevo	CH/CB	501,503,2006,2012	hib-gros-px-mel-sp	13–214		13.1	4.3	13.5	7.4	0.2492	0.0005	13	0.7	1.8	✓
Gounelle et al. 2013	Isheyevo	CH/CB	Isheyevo	hib-gros-px-mel-sp	6–300		104.0	16.0	103.9	31.3	0.2537	0.0033	4	4.5	2.6	×
Marhas et al. 2002	Murchison	CM2	many PLACS	PLAC			5.2	2.8	5.2	2.6	0.2723	0.0160	9	1.4	2.0	✓
Liu et al. 2010	Murchison	CM2	many PLACS	PLAC	1–1526	14–819	5.5	2.6	5.3	1.0	0.2513	0.0013	23	1.1	1.6	✓
MacPherson et al. 2003	Axtell	CV3ox	AXCAI 2771	FUN A	1–10	56–400	3.0	1.2	3.0	1.2	0.2470	0.0220	6	5.2	2.3	×
Wielandt et al. 2012	Axtell	CV3ox	AXCAI 2771	FUN A	1–11	54–464	2.8	0.2	4.0	0.4	0.2518	0.0036	10	1.1	1.9	✓
Wielandt et al. 2012	NWA 779	CV3ox	KTI	FUN A	1–63	25–1214	3.4	0.2	5.0	0.4	0.2543	0.0032	12	0.9	1.9	✓
MacPherson et al. 2003	Allende	CV3ox	3898	CTA	5–156	120–790	4.8	1.7	4.8	1.7	0.2573	0.0080	7	0.3	2.2	✓
Sujura et al. 2001	Allende	CV3ox	001	B	4–23		5.3	2.4	5.5	2.6	0.2550	0.0280	7	1.0	2.2	✓
Sujura et al. 2001	Allende	CV3ox	002	B	7–695		6.9	0.5	7.0	1.1	0.2513	0.0019	12	1.5	1.9	✓
Sossi et al. 2017[1]	Allende, NWA8616	CV3ox	2 coarse-grained	B	<10–80	<10-40	12.0	3.0	9.3	0.8	0.2488	0.0006	20	8.2	1.6	×
McKeegan et al. 2000	Allende	CV3ox	3529-41	B	6–927		9.5	1.9	9.8	2.2	0.2540	0.0007	10	0.4	1.9	✓
Chaussidon et al. 2006	Allende	CV3ox	3529-41	B	10–300		8.8	0.6	10.0	0.9	0.2549	0.0004	51	12.0	1.4	×
Sossi et al. 2017[1]	Allende	CV3ox	3 fine-grained	FTA	70–910	<10–30	71.0	24.0	54.5	9.4	0.2472	0.0007	19	4.4	1.7	×
MacPherson et al. 2003	Vigarano	CV3red	477-4b	B1	2–85	120–450	5.3	1.7	5.3	1.7	0.2444	0.0022	13	1.0	1.8	✓
Sujura et al. 2001	Efremovka	CV3red	E38	B	4–106		6.0	1.2	5.7	1.2	0.2550	0.0048	17	0.8	1.7	✓
MacPherson et al. 2003	Vigarano	CV3red	1623-9	CTA	1–10	39–570	5.8	1.9	5.8	1.9	0.2422	0.0100	8	1.2	2.1	✓
Sujura et al. 2001	Efremovka	CV3red	E69	B	5–34		6.1	1.9	6.2	2.0	0.2459	0.0180	12	1.3	1.9	✓
Wielandt et al. 2012	Efremovka	CV3red	E38	B	1–52	14–1677	4.4	0.6	6.5	1.0	0.2503	0.0046	8	0.9	2.1	✓
MacPherson et al. 2003	Leoville	CV3red	3535-3b	CTA	1–14	70–190	6.7	2.4	6.7	2.4	0.2481	0.0126	9	1.7	2.0	✓
Wielandt et al. 2012	Efremovka	CV3red	31E	B	8–79	52–968	4.7	0.8	6.9	1.2	0.2510	0.0026	7	1.0	2.2	✓
Srinivasan et al. 2013	Efremovka	CV3red	E36	B2			7.0	1.4	7.0	1.1	0.2510	0.0008	20	1.4	1.6	✓
Srinivasan et al. 2013	Efremovka	CV3red	E65	CTA			7.0	1.7	7.0	1.8	0.2493	0.0014	17	0.8	1.7	✓
Wielandt et al. 2012	Efremovka	CV3red	E48	B	2–90	59–867	4.8	0.3	7.1	0.4	0.2500	0.0020	9	0.9	2.0	✓
MacPherson et al. 2003	Vigarano	CV3red	477-5	FTA	1–20	29–340	7.5	1.9	7.4	1.9	0.2381	0.0138	13	1.6	1.8	✓
MacPherson et al. 2003	Efremovka	CV3red	6456-1	CTA	9–75	300–2160	7.6	1.6	7.6	1.6	0.2520	0.0102	6	1.9	2.3	✓
Srinivasan et al. 2013	Efremovka	CV3red	E66	B			7.6	2.9	7.6	1.8	0.2498	0.0010	20	2.3	1.6	×
Sujura et al. 2001	Efremovka	CV3red	E44	B	10–100		7.6	1.9	7.6	2.4	0.2502	0.0046	13	0.7	1.8	✓
Wielandt et al. 2012	Efremovka	CV3red	E104	CTA	7–66	334–614	5.5	1.4	8.1	2.0	0.2426	0.0062	5	0.5	2.4	✓
Sujura et al. 2001	Efremovka	CV3red	E48	B	19–96		8.1	3.1	8.2	3.4	0.2490	0.0074	5	0.8	2.4	✓
Wielandt et al. 2012	Efremovka	CV3red	E104	FTA	19–127	165–786	6.7	0.9	9.8	1.3	0.2482	0.0006	8	1.1	2.1	✓
Mishra et al. 2019	Efremovka	CV3red	E40	B1	4–632	73–536	16.0	10.0	16.0	5.2	0.2347	0.0147	8	3.0	2.1	×

[1] The $^{9}Be/^{11}B$ values and errors were estimated, so the final regressions are different

[2]concentrations in ng/g

[3]These $^{10}Be/^{9}Be$ ($\times 10^{-4}$) values are the original published data

[4]These $^{10}Be/^{9}Be$ ($\times 10^{-4}$) values are our re-evaluated data based on raw published data

[5]The is the maximum allowable MSWD based on the number of analysis points (n),

[6]Evaluation of regression, MSWD: ✓ if MSWD > $1+2\sigma_{MSWD}$, × if MSWD < $1+2\sigma_{MSWD}$

CTA=compact Type-A; FTA=fluffy Type-A; PLAC=platy hibonite; FUN=fractionated and unidentified nuclear effects

2.4. Evidence for Irradiation

Even after checking that the SIMS analyses are conducted on clean, crack-free areas of pristine (i.e., no evidence of aqueous alteration) CAIs, and selecting only regressions with acceptable MSWD values, the inferred $^{10}Be/^{9}Be$ ratios still may not represent the original $^{10}Be/^{9}Be$ ratios at the time the CAI formed. In fact, irradiation can artificially elevate the inferred initial $^{10}Be/^{9}Be$ ratio. In the top 1-2 meters of parent body regolith, energetic ions such as galactic cosmic rays (GCRs) can irradiate heavy nuclei, such as O, Mg, or Si, to generate light nuclei. Or, secondary protons and neutrons generated by this process can spall nuclei. Because the concentration of secondary protons and neutrons generated depends on the types of nuclei in the meteorite, the production rates of Be and B depend on the parent body composition, and are uncertain to within ~50% (Leya et al., 2000). For the GCR fluences ($\sim 10^{14}$ -10^{15} cm^{-2}) typically experienced by meteorites within a few meters of their parent body's surface, ng/g changes in the concentrations of Be and B can be generated. Typically, the spallogenic $^{10}B/^{11}B$ ratio is ~ 0.44, significantly higher than the chondritic ratio $^{10}B/^{11}B$ ~0.248 (Liu et al., 2010). Because B concentrations are sometimes as low as a few ng/g in CAIs, this spallogenic component cannot always be neglected.

Addition of spallogenic B to a CAI would lower the $^{9}Be/^{11}B$ ratios and raise the $^{10}B/^{11}B$ ratios, both effects tending to artificially increase the slope, steepening the isochron. Addition of spallogenic Be would have the opposite effect, but in general its effect on the total Be concentration is comparatively negligible because Be contents are much higher than B contents in melilite (typically, [Be]~500 μg/g and [B]~10 ng/g). To

approximate Be and B production by irradiation, we consider an oxygen target because it has a significantly higher abundance than nitrogen or carbon in CAIs and the reactions to produce Be and B from O are efficient. Using the cross sections for spallation of ^{16}O by high-energy protons ($^{16}O(p,x)^{11}B$ ~ 25 mbarn while $^{16}O(p,x)^{10}Be$ ~ 2 mbarn; Moskalenko and Mashnik 2003), we estimate the ratio of spallogenic Be to spallogenic B (Δ[Be]/ Δ[B]) of ~0.1. It might be expected that addition of spallogenic Be or B might also increase the scatter in the data and the MSWD, but in fact the isochron is not automatically worsened by irradiation.

We use the example of CAI Lisa, from the Northwest Africa (NWA) 6991 ($CV3_{ox}$) carbonaceous chondrite, to examine how a regression would change due to irradiation. We used this CAI specifically for this example because its Sm isotope composition suggests that it was irradiated by thermal neutrons (Shollenberger et al., 2018). The major element composition of phases in this CAI were determined using the JEOL JXA-8530F electron probe microanalyzer (EPMA) at ASU using conditions similar to those described in Section 2.2. The ^{10}Be–^{10}B isotope systematics of this CAI were measured with the IMS-1290 SIMS at UCLA using analysis conditions similar to those described earlier in Section 2.3.2. These data are reported in Table 2.4.

Table 2.4

^{10}Be–^{10}B isotope systematics of NWA 6991 (CV3ox) CAI Lisa.

CAI SIMS						[Be]				
spot	^{9}Be/^{11}B	Uncertainty[1]	^{10}B/^{11}B	Uncertainty[1]	r[2]	µg/g	[B] µg/g	Al_2O_3[3]	Ak[4]	SiO_2[3]
Lisa(1290)_1	15.21	0.46	0.2922	0.0110	0.19	0.183	0.018	23	38	27
Lisa(1290)_3	1.72	0.04	0.2481	0.0032	0.20	0.145	0.126	26	28	26
Lisa(1290)_4	17.29	0.55	0.2794	0.0120	0.40	0.250	0.022	24	34	27
Lisa(1290)_5	12.89	0.35	0.2821	0.0070	0.33	0.257	0.030	26	26	25
Lisa(1290)_6	15.27	0.42	0.2756	0.0074	0.35	0.356	0.035	21	43	28
Lisa(1290)_7	6.36	0.16	0.2620	0.0044	0.06	0.349	0.082	24	35	27
Lisa(1290)_8	15.54	0.45	0.2679	0.0086	0.38	0.273	0.026	24	32	26

[1]1 sigma standard errors

[2]r is the correlation coefficient

[3]Abundances in wt. %

[4]Abundances in mol %

From the ^{9}Be/^{11}B and ^{10}B/^{11}B ratios of phases in this CAI (Table 2.4), we calculated an inferred initial ^{10}Be/^{9}Be = $(2.2 \pm 0.7) \times 10^{-3}$ (MSWD = 1.1). This is much higher (by about 3 times) than in typical CAIs, so we tested whether CAI Lisa could have a high inferred ^{10}Be/^{9}Be ratio because its original ^{10}Be/^{9}Be ratio was overprinted by an irradiation signature. To do so, we subtracted an assumed spallogenic B contribution (Δ[B]) from the measured B concentrations (which ranged from ~20 to ~130 ng/g) and reconstructed the regression. If we can produce a regression with MSWD ~ 1 with a resolvably lower ^{10}Be/^{9}Be (say ~ 7×10^{-4}, a value similar to most other CAIs; Table 2.3)

by subtracting a reasonable $\Delta[\mathrm{B}]$, then disturbance of the isochron by addition of spallogenic B produced by irradiation of the CAI on the parent body cannot be ruled out.

To determine the original $^{9}Be/^{11}B$ and $^{10}B/^{11}B$ ratios before irradiation, we derived and used the following equations:

$$\left(\frac{^{9}\mathrm{Be}}{^{11}\mathrm{B}}\right)_{\mathrm{original}} = \left(\frac{^{9}\mathrm{Be}}{^{11}\mathrm{B}}\right)_{\mathrm{measured}} \times \frac{\left[1 - \frac{\Delta[\mathrm{Be}]}{[\mathrm{Be}]}\right]}{\left[1 - \frac{\Delta[\mathrm{B}]}{[\mathrm{B}]}\left(\frac{11.01 + 10.01 \times \left(^{10}\mathrm{B}/^{11}\mathrm{B}\right)_{\mathrm{measured}}}{11.01 + 10.01 \times 0.44}\right)\right]}$$

$$\left(\frac{^{10}\mathrm{B}}{^{11}\mathrm{B}}\right)_{\mathrm{original}} = \left(\frac{^{10}\mathrm{B}}{^{11}\mathrm{B}}\right)_{\mathrm{measured}} \times \frac{\left[1 - \frac{\Delta[\mathrm{Be}]}{[\mathrm{Be}]}\frac{0.44}{\left(^{10}\mathrm{B}/^{11}\mathrm{B}\right)_{\mathrm{measured}}}\left(\frac{11.01 + 10.01 \times \left(^{10}\mathrm{B}/^{11}\mathrm{B}\right)_{\mathrm{measured}}}{11.01 + 10.01 \times 0.44}\right)\right]}{\left[1 - \frac{\Delta[\mathrm{B}]}{[\mathrm{B}]}\left(\frac{11.01 + 10.01 \times \left(^{10}\mathrm{B}/^{11}\mathrm{B}\right)_{\mathrm{measured}}}{11.01 + 10.01 \times 0.44}\right)\right]}$$

We varied $\Delta[\mathrm{B}]$ and $\Delta[\mathrm{Be}]$, assuming $\Delta[\mathrm{Be}]/\Delta[\mathrm{B}] = 0.1$, then calculated original ratios for each CAI Lisa analysis spot, and constructed a new (pre-irradiation) regression. We find that subtracting only ~2.5 ng/g of spallogenic B from each analysis point results in a regression consistent at the 2-sigma level with $^{10}Be/^{9}Be \sim 7\times10^{-4}$ and with MSWD ~ 1 (Figure 2.4). The intercept, i.e., the initial $(^{10}B/^{11}B)_0$, does not change resolvably. In plotting the inferred initial $^{10}Be/^{9}Be$ vs $\Delta[\mathrm{B}]$ (Figure 2.5a), we show that as we subtract more hypothetical spallogenic B from the measured abundance, the apparent $^{10}Be/^{9}Be$ decreases systematically. In plotting the inferred initial $^{10}Be/^{9}Be$ vs MSWD, we show that the MSWD increases slightly as the apparent $^{10}Be/^{9}Be$ decreases, but not drastically enough that the regression could be considered an errorchron (Figure 2.5b).

When high-energy Galactic cosmic ray protons interact with nuclei within the first few meters of the surface of a parent body, a cascade of particle reactions occurs. The cascade produces high-energy neutrons, thermal neutrons (from the deceleration of

fast neutrons; Leya et al. 2000), protons, and likely some ^{10}Be, ^{10}B, and ^{11}B (from protons spalling oxygen nuclei). The isotope ^{149}Sm has a large thermal neutron capture cross section, so it is likely to capture the thermal neutrons (Shollenberger et al., 2018). CAI Lisa is measured to have an excess in ^{150}Sm (relative to terrestrial reference materials), the result of neutron capture on ^{149}Sm. This indicates that CAI Lisa experienced an especially high neutron fluence, when compared to other CAIs, of 2.11×10^{15} n/cm^2 (Shollenberger et al., 2018). This high neutron fluence provides evidence that CAI Lisa was close to the surface of its NWA 6991 parent body, which also had to be bombarded with high energy cosmic ray protons. We estimate that high-energy proton irradiation of CAIs near the surface of the NWA 6991 parent body can produce ng/g levels of spallogenic B. We base our findings on Leya et al. (2000): irradiation of the uppermost tens of cm of near-surface H chondrite material by the present-day Galactic cosmic ray flux at 1 AU can produce the similar isotope ^{10}Be at a rate of 17 disintegrations per minute per kg. If multiplied by 1 Gyr, this would yield a concentration of [^{10}Be] = 0.15 ng/g. The cross sections for spallation of ^{16}O to produce the stable isotopes ^{10}B and ^{11}B are, respectively, about 5 and 12 times the cross section for spallation of ^{16}O to produce ^{10}Be (Moskalenko & Mashnik, 2003), so we estimate that irradiation of near-surface chondritic material could raise the concentration of boron by 2.8 ng/g. It is then plausible that high-energy proton irradiation of CAIs near the surface of the NWA 6991 parent body could produce ng/g levels of spallogenic B necessary to artificially shift the ^{10}Be–^{10}B systematics of CAI Lisa as illustrated in Figure 2.4. Future correlated measurements of ^{150}Sm and ^{10}Be in CAIs could verify the possibility that proton irradiation on the

surfaces of chondritic parent bodies altered the original ^{10}Be–^{10}B systematics in some CAIs.

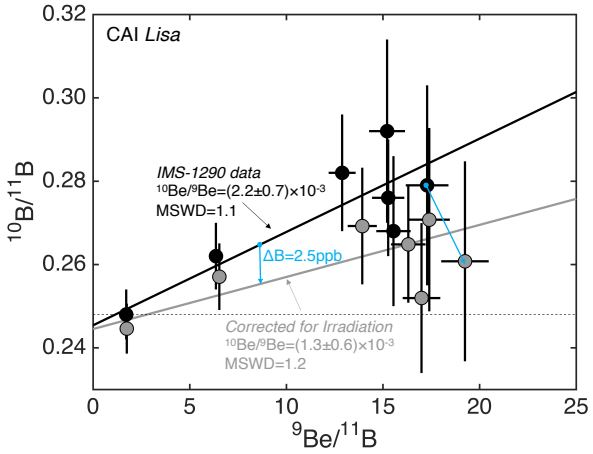


Figure 2.3. Measured and modeled data for CAI Lisa. The black symbols represent the original IMS-1290 data and the gray symbols represent the re-calculated regression after subtracting 2.5 ng/g of spallogenic B from the original data. The isochron regression results are shown. The horizontal dashed line is the chondritic B isotope ratio (^{10}B/^{11}B=0.2481; Zhai et al., 1998). Uncertainties are 2σ.

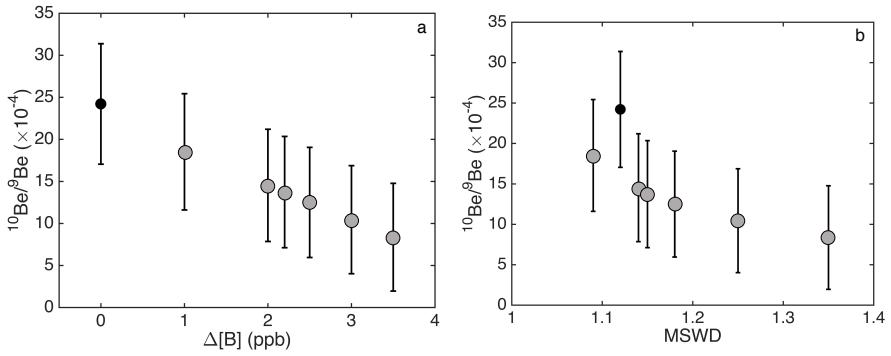


Figure 2.4. The estimated ^{10}Be/^{9}Be ratios based on the measured (black symbol) and modeled (gray symbols) data for CAI Lisa versus (a) the amount of spallogenic B (ΔB) subtracted from the total B and (b) MSWD. Panel (a) shows that the inferred initial ^{10}Be/^{9}Be ratio decreases as greater amounts of spallogenic B (ΔB) are subtracted. Panel (b) shows that the MSWD does not change significantly as more spallogenic B is subtracted, even as the inferred ^{10}Be/^{9}Be ratio decreases.

When high-energy Galactic cosmic ray protons interact with nuclei within the first few meters of the surface of a parent body, a cascade of particle reactions occurs. The cascade produces high-energy neutrons, thermal neutrons (from the deceleration of fast neutrons; Leya et al. 2000), protons, and likely some ^{10}Be, ^{10}B, and ^{11}B (from protons spalling oxygen nuclei). The isotope ^{149}Sm has a large thermal neutron capture cross section, so it is likely to capture the thermal neutrons (Shollenberger et al., 2018). CAI Lisa is measured to have an excess in ^{150}Sm (relative to terrestrial reference materials), the result of neutron capture on ^{149}Sm. This indicates that CAI Lisa experienced an especially high neutron fluence, when compared to other CAIs, of 2.11×10^{15} n/cm^2 (Shollenberger et al., 2018). This high neutron fluence provides evidence that CAI Lisa

was close to the surface of its NWA 6991 parent body, which also had to be bombarded with high energy cosmic ray protons. We estimate that high-energy proton irradiation of CAIs near the surface of the NWA 6991 parent body can produce ng/g levels of spallogenic B. We base our findings on Leya et al. (2000): irradiation of the uppermost tens of cm of near-surface H chondrite material by the present-day Galactic cosmic ray flux at 1 AU can produce the similar isotope ^{10}Be at a rate of 17 disintegrations per minute per kg. If multiplied by 1 Gyr, this would yield a concentration of [^{10}Be] = 0.15 ng/g. The cross sections for spallation of ^{16}O to produce the stable isotopes ^{10}B and ^{11}B are, respectively, about 5 and 12 times the cross section for spallation of ^{16}O to produce ^{10}Be (Moskalenko & Mashnik, 2003), so we estimate that irradiation of near-surface chondritic material could raise the concentration of boron by 2.8 ng/g. It is then plausible that high-energy proton irradiation of CAIs near the surface of the NWA 6991 parent body could produce ng/g levels of spallogenic B necessary to artificially shift the ^{10}Be–^{10}B systematics of CAI Lisa as illustrated in Figure 2.4. Future correlated measurements of ^{150}Sm and ^{10}Be in CAIs could verify the possibility that proton irradiation on the surfaces of chondritic parent bodies altered the original ^{10}Be–^{10}B systematics in some CAIs.

2.5. Evidence for Aqueous Alteration

Another secondary process that could affect the ^{10}Be–^{10}B system is thermal metamorphism and/or aqueous alteration on the meteorite parent body. We focus on aqueous alteration here because the diffusion coefficients for B in silicates are quite slow

(Zhang et al., 2010); thermal metamorphism would only cause B to move if a B-bearing phase actually broke down and/or a new boron phase began to grow. Podosek et al. (1991) demonstrated that some Allende ($CV3_{ox}$) CAIs display disturbances in the ^{26}Al-^{26}Mg system, especially in melilite. Be is refractory and was likely introduced into the CAI at an early stage. It has a 50% condensation temperature of 1500 K as gugiate ($Ca_2BeSi_2O_7$) in solid solution with melilite (Lauretta and Lodders 1997). On the other hand, B has a 50% condensation temperature of only 964 K and was incorporated mostly as danburite ($NaBSi_3O_8$) in solid solution with anorthite (Lauretta & Lodders, 1997). The moderately volatile nature of B causes its depletion in characteristic CAI minerals. Although B diffuses more slowly than Mg (at least in anorthite; Sugiura et al. 2001), it may be released to, or precipitated from, an aqueous fluid during parent body alteration.

There are a number of unknowns when discussing the effect of aqueous alteration on the ^{10}Be–^{10}B regression. What is the temperature and composition of the aqueous phase? Specifically, what is the B concentration and isotopic composition of this phase? What are the diffusion characteristics of B in melilite? It is likely that the fluid-rock interaction is heterogeneous and may only affect a few data points, which would increase the scatter of the data points (adding B to some, subtracting B from others) that define the regression without necessarily altering the inferred initial $^{10}Be/^{9}Be$ ratio. If secondary mineralization (replacement of melilite by nepheline, sodalite, hedenbergite, and andradite; Wasson et al. 2001) is present, it proves that alteration by an H_2O-bearing phase occurred. Overall, little information exists about B behavior during aqueous alteration, especially with regard to melilite, but we expect that any chondritic B

exchange between parent body aqueous fluids and melilite would result in more scatter (i.e., higher MSWD) in the CAI ^{10}Be–^{10}B regression.

2.6. Method for Future Reporting of ^{10}Be–^{10}B Isotope Systematics

Integrating the results from future studies of ^{10}Be–^{10}B isotope systematics in primitive meteoritic materials into a consistently reported data set will increase the scientific impact of this work by allowing comparisons and by enabling an assessment of the original distribution of ^{10}Be in the early Solar System (which has implications for its origin). Comparisons between datasets are only possible if studies follow a standardized reporting procedure. The linear regressions are reproducible only if the authors report these five quantities for each analysis point: $x = {}^{9}\text{Be}/{}^{11}\text{B}$, uncertainty in x, $y = {}^{10}\text{B}/{}^{11}\text{B}$, and uncertainty in y. The next quantities are also key to report, but are not necessary to reproduce the isochrons: 1) MSWD to assess the robustness of the regression (ideally, authors should also report whether their MSWD exceeds the critical value $1 + 2(2/(n-2))^{1/2}$, and if so, provide a discussion about the validity of that isochron); 2) the specific reference materials utilized in the study, along with the resulting RSF and IMF values; 3) the compositional data for the phases that are analyzed; specifically [B] and [Be] in μg/g or ng/g (to enable corrections, as needed, for irradiation), Åk content, and abundances of SiO_2, and Al_2O_3; and 4) error correlations (which may not significantly affect the slope of the isochron but can alter the MSWD). In following this reporting strategy, researchers will be able to more easily compare results from different studies and interpret the available ^{10}Be–^{10}B data as a whole.

2.7. Conclusions

In the context of determining the origin of ^{10}Be in the early Solar System, we have re-evaluated previous ^{10}Be–^{10}B studies, while examining the importance of analytical and data reduction factors such as Relative Sensitivity Factor (RSF), mean square weighted deviation (MSWD), and correlation coefficient, as well as natural factors such as irradiation and aqueous alteration. To properly compare ^{10}Be/^{9}Be values between samples to determine if the distribution of ^{10}Be in the early Solar System was homogeneous or heterogeneous, it is vital to standardize the processing of data obtained via SIMS analyses. Using an inappropriate RSF can change the inferred initial ^{10}Be/^{9}Be ratio; we synthesized melilite-composition glass reference materials and agree with Fukuda et al. (2018) that matrix-matched reference materials for RSF determination are not necessary to establish accurately determine ^{10}Be–^{10}B isotope systematics in CAIs. Another measurement consideration to take into account is that individual SIMS analyses should only be made on single-phase, crack-free grains. It is also important to standardize how data are reported. MSWD is essential to report because this quantity allows us to assess the validity of an isochron; specifically, if the MSWD exceeds $1 + 2(2/(n\text{-}2))^{1/2}$, where n is the number of datapoints in the regression, the regression has < 5% probability of being an isochron (Wendt & Carl, 1991). Correlated errors should be taken into consideration when generating a ^{10}Be–^{10}B isochron because they can affect the uncertainties in the slope and intercept, and the MSWD of a regression.

Even after these analytical and data reduction factors are taken into consideration, the inferred initial ^{10}Be/^{9}Be ratio may not be the original one in a given CAI. Because B

concentrations in CAI phases are typically low and this element can be produced by proton irradiation, some data sets may need to be corrected for spallogenic B; even a few ng/g of spallogenic B can change the inferred initial $^{10}Be/^{9}Be$ ratio significantly without affecting the MSWD. Aqueous alteration on the chondrite parent body likely introduces scatter in the ^{10}Be–^{10}B data and increases the MSWD. The re-evaluated dataset presented here (based on data reported previously for 32 CAIs), along with implications presented here for the ^{10}Be–^{10}B isotope system, can be integrated with future studies to constrain the origin of ^{10}Be in the early Solar System.

CHAPTER 3

UNIFORM LEVEL OF ^{10}BE IN CR2 CAIs SUGGESTS IT WAS INHERITED DURING SOLAR SYSTEM FORMATION

3.1 Introduction

The initial abundances and distributions of now-extinct short-lived radionuclides (SLRs) provide important constraints on the astrophysical environment in which the Solar System formed. Among all SLRs that were present in the early Solar System, ^{10}Be ($t_{1/2}$ = 1.4 Ma) is of special interest because it is exclusively produced by non-thermal nuclear reactions induced by energetic charged particles. Therefore, this radionuclide allows us to constrain the irradiation conditions in the molecular cloud core and the solar nebula. Previous studies of calcium-aluminum-rich inclusions (CAIs) in meteorites from the Vigarano-type carbonaceous (CV) and High-metal/Bencubbin-type carbonaceous (CH/CB) chondrite groups have revealed that ^{10}Be existed in the early Solar System at the abundance levels of ^{10}Be/^{9}Be ~$(3 - 100) \times 10^{-4}$, although the majority of CAIs are characterized by a value of ~7×10^{-4} within analytical uncertainties (McKeegan et al., 2000; Sugiura et al., 2001; Marhas et al., 2002; MacPherson et al., 2003; Chaussidon, 2006; Liu et al., 2010; Wielandt et al., 2012; Srinivasan & Chaussidon, 2013; Gounelle et al., 2013; Sossi et al., 2017; Fukuda et al., 2018, 2019; Mishra & Marhas, 2019; Dunham et al., 2020).

Three astrophysical models proposed to account for such ^{10}Be abundances in the Solar System include: (1) spallation reactions by galactic cosmic ray (GCR) reactions in

the molecular cloud just before the Sun's formation (Gounelle et al., 2001; Desch et al., 2004; Tatischeff et al., 2014); (2) spallation reactions by solar energetic particles (SEPs) accelerated by flares from the young Sun in the CAI-forming region (McKeegan et al., 2000; MacPherson et al., 2003; Bricker & Caffee, 2010; Jacquet, 2019); and (3) production by neutrino reactions in the ejecta of a low-mass supernova, injected into the solar system during its formation (Banerjee et al., 2016). These models are expected to result in different spatial and temporal distributions of ^{10}Be in the solar nebula. A molecular cloud or supernova origin would likely lead to spatial uniformity, as mixing would occur rapidly during the collapse of the cloud (< ~10^5 years) to form the Solar System (Ouellette et al., 2009; Everett & Zweibel, 2011; Tatischeff et al., 2014). In contrast, the *in situ* production of ^{10}Be in the solar nebula depends on several parameters, such as the flux of energetic charged particles, solid or gas irradiation, heliocentric distance, and irradiation time; as such, CAIs that formed at somewhat different times or at different distances from the Sun are expected to have incorporated different abundances of ^{10}Be (Jacquet, 2019). Therefore, a quantitative constraint on the ^{10}Be abundance variation (or lack thereof) in CAIs may shed light on the astrophysical origin of this radionuclide. In addition to ^{10}Be, it is also important to consider the initial abundance of another SLR, ^{26}Al ($t_{1/2}$ = 0.705 Ma), in CAIs, as this radionuclide is thought to have been homogeneously distributed in the solar nebula and has been widely accepted to place constraints on the timing of high-temperature processing (Jacobsen et al., 2008; MacPherson et al., 2012b; Kita et al., 2013; Gregory et al., 2020). The relationship

between ^{26}Al and ^{10}Be provides further constraints on the astrophysical process that created ^{10}Be.

Our knowledge about the abundance of ^{10}Be is largely derived from CAIs in CV chondrites because they are large (up to centimeters in diameter) and abundant (~3−4 volume %) compared to those in other meteorite types (MacPherson, 2013). However, many CV3 chondrites, such as Allende, are known to have undergone aqueous alteration and thermal metamorphism in a parent body setting [25] that could potentially compromise the boron isotopic compositions of CAIs. This calls into question whether the initial ^{10}Be/^{9}Be values derived from CV3 CAIs are representative of the true variation in the solar nebula. Other CAIs previously measured for ^{10}Be–^{10}B systematics come from Murchison-type carbonaceous (CM) chondrites, which also experienced extensive parent body aqueous alteration (Rubin et al., 2007), and CH/CB chondrites, which experienced an unusual accretionary history likely involving impact processes (Garvie et al., 2017).

To minimize any effects of parent body alteration on the ^{10}Be–^{10}B isotopic system, we report measurements of five CAIs from CR2 chondrites, which are among the least altered chondrites (Aléon et al., 2002; Makide et al., 2009; Schrader et al., 2011, 2015; Davidson et al., 2019). Although CR2 chondrites experienced varying degrees of low-temperature aqueous alteration (at 55 to 88°C), they are significantly less thermally metamorphosed than many other chondrites (Jilly-Rehak et al., 2018). Most CR2 CAIs, albeit small (<500 μm) and rare (<1 volume% (Scott & Krot, 2013)), are mineralogically pristine and lack secondary alteration products (Aléon et al., 2002; Makide et al., 2009;

Schrader et al., 2011, 2015; Davidson et al., 2019). Thus, CR2 CAIs provide an opportunity to better evaluate whether there was $^{10}Be/^{9}Be$ variation in the solar nebula.

3.2 CR2 CAI Petrologic Characterization Results

We carried out *in situ* isotopic studies of ^{10}Be–^{10}B systematics in melilite (solid solution between $Ca_2Al_2SiO_7$ and $Ca_2MgSi_2O_7$) of five CR2 CAIs and ^{26}Al–^{26}Mg systematics in melilite, spinel, pyroxene, and anorthite of three of these CAIs. We investigated the following CAIs from four pristine CR2 chondrites: One ("Cereus") from LaPaz Icefield (LAP) 02342 (CR2.7 (Howard et al., 2015)), two ("Yucca" and "Creosote") from Miller Range (MIL) 090657 (CR2.7 (Davidson et al., 2019)), one ("Dalea") from Shişr 033, and one ("Palo Verde") from Northwest Africa (NWA) 801. Petrologic subtypes have not been determined for Shişr 033 and NWA 801 beyond their characterization as CR2, but based on their oxygen isotope data and modal mineralogy, they are both between 2.3 and 2.7 (Schrader et al., 2011, 2014; Howard et al., 2015). CAIs were characterized via electron probe microanalysis (EPMA; see Supplemental Materials Figures 3.4–3.8 for backscattered electron images and elemental maps of CAIs and Table S1 for major element compositions). It is important to note that although all four of these chondrites are considered pristine compared to other types of carbonaceous chondrites, some are more so than others; even though LAP 02342 and MIL 090657 are both classified as 2.7, MIL 090657 is generally more pristine and the matrix of LAP 02342 has been heterogeneously aqueously altered (Davidson et al., 2019; Nittler et al., 2019).

The CAIs range in diameter from 40 μm to 950 μm, and vary mineralogically, texturally, and morphologically. The CAIs *Cereus* (from LAP 02342), *Creosote*, and *Yucca* (both from MIL 090657), which are mineralogically most comparable to compact type A (CTA) CAIs (MacPherson, 2013), are rounded or fragmented inclusions predominantly containing coarse melilite enclosing spinel, pyroxene, and sometimes anorthite. The CAI *Dalea* (from Shişr 033) is an irregularly-shaped, fine-grained/unmelted CAI composed of spinel-pyroxene-melilite nodules formed into aggregates. The CAI *Palo Verde* (from NWA 801) is a small, rounded melilite grain (see Supplement Figures 3.4–3.8 for more detailed characterization of these CAIs). The CAIs show little or no evidence for the presence of alteration minerals (such as phyllosilicates, calcite, and sodalite (Harju et al., 2014)); only *Creosote* has minor calcite grains in its interior (Figures 3.4, 3.5). We were careful to avoid these alteration phases when undertaking isotopic analyses. We measured the CAI interiors for ^{10}Be–^{10}B and ^{26}Al–^{26}Mg isotope systematics, and additionally measured thin rims, when present, for ^{26}Al–^{26}Mg isotope systematics.

3.3 CR2 CAI Isotope Characteristic Results

The ^{10}Be–^{10}B and ^{26}Al–^{26}Mg isotopic analyses were carried out using the Cameca IMS-1290 secondary ion mass spectrometer (SIMS) at the University of California, Los Angeles (UCLA) and the IMS-1280 SIMS at the University of Wisconsin, Madison, respectively (see Tables S2 and S3 for ^{10}Be–^{10}B and ^{26}Al–^{26}Mg data, respectively). The Be and B concentrations in all eight CAIs vary from 400 to 2,400 ng/g and 16 to 11,840

ng/g, respectively. Ratios of $^{9}Be/^{11}B$ in the CAIs correlate linearly with $^{10}B/^{11}B$, indicative of the decay of live ^{10}Be. Comparing CAI $^{10}B/^{11}B$ vs. B concentration ([B]) to mixing trends between reservoirs of chondritic B and spallogenic B indicates that the CAI $^{10}B/^{11}B$ variation is not a result of mixing (Figure 3.9). The initial $^{10}Be/^{9}Be$ ratios of these inclusions, inferred from the slopes of ^{10}Be–^{10}B isochrons (calculated using a York Regression via Model 1 fit of Isoplot R(Vermeesch, 2018)) are shown in Table 3.1 and Figure 3.1. Within the analytical uncertainties, the $^{10}Be/^{9}Be$ ratios of the CAIs are indistinguishable from one another. All five regressions, although some have large uncertainties, can be considered well-correlated lines, as they have mean square weighted deviation (MSWD) $<1+2\sigma_{MSWD}$ (Wendt & Carl, 1991) where σ_{MSWD} is $\sqrt{2/(n-2)}$ (with n number of data points for 2 degrees of freedom; if MSWD is above this limit, there is less than 5% likelihood that the regression data points are fit by a line.

CAIs *Yucca, Dalea, Palo Verde,* and *Cereus* yield initial $^{10}Be/^{9}Be = (8.7 \pm 3.4) \times 10^{-4}$, $(7.3 \pm 1.4) \times 10^{-4}$, $(10.7 \pm 6.6) \times 10^{-4}$, and $(9.5 \pm 7.6) \times 10^{-4}$, respectively (Table 3.1). The isochrons for the CAIs *Palo Verde* and *Cereus* are not as well-resolved because the spread in the $^{9}Be/^{11}B$ ratios in these CAIs is low (due to their intrinsically low Be and/or high B concentrations) which introduces considerable uncertainty in the slope. CAI *Creosote* shows only marginally resolved ^{10}B excesses correlated with $^{9}Be/^{11}B$ in the range of ~10−40, which yields an isochron corresponding to $^{10}Be/^{9}Be = (2.1 \pm 6.4) \times 10^{-4}$. The B concentrations of melilite in CAI *Creosote* fall within a narrow range (30−70 ng/g), yielding a narrow range of $^{9}Be/^{11}B$; this is the reason for the large uncertainty in the slope of the isochron. However, the initial $^{10}Be/^{9}Be$ ratios inferred for all five of these

CAIs are entirely consistent with each other within the uncertainties. We can calculate the weighted mean initial $^{10}Be/^{9}Be$ of all five CAI regressions to test if the individual CAI regressions lie within uncertainty of the mean and if the CAIs are part of a single population. The weighted mean of the initial $^{10}Be/^{9}Be$ inferred for these five CAIs is (7.5 ± 1.2) × 10^{-4}, a value that lies within the uncertainty of each individual CAI ^{10}Be–^{10}B regression. The MSWD of the weighted mean is 1.2, less than the maximum allowed MSWD (one degree of freedom $1+2\sigma_{MSWD,}$ n=5); as such, the five CR2 CAIs belong in a single population in terms of ^{10}Be abundance.

The ^{26}Al–^{26}Mg isotope systematics were additionally determined in the CAIs *Yucca*, *Dalea*, and *Creosote* to assess whether their inferred $^{10}Be/^{9}Be$ ratios show any correlation with $^{26}Al/^{27}Al$ ratios. Melilite, spinel, and anorthite were analyzed in the interior of the CAIs, and diopside and anorthite in the CAI rims (when present). The three CAIs were found to have the same initial $^{26}Al/^{27}Al$ within uncertainties (Figure 3.2, Table 3.1), with values in the range (4.4 – 4.7) × 10^{-5} and a weighted average initial $^{26}Al/^{27}Al$ = (4.7 ± 0.1) × 10^{-5} (2SE; MSWD = 2.3, less than the allowable MSWD of 3 [n = 3]). All three CAIs are consistent with this value at the 2σ level. The slightly sub-canonical values are indicative of the CAIs forming ~100,000 years after the beginning of the Solar System when $^{26}Al/^{27}Al$ = 5.23× 10^{-5} (Jacobsen et al., 2008). This is in agreement with other CR2 CAIs, which record initial $^{26}Al/^{27}Al$ = (4.5 – 5.0) × 10^{-5} (Makide et al., 2009).

Table 3.1

CR2 CAI ^{10}Be–^{10}B and ^{26}Al–^{26}Mg Isotope Systematics.

Sample	**$(^{10}Be/^{9}Be)_0$**	**$(^{10}B/^{11}B)_0$**	**MSWD^**	**Max $^{9}Be/^{11}B$**	**n**	**$(^{27}Al/^{26}Al)_0$**	**MSWD**	**$\delta^{26}Mg$***	**n**
Yucca[1]	$8.7\pm3.4\times10^{-4}$	0.2438±0.0082	0.4	46	5	$4.37\pm0.36\times10^{-5}$	1.7	0.109±0.106	12
Dalea[2]	$7.3\pm1.4\times10^{-4}$	0.2450±0.0012	0.2	123	5	$4.54\pm0.46\times10^{-5}$	1.7	-0.0081±0.126	4
Creosote[1]	$2.1\pm6.4\times10^{-4}$	0.2562±0.0242	0.4	34	8	$4.69\pm0.12\times10^{-5}$	0.9	-0.066±0.054	21
Cereus[3]	$9.5\pm7.6\times10^{-4}$	0.2504±0.0013	0.9	5	5				
Palo Verde[4]	$10.7\pm6.6\times10^{-4}$	0.2457±0.0014	0.9	8	5				

Notes: errors are 2SE

[1] CR2.7 MIL 090657,6 (Davidson et al., 2019)

[2] CR2 Shişr 033 (Schrader et al., 2015)

[3] CR2.7 LAP 02342,14 (Schrader et al., 2011; Howard et al., 2015)

[4] CR2 NWA 801 (Schrader et al., 2011)

[+]CAIs Sonoran and Rosewood

^All ^{10}Be–^{10}B regressions are robust with MSWD $< 1+2\sigma_{MSWD}$

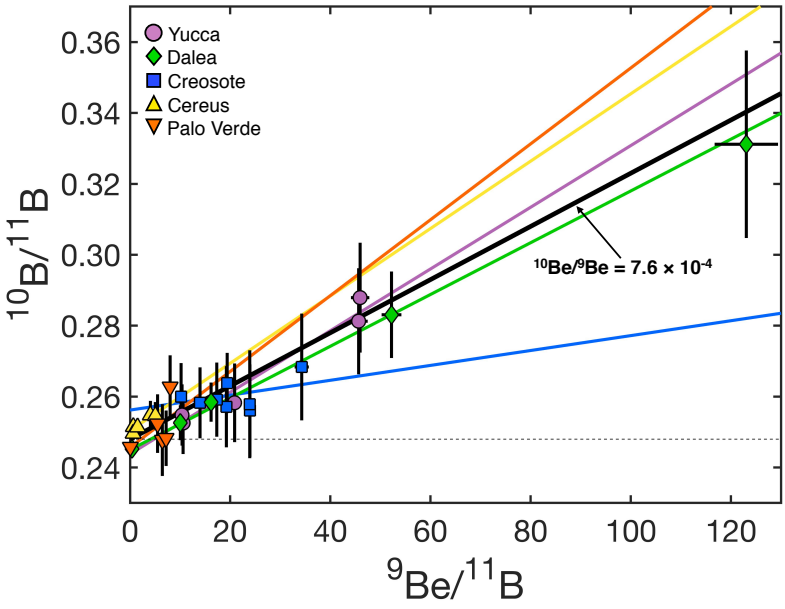


Figure 3.1. ^{10}Be–^{10}B isotope systematics for the five CR2 CAIs studied here. The regression results are shown in Table 3.1. The weighted mean of *Yucca*, *Dalea*, *Creosote, Cereus,* and *Palo Verdo* regressions is shown as the black line and corresponds to an initial ^{10}Be/^{9}Be ratio of (7.5 ± 1.2) × 10^{-4}; all five CAI isochrons yield ^{10}Be/^{9}Be values that are consistent within uncertainty of this line. The horizontal dashed line is the chondritic B isotopic ratio (^{10}B/^{11}B = 0.2481) (Zhai et al., 1996). Uncertainties are 2SE.

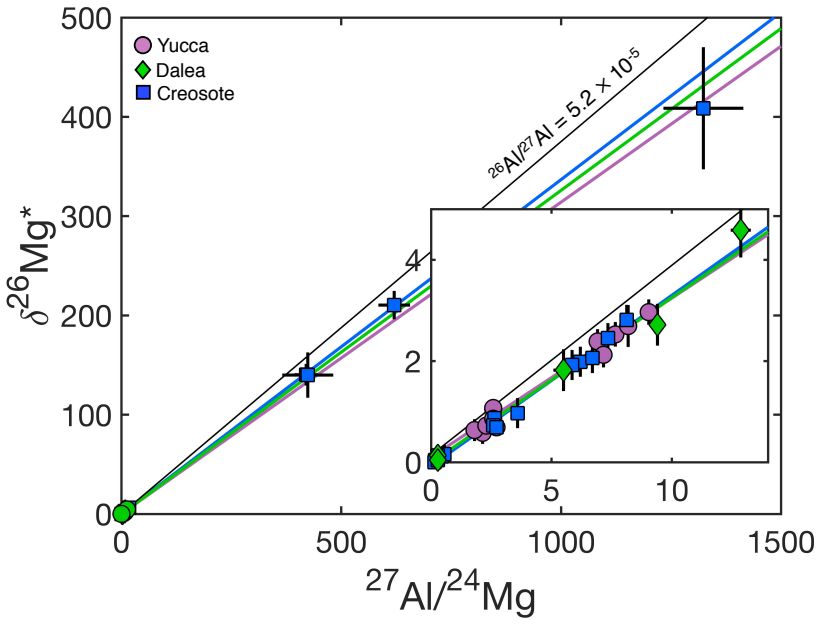


Figure 3.2. ^{26}Al–^{26}Mg systematics of three CR2 CAIs. The isochrons yield $^{26}Al/^{27}Al$ = $(4.36 \pm 0.34) \times 10^{-5}$ (*Yucca*), $(4.54 \pm 0.46) \times 10^{-5}$ (*Dalea*), and $(4.69 \pm 0.12) \times 10^{-5}$ (*Creosote*); the ^{26}Al–^{26}Mg data are given in Table 3.1. The inset shows the region of the plot with $^{27}Al/^{24}Mg$ <20 in more detail; data points in this region include melilite ($^{27}Al/^{24}Mg$ ~5 – 20), pyroxene ($^{27}Al/^{24}Mg$ < 0.6), and spinel ($^{27}Al/^{24}Mg$ ~2.5). Data with the highest $^{27}Al/^{24}Mg$ ratios (>400) are anorthite. For reference, the black line shows canonical $^{26}Al/^{27}Al = 5.23 \times 10^{-5}$ (Jacobsen et al., 2008). Uncertainties are 2SE.

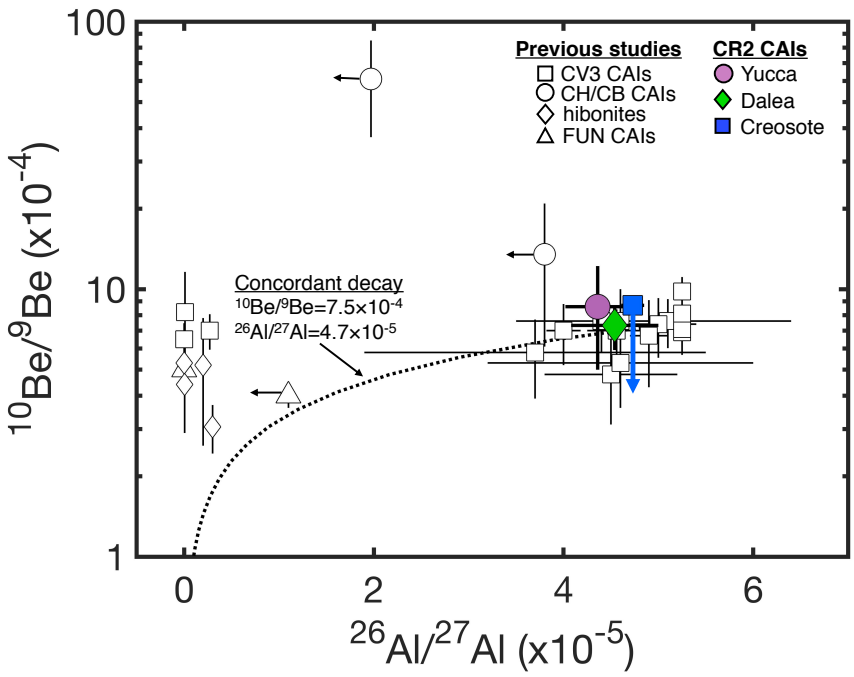


Figure 3.3. CR2 CAI ^{10}Be/^{9}Be and ^{26}Al/^{27}Al systematics. Data obtained in this study (colored symbols) are compared with CV and CH/CB CAI and hibonite literature data (open symbols)(Sugiura et al., 2001; Marhas et al., 2002; MacPherson et al., 2003; Liu et al., 2010; Wielandt et al., 2012; Srinivasan & Chaussidon, 2013) (^{26}Al-poor CV3 CAIs from (Sugiura et al., 2001)). The ^{10}Be/^{9}Be value for CAI Creosote is an upper limit indicated by the arrow. The dashed curve is the concordant decay line if the initial ratios were ^{10}Be/^{9}Be = 7.5 × 10^{-4} (weighted mean of the regressions for the five CR2 CAIs studied here) and ^{26}Al/^{27}Al = 4.7 × 10^{-5} (weighted mean of the regressions for three of these CR2 CAIs, *Yucca*, *Dalea*, and *Creosote*). It is apparent that the ^{26}Al-poor and CH/CB samples represent distinct populations of CAIs. Uncertainties are 2SE.

3.4 CR2 CAIs Record a Uniform ^{10}Be Distribution

Because CR2 CAIs are among the most pristine early Solar System materials that escaped secondary thermal metamorphism and most aqueous alteration (Aléon et al., 2002; Makide et al., 2009; Schrader et al., 2011, 2015; Davidson et al., 2019), and given that their ^{26}Al–^{26}Mg isotope systematics yield good isochrons that do not appear to have been disturbed by secondary processes (Table 3.1; Figure 3.2), they represent ideal targets to test the distribution of ^{10}Be. The measurements presented here provide evidence that CR2 CAIs formed in an environment where ^{10}Be was distributed uniformly because the five CR2 CAIs considered here record the same initial ^{10}Be/^{9}Be value within uncertainty (Table 3.1). It is evident that these CR2 CAIs all formed from a nebular reservoir with ^{10}Be/^{9}Be = (7.5 ± 1.2) × 10^{-4} (i.e., the weighted mean of the regressions for the five CR2 CAIs studied here). Moreover, the ^{26}Al–^{26}Mg systematics in three of these CR2 CAIs additionally suggest that this nebular reservoir was characterized with a uniform ^{27}Al/^{26}Al = (4.7 ± 0.1) × 10^{-5} (Figure 3.3).

It is relevant to put these results in context with previous studies. In a recent study, all previous ^{10}Be data were re-evaluated consistently and MSWDs of the ^{10}Be–^{10}B isochron regressions were determined (Dunham et al., 2020). In this dataset, there is a population of CAIs called the "FUN CAIs" (for Fractionation and Unknown Nuclear effects). When compared to "normal" CAIs that do not have significant fractionations or nuclear effects, FUN CAIs tend to be ^{26}Al-poor and record low ^{10}Be/^{9}Be ratios of ~ 3 – 4 × 10^{-4} (Wielandt et al., 2012). Although we show this data in Figure 3.3, we focus on normal CAIs because isotopically anomalous inclusions represent a distinct population

which likely experienced different formation environments and conditions. There are 27 normal CV3 and CH/CB CAIs with initial $^{10}Be/^{9}Be$ ratios reported in the literature (some ratios were determined from multi-CAI isochrons) (Sugiura et al., 2001; MacPherson et al., 2003; Chaussidon, 2006; Wielandt et al., 2012; Gounelle et al., 2013; Srinivasan & Chaussidon, 2013; Sossi et al., 2017; Fukuda et al., 2019; Dunham et al., 2020). Six of these normal CAIs have regressions associated with high mean square weighted deviation (MSWD $>1+2\sigma_{MSWD}$) which means that the scatter of the data points is greater than can be accounted for by analytical uncertainties; they represent disturbed isochrons. These CAI regressions are then interpreted to not have statistically meaningful $^{10}Be/^{9}Be$ ratios (Dunham et al., 2020). Out of the 21 normal CAIs with MSWD~1, 19 have initial $^{10}Be/^{9}Be$ ratios consistent with $^{10}Be/^{9}Be = (7.5 \pm 1.2) \times 10^{-4}$, and two have initial $^{10}Be/^{9}Be$ ratios more than 3 times higher. Of the latter two, CAI *Lisa* from CV3 chondrite NWA 6991 has $^{10}Be/^{9}Be = (22 \pm 7) \times 10^{-4}$ (Dunham et al., 2020) (2σ; MSWD = 1.1), and CAI SA301 from CH chondrite Sayh al Uhaymir (SaU) 290 has $^{10}Be/^{9}Be = (61 \pm 24) \times 10^{-4}$ (Gounelle et al., 2013; Fukuda et al., 2019) (2σ; MSWD = 0.5). Taking these data at face value and assuming that all 21 CAIs could be representative of the whole population of normal CAIs, we expect that there is a ~90% probability that a randomly selected CAI is consistent with $^{10}Be/^{9}Be = (7.5 \pm 1.2) \times 10^{-4}$ at the < 2σ level, a $(19/21)^5 = 61\%$ probability that 5 randomly selected CAIs all have $^{10}Be/^{9}Be = (7.5 \pm 1.2) \times 10^{-4}$ and a $1-(19/21)^5 = 39\%$ probability that at least 1 out of 5 randomly selected CAIs would yield $^{10}Be/^{9}Be >> 10^{-3}$. Although 90% is a high probability, it nevertheless implies a heterogenous distribution of ^{10}Be as 10% of CAIs would not be characterized by this

ratio. Such ratio differences could not be attributed to the radioactive decay of ^{10}Be because decaying from ^{10}Be/^{9}Be of ~6×10^{-3} to ~7×10^{-4} would take ~4 Myr.

However, one must consider the outliers carefully. The CV chondrite CAI *Lisa* experienced secondary irradiation on the parent body indicated by its high ^{149}Sm (Shollenberger et al., 2018; Dunham et al., 2020); this CAI is suggested to have recorded high ^{10}Be overprinted on the initial signature (Dunham et al., 2020). In addition, some materials (including CAIs) in CH/CB chondrites likely interacted with a high-temperature impact plume before reaccretion to form the CH and CB chondrite parent bodies (Garvie et al., 2017). Accretion and recrystallized in the formation environment of the CH/CB chondrites may imply that some of their CAIs do not record solar nebula conditions while others were not modified by the impact plume as evidenced by their ^{16}O-rich signatures (Krot et al., 2008a). Or it is possible that the two CAIs *Lisa* and *SA301* experienced extra irradiation by an intense flare in the solar nebula. These few CAIs may have unusual histories and care should be applied when comparing them with other data sets and including them in interpretations about the uniformity of ^{10}Be. Therefore, the two CAIs with distinct ^{10}Be/^{9}Be values may be explained by other means and the other 19 previously studied normal CAIs have ^{10}Be/^{9}Be consistent with the weighted mean ^{10}Be/^{9}Be ratio of $(7.5 \pm 1.2) \times 10^{-4}$ determined from the five pristine CR2 CAIs studied here. This supports the uniform distribution of ^{10}Be in the CAI-forming region and the hypothesis that CAIs from different chondrites are genetically linked and likely formed in a common nebular reservoir (Desch et al., 2018; Render et al., 2019). Correlated ^{10}Be and ^{26}Al systematics reported for CAI subsets (Figure 3.3) (Sugiura et al., 2001; MacPherson

et al., 2003; Wielandt et al., 2012; Gounelle et al., 2013; Fukuda et al., 2019) add evidence that most normal CAIs with near-canonical $^{27}Al/^{26}Al$ ratios are characterized by uniform initial $^{10}Be/^{9}Be$ ratios.

3.5 Implications for the Origin of ^{10}Be

The apparently uniform values of $^{10}Be/^{9}Be$ and $^{26}Al/^{27}Al$ among CR2 CAIs argue in favor of an inherited origin for ^{10}Be, and against production by *in situ* irradiation, which would likely lead to CAIs with a wide range of values. Production of ^{10}Be by SEPs will likely lead to higher $^{10}Be/^{9}Be$ values near the Sun that will tend to increase over time. A recent model (Jacquet, 2019) quantified these effects, considering production of ^{10}Be by SEPs traveling along magnetic field lines and intersecting the protoplanetary disk at 0.1 to 1 AU, where they spall isotopes such as ^{16}O, ^{12}C, and ^{14}N, in the nebular gas. This production is balanced against loss of ^{10}Be by inward and outward diffusion in the disk and accretion onto the Sun. The $^{10}Be/^{9}Be$ value is found to vary strongly with distance from the Sun and to increase over time (Jacquet, 2019). The variation with heliocentric distance is significant, dropping by an order of magnitude over just a few tenths of an AU. At all locations, the $^{10}Be/^{9}Be$ value will be proportional to the protostellar X-ray luminosity divided by the disk mass accretion rate, which is estimated to increase roughly linearly with time (Jacquet, 2019). That is, CAIs formed at 200,000 years into disk evolution should have two times higher $^{10}Be/^{9}Be$ compared to CAIs that formed at 100,000 years, and even larger variations can be expected across the CAI-forming region (~0.1 to 1 AU). These variations are not seen in our CR2 CAIs, which are

instead consistent with having formed from a nebular reservoir with a single value of $^{10}Be/^{9}Be = 7.5 \times 10^{-4}$. The initial ^{26}Al abundance in these CAIs is also consistent, within uncertainty, with a single value ($^{27}Al/^{26}Al = 4.7 \times 10^{-5}$); these CR2 CAIs formed ~100,000 years after the first CAIs (that formed with a canonical $^{27}Al/^{26}Al = 5.23 \times 10^{-5}$ (Jacobsen et al., 2008)). Normal CAIs in other chondrites are consistent with this same value, with the few outliers that have a distinct initial ^{10}Be, potentially attributable to irradiation (in the nebula or on the parent body) or alteration on the parent body (Dunham et al., 2020). Because we do not observe a wide range of initial $^{10}Be/^{9}Be$ ratios for the pristine, ^{26}Al-bearing CR2 CAIs, we suggest that ^{10}Be was not produced by irradiation of solar nebula material. If ^{10}Be is not predominantly produced in the solar nebula (MacPherson et al., 2003), it was likely inherited from an external source. It was recently suggested that ^{10}Be could be produced in the ejecta of a low-mass supernova by neutrino reactions (Banerjee et al., 2016). Although we cannot rule out this mechanism for ^{10}Be production using our CR2 CAI dataset, we find it less favorable because supernova neutrino modeling suggests that the amount of ^{60}Fe that would be injected along with the ^{10}Be would lead to initial solar system $^{60}Fe/^{56}Fe$ ratios of $\sim(1–10) \times 10^{-7}$, which is not supported by recent high-precision data that shows that the initial $^{60}Fe/^{56}Fe$ ratio in the solar nebula was $\sim 1 \times 10^{-8}$ (Tang & Dauphas, 2015). Another possible astrophysical environment for the production of ^{10}Be is in the molecular cloud core that collapsed to form our protoplanetary disk. The uniform $^{10}Be/^{9}Be$ values we observe among CAIs provide strong support that inheritance from the molecular cloud is possible. Beryllium-10 is continuously produced in the interstellar medium by spallation reactions induced by

GCR protons interacting with ambient ^{12}C, ^{14}N, and ^{16}O nuclei. Notably, even if ^{10}Be was produced heterogeneously in the molecular cloud, it would have been homogenized during the collapse of the Sun's molecular cloud core (Seifried et al., 2017). It is estimated (Tatischeff et al., 2014) that the spatially averaged, steady-state $^{10}Be/^{9}Be$ value in molecular clouds at the Sun's galactocentric distance 4.57 billion years ago, when the GCR flux is estimated to have been ~1.5 times higher than today, was $\approx 1.3 \times 10^{-4}$. This is lower than our inferred initial $^{10}Be/^{9}Be \approx 7.5 \times 10^{-4}$ in CR2 CAIs, by a factor of ~5–6. Despite this apparent discrepancy, the uniformity of $^{10}Be/^{9}Be$ argues for a molecular cloud origin of ^{10}Be. Because GCR flux traces star formation, we suggest that the Sun formed in a region of higher-than-average star formation.

We have measured the ^{10}Be–^{10}B and ^{26}Al–^{26}Mg isotope systematics in a suite of pristine CR2 CAIs to constrain the origin of the SLR ^{10}Be with the goal of better understanding the astrophysical environment of Solar System formation. We find that CR2 CAIs recorded a weighted mean initial $^{10}Be/^{9}Be = (7.5 \pm 1.2) \times 10^{-4}$ (2SE). This uniform value argues against production of ^{10}Be within the solar nebula, and instead indicates that ^{10}Be is more likely to have been inherited from the molecular cloud. As such, measurements of ^{10}Be–^{10}B isotope systematics in CAIs may be a powerful tracer of the star formation rate in the Sun's birth environment.

3.6. Methods

3.6.1 Sample Preparation and Characterization

The CR2 CAIs were provided as polished thin sections: LAP 02342,14; MIL 090657,6; Northwest Africa 801, UA2300,1; and Shişr 033, UA 2159,1. The JEOL JXA-8530F EPMA at Arizona State University (ASU) was used for sample characterization in preparation for SIMS analyses: elemental maps, backscattered electron (BSE) and secondary electron (SE) images, and mineral compositions using electron dispersive and wavelength dispersive spectroscopy (EDS and WDS). The analytical conditions were 20 kV, 20 nA, and the standards used for ZAF corrections included San Carlos augite, anorthite, Hakone, orthoclase, hornblende, Kakanui, rutile, Johnstown hypersthene, chromite, and Durango apatite. Representative maps and images of the CAIs are shown in Figure 3.4-3.9.

3.6.2 Secondary Ion Mass Spectrometry: ^{10}Be–^{10}B

The ^{10}Be–^{10}B isotope systematics in these five CAIs were determined using the Cameca IMS-1290 secondary ion mass spectrometer (SIMS) at UCLA with a 5−10 nA $^{16}O^-$ primary beam (~5−10 μm diameter), generated by a *Hyperion-II* source (Liu et al., 2018). Secondary ion intensities were measured with multiple electron multipliers (EMs) with a mass resolving power of ~2,500 in dynamic multi-collection mode (first mass jump, 5 sec count time: $^{27}Al^{+++}$, $^{28}Si^{+++}$; second mass jump, 10 sec count time: $^{9}Be^{+}$; third mass jump, 40 sec count time: $^{10}B^{+}$, $^{11}B^{+}$). Analysis spots were pre-sputtered for 3 minutes to remove surface B contamination and the conductive C coat. A NIST 614 glass

was used as a running standard to obtain the $^{9}Be/^{11}B$ relative sensitivity factor (RSF; measured SIMS ion ratio / true atomic ratio) of 3.04 ± 0.05, and the $^{10}B/^{11}B$ instrumental bias (measured / true) of 1.0365 ± 0.0009. All SIMS pits were imaged in BSE and SE mode via EPMA post-analysis; any analyses on cracks, pits, or small inclusions were discarded.

3.6.3 Secondary Ion Mass Spectrometry: ^{26}Al–^{26}Mg Isotope Systematics

The Cameca IMS-1280 WiscSIMS instrument was used to obtain the ^{26}Al–^{26}Mg isotope systematics**.** Due to the small size (~3 μm diameter) of the anorthite grains in CAI *Yucca*, candidate grains were marked using a focused ion beam (FIB)(Defouilloy et al., 2017; Hertwig et al., 2019) with the Nova 200 NanoLab FEI at ASU. These marks in the carbon coat above underlying grains were later located with a SIMS $^{27}Al^{+}$ raster ion image, enabling accurate positioning of SIMS analyses. For anorthite spot analyses, we used a 20 pA $^{16}O_2^{-}$ beam to produce a 3 μm diameter spot, and measurements were made in mono-collection EM mode. The analyses on melilite, spinel, and pyroxene were made with Faraday cups (with three 10^{12} ohm amplifiers for Mg isotopes) in multicollection mode, with a beam current that varied from 0.5 to 2 nA to produce 5−12 μm diameter spots. Detailed data reduction procedures used, including calibration of standards, can be found in (Kita et al., 2012a; Ushikubo et al., 2017). Similar to the ^{10}Be–^{10}B analyses, all ^{26}Al–^{26}Mg SIMS pits were imaged via EPMA post-analysis; if they were located on cracks, pits, or small inclusions, the analyses were discarded and not included in the final regression.

3.7 Sample Characterization

The three-color RGB elemental maps presented here show Mg=red, Ca=green, and Al=blue. The combination of these three elements displays different CAI minerals as different colors; melilite (solid solution between $Ca_2Al_2SiO_7$ and $Ca_2MgSi_2O_7$) is blue/green, spinel ($MgAl_2O_4$) is purple, pyroxene is dark green (diopside ($CaMgSi_2O_6$) while fassaite ($Ca(Mg,Fe,Al,Ti)(Si,Al)_2O_6$ is dark blue/green, anorthite ($CaAl_2Si_2O_8$) is light blue, hibonite ($Ca(Al,Ti,Mg)_{12}O_{19}$) is bright blue, perovskite ($CaTiO_3$) is light green, and calcite ($CaCO_3$) alteration is bright green.

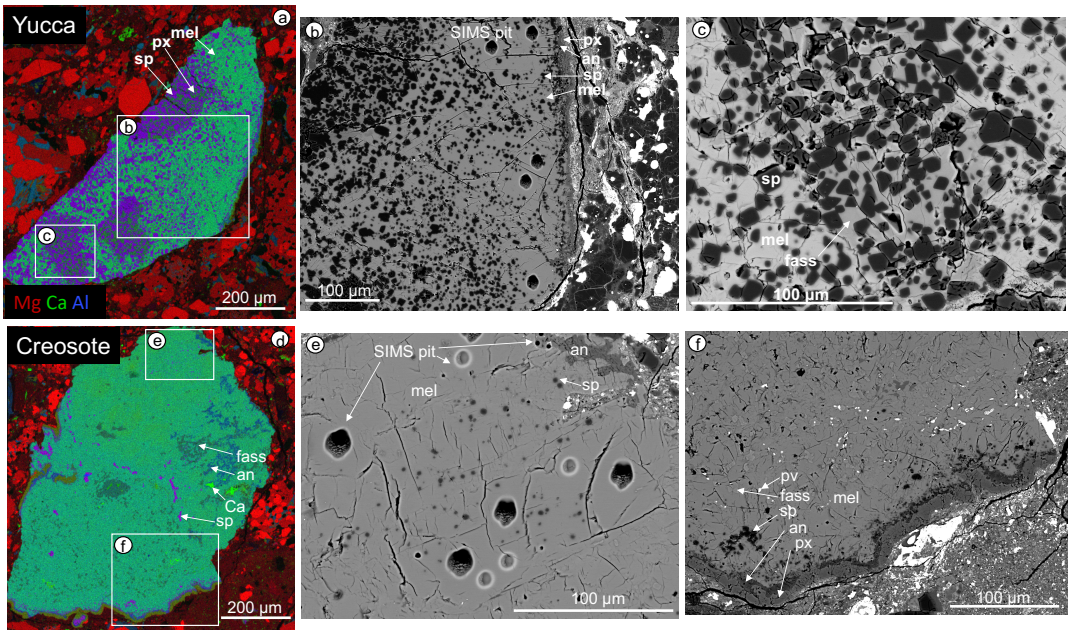


Figure 3.4. **CAIs Yucca and Creosote from CR2.7 chondrite MIL 090657,6.** Panels (a), (b), and (c) show CAI *Yucca*: (a) is an elemental map of the whole CAI, and (b) and (c) are enlarged BSE images of areas indicated in (a). Panels (d), (e), and (f) show CAI *Creosote*: (d) is an elemental map of the whole CAI, and (e) and (f) are enlarged BSE images of areas indicated in (d). The larger SIMS pits (~17 µm diameter) are from the Cameca IMS-1290 ^{10}Be–^{10}B measurements while the smaller SIMS pits (~3 µm and ~10 µm diameters) are from the Cameca IMS-1280 ^{26}Al–^{26}Mg measurements. CAI *Yucca* (longest axis 950 µm) is a rounded fragment composed of melilite ($Ak_{23–30}$) enclosing fassaite (TiO_2; 11–13 wt.%) and large euhedral spinel grains (up to ~40 µm diameter and are concentrated near fassaite). *Yucca* is surrounded by a partial rim that consists of a layer of spinel, anorthite, and diopside moving outwards. No secondary alteration is noted for *Yucca*. CAI *Creosote* (longest axis 900 µm) is a fragment dominated by melilite ($Ak_{16–32}$) enclosing chains of small round spinel grains, and patches of small anorthite

and fassaite (TiO_2 up to 18%) grains. *Creosote* has a partial rim that occasionally curves into the CAI interior; it is composed of layers of spinel, anorthite, and diopside moving outwards. *Creosote* experienced some Ca alteration as evidenced by the presence of a Ca-alteration mineral but the exact phase could not be determined due to electron beam damage. These CAIs are most similar to CAIs from CV3s classified as compact Type A (CTA) CAIs; they are melilite-rich and appear to be igneous based on the coarse-grained texture.

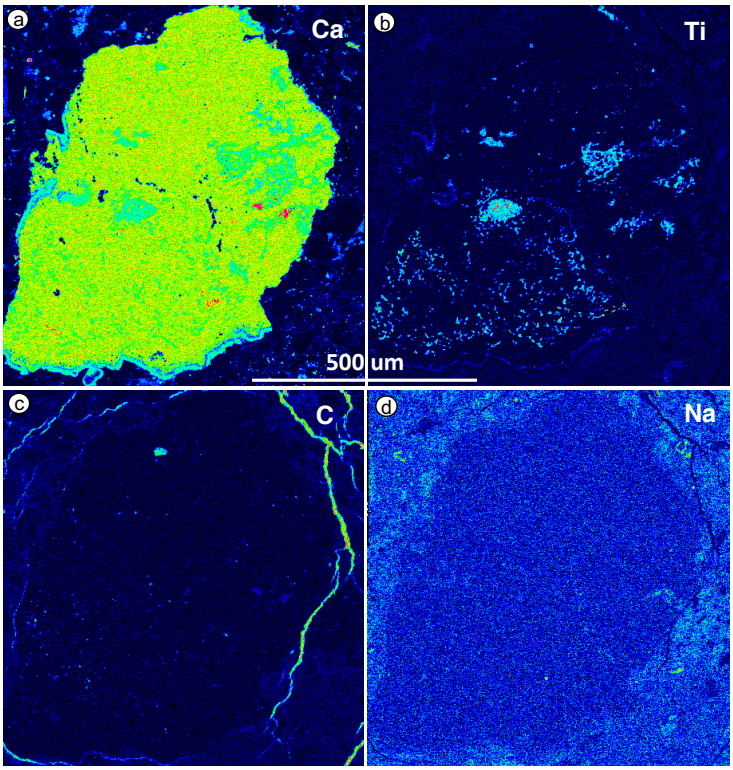


Figure 3.5. Compositional maps of CAI Creosote. Panels (a), (b), (c), and d show elemental maps of Ca, Ti, C, and Na respectively. The Ca and C maps suggest the presence of $CaCO_3$; beam damage to the phase, though, prevented further study. The Ti map indicates the extreme concentration of Ti (up to ~20 wt. %) in fassaite clumped throughout the CAI. The Na map shows that little Na is present in Creosote indicating that the CAI overall was not altered to a high degree. We avoided the Ca alteration during SIMS measurements.

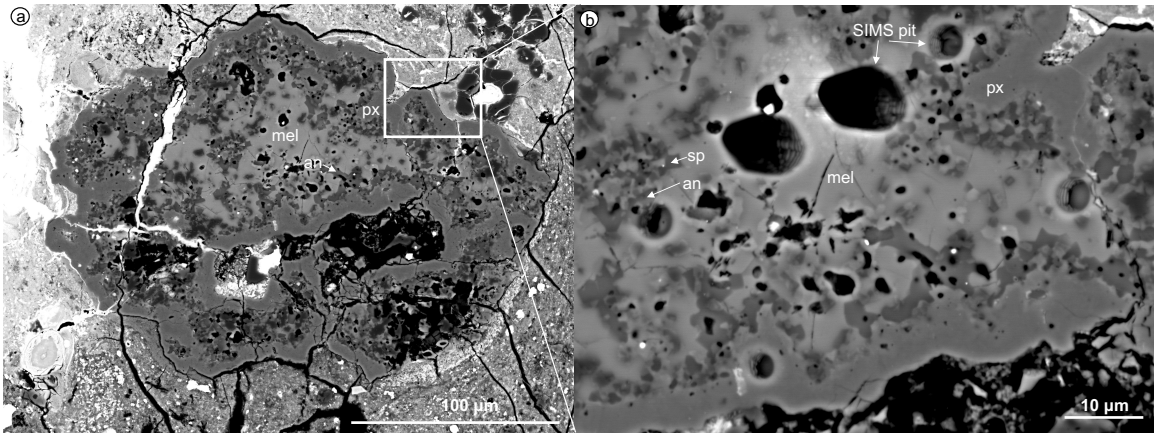


Figure 3.6. CAI *Dalea* from CR2 chondrite Shişr 033 UA 2159,1. Panel (a) shows a BSE image of CAIs *Dalea* in close proximity. Enlarged regions, indicated in (a), show locations of BSE images in panel (b). *Dalea* (longest axis 220 µm) is a rounded porous CAI composed of melilite ($Ak_{12–38}$) enclosing small intermixed euhedral anorthite and spinel. *Dalea* has a thick diopside rim; it appears that *Dalea* was long but curled into a rounded object when it accreted. An Fe-oxide vein passes through the edge of *Dalea*. *Dalea* is most similar to a CTA CAI like *Yucca* and *Creosote*.

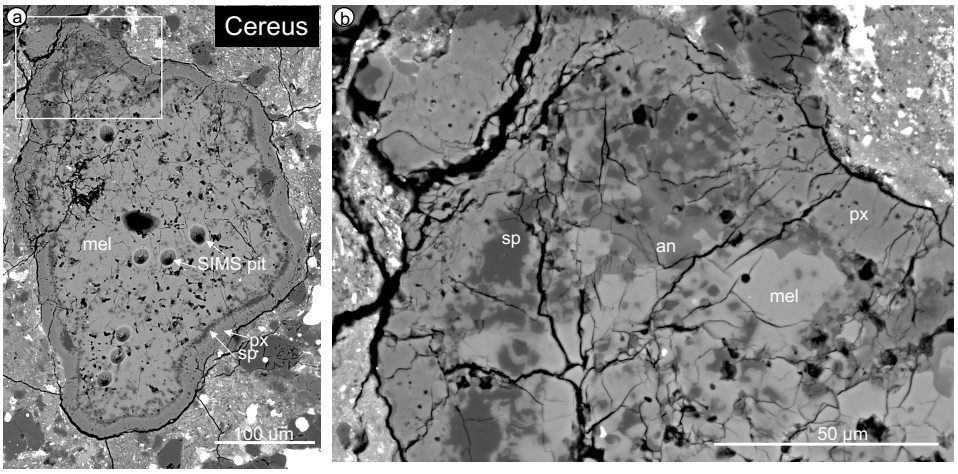


Figure 3.7. CAI *Cereus* from CR2.7 chondrite LAP 02342,14. Panel (a) shows a BSE image of the whole CAI Cereus, panel (b) shows the enlarged region indicated in (a). *Cereus* (longest axis 900 µm) is a rounded porous CAI consisting of predominantly melilite ($Ak_{10–14}$) enclosing small rounded spinel grains and minimal anorthite (concentrated near the upper rim of the inclusion). The rim is composed of a thin layer of clustered spinel grains and a ~10 µm thick layer of diopside. No secondary mineralization is noted. Like CAIs *Yucca, Creosote*, and *Dalea*, this CAI is most similar to a melilite-rich CTA.

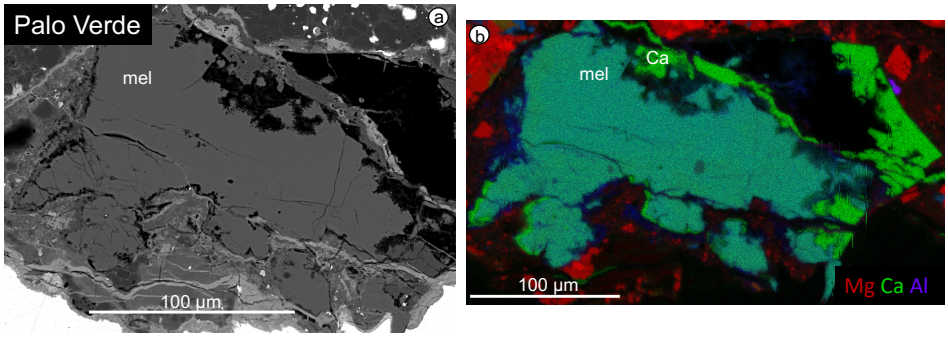


Figure 3.8. CAI *Palo Verde* from CR2 chondrite NWA 801 UA 2300,1. Panel (a) shows a BSE image and (b) the elemental map of the whole CAI *Palo Verde*. *Palo Verde* (longest axis 250 µm) is an irregularly-shaped inclusion consisting only of melilite ($Ak_{18–23}$), which is medium gray in the BSE image on the left. Some secondary calcite (bright green in the three-color map on the right) rims part of the inclusion.

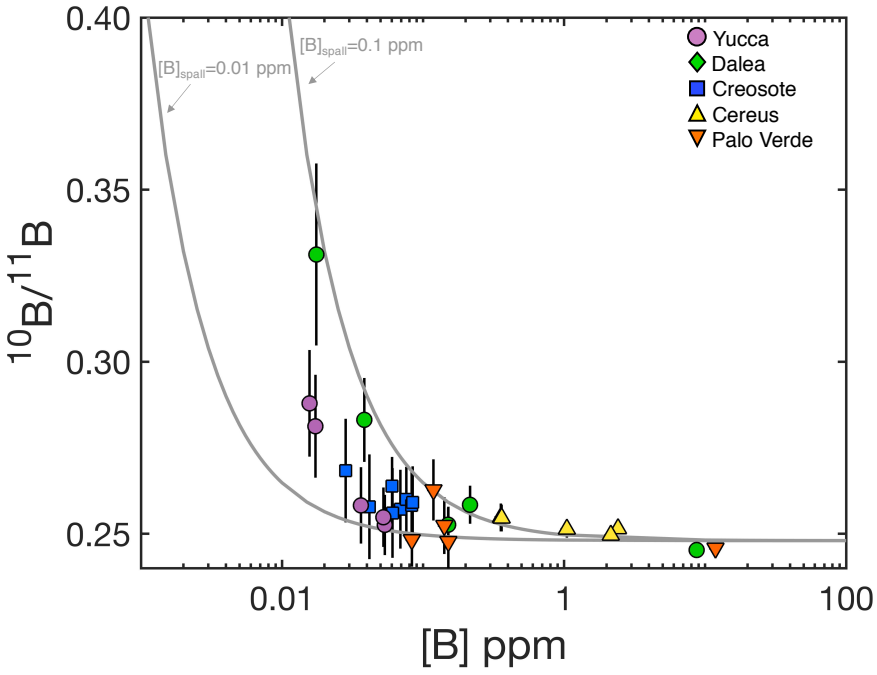


Figure 3.9. All CR2 CAI data points $^{10}B/^{11}B$ versus [B]. Variations in $^{10}B/^{11}B$ isotopic ratios with B concentration (μg/g) for the five CAIs. The gray lines are mixing lines between chondritic ($^{10}B/^{11}B = 0.248$) and spallogenic ($^{10}B/^{11}B = 0.44$) B reservoirs. The lower mixing line was calculated with the addition of $[B]_{spallogenic} = 0.01$ ppm, while the upper mixing line with the addition of $[B]_{spallogenic} = 0.1$ ppm. Because the data for individual CAIs, as well as all CAIs combined, do not fall along mixing lines (between 0.01 and 0.1 ppm spallogenic B), the measured CAI $^{10}B/^{11}B$ excess is likely due to decay of ^{10}Be. The mixing lines were calculated using the equation $^{10}B/^{11}B_{mixing} \sim 0.248(1 + 0.68 \times \Delta B/B)$, where $\Delta B = [B]_{spallogenic.}$ We cannot rule out the possibility of two component mixing (Chapter 1).

CHAPTER 4

CAIs RECORD UNIFORM $^{10}Be/^{9}Be$: EVIDENCE THAT ^{10}Be WAS PRODUCED IN THE MOLECULAR CLOUD

4.1 Introduction

Our understanding of the history and evolution of the Milky Way galaxy has principally relied on astrophysical observations, which can provide information about the environment of our Solar System's formation. However, questions remain about the Milky Way's star formation rate (SFR) over time and what influence this has on our Solar System. We can see that other galaxies of similar ages to the Milky Way have a variety of SFRs; some have starburst regions with SFRs >10 times the average. Many galaxies have SFRs that vary spatially; often, the highest star formation rates are observed in the spiral arms of a galaxy due to compression of gas and dust (Foyle et al., 2010). The SFR of the Milky Way is probed by observations, especially of G stars (Rocha-Pinto et al., 2000a) or ages of white dwarfs (Noh & Scalo, 1990). These studies reveal that the SFR was high (~2 times today's SFR) about 4-6 Gyr ago, declined, increased again 2-3 Gyr ago, and declined again to the present day. But the temporal resolution of these observations is about 400 Ma, so it is possible that there is even more variability on shorter timescales (Rocha-Pinto et al., 2000b).

Meteoritic materials recorded conditions in the solar nebula 4.56 Gyr ago, so can potentially be used as probes of star formation (e.g., Nittler & Dauphas, 2006). Short-lived radionuclides (SLRs), like ^{26}Al ($t_{1/2}$=0.7 Ma; Norris et al., 1983), have been used to

infer the number and proximity of Wolf-Rayet stars and or supernovae in the local region of the forming Solar System (e.g., Davis & McKeegan, 2014). In order to explain the abundance of ^{26}Al, and other SLR such as ^{41}Ca and ^{53}Mn (possibly including ^{36}Cl and ^{60}Fe), the Sun likely formed in a high-mass star-forming region. However, these SLRs can only predict astrophysical events in the very local (a few parsecs) star-forming region (Kuffmeier et al., 2016). The SLR ^{10}Be, which is known to be created by the spallation of ambient nuclei by distantly created galactic cosmic rays, (GCRs) is able to probe the Milky Way SFR over the nearest ~1 kpc, if other sources of ^{10}Be can be excluded.

GCR flux is a quantity related to SFR because GCRs are produced by supernovae which arise from stars that spend <15 Ma on the main sequence (Zapartas et al., 2017). GCR flux is then a tracer of the previous ~15 Ma of star formation over ~1 kpc (the distance GCRs diffuse in the galaxy at that time (Yanasak et al., 2001)). The abundance of the SLR ^{10}Be in the early Solar System can be indicative of the GCR flux, and therefore the SFR, in the local ISM environment. The ^{10}Be abundance is determined by measuring initial ^{10}Be/^{9}Be in the Solar System's first-formed solids, calcium- and aluminum-rich inclusions (CAIs). Because the half-life of ^{10}Be (decays to ^{10}B, $t_{1/2}$ = 1.4 Ma; Korschinek et al., 2010) is so short, CAIs forming over the first ~300,000 years of Solar System formation can crystallize with live ^{10}Be. Although no ^{10}Be remains today in CAIs, we measure an overabundance of the daughter product ^{10}B correlated to a stable isotope, ^{9}Be, to predict the initial abundance of ^{10}Be.

There exist a number of astrophysical environments in which ^{10}Be can be produced: 1) spallation reactions by GCRs in the molecular cloud just before the Sun's

formation (Desch et al., 2004; Tatischeff et al., 2014); 2) spallation reactions by solar energetic particles accelerated by flares from the young Sun, in the CAI forming region (McKeegan et al., 2000; MacPherson et al., 2003; Bricker & Caffee, 2010; Jacquet, 2019); and 3) production by neutrino reactions in the ejecta of a low-mass supernova, injected into the solar system during its formation (Banerjee et al., 2016). These scenarios predict distinct spatial temporal trends; determining how ^{10}Be is distributed among CAIs indicates where ^{10}Be originated. Inheritance of ^{10}Be would result in a uniform spatial distribution that would decrease in time as ^{10}Be decays. On the other hand, production of ^{10}Be from spallation of primarily gas in the solar nebula would result in large spatial and temporal variations of ^{10}Be (Jacquet, 2019). Currently, over 30 CAIs have been measured for ^{10}Be–^{10}B isotopic systematics via secondary ion mass spectrometry (SIMS). Most CAIs yield a uniform ^{10}Be/^{9}Be ~7×10^{-4} (McKeegan et al., 2000; Sugiura et al., 2001; Marhas et al., 2002; MacPherson et al., 2003; Chaussidon, 2006; Liu et al., 2009, 2010; Wielandt et al., 2012; Srinivasan & Chaussidon, 2013; Sossi et al., 2017; Mishra & Marhas, 2019), but there are clearly some CAIs that do not match this value (Gounelle et al., 2013; Sossi et al., 2017). This observation suggests a heterogeneous distribution of ^{10}Be, favoring a solar nebula irradiation origin. But before rejecting the inheritance origin, more evidence is needed. Most of the CAIs measured for ^{10}Be–^{10}B systematics were found in CV (Vigarano-type) carbonaceous chondrites because they are large (>500 μm) and generally coarse-grained (>20 μm). However, some CV3 chondrites, especially in the oxidized subgroup, are known to have undergone thermal metamorphism and aqueous alteration (Krot et al., 1998). These secondary processes could potentially alter

the original $^{10}Be/^{9}Be$ CAI signature, so it is necessary to measure CAIs from more pristine meteorites.

We measured 25 CAIs from a variety of carbonaceous chondrites, which formed and were processed under different conditions, to determine initial $^{10}Be/^{9}Be$ ratios. Twelve CAIs are from CV chondrites (6 $CV3_{red}$, 5 $CV3_{ox}$, and 1 $CV3_{an}$) and include a CAI with fractionations and unidentified nuclear effects (FUN; Williams et al., 2017), a forsterite-bearing type B (FoB) CAI (MacPherson et al., 2017), and a CAI which is known to have been irradiated on the parent body (Shollenberger et al., 2018). Eight CAIs are from Ornans-type (CO3) chondrites and add to a suite of previously reported pristine CR2 CAIs (Chapter 3). The CO3 CAI group includes a CAI with unidentified nuclear effects (UN). Five CAIs are from a High iron/Bencubin-type (CH/CB) chondrite, Isheyevo, which experienced a complicated impact history that could have an effect on CAI isotopic records (Gounelle et al., 2013). The CH/CB and F(UN) CAIs were analyzed to validate if these unique inclusions have anomalously high and low $^{10}Be/^{9}Be$ respectively, as reported previously (MacPherson et al., 2003; Wielandt et al., 2012; Gounelle et al., 2013). We integrate this data with existing $^{10}Be–^{10}B$ measurements from literature, including a CR2 CAI dataset (Chapter 3), with the goal of revealing the distribution of ^{10}Be: was it inherited by the Solar System (uniform distribution), or produced in the solar nebula (variable distribution)? We also correlate $^{10}Be/^{9}Be$ with $^{26}Al/^{27}Al$ in some CAIs because ^{26}Al can be used as a chronometer and can allow us to test if the CAI was melted enough to reset the system.

4.2 Results and Discussion

We measured the ^{10}Be–^{10}B isotope systematics for 25 CAIs using both the ims-6f at ASU and the ims-1290 at UCLA. Similar analytical conditions were used for each session, but calibration details such as the current, spot size, and standardization varied over the sessions (Table S6). Analysis results are listed in table S7, resulting regressions are listed in table 4.1 (see Figures 4.5-4.25 for individual regressions and Figure 4.1 and 4.3 for overall $^{10}Be/^{9}Be$ results). Most measurements were made in melilite (solid solution between gehlinite, $Ca_2Al_2SiO_7$, and akermanite, $Ca_2MgSi_2O_7$), so we specify the Åk content of analyses.

4.2.1 ^{10}Be–^{10}B Isotope Systematics

The 12 CV3 CAIs were found in sections of chondrites Vigarano ($CV3_{red}$), Leoville ($CV3_{red}$), and NWA 5028 ($CV3_{red}$), Allende ($CV3_{ox}$), NWA 6991 ($CV3_{ox}$), NWA 5508 ($CV3_{red}$), and NWA 7891 ($CV3_{ox\text{-}anomalous}$). The melilite-rich CAIs we measured in these CV3 chondrites include a fluffy Type-A, compact Type-As, Type-Bs (1&2), FUN, and a forsterite-bearing type-B (FoB) CAI (see supplementary table S5 for more details and descriptions). These CAIs have minimal secondary alteration, and any secondary mineralization present was avoided when measuring ^{10}Be–^{10}B isotope systematics. The $CV3_{red}$ CAIs (n=6) recorded initial $^{10}Be/^{9}Be = (7.1–11.6) \times 10^{-4}$ and normal (i.e., no fractionations or isotopic anomalies) $CV3_{ox}$ CAIs (n=5) recorded initial $^{10}Be/^{9}Be = (4.3–22.1) \times 10^{-4}$. FUN CAI *CMS-1* and FoB CAI *3137-2* are discussed

below. The [Be] concentration ranges from 108 – 2954 ppb and [B] from 6 to 6974 ppb ($Åk_{6\text{-}87}$).

This chapter reports ^{10}Be–^{10}B systematics of CO3 CAIs. Although CAIs in CO3s are <1% by volume and are small (<500 μm), we obtained 12 inclusions to measure for ^{10}Be–^{10}B. Pristine carbonaceous chondrites are valuable to study because they contain nebular and presolar materials which indicates that they have undergone little or no modification by planetary processes in meteoritic parent bodies (Simon & Grossman, 2015); CAIs from CO3.0 CAIs typically show no textural evidence of secondary alteration (Russell et al., 1998), although COs can exhibit metamorphic grade up to CO3.8 (Simon & Grossman, 2015). The particular CO3 CAIs analyzed here are from DOM 08006 (CO3.0, n=1; Davidson et al., 2015), NWA 7892 (CO3.0, n=1), DaG 027 (CO3, n=4; Render et al., 2019) and DaG 005 (CO3, n=2; Render et al., 2019). We additionally measured 4 other CAIs from DOM 08004 and ALHA 77307, but they were too fine-grained or small for more than a few analyses, had $^{9}Be/^{11}B$ <10 and most data had $^{10}B/^{11}B$ unresolved from chondritic values. These data, when regressed together, are consistent with the other CO3 CAIs (yielding $^{10}Be/^{9}Be = (0 \pm 6) \times 10^{-4}$ (MSWD~3)).

The CO3 CAIs, except for the grossite-rich UN CAI *31-2*, are melilite-rich ± spinel ± pyroxene ± anorthite ± perovskite ± hibonite most similar to compact Type-As (see supplemental Table S5 for detailed descriptions). Normal (i.e., without isotope anomalies) CO3 CAIs recorded initial $^{10}Be/^{9}Be = (6.9\text{-}10.9) \times 10^{-4}$, and UN CAI *31-2* recorded initial $^{10}Be/^{9}Be = (14.6 \pm 6.6) \times 10^{-4}$. The [Be] ranges from 91 – 727 ppb, and [B] from 4 – 110 ppb ($Åk_{5\text{-}34}$).

One study measured CAIs from CH/CB chondrites and found that one CAI recorded rather high $^{10}Be/^{9}Be$ ~10^{-2}. We elementally mapped 3 polished thick sections of Isheyevo (CH/CB) (1580_C1, 1580_C2, and 1580_C5) and located, characterized, and measured 5 rounded, melilite-rich (± spinel ± perovskite ± grossite ± pyroxene) CAIs for ^{10}Be–^{10}B isotope systematics. Metal-rich CH and CB chondrites are thought to have formed from a vapor melt impact plume produced by a giant impact between planetary embryos after dust in the protoplanetary disk had largely dissipated. Isheyevo (CH/CB) has metal-poor and metal-rich lithologies, <1% by volume CAIs, and it may have experienced mild thermal metamorphism, but appears to have largely escaped post-accretionary aqueous alteration (Krot et al., 2008b). Only a fraction of CH/CB CAIs contained ^{26}Al consistent with the canonical level (implying either late-stage formation after the decay of ^{26}Al, or with late-stage re-equilibration with a gaseous reservoir having isotopically normal magnesium and oxygen isotopic composition). Combining the ^{10}Be–^{10}B data from 5 CAIs into a single regression yields an initial $^{10}Be/^{9}Be = (10.6 \pm 2.8) \times 10^{-4}$. The [Be] ranges from 82 – 746 ppm and [B] from 6 – 195 ppm ($Åk_{5\text{-}17}$).

Within this dataset, we measured four unique CAIs: FoB CAI *3137-2* (MacPherson et al., 2017), Type-B CAI *Lisa* which is known to have been irradiated (Shollenberger et al., 2018), FUN CAI *CMS-1* (Williams et al., 2017), and UN CAI *31-2* (Simon et al., 2018). FoB CAIs are of interest because they are uncommon, experienced evaporation, and have bulk compositions which most closely resemble Al-rich chondrules but which formed contemporaneously with normal CAIs (Bullock et al., 2012). FoB CAI *3137-2* from $CV3_{red}$ Vigarano has outer zones which are forsterite-free

but melilite-rich ($Åk_{50\text{-}86}$) and an interior forsterite region enclosed in diopside and melilite (Bullock et al., 2012). The FoB CAI has initial $^{10}Be/^{9}Be = (7.1 \pm 2.9) \times 10^{-4}$ (MSWD = 0.8) with [Be] ranging from 170 – 815 ppm and [B] from 51 – 917 ppm. CAI *Lisa* (from NWA 6991, $CV3_{ox}$) is an otherwise normal melilite-rich ($Åk_{28\text{-}38}$) type-B, but ^{149}Sm isotope results show that it experienced a high thermal neutron fluence indicating it was sited close to the surface of its parent body asteroid. We find that it recorded a $^{10}Be/^{9}Be = (22.1 \pm 7.4) \times 10^{-4}$ (MSWD=1.2) by combining data from 2 sessions (ims-6f and ims-1290).

FUN CAI *CMS-1* from Allende ($CV3.6_{oxA}$) is an irregularly-shaped ~3×5 mm igneous inclusion composed mainly of fassaite and melilite ($\sim Åk_{18\text{–}48}$) grains poikilitically enclosing abundant spinel and distinct generations of melilite (Williams et al., 2017). It is inferred to have been a forsterite-bearing inclusion before thermal processing (Mendybaev et al., 2017). In compiling data from 3 separate SIMS sessions, we found spots with $^{9}Be/^{11}B$ up to 80 via the ims-1290, but the errors are large ($^{9}Be/^{11}B$ ratio 2σ errors varied between 1-9%) because there were only ~20 stable cycles per analysis; the primary beam bombarded a more B-rich phase (usually spinel) after this time. The combined regression yields $^{10}Be/^{9}Be = (1.8 \pm 3.2) \times 10^{-4}$, with initial $^{10}B/^{11}B = 0.253 \pm 0.002$ (MSWD = 0.7). Due to this uncertainty, we report an upper limit of the inferred initial $^{10}Be/^{9}Be$ ratio for *CMS-1* of $<3.7\times10^{-4}$. The [Be] ranges from 410 – 1048 ppb and [B] from 14 – 903 ppb. UN CAI *31-2* (Simon et al., 2019) from DOM 08006 (CO3.0) is an irregularly shaped CAI composed of concentric layers of hibonite, grossite, melilite, and pyroxene (Simon et al., 2018). Measuring the grossite ($CaAl_4O_7$) phase

yielded initial $^{10}Be/^{9}Be = (1.5 \pm 0.7) \times 10^{-3}$ and an initial $^{10}B/^{11}B$ ratio of 0.245 ± 0.002 (MSWD = 0.9). The [Be] ranges from 156 – 555 ppb and [B] from 24 – 336 ppb.

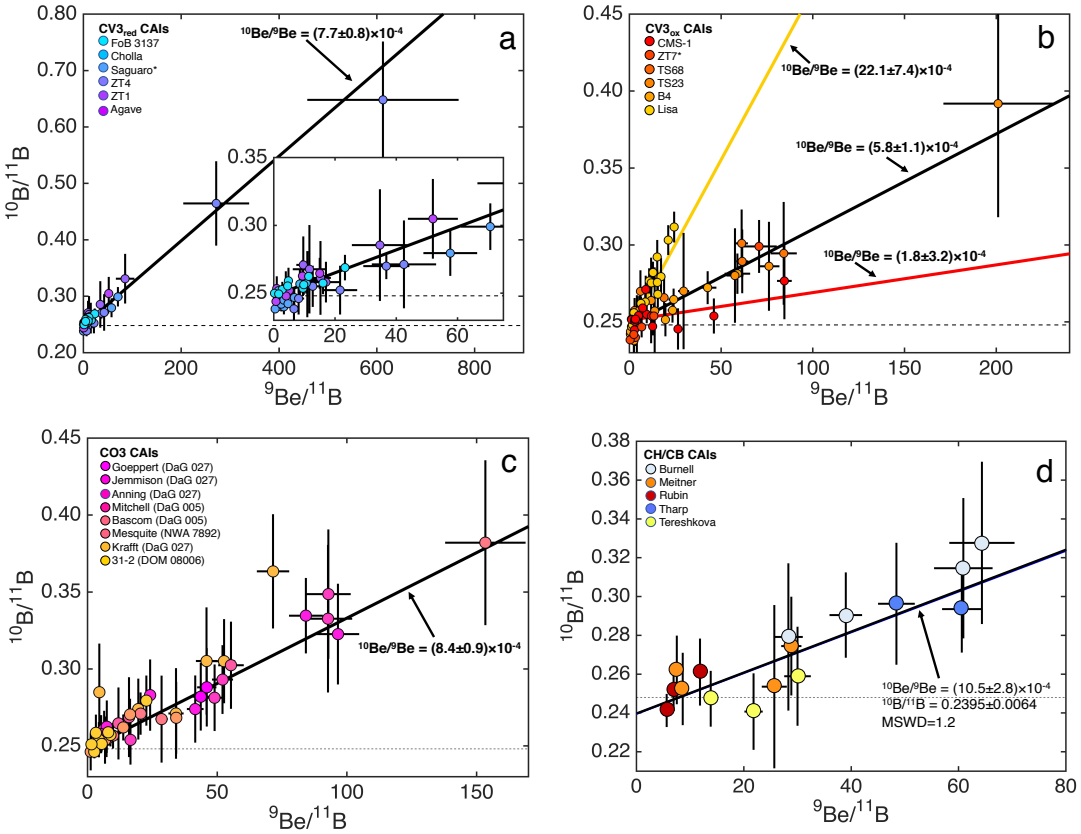


Figure 4.1. ^{10}Be–^{10}B isotope regressions for 25 CAIs. Compiled results are grouped into $CV3_{red}$ CAIs (a), $CV3_{ox}$ CAIs (b), CO3 CAIs (c), and CH/CB CAIs (d). For clarity, we show the weighted mean initial $^{10}Be/^{9}Be$ (2SE) for grouped regressions. We show two distinct $CV3_{ox}$ regressions (b; FUN CAI CMS-1 as red and CAI Lisa as yellow). The CH/CB regression (d) is a multi-CAI isochron with MSWD~1.

Table 4.1

^{10}Be–^{10}B isotope systematics for 25 CAIs from CH/CB, CO3 and CV3 chondrites

Chondrite	Type	CAI name	CAI type	$^{10}Be/^{9}Be$	2SE	$^{10}B/^{11}B$	2SE	n	MSWD	$1+2\sigma_{MSWD}$*
Isheyevo	CH/CB	5 Isheyevo CAIs	mel-rich	10.6	2.8	0.2390	0.0060	16	1.2	1.7
DaG 027	CO3	Goeppert	CTA-like	6.9	5.2	0.2539	0.0142	3	0.1	3.0
DaG 027	CO3	Jemmison	CTA-like	7.9	3.0	0.2554	0.0156	5	1.3	2.4
DaG 027	CO3	Anning	CTA-like	8.5	3.0	0.2493	0.0079	6	1.1	2.3
DaG 005	CO3	Mitchell	CTA-like	8.7	7.6	0.2544	0.0246	3	0.0	3.0
DaG 005	CO3	Bascom	CTA-like	8.8	3.4	0.2489	0.0088	4	0.3	2.6
NWA 7892	CO3	Mesquite	CTA-like	9.8	6.6	0.2481	0.0090	6	0.8	2.3
DaG 027	CO3	Krafft	CTA-like	10.9	5.6	0.2560	0.0220	6	2.0	2.3
DOM 08006	CO3	31-2	grossite-rich	14.6	6.6	0.2451	0.0038	9	0.9	2.0
Allende	$CV3_{ox}$	CMS-1	FUN B	1.8	3.2	0.2510	0.0020	18	0.7	1.7
NWA 7891	$CV3_{an}$	ZT7	CTA	4.3	2.6	0.2499	0.0058	7	1.1	2.2
Allende	$CV3_{ox}$	TS68	CTA	5.7	2.2	0.2569	0.0066	7	1.0	2.2
NWA 6991	$CV3_{ox}$	B4	CTA	6.7	2.2	0.2435	0.0022	8	0.6	2.1
Allende	$CV3_{ox}$	TS23A	B1	6.1	2.2	0.2488	0.0064	9	0.9	2.0
NWA 6991	$CV3_{ox}$	Lisa	B1	22.1	7.4	0.2452	0.0066	14	1.2	1.8
Vigarano	$CV3_{red}$	3137	FoB	7.1	2.9	0.2497	0.0017	10	0.8	1.9
Leoville	$CV3_{red}$	ZT4	CTA	7.3	1.0	0.2391	0.0054	9	0.9	2.0
NWA 5028	$CV3_{red}$	Cholla	FTA	7.8	6.6	0.2504	0.0044	4	0.2	2.6
NWA 5508	$CV3_{red}$	Saguaro	CTA	8.1	1.5	0.2387	0.0014	9	0.8	2.0
Leoville	$CV3_{red}$	ZT1	B1	9.0	4.3	0.2504	0.0091	9	0.6	2.0
NWA 5028	$CV3_{red}$	Agave	B2	11.9	4.0	0.2445	0.0036	10	1.4	1.9

Notes: allowed MSWD $=1+2\sigma_{MSWD}$ ($\sigma_{MSWD}=\sqrt{2/(n-2)}$)

*CAI *ZT7* is classified as anomalous and CAI *Saguaro* is not subclassified in the meteoritical bulletin. Upon careful examination of opaque phases in the available sections, we group CAI *ZT7* into the oxidized class and *Saguaro* into the reduced class.

4.2.2 ^{26}Al–^{26}Mg Isotope Systematics

In addition to ^{10}Be–^{10}B, we measured the ^{26}Al–^{26}Mg isotope systematics for two CAIs from NWA 5028 ($CV3_{red}$), *Agave* and *Cholla*. Figure 4.26 shows that CAI *Agave* recorded initial $^{26}Al/^{27}Al = (5.01 \pm 0.02) \times 10^{-5}$, $\delta^{26}Mg = -0.36 \pm 0.40$ (MSWD = 3.1) and CAI *Cholla* recorded initial $^{26}Al/^{27}Al = (5.22 \pm 0.27) \times 10^{-5}$, $\delta^{26}Mg = -0.063 \pm 0.10$ (MSWD = 0.8). There is previous ^{26}Al–^{26}Mg isotope data for 5 other CAIs measured here

for ^{10}Be–^{10}B systematics: CAIs *CMS-1* (FUN) and *31-2* (UN) are ^{26}Al-poor while CAIs *B4* (CTA), *3137-2* (FoB), and *TS23* (B) have ^{26}Al/^{27}Al = 4.7×10^{-5} and 4.4×10^{-5} respectively (Figure 4.2, Figure 4.26).

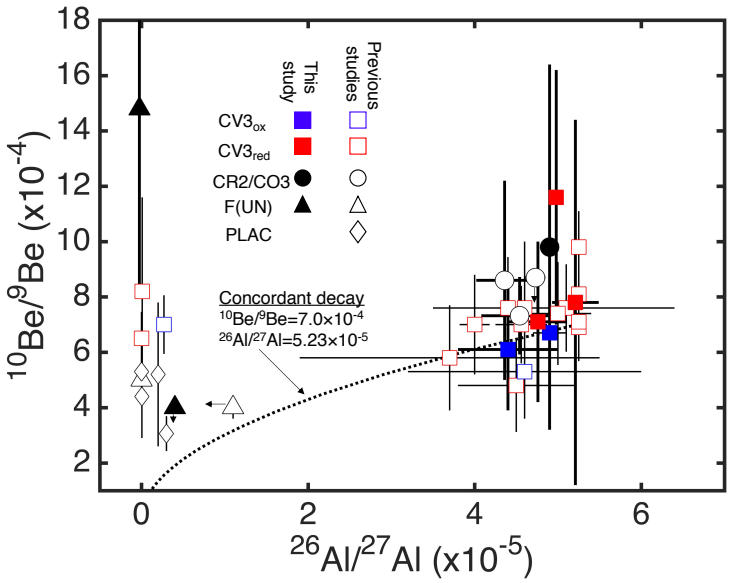


Figure 4.2. Correlated ^{10}Be vs. ^{26}Al. Results from this chapter are shown as closed symbols and from previous studies as open symbols. The concordant decay line represents decay from initially canonical values ^{10}Be/^{9}Be = 7×10^{-4} from this study and ^{26}Al/^{27}Al= 5.23×10^{-5} the CAI canonical value (Jacobsen et al., 2008). Two distinct populations of CAIs, ^{26}Al-poor and ^{26}Al-bearing, are clearly seen. The majority of normal ^{26}Al-bearing CAIs fall on the concordant decay line, while ^{26}Al-poor CAIs do not. This suggests ^{10}Be and ^{26}Al were not produced by the same astrophysical source.

4.2.3 Integrating Results with Literature Data

This chapter presents ^{10}Be–^{10}B data for 25 CAIs. We integrate this data with previously measured CAIs to statistically test our hypothesis that $^{10}Be/^{9}Be$ is uniform among CAIs. First, we evaluate our standardized dataset carefully to determine which regressions are valid. We standardized the dataset by using appropriate RSFs (Chapter 2) and consistent methods to construct the regressions. Although we used different standards throughout the multiple SIMS sessions (NIST 610, NIST 614, and melilite-composition glasses; Table S6), we argue that the CAI $^{10}Be/^{9}Be$ ratios are all comparable; melilite-composition glass analyses on the ims-6f and ims-1290 suggest that accurate $^{10}Be/^{9}Be$ ratios are determined even with common standards that are not of melilite-composition (Chapter 2). Next, we evaluate the regressions as there are a number of reasons why a regression could be considered incomparable to other CAIs.

In our dataset, we find a peculiar outlier, CAI *Lisa* from NWA 6991 ($CV3_{ox}$), which has a robust regression of $^{10}Be/^{9}Be = (22.1 \pm 7.4) \times 10^{-4}$ (MSWD = 1.2, n = 14). CAI *Lisa* has a high ^{149}Sm abundance that indicates it experienced a high fluence of thermal neutrons (flux = 2.11×10^{-15} n/cm^2 (Shollenberger et al., 2018)). Thermal neutrons are produced within meters of a parent body surface by a particle cascade beginning with surface proton irradiation. It is difficult to estimate the initial proton flux, but if the high energy proton irradiation produced just 2.5 ppb of spallogenic B (with $^{10}B/^{11}B = 0.44$; Liu et al., 2010) in the CAI, it would raise the $^{10}Be/^{9}Be$ from ~7×10^{-4} to ~22×10^{-4} while leaving the MSWD close to 1 (Chapter 2). The $^{10}B/^{11}B$ vs. $^{9}Be/^{11}B$

measured in this CAI is likely an overprint of parent-body irradiation on the initial ^{10}Be signature. Other secondary effects, such as irradiation in the nebula by solar energetic particles or parent body aqueous alteration, could also potentially be responsible for the outlier CAI *Lisa*.

In previous datasets (McKeegan et al., 2000; Sugiura et al., 2001; Marhas et al., 2002; MacPherson et al., 2003; Chaussidon, 2006; Liu et al., 2009, 2010; Wielandt et al., 2012; Gounelle et al., 2013; Srinivasan & Chaussidon, 2013; Sossi et al., 2017; Mishra & Marhas, 2019), a total of 32 CAI regressions were reported, 7 of which have regressions associated with high MSWDs (Chapter 2). Of the 7 regressions, 1 CAI is from a CH/CB chondrite (total 2 regressions), 4 CAIs are from $CV3_{ox}$ chondrites (total 10 regressions), and 2 CAIs are from $CV3_{red}$ chondrites (total 18 regressions). Of the 7 regressions, 3 have inferred ^{10}Be/^{9}Be ratios resolvably higher than the 7×10^{-4} level, 1 from CH/CB and 2 from $CV3_{ox}$. The CAIs with high ^{10}Be/^{9}Be and high MSWD have a small ^{9}Be/^{11}B spread and/or few data points with high ^{9}Be/^{11}B; this could be due to secondary effects (irradiation and/or alteration) on the ^{10}Be–^{10}B system, but because these effects are difficult to predict, we are not able to confidently ascribe the outliers to irradiation and/or alteration. In any case, regressions with MSWD $>1+2\sigma_{MSWD}$ have <5% probability of being an undisturbed isochron (Wendt & Carl, 1991), so these ^{10}Be/^{9}Be values are statistically not robust and should not be used in comparisons with other datasets and interpretations. These samples should be re-measured to clarify the situation. The other ~80% of the 32 regressions are robust; within 2 sigma the data are consistent with those CAIs having recorded a single ^{10}Be/^{9}Be value ~ 7×10^{-4}.

4.2.4 Statistically Examining the Dataset

We identified and scrutinized the few CAIs from this chapter and previous studies (McKeegan et al., 2000; Sugiura et al., 2001; Marhas et al., 2002; MacPherson et al., 2003; Chaussidon, 2006; Liu et al., 2009, 2010; Wielandt et al., 2012; Gounelle et al., 2013; Srinivasan & Chaussidon, 2013; Sossi et al., 2017; Mishra & Marhas, 2019) which have a $^{10}Be/^{9}Be$ signature distinct from the majority of normal CAIs and/or lack a robust isochron; this data should not be used for comparisons across datasets. We statistically examine the remaining data (n=55) together. For each given chondrite group, we calculate the mean of all measured $^{10}Be/^{9}Be$ values weighted by the measurement uncertainties and the associated two standard error and MSWD (i.e., reduced chi squared) for this weighted mean. The χ^2 *p*-value is the probability of randomly obtaining a χ^2 at least as large as what we observed assuming the CAIs were drawn from the same $^{10}Be/^{9}Be$ reservoir. A *p*-value greater than 0.05 (or 5%, the usual significance level) is equivalent to an MSWD less than the $2\sigma_{MSWD}$ away from 1. We can use the *p*-value or $2\sigma_{MSWD}$ criterion to test our hypothesis: if MSWD < $1+2\sigma_{MSWD}$ (*p*-value greater than 5%), the CAIs are normally distributed about the calculated mean and are from a single ^{10}Be population; if the MSWD > $1+2\sigma_{MSWD}$ (*p*-value is less than 5%), then we reject our hypothesis (Schrader et al., 2017).

Using this test, we evaluate CAI groups based on chondrite type and CAI type. There are only two CH/CB CAI regressions (also likely part of the ^{26}Al-poor group; Krot

et al., 2008), so it is not statistically significant to evaluate this data as a group. The weighted mean of these two regressions is $^{10}Be/^{9}Be = (11.0 \pm 2.6) \times 10^{-4}$.

In combining all normal CO3 CAI data (n = 7), $^{10}Be/^{9}Be = (8.5 \pm 1.5) \times 10^{-4}$ (MSWD = 0.2, $1+2\sigma_{MSWD} = 2.2$); this group is normally distributed about the mean for the CO3 CAIs. In combining all CR2 data (n = 5, Chapter 3), $^{10}Be/^{9}Be = (7.5 \pm 1.2) \times 10^{-4}$ (MSWD = 1.2, $1+2\sigma_{MSWD} = 2.4$); this group is normally distributed about the mean for the CR2 CAIs.

In combining all $CV3_{red}$ data (n = 21), $^{10}Be/^{9}Be = (7.1 \pm 0.3) \times 10^{-4}$ (MSWD = 1.9, $1+2\sigma_{MSWD} = 1.6$). Because the $1+2\sigma_{MSWD}$ is less than the MSWD, this group is not normally distributed. However, there is one regression that is skewing the group: CAI *E104-FTA* from Efremovka ($CV3_{red}$; Wielandt et al., 2012) with $^{10}Be/^{9}Be = (9.8 \pm 1.3) \times 10^{-4}$. Because this CAI is fine-grained, which can be difficult to measure (a small SIMS spot is necessary to analyze single, crack-free, grains), and the (Wielandt et al., 2012) dataset did not use typical standards, we are justified in removing this sample from the overall analysis. If we systematically exclude all of the fine-grained fluffy type-A CAIs from the analysis (because of measurement difficulties), the MSWD of the $CV3_{red}$ CAIs distributions drops, and our conclusions about the uniformity of ^{10}Be in other chondrite groups become stronger. Excluding CAI *E104-FTA*, the $CV3_{red}$ data (n = 20) is normally distributed about the $CV3_{red}$ mean; $^{10}Be/^{9}Be = (7.0 \pm 0.3) \times 10^{-4}$ (MSWD = 1.1, $1+2\sigma_{MSWD} = 1.6$).

In combining $CV3_{ox}$ data (n = 7), $^{10}Be/^{9}Be = (6.1 \pm 0.7) \times 10^{-4}$ (MSWD = 1.3, $1+2\sigma_{MSWD} = 2.2$); this group is normally distributed about the mean for $CV3_{ox}$ CAIs.

Another way to group CV3 CAIs is by type: melilite-rich type-A CAIs versus more melted melilite+pyroxene+anorthite type-B CAIs. We find that compact type-As (CTA) (n = 11) and type-Bs (n = 14) have the same $^{10}Be/^{9}Be = (6.9 \pm 0.5) \times 10^{-4}$ (MSWD = 1.8) and $(6.9 \pm 0.3) \times 10^{-4}$ (MSWD = 1.3), respectively. There are only 3 fine-grained fluffy type-As (FTA) with robust regressions, so statistically testing the group is not meaningful.

All CV3s together (n = 28), are also normally distributed about the CV3 mean $^{10}Be/^{9}Be = (6.9 \pm 0.3) \times 10^{-4}$ (MSWD = 1.3, $1+2\sigma_{MSWD} = 1.5$). FUN CAIs and hibonite PLACs combined (n = 5) have $^{10}Be/^{9}Be = (4.5 \pm 0.3) \times 10^{-4}$ (MSWD = 4.8, $1+2\sigma_{MSWD} = 2.4$); they are not normally distributed about the mean, indicating that although FUN CAIs and PLACs record low $^{10}Be/^{9}Be$, they are not necessarily part of a single population. Because ^{26}Al-poor CAIs (FUN CAIs, PLACs, CH/CB CAIs) record initial ^{10}Be distinct from normal CAIs, they are not recording the same ^{10}Be as the vast majority of CAIs. In combining ^{26}Al-bearing normal CAIs from CV3, CR2, and CO3 chondrites (n = 42), $^{10}Be/^{9}Be = (7.0 \pm 0.2) \times 10^{-4}$ (MSWD = 1.3, $1+2\sigma_{MSWD} = 1.4$); these CAIs are normally distributed and belong to a single ^{10}Be population. This statistical analysis shows that ^{10}Be was distributed uniformly in the reservoir when/where CV3, CR2, and CO3 chondrite CAIs were forming (Figure 4.3).

When compared to the overall normal CAI weighted mean $^{10}Be/^{9}Be = (7.0 \pm 0.2) \times 10^{-4}$, the CH/CB group has slightly higher $^{10}Be/^{9}Be$. This could have to do with the unique impact origin of the CH/CB chondrite parent body, however more data is needed to prove if CH/CB CAIs have statistically high $^{10}Be/^{9}Be$.

4.2.5 FUN CAIs and PLACs

FUN inclusions and PLACs have resolvably lower $^{10}Be/^{9}Be$ than normal CAIs. In order to fully understand ^{10}Be–^{10}B isotope systematics, it is necessary to determine why FUN CAIs exhibit these characteristics. FUN CAIs are part of a general family of refractory inclusions that show various degrees of fractionation effects (F) due to evaporative processes superimposed on sampling of isotopically heterogeneous (UN) material. They also often lack canonical ^{26}Al (Park et al., 2017); relative to the mean, the standard deviation of $^{26}Al/^{27}Al$ in FUN CAIs is ~150%. This hints that FUN CAIs and PLACs were formed before introduction of ^{26}Al into the Solar System, or possibly formed > 1 Ma after canonical CAIs (Krot et al., 2014; Park et al., 2017). Although they are mineralogically identical to normal CAIs, FUN CAIs are highly fractionated, with large mass-dependent fractionations in Mg, Si, and O, as well as mass-independent fractionations in Ca, Ti, Cr, Sr, Ba, Nd, and Sm. The main difficulty in determining the relationship between FUN and non-FUN CAIs is that they are rare objects; at the time of writing this manuscript only 21 FUN CAIs have been found in all meteorite collections (Krot et al., 2014; Williams et al., 2017). All FUN CAIs are coarse-grained (Type B, CTA, or forsterite-bearing B) and evaporation experiments suggest that they melted in a lower pressure vacuum environment (Krot et al., 2014; Mendybaev et al., 2017). The generic scenario for their formation is thought to be: i) condensation of isotopically normal solids in a ^{16}O-rich gas of approximately solar composition, ii) aggregation of

these solids together with variable abundances of isotopically anomalous grains (possible carriers of unidentified nuclear (UN) effects), and iii) evaporation of these precursors and crystallization under different temperatures and gas pressures to produce variations in the mass-dependent isotopic fractionations (F) (Park et al., 2017).

In this chapter, we measured the ^{10}Be–^{10}B isotope systematics of two inclusions with UN anomalies, one of which also has isotope fractionations indicative of melting and evaporation events. Only two other FUN inclusions and a group of Platy hibonites (PLACs), which have isotopic anomalies similar to UN CAIs, have been measured for ^{10}Be–^{10}B systematics (MacPherson et al., 2003; Wielandt et al., 2012). FUN CAI *CMS-1* in particular has comparatively more initial ^{26}Al (^{26}Al/^{27}Al ~ 2×10^{-5} (Williams et al., 2017) than other FUN CAIs, which show a range of ^{26}Al/^{27}Al ~6×10^{-8} to 2.1×10^{-5} (Park et al., 2017). *CMS-1* also has negative δ^{26}Mg* (radiogenic excess) values (depending on which phases are included in the regression), and very fractionated δ^{25}Mg (30.7-39.3‰); these results are similar to most other FUN CAIs (Park et al., 2017; Williams et al., 2017). FUN CAIs measured for ^{10}Be include *AXCAI 2771*($CV3_{ox}$ Axtell) and *KT-1* ($CV3_{ox}$ NWA 779), CM hibonite PLAty Crystal (PLAC) inclusions are also similar to FUN CAIs due to their low ^{26}Al content, and some also display UN effects (Liu et al., 2009). CAIs *AXCAI 2771* and *KT-1* recorded initial ^{26}Al/^{27}Al ratios of $<1.1\times10^{-5}$ (Srinivasan et al., 2000) and unresolved (Thrane et al., 2008), respectively. CAI *CMS-1* is has ^{10}Be–^{10}B systematics (^{10}Be/^{9}Be = $(1.8 \pm 3.2) \times 10^{-4}$, elevated ^{10}B/^{11}B = 0.252 ± 0.002, [B] ~ 15 – 200), consistent with other FUN CAIs (^{10}Be/^{9}Be ~$(3 – 5) \times 10^{-4}$ and elevated B isotope intercept).

The ^{26}Al-poor nature of the CAIs *CMS-1* and *31-2* suggests that they formed at a different time or place in the solar nebula than CAIs characterized by canonical ^{26}Al/^{27}Al. The distinct population of ^{26}Al-poor CAIs is clearly evidenced in Figure 4.2. Oxygen isotope compositions suggest that all phases in CAI *31-2* are relatively pristine and formed in an ^{16}O-rich reservoir (Simon et al., 2019). In contrast, only the spinel grains in *CMS-1* preserve the isotopic signature of the ^{16}O-rich nebular reservoir from which this FUN CAI was originally formed, while melilite and fassaite have exchanged with other relatively ^{16}O-poor reservoirs that this CAI was subsequently exposed to (Williams et al., 2017). The initial ^{10}Be abundances of these two inclusions provide additional insights into their formation environments and the subsequent thermal processing they may have encountered; FUN CAI *CMS-1* recorded low initial ^{10}Be/^{9}Be (and elevated ^{10}B/^{11}B) consistent with other FUN CAIs, while UN CAI *31-2*, which did not experience fractionation due to thermal processing, recorded initial ^{10}Be/^{9}Be (and chondritic ^{10}B/^{11}B) consistent with most normal CAIs. We suggest that the ^{26}Al-poor UN and FUN CAIs could have distinct ^{10}Be signatures due to the thermal event that produced the fractionations. A furnace experiment (Mendybaev, 2016) was specifically conducted using the proposed starting composition of FUN CAI *CMS-1*. After 1 hour, the study concluded that 80% of SiO_2 and 85% of MgO escaped from the residue during an evaporation event(s). It is unknown how exactly B or Be would behave during such an event because evaporation or diffusion coefficients have not been experimentally determined.

However, we suggest two scenarios that could occur to lower the FUN CAI initial $^{10}Be/^{9}Be$, both assuming that the thermal event took place after ^{26}Al decayed away. In the first scenario, we presume that volatile B would be partially lost from a CAI during evaporation and assume that B would not fractionate during this event. If 1–2 ppb of chondritic B is subtracted from a bulk normal CAI with $^{10}Be/^{9}Be \sim 7 \times 10^{-4}$, the regression remains robust (MSWD close to 1) but has $^{10}Be/^{9}Be \sim(4–5) \times 10^{-4}$, with a chondritic intercept. This suggests that by losing a little B the regression can change from recording the canonical $^{10}Be/^{9}Be$ to recording the FUN CAI $^{10}Be/^{9}Be$ level. In the second scenario, the ^{10}Be–^{10}B would be reset by the thermal event, lowering the $^{10}Be/^{9}Be$ signature because of ^{10}Be decay. Comparable to ^{26}Al–^{26}Mg resetting, ^{10}Be–^{10}B resetting would cause the regression to pivot around bulk $^{9}Be/^{11}B$ (~2-10; Srinivasan & Chaussidon, 2013), resulting in an elevated intercept and lowered slope.

Our proposals for how evaporation or resetting would lower the inferred initial $^{10}Be/^{9}Be$ in a CAI are speculative and demand additional data to test. But they highlight that FUN CAIs and PLACs may differ in inferred initial $^{10}Be/^{9}Be$ even if they originally formed from material with the same $^{10}Be/^{9}Be$ ratio. FUN CAIs and PLACs are the only group distinct from the majority of CAIs (in a statistically significant sense), but they do not themselves form a single population, and they uniquely suffered variable amounts of thermal effects that plausibly could have led to the observed variations in $^{10}Be/^{9}Be$. We therefore feel justified in deferring consideration of whether FUN CAIs and PLACs can test the hypothesis that ^{10}Be was homogeneously distributed, recognizing that additional

measurements of these inclusions could provide the sharpest tests of whether ^{10}Be was uniform.

4.2.6 Astrophysical Modeling

We provide strong evidence that there is a canonical ^{10}Be/^{9}Be ratio of $(7.0 \pm 0.2) \times 10^{-4}$. The few objects with higher or lower values than this likely recorded the canonical signature value initially but were subsequently overprinted or disturbed by irradiation, aqueous alteration and/or evaporation effects. This indicates that ^{10}Be was distributed uniformly in the region where these CAIs were forming. Because the model in which ^{10}Be is produced by irradiation in the solar nebula (14) predicts a temporally and spatially variable distribution of ^{10}Be (over 0.1 to 1 AU and a few 100,000 years) that we do not observe, we argue that ^{10}Be was inherited into the Solar System (more details of this argument are presented in (Chapter 3)). The astrophysical source of ^{10}Be then is either supernova material injected into the Sun's protoplanetary disk or molecular cloud, or ^{10}Be created in the molecular cloud itself. We argue that the molecular cloud is the most likely source because a supernova source would result in concordance between ^{10}Be and ^{26}Al, which we do not observe (Figure 4.2; Chapter 3). Therefore, the data presented here, combined with previous ^{10}Be results, suggest that ^{10}Be was inherited from the molecular cloud.

However, GCRs in the broad region of the protosolar molecular cloud only produce a spatially-averaged steady-state background level of ^{10}Be/^{9}Be = 0.9×10^{-4},

using the present-day GCR flux near the Sun, or $^{10}Be/^{9}Be = 1.3 \times 10^{-4}$ assuming the average SFR in the Milky Way was a factor of 1.5 higher 4.56 billion years ago (Tatischeff et al., 2014). Trapping of ^{10}Be cosmic rays in the molecular cloud (Desch et al., 2004) has been demonstrated to be far too inefficient (Tatischeff et al., 2014). Irradiation of the molecular cloud by GCRs from many supernovae in a large star cluster is more efficient but is predicted to increase this $^{10}Be/^{9}Be$ only to $\sim 4 \times 10^{-4}$ (Desch et al., 2004; Tatischeff et al., 2014). To explain the measured level of $^{10}Be/^{9}Be \sim 7 \times 10^{-4}$, it is necessary to invoke a GCR flux that was ~5 times higher than the background level 4.56 billion years ago.

To determine whether such an enhancement in GCR flux is reasonable, we consider how GCRs are generated. GCRs are ions accelerated to high energies by shocks driven by supernovae. They tend to diffuse from their point of origin for on average ~15 Ma before they are thermalized or escape the Galaxy, during which time they propagate ~1 kpc. Massive stars undergo core collapse supernovae after lifetimes ranging from 4 to 50 Ma. The GCR flux in the Sun's molecular cloud therefore traced the SFR averaged over the nearest ~1 kpc, over the previous 15 Ma before Solar System formation (Yanasak et al., 2001). On these lengthscales and timescales, star formation in the galaxy is not homogeneous.

At the moment, the Sun is in a calm inter-arm environment between the Perseus and Sagittarius spiral arms, at the inner edge of the Orion spur on the Local Arm (Frisch et al., 2009). The GCR flux in the Solar System today appears representative of a uniform GCR flux in local molecular clouds (Desch et al., 2004) and the average GCR flux over

the nearest several kpc in the galaxy today, and does not appear to probe the high GCR fluxes associated with regions of high star formation. The GCR flux in the Sun's vicinity today has been directly measured by spacecraft and inferred using observed chemical abundances (Stone et al., 2013). The production rate of ^{10}Be in a molecular cloud is directly proportional to the GCR flux (mostly energetic protons spalling gas nuclei, e.g., ^{16}O(p,x)^{10}Be); this production rate is balanced by the decay of ^{10}Be. The present-day GCR flux in the galaxy has been used to calculate that ^{10}Be/^{9}Be ~ 0.9×10^{-4} in nearby molecular clouds today (Gounelle et al., 2001; Tatischeff et al., 2014).

To extrapolate this GCR flux to that 4.56 Gyr ago, the ages of G dwarfs and white dwarfs are determined, to derive the numbers formed in past epochs. G dwarf ages can only be modeled to within ~400 Ma, so the inferred SFRs are averages over 400 Ma timescales, and spatially averaged over Sun's orbital annulus at 8.5 kpc (Rocha-Pinto et al., 2000b). Alternatively, models of galactic chemical evolution can constrain the SFR, again spatially averaged over the Sun's orbital annulus and averaged over ~10^8 yr timescales (Rocha-Pinto et al., 2000b). These studies show that the SFR 4.56 Ga was perhaps a factor of ψ = 1.5 to 2.0 higher than today (Desch et al., 2004; Tatischeff et al., 2014). This implies ^{10}Be/^{9}Be ~ $1.3 - 1.8 \times 10^{-4}$ in molecular clouds randomly distributed in the Sun's 8.5 kpc orbital annulus, 4.56 Gyr ago.

For this chapter, it is necessary to quantify the spatial heterogeneity of SFR in a galaxy because we want to know the SFR near a new star forming in the galaxy, not just the spatially averaged SFR in the galaxy. We draw on the work of (Fujimoto et al., 2019), who have performed a hydrodynamical simulation of the ISM of a Milky Way-like

galaxy. The simulation includes hydrodynamics, self-gravity, radiative cooling, photoelectric heating, stellar feedback in the form of photoionization, stellar winds, and supernovae to represent dynamical evolution of the turbulent multiphase ISM. This simulation shows excellent agreement with observables, including total star formation rates of the galaxy and radial profiles of CO, HI, and star formation through the galactic disk.

By producing histograms of the mass of stars generated per time per area of the galactic disk ($M_\odot$ yr kpc^{-2}) in the present-day solar annulus at 8.5 kpc, we find the probabilities that a patch of the galaxy experiences a particular SFR, and that the region of a new star experiences a particular SFR. By comparing the distribution representing the most likely value of average SFR within 1 kpc at a random point in the galaxy to that representing the most likely value of average SFR within 1 kpc of a random new star in the galaxy, we find that newly formed stars on average see a SFR 3.7 times higher than the spatially averaged SFR in the galaxy at the same epoch, with some width in the distribution (Figure 4.4). This is simply due to new stars being nearer to supernovae in spiral arms where most stars form. While the overall SFR in the galaxy may vary with time, and was likely 1.5 to 2 times higher 4.56 Gyr ago, we assume that the spatial inhomogeneity of the SFR was the same 4.56 Gyr as today. This implies that the typical star forming in either epoch experiences a GCR flux at its birth that is a factor of ~3.7 times higher than the average GCR flux in the galaxy.

Multiplying all the factors determined above, we can calculate the expected ^{10}Be/^{9}Be value 4.56 Ga in the Sun's molecular cloud core. The most likely value of

$^{10}Be/^{9}Be$ in a cloud core of a new star 4.56 Gyr ago is approximately $(0.9 \times 10^{-4}) \times (\psi) \times (3.7) = (5.0–6.6) \times 10^{-4}$. The range is due to the uncertainty of the SFR extrapolated 4.56 Gyr ago; we assume ψ in the range 1.5 to 2.0. These represent the mean values of $^{10}Be/^{9}Be$ inherited by new stars from their molecular clouds, but there is a distribution about these means; half of new stars will inherit a higher value and half will inherit a lower value. From the cumulative distributions (Figure 4.4), we calculate a 20% probability that a new star will inherit $^{10}Be/^{9}Be \geq 7 \times 10^{-4}$ if $\psi = 1.5$, and a 40% probability of $^{10}Be/^{9}Be \geq 7 \times 10^{-4}$ if $\psi = 2.0$. Thus, the measured $^{10}Be/^{9}Be = 7 \times 10^{-4}$ we find in this study is a highly probable value for a star forming region 4.56 Gyr ago. The ^{10}Be abundance from meteorites probes the very local molecular cloud environment ~1 kpc and within 15 Ma of Solar System formation and suggests our Sun formed in a region with many other stars, with slightly higher-than-average SFR.

4.3 Conclusions

The SLR ^{10}Be can be used as a probe of the Sun's galactic environment if it can be proven that ^{10}Be was inherited from the molecular cloud. This study combines ^{10}Be–^{10}B systematics of 25 new CAIs, from CV3, CO3, and CH/CB chondrites, with about 30 previously measured CAIs to provide evidence that $^{10}Be/^{9}Be$ was distributed uniformly in the early Solar System. In considering all measurements together, it was important to apply consistent standardization, carefully examine analyses with high MSWD, and to determine whether some CAI results were affected by parent body irradiation or other secondary effects (Chapter 2). We statistically tested the data to find that, except for ^{26}Al-

poor CAIs and outliers with identifiable disturbances, normal ^{26}Al-bearing CAIs (n = 42) are consistent with a single uniform value of ^{10}Be/^{9}Be = (7.0 ± 0.2) × 10^{-4}. It remains inconclusive why FUN CAIs recorded a lower level of ^{10}Be/^{9}Be than normal CAIs. A temporal interpretation using ^{26}Al does not seem likely; but in comparing an UN CAI, which recorded a ^{10}Be/^{9}Be value consistent with normal CAIs, with FUN CAIs, we suggest evaporation post formation that produced the isotopic fractionations is key. However, this does not explain the low ^{10}Be/^{9}Be recorded by hibonites and FUN CAIs. Future modeling efforts should account for distribution coefficients, B loss during evaporation, duration of evaporation, etc., to test this idea. Evaporation would not explain the low value of ^{10}Be/^{9}Be in hibonite grains, but as isolated grains lacking petrologic context, a late formation ~1 Ma after other CAIs cannot be ruled out. We note that the ^{10}Be/^{9}Be values from FUN CAIs and hibonite grains are spread out and not consistent with a single value; these inclusions do not define a single population.

In contrast, normal ^{26}Al-bearing CAIs are consistent with a single ^{10}Be/^{9}Be value, which indicates that there is a canonical ^{10}Be/^{9}Be ratio. Theoretically, this means that ^{10}Be can be used as a chronometer, although it is not an especially useful one, due to the low counts and large uncertainties, as well as the limitation that measurements in melilite/grossite/hibonite are needed to construct resolvable isochrons. We focus on the other implication of a canonical ^{10}Be/^{9}Be value: ^{10}Be was likely inherited from the molecular cloud, where it was produced before Solar System formation by GCR spallation of ambient nuclei. Because GCRs can trace star formation, the measured amount of ^{10}Be in CAIs allow us to infer the star-forming environment of our Sun. In

modeling present-day star formation in a galaxy like the Milky Way, we find that the GCR flux in the local area of a new star is about 3.7 times higher than a random point in the galaxy. With this factor, we calculate that our measured $^{10}Be/^{9}Be = 7 \times 10^{-4}$ is a highly probable value in star-forming regions 4.56 Gyr ago. The SLR ^{10}Be measured in CAIs is a sensitive probe to the very local molecular cloud environment (~1 kpc and 15 Ma) and suggests our molecular cloud existed in a region with many other forming stars. We summarize these conclusions in Figure 4.3: the majority of CAIs formed with $^{10}Be/^{9}Be = (7.0 \pm 0.2) \times 10^{-4}$, higher than the spatial average because our molecular cloud was irradiated by GCRs in a star forming region (event 1), later events (2 and 3) explain the few outliers with lower and higher $^{10}Be/^{9}Be$ by thermal heating and irradiation, respectively. This conclusion is consistent with recent studies that suggest that the abundances of other SLRs (e.g., ^{60}Fe, ^{26}Al, ^{36}Cl, ^{41}Ca) were elevated above average galactic background values by self-enrichment of molecular clouds by previous generations of star formation and supernovae (Young, 2016).

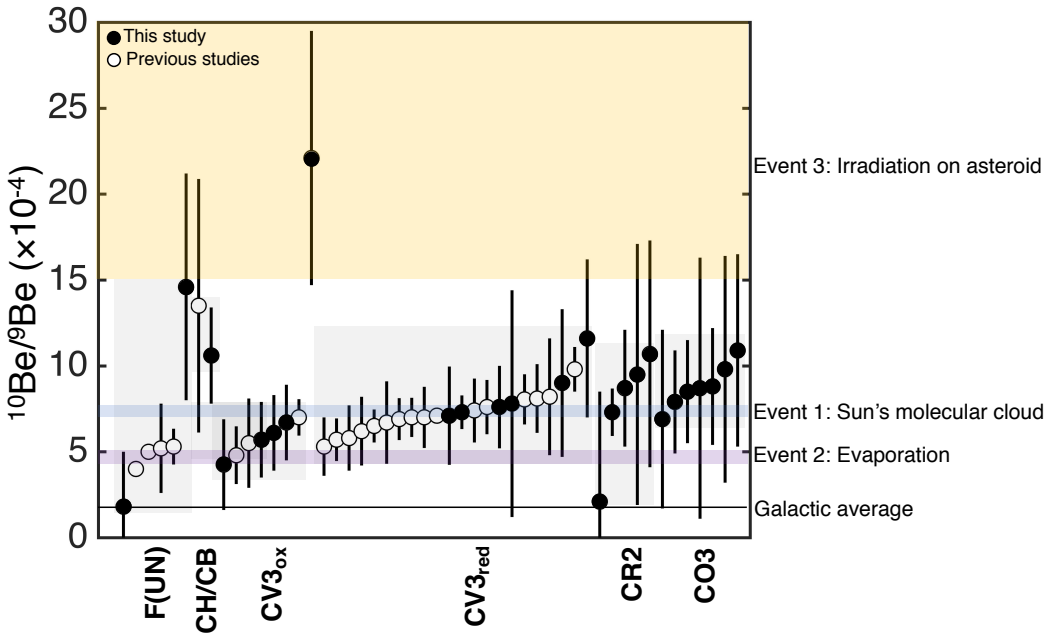


Figure 4.3. $^{10}Be/^{9}Be$ results for CAI measured in this study and previous studies. All regressions are robust (MSWD~1) and data are grouped based on CAI type or chondrite type (gray boxes). Normal, ^{26}Al-bearing CAIs recorded $^{10}Be/^{9}Be = (7.0 \pm 0.2) \times 10^{-4}$. Because this value is higher than that estimated for the spatially averaged galaxy 4.56 Gyr ago, we suggest that our Sun formed in a star-forming region that experienced a higher GCR flux than the average galaxy (Event 1 $^{10}Be/^{9}Be = 7.0 \times 10^{-4}$; blue bar). Later events such as evaporation (Event 2 $^{10}Be/^{9}Be = 4.6 \times 10^{-4}$; purple bar) or irradiation either on the parent body (which is likely the case for the CAI with high $^{10}Be/^{9}Be$ as evidenced by its high ^{149}Sm) or in the nebula by solar energetic particles (Event 3 $^{10}Be/^{9}Be = 22.0 \times 10^{-4}$; yellow bar).

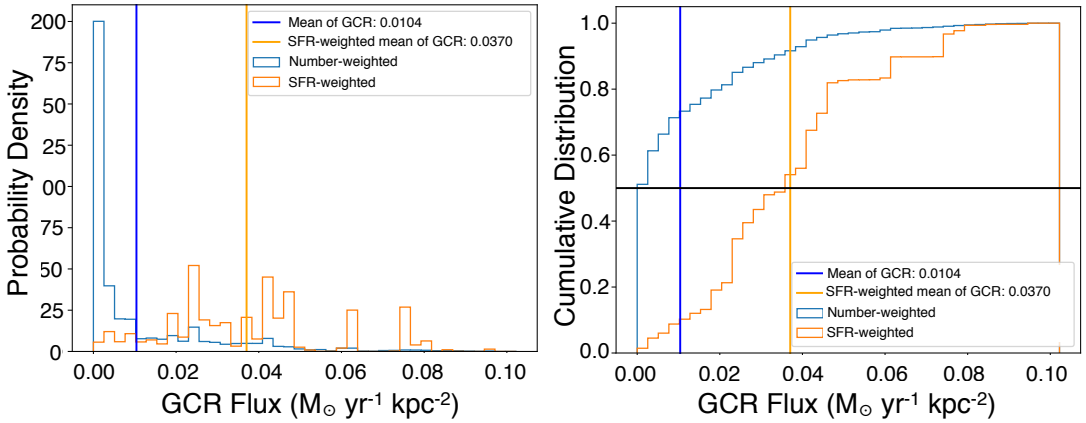


Figure 4.4. Distribution of Star Formation Rates (SFRs) in the Sun's annulus (galactocentric distance 7.2 to 9.8 kpc) in a simulation of the modern-day Milky Way. Right: Histograms of different nearby star formation rates $Sigma_{SFR}$, measured in solar masses per year per square kiloparsec of galactic area. Here 'nearby' means within a square 2 kpc x 2 kpc, centered on a particular zone; this will be proportional to the galactic cosmic ray (GCR) flux. Blue boxes denote probability P_{space} of a zone 32pc x 32pc in size experiencing a 'nearby' $Sigma_{SFR}$. These are weighted to low values, with a mean of 0.010 Msol/yr/kpc^2, signifying that star formation is low throughout most of the galaxy, but reaches high values in a small number of spatial zones. Orange boxes denote the probability per newly formed star, $P_{star} \sim P_{space} * Sigma_{SFR}$. These are weighted to higher values, and the mean SFR experienced by newly formed stars is 0.037 Msol/yr/kpc^2. This signifies that higher nearby SFR is experienced by newly formed stars, which preferentially form in regions of high SFR. Left: Cumulative distributions of the $Sigma_{SFR}$ experienced by spatial zones (blue) and newly formed stars (orange). Over half the spatial zones experience $Sigma_{SFR} < 0.05$ Msol/yr/kpc^2, and 75% of zones

experience $Sigma_{SFR}$ less than the mean value 0.010 Msol/yr/kpc^2. In contrast, the median $Sigma_{SFR}$ experienced by newly formed stars is essentially the mean value, 0.037 Msol/yr/kpc^2, so 50% of stars form in a region with nearby SFR a factor of 3.7 higher than the large-scale spatial mean. About 40% of stars form in regions with nearby SFR (proportional to GCR flux) a factor of 4.0 higher than the spatial mean; and 20% of stars form in regions with GCR flux a factor of 5.2 higher than the spatial mean.

4.4 Methods Summary

Some CAIs were located by elementally mapping (via the JEOL JXA-8530F at ASU) meteorite sections and finding objects high in Ca and Al (Isheyevo CAIs, NWA 5028 CAIs). The remaining CAIs were obtained from ASU and collaborators (CO3s NWA 7892, DaG 027, DaG 005, and DOM 08006, CV3s Allende, Vigarano, Leoville, NWA 6991 and NWA 7891). Polished sections containing identified CAIs were first characterized using electron microprobe analysis using the JEOL JXA-8530F (ASU). The Cameca IMS-6f at ASU and Cameca IMS-1290 at UCLA were used to conduct ^{10}Be–^{10}B isotope systematics measurements (see Appendix A for additional details and analytical conditions [Table S6]), and a selected set of samples was then analyzed for ^{26}Al–^{26}Mg isotope systematics by the Cameca IMS-1280 at UW-Madison. The placement and quality of the SIMS pits were subsequently checked on ASU's JEOL JXA-8530F EPMA.

4.5 Detailed Results

The three-color RGB elemental maps presented here show Mg=red, Ca=green, and Al=blue. The combination of these three elements displays the most important CAI minerals as different colors; melilite (solid solution between $Ca_2Al_2SiO_7$ and $Ca_2MgSi_2O_7$) is blue/green, spinel ($MgAl_2O_4$) is purple, pyroxene ($XYSi_2Al_2O_6$) is dark green (diopside ($CaMgSi_2O_6$) looks slightly browner while fassaite ($Ca(Mg,Fe,Al,Ti)(Si,Al)_2O_6$ looks dark blue/green), anorthite ($CaAl_2Si_2O_8$) is light blue, hibonite ($Ca(Al,Ti,Mg)_{12}O_{19}$) is bright blue, perovskite ($CaTiO_3$) is light green, and calcite ($CaCO_3$) alteration is bright green. In grayscale back-scattered electron (BSE) images (which show z-contrast with higher atomic number elements appearing brighter), spinel is nearly black, perovskite is nearly white, melilite and fassaite are the lightest gray, diopside is medium gray, anorthite is darkest gray, and Fe-alteration is white. Abbreviations are: sp=spinel, mel=melilite, px=pyroxene, fass=fassaite, an=anorthite, pv=perovskite, cal=calcite.

The following figures show BSE and/or elemental map images of the whole CAIs as well as magnified areas (in the order of the above table). Images with black circular regions were analyzed for Ti isotopes so the majority of the CAI was micro-drilled and later filled with epoxy. Major minerals are indicated. Also shown are the ^{10}Be-^{10}B isotope systematic isochrons (with results listed) and $^{10}B/^{11}B$ vs 1/[B] to indicate the correlation that the $^{9}Be/^{10}B$ vs $^{10}B/^{11}B$ linear correlation is due to the decay of ^{10}Be (as evidenced by a high MSWD in most cases).

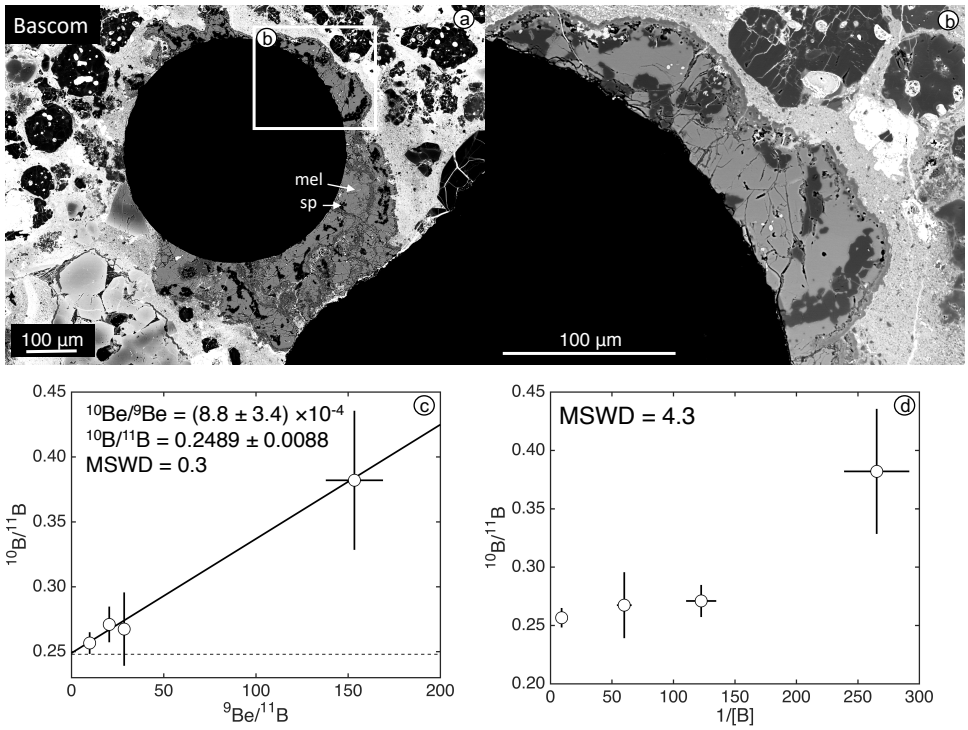


Figure 4.5. CAI *Bascom* (DaG 005, CO3) characterization and isotope results: Whole CAI (a) and enlarged region (b) with ^{10}Be-^{10}B regression results (c, d).

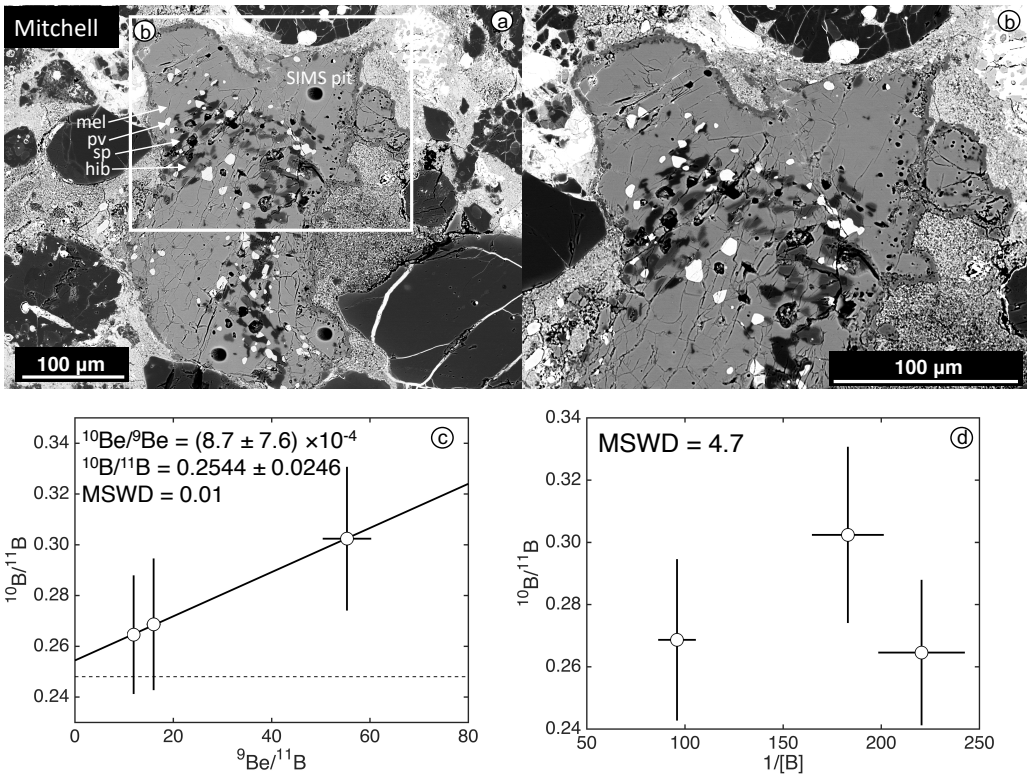


Figure 4.6. CAI *Mitchell* (DaG 005, CO3) characterization and isotope results: Whole CAI (a) and enlarged region (b) with ^{10}Be-^{10}B regression results (c, d).

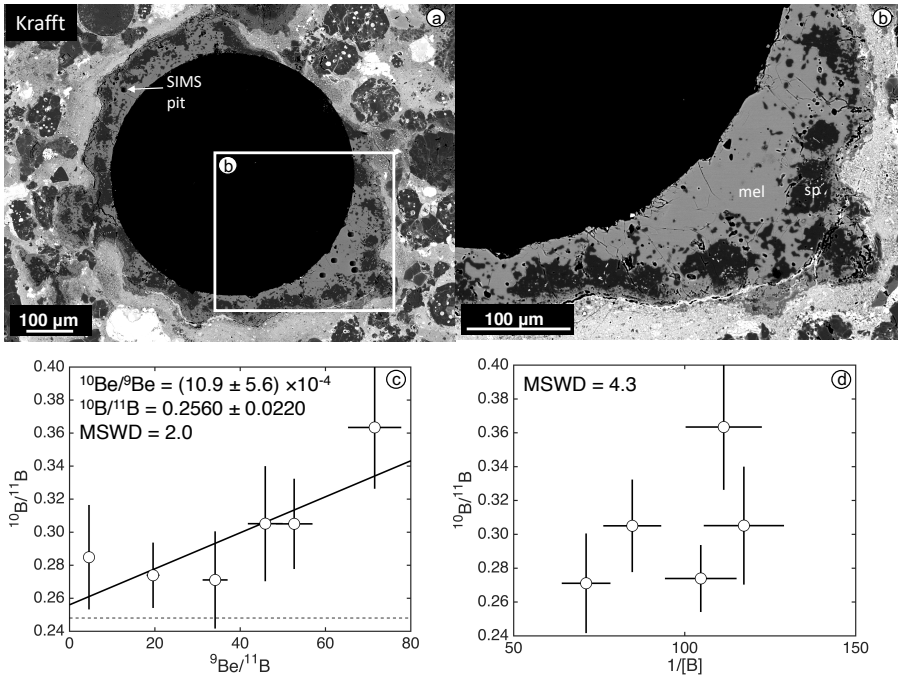


Figure 4.7. CAI *Krafft* (DaG 027, CO3) characterization and isotope results: Whole CAI (a) and enlarged region (b) with ^{10}Be-^{10}B regression results (c, d).

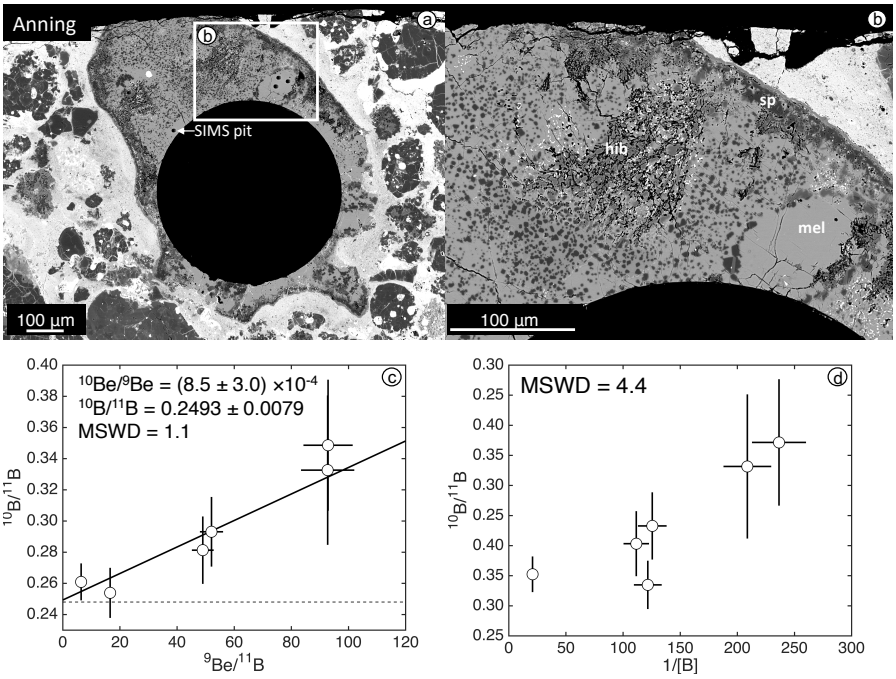


Figure 4.8. CAI *Anning* (DaG 027, CO3) characterization and isotope results: Whole CAI (a) and enlarged region (b) with ^{10}Be-^{10}B regression results (c, d).

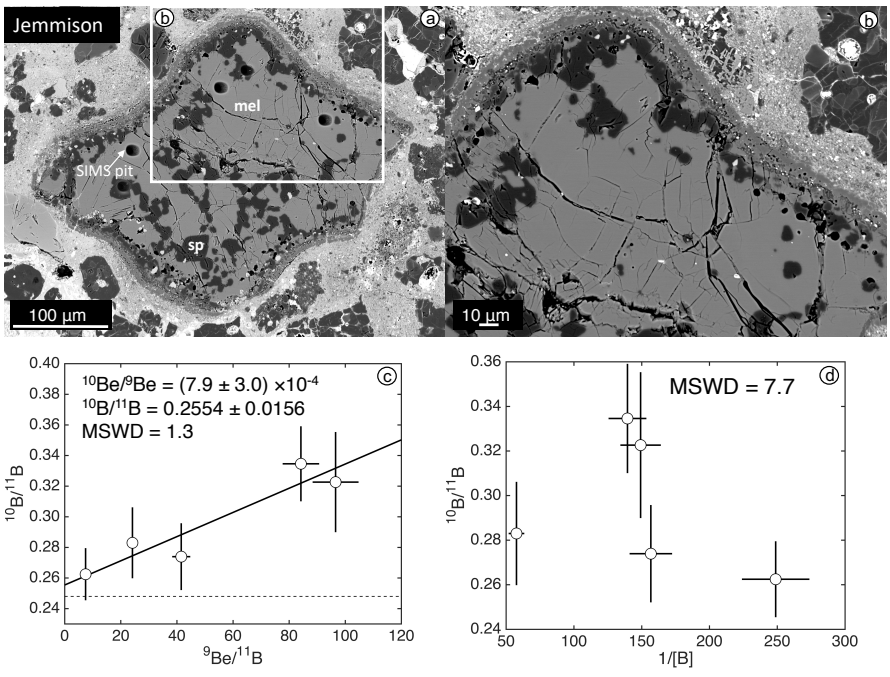


Figure 4.9. CAI *Jemmison* (DaG 027, CO3) characterization and isotope results: Whole CAI (a) and enlarged region (b) with ^{10}Be-^{10}B regression results (c, d).

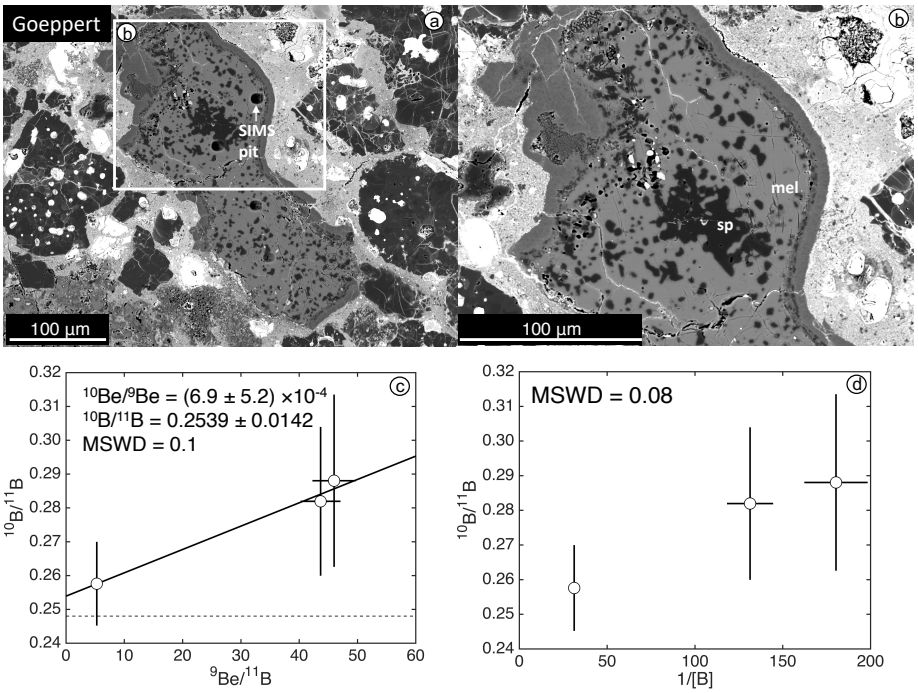


Figure 4.10. CAI *Goeppert* (DaG 027, CO3) characterization and isotope results: Whole CAI (a) and enlarged region (b) with ^{10}Be-^{10}B regression results (c, d).

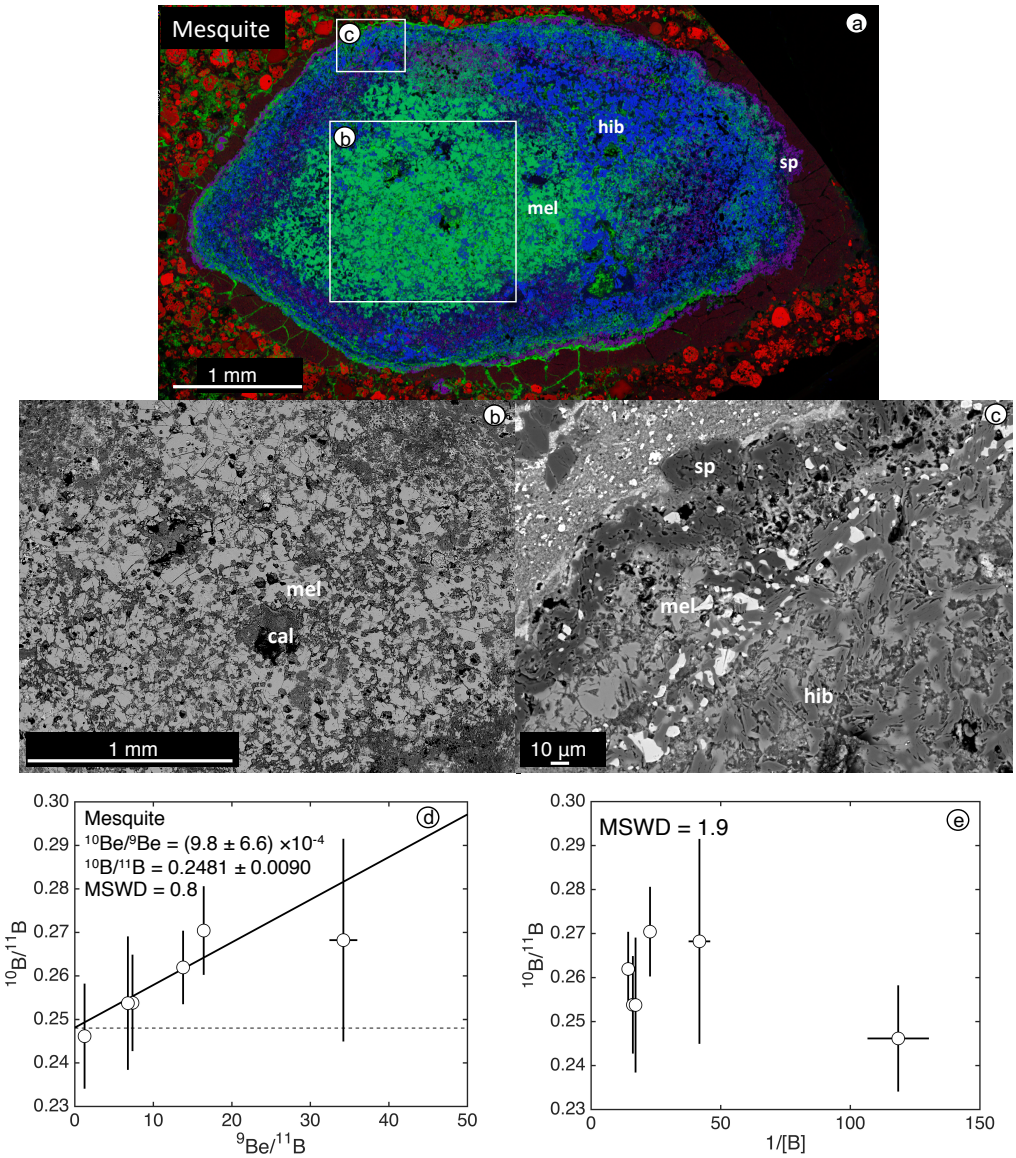


Figure 4.11. CAI *Mesquite* (NWA 7892, CO3.0) characterization and isotope results: Whole CAI (a) and enlarged regions (b, c) with ^{10}Be-^{10}B regression results (d, e).

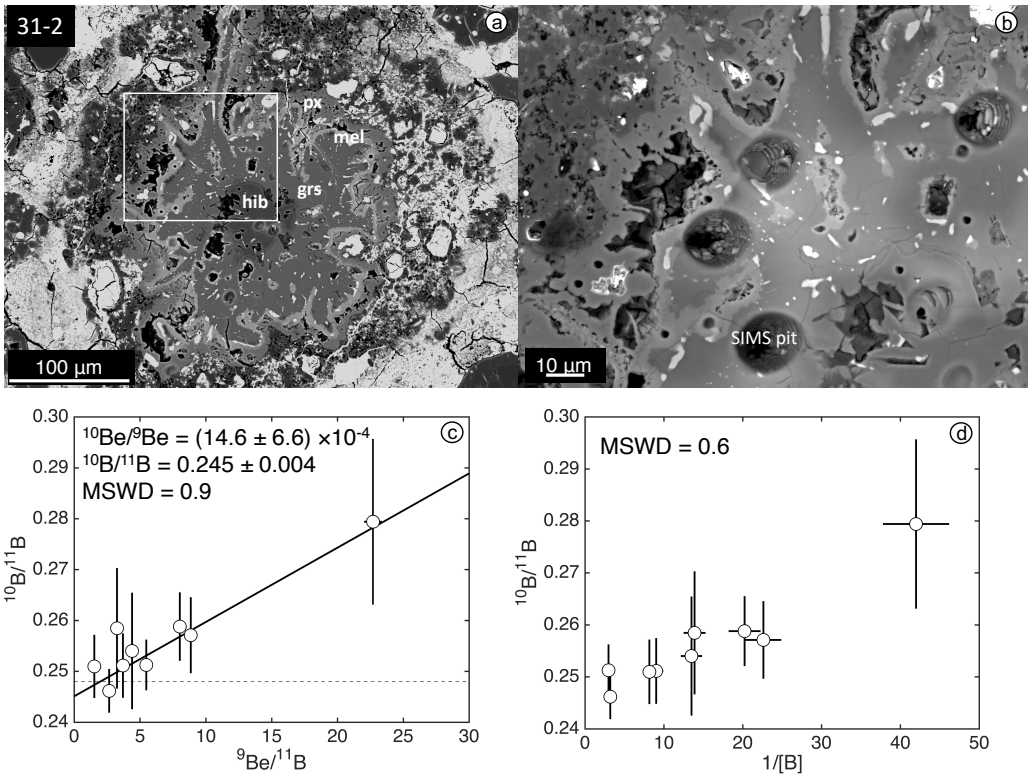
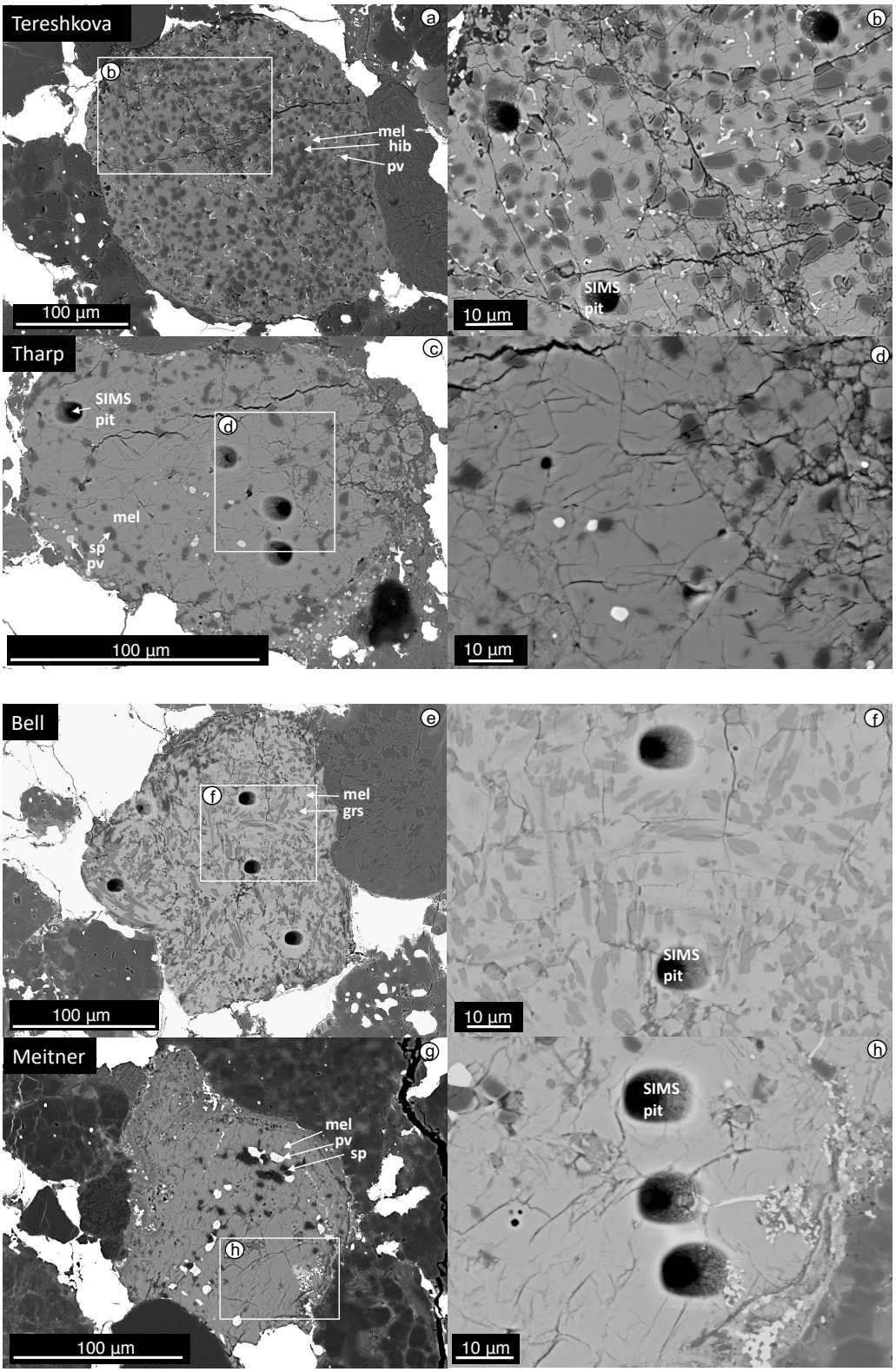


Figure 4.12. CAI *31-2* (DOM 08006, CO3.0) characterization and isotope results: Whole CAI (a) and enlarged region (b) with ^{10}Be-^{10}B regression results (c, d).


Tereshkova
a
b
mel
hib
pv
100 µm
b
SIMS
pit
10 µm
Tharp
c
SIMS
pit
d
mel
sp
pv
100 µm
d
10 µm
Bell
e
f
mel
grs
100 µm
f
SIMS
pit
10 µm
Meitner
g
mel
pv
sp
h
100 µm
h
SIMS
pit
10 µm

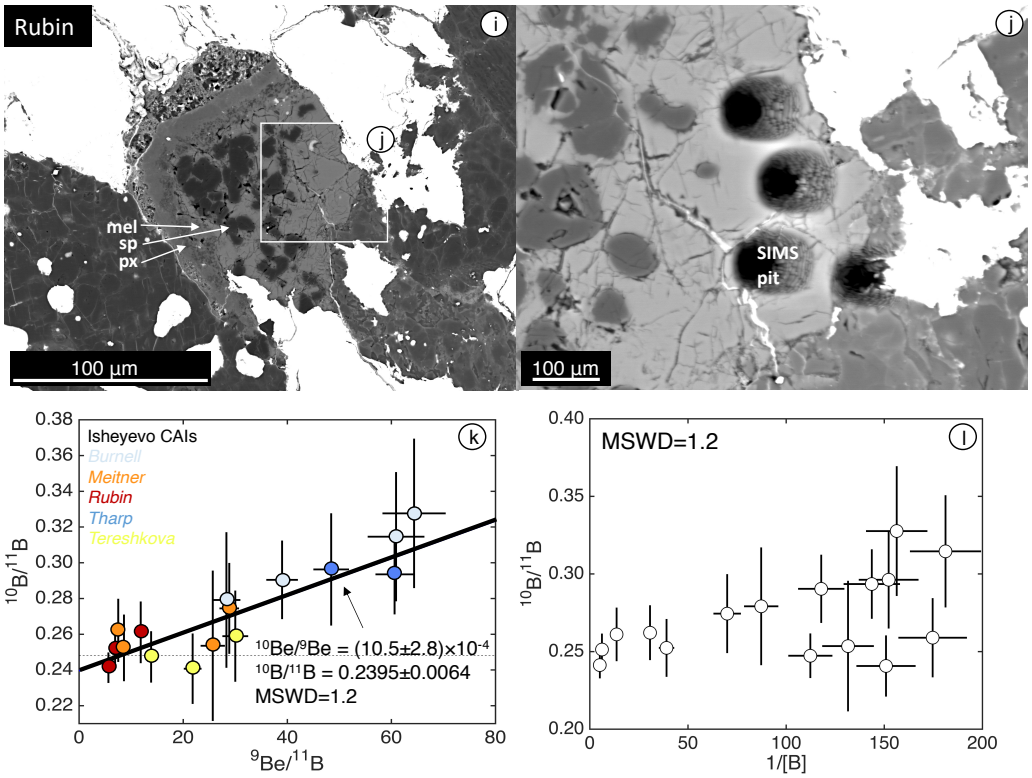


Figure 4.13 Isheyevo CAI (*Tereshkova, Tharp, Bell, Meitner*, and *Rubin*) characterization and isotope results: Whole CAI (a, c, e, g, i) and enlarged region (b, d, f, h, i) with ^{10}Be-^{10}B regression results (k, l).

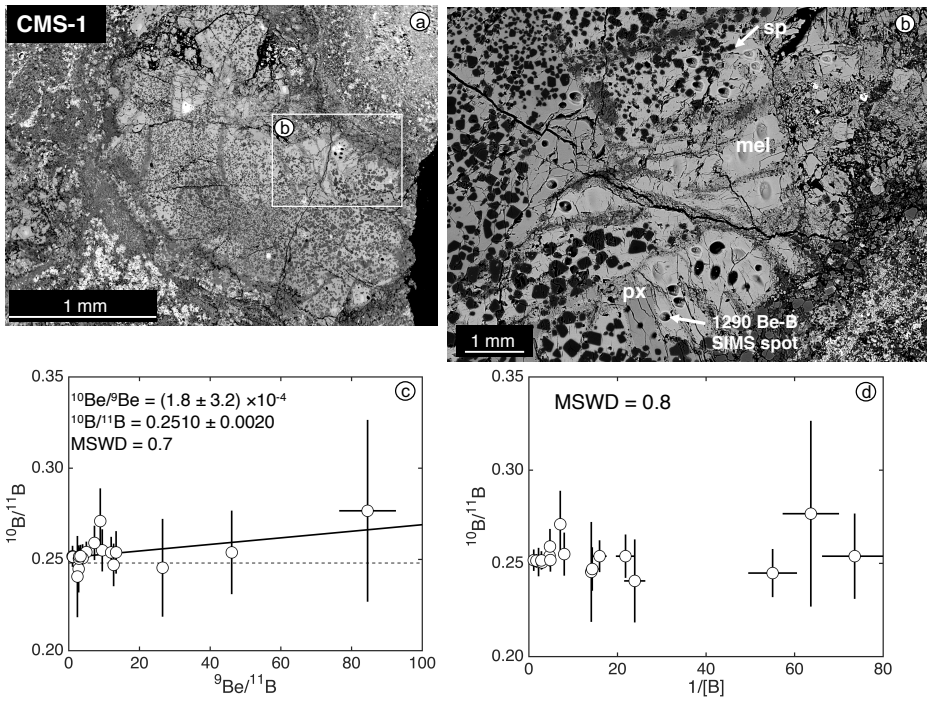
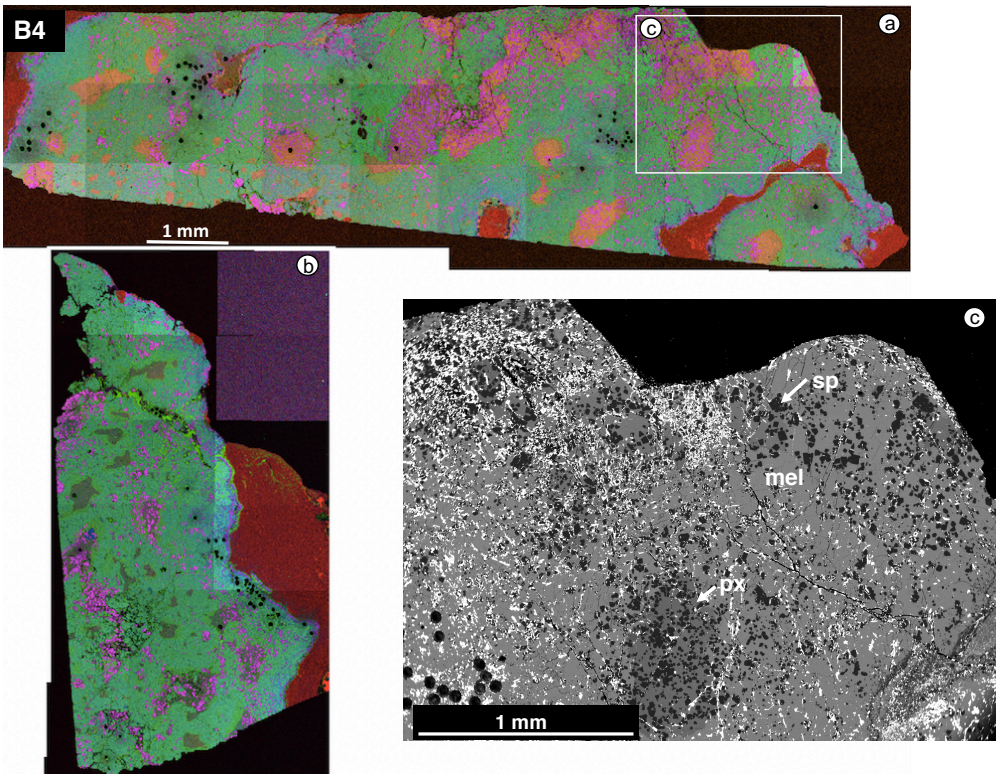


Figure 4.14. CAI *CMS-1* (Allende, $CV3_{ox}$) characterization and isotope results: Whole CAI (a) and enlarged region (b) with ^{10}Be-^{10}B regression results (c, d).



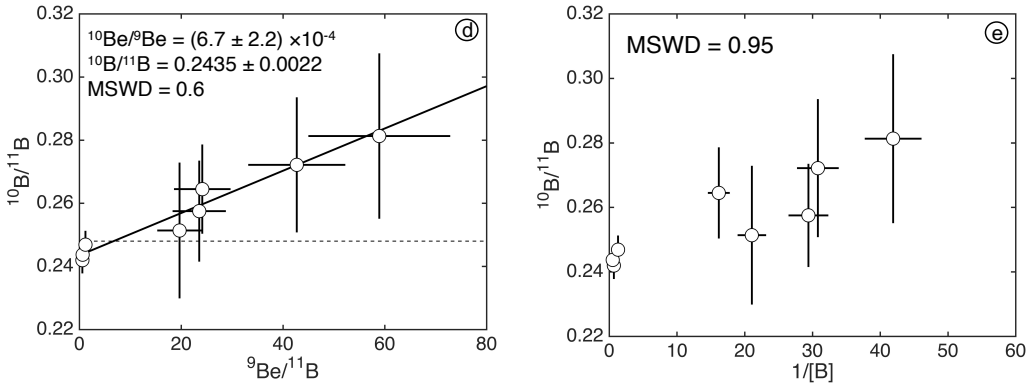


Figure 4.15. CAI *B4* (NWA 6991, $CV3_{ox}$) characterization and isotope results: Whole CAI (a, b) and enlarged region (c) with ^{10}Be-^{10}B regression results (d, e).

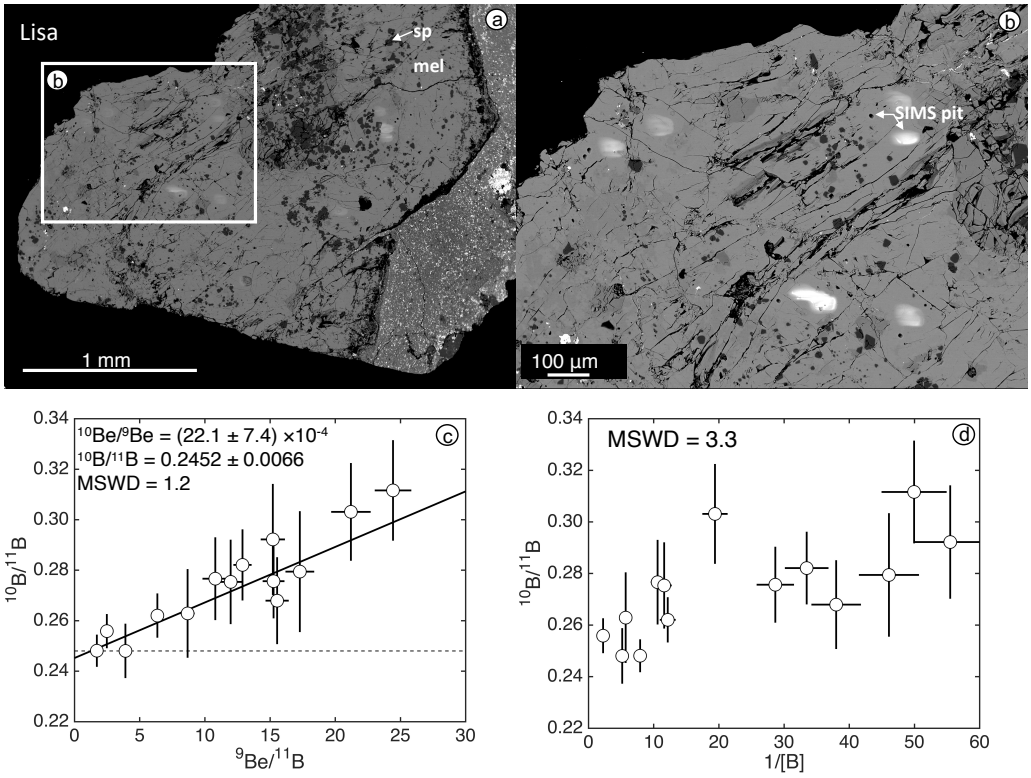


Figure 4.16. CAI *Lisa* (NWA 6991, $CV3_{ox}$) characterization and isotope results: Whole CAI (a) and enlarged region (b) with ^{10}Be-^{10}B regression results (c, d).

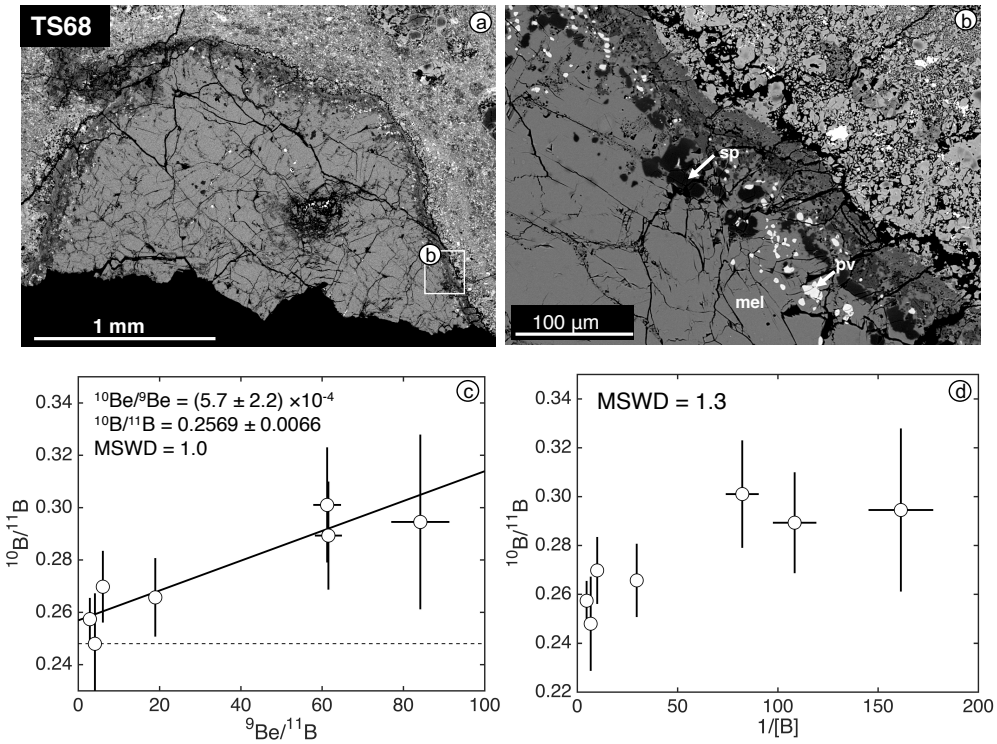


Figure 4.17. CAI *TS68* (Allende, $CV3_{ox}$) characterization and isotope results: Whole CAI (a) and enlarged region (b) with ^{10}Be-^{10}B regression results (c, d).

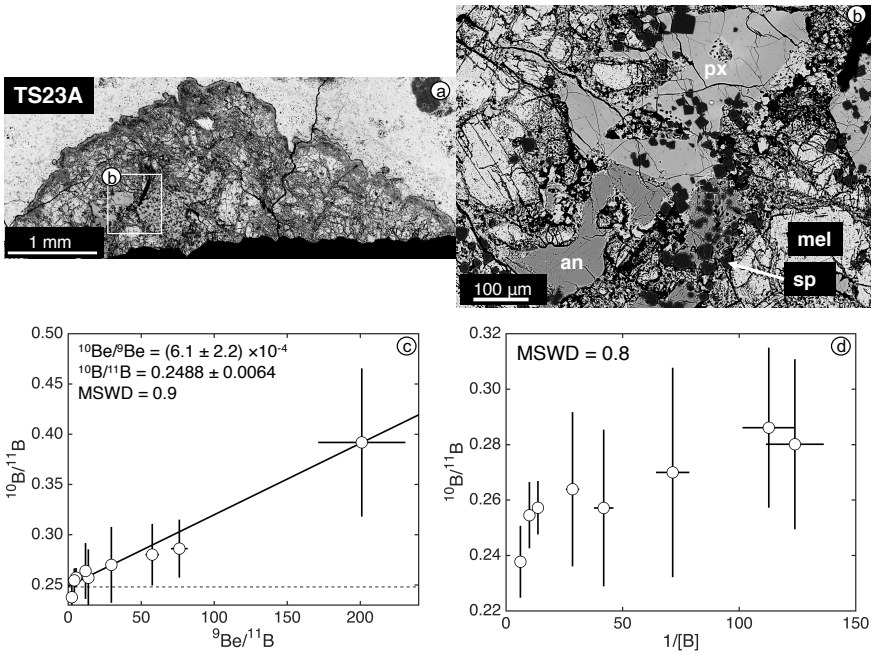


Figure 4.18. CAI *TS23* (Allende, $CV3_{ox}$) characterization and isotope results: Whole CAI (a) and enlarged region (b) with ^{10}Be-^{10}B regression results (c, d).

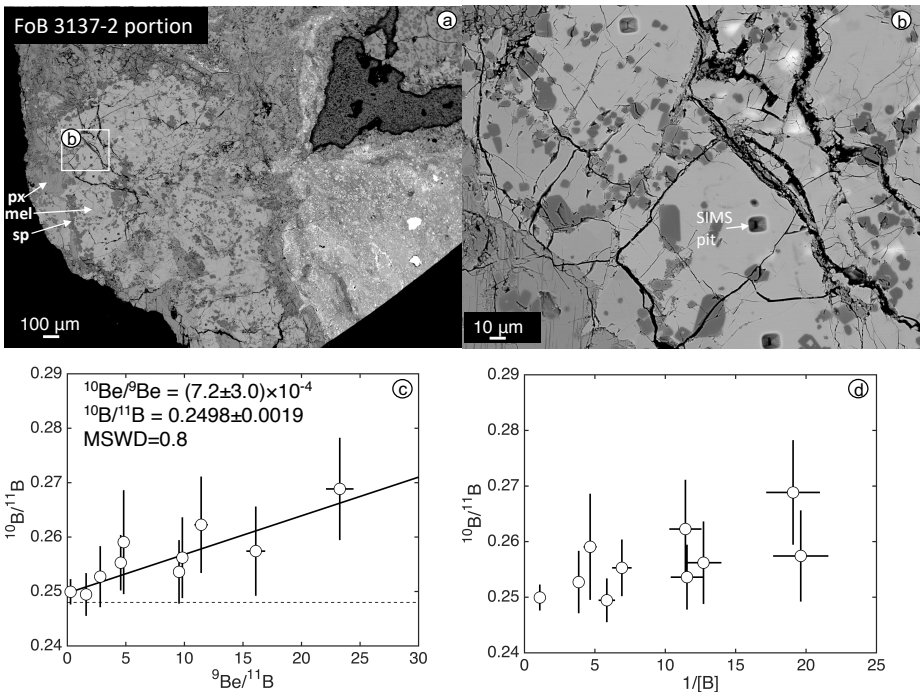


Figure 4.19. CAI FoB *3137-2* (Vigarano, $CV3_{red}$) characterization and isotope results: Whole CAI (a) and enlarged region (b) with ^{10}Be-^{10}B regression results (c, d).

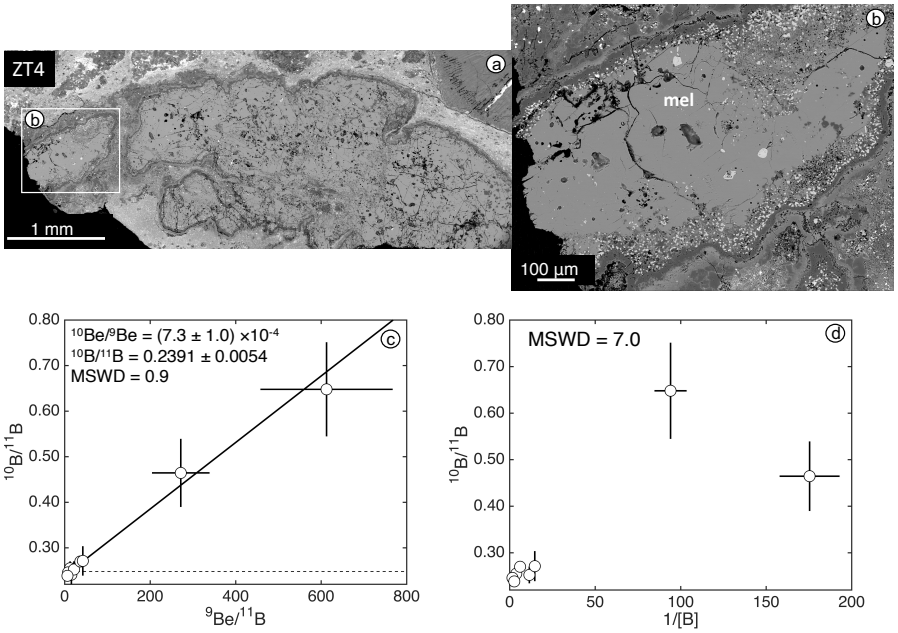


Figure 4.20. CAI *ZT4* (Leoville, $CV3_{red}$) characterization and isotope results: Whole CAI (a) and enlarged region (b) with ^{10}Be-^{10}B regression results (c, d).

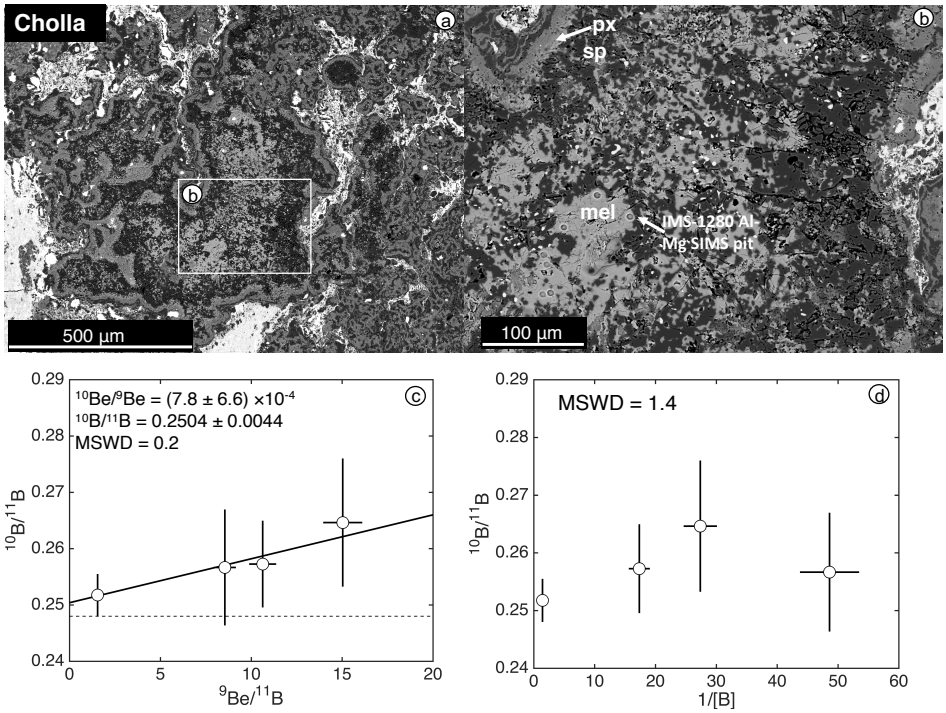


Figure 4.21. CAI *Cholla* (NWA 5028, $CV3_{red}$) characterization and isotope results: Whole CAI (a) and enlarged region (b) with ^{10}Be-^{10}B regression results (c, d).

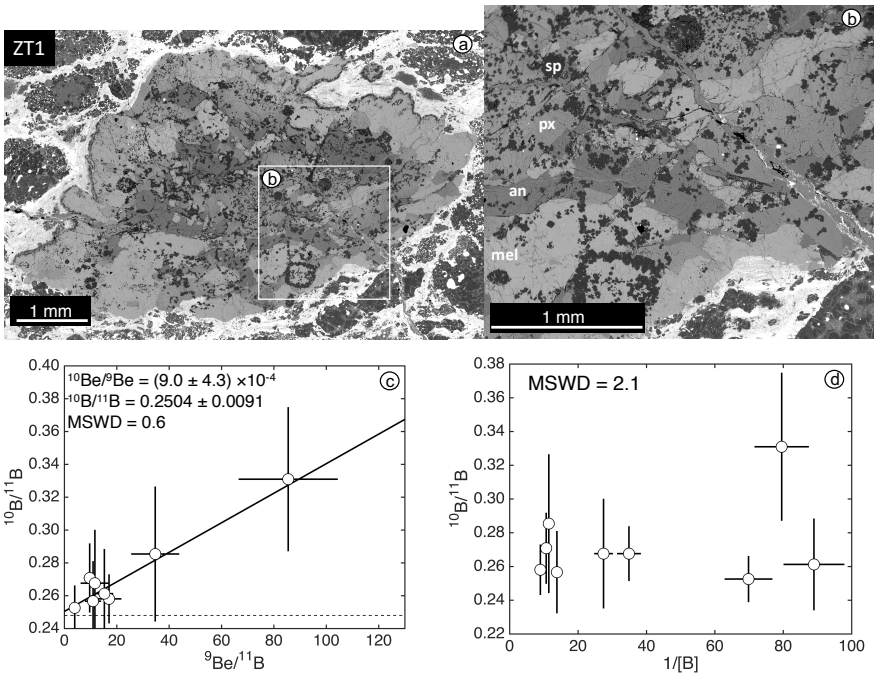


Figure 4.22. CAI *ZT1* (Leoville, CV3$_{red}$) characterization and isotope results: Whole CAI (a) and enlarged region (b) with ^{10}Be-^{10}B regression results (c, d).

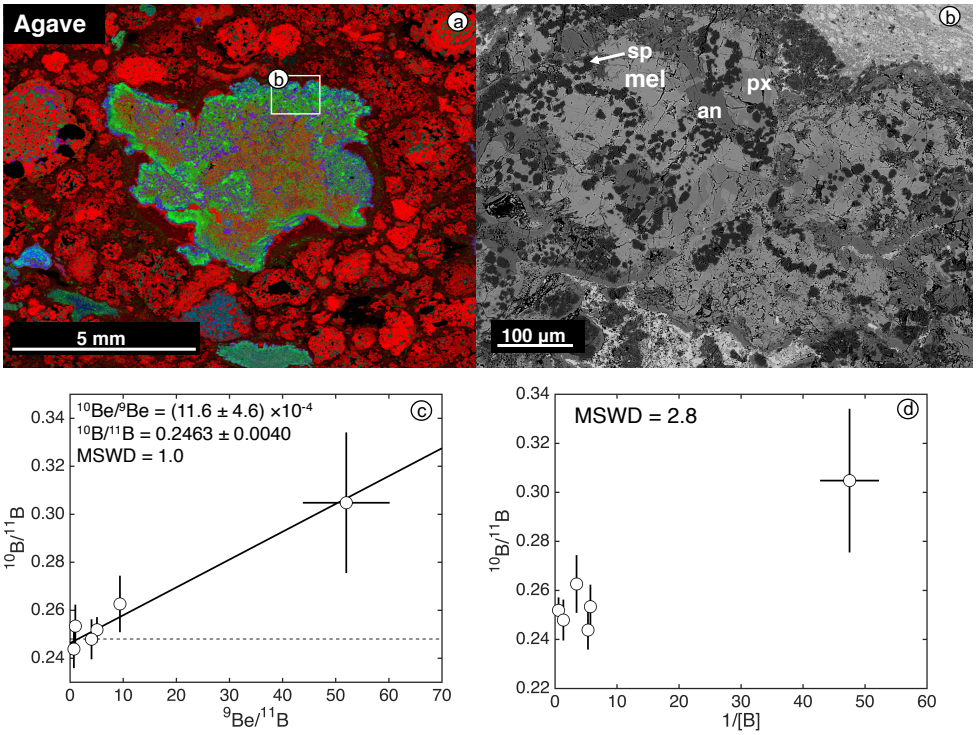


Figure 4.23. CAI *Agave* (NWA 5028, CV3$_{red}$) characterization and isotope results: Whole CAI (a) and enlarged region (b) with ^{10}Be-^{10}B regression results (c, d).

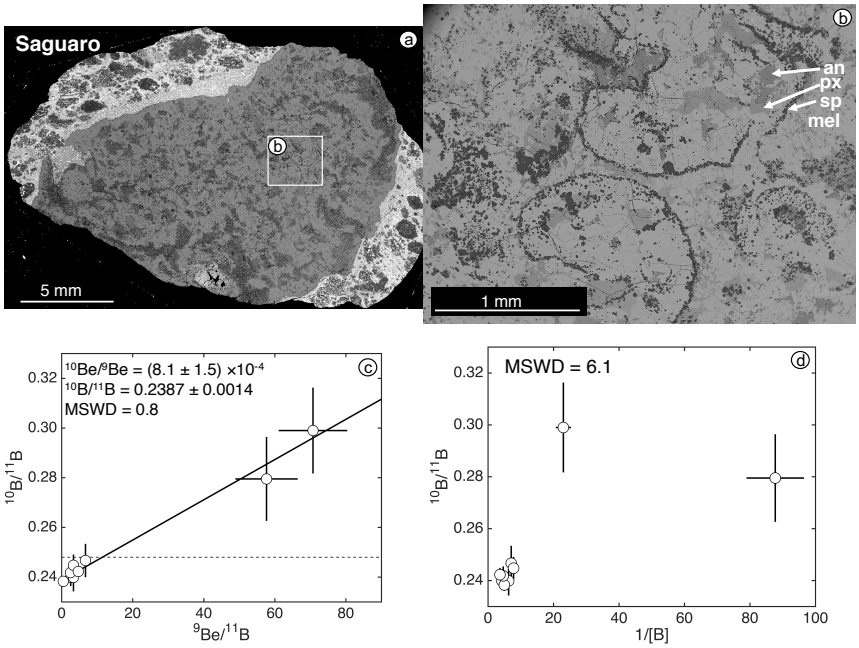


Figure 4.24. CAI *Saguaro* (NWA 5508, CV3) characterization and isotope results: Whole CAI (a) and enlarged region (b) with ^{10}Be-^{10}B regression results (c, d).

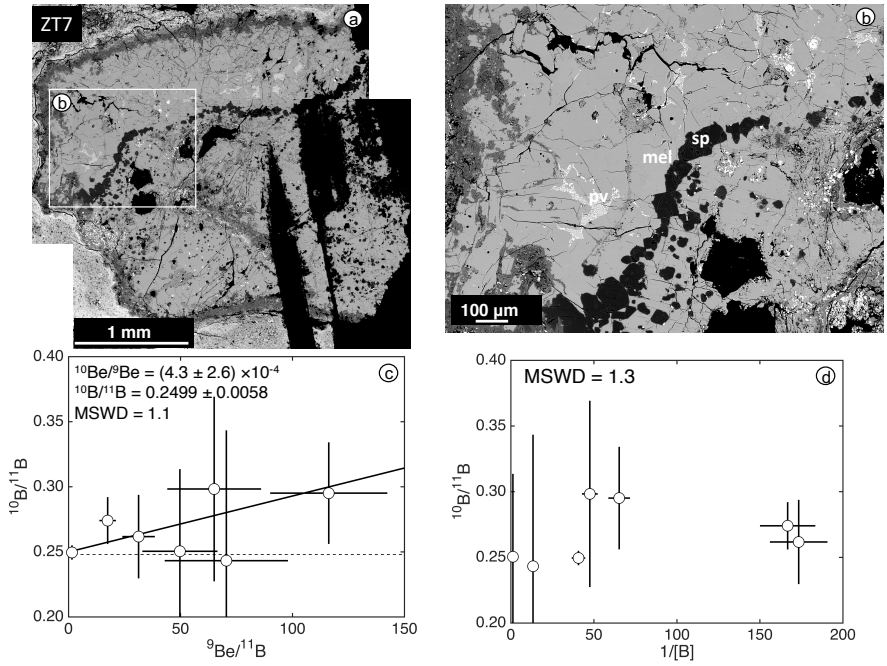


Figure 4.25. CAI *ZT7* (NWA 7891, CV3$_{an}$) characterization and isotope results: Whole CAI (a) and enlarged region (b) with ^{10}Be-^{10}B regression results (c, d).

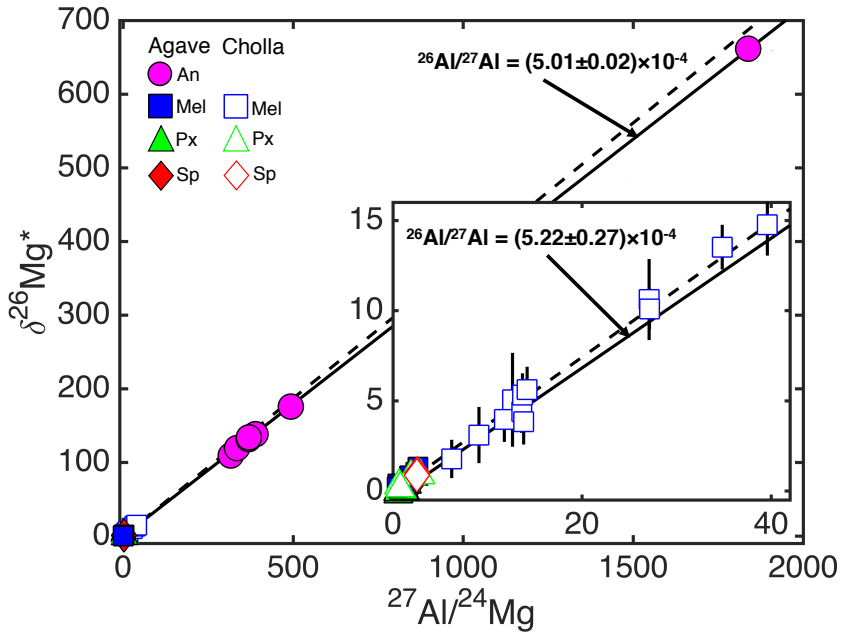


Figure 4.26. ^{26}Al–^{26}Mg systematics of two CV3 CAIs from NWA 5028, *Agave* and *Cholla*. For reference, the black line shows canonical ^{26}Al/^{27}Al = 5.23 × 10^{-5} (Jacobsen et al., 2008). Uncertainties are 2SE.

4.6 CAI Characterization Methods

Polished sections from each of the meteorites investigated here were initially studied with a petrographic microscope in order to locate CAIs of interest. Characterization, including mapping of mineral phases, determination of mineral chemistries, and degree of alteration (based on the abundances of secondary phases such as nepheline, sodalite, and phyllosilicates; (MacPherson, 2013)) in the selected CAIs was performed using the JEOL JXA-8530F electron microprobe in the *Eyring Materials Center* at ASU and the Cameca SX-50 at U. Chicago. It was important to locate areas with clean

melilite for our SIMS studies since this phase typically has high Be/B ratios (Lauretta & Lodders, 1997; Sugiura et al., 2001; Chaussidon, 2006).

4.7 IMS-6f (ASU) Measurements of Be-B Systematics

The $^{10}B/^{11}B$ and $^{9}Be/^{11}B$ ratios were measured in melilite in the selected CAIs using the Cameca IMS-6f at ASU. Following the methods of (Sugiura et al., 2001; MacPherson et al., 2003), analyses of the B isotopic composition and the $^{9}Be/^{11}B$ ratios were obtained with the Cameca ims-6f SIMS at ASU using a $^{16}O^-$ primary beam. The primary accelerating voltage was 12.5 kV and the primary beam current varied from 15 to 30 nA (resulting in a beam diameter of ~20-30 μm). Analytical spots in each inclusion were chosen based on our electron microprobe documentation and characterization to avoid cracks, fine inclusions, and secondary minerals (although it was sometimes impossible to avoid the surrounding spinel grains). We operated the mass spectrometer at a mass resolution M/ΔM of >1300 to resolve and avoid hydride (especially $^{9}BeH^+$) and Al^{3+} interferences. We measured ^{9}Be (8 seconds), ^{10}B (16 seconds) and ^{11}B (4 seconds) on the electron multiplier during 20 and 150 cycles of measurement for each data point to obtain adequate counting statistics. At the end of each analysis, ^{28}Si was also measured to help in determining B and Be concentrations. Because the standard IMt-1 illite ([B]=350 ppm, $^{11}B/^{10}B = 4.007$) was placed as a suspension on the thin sections (Williams et al., 2001), analyses of unknowns and standards were obtained without the requirement to replace the sample with a standard block. The alpha factor was calculated using the equation $\alpha_{inst} = (^{10}B^+/^{11}B^+)/(^{10}B/^{11}B)_{IMt}$. During a single analytical session, the melilite composition glasses and NIST glasses (at

least six spots on each averaged) were measured to determine the difference in RSF. The NIST 610 standard was analyzed before and after each meteorite section to correct for the Be/B ion yield. The calculated RSF_{NIST} ($^{9}Be^{+}/^{11}B^{+}$)/($^{9}Be/^{11}B_{atomic}$) was divided by the uncorrected integrated $^{9}Be^{+}/^{11}B^{+}$ ion ratio measured at each spot to provide the corrected ratio. Resulting data are shown in Table S6.

4.8 IMS-1290 (UCLA) Measurements of Be-B Systematics

We used 3 distinct calibration techniques for the CAIs analyzed via this instrument. In all cases, we generated the primary ion beam with the *Hyperion-II* source.

4.8.1 First Session with Monocollection Spot Analysis

We analyzed CAI *CMS-1* with a primary $^{16}O^{-}$ beam current of 10-15 nA resulting in a beam size ~5 × 4 μm^2, the mass resolving power ~2000, and ^{9}Be (10s), ^{10}B (20s), ^{11}B (15s), and $^{28}Si^{++}$ (3s) were counted for 10-50 cycles depending on the B count rates. NIST 614 was used as the running standard through the session for RSF and IMF corrections.

4.8.2 Second Session with Multicollection Spot Analysis

We analyzed CAI *CMS-1* again as well as a suite of CO3 CAIs. The primary $^{16}O^{-}$ beam current of 10 nA resulted in a beam size ~5 × 4 μm^2. Secondary ion intensities were measured under mass resolving power of ~2,500 in dynamic multi-collection mode. In this setting, we first collected $^{27}Al^{3+}$ and $^{28}Si^{3+}$ simultaneously for 5 sec, then ^{9}Be for 10 sec after one mass jump, and then ^{10}B and ^{11}B for 30 sec as the last step. The NIST 614 glass

standard was measured throughout the analysis session to obtain the $^{9}Be/^{11}B$ relative sensitivity factor (RSF), and to correct for the instrumental mass fractionation on the $^{10}B/^{11}B$ ratio. Melilite-composition glasses with a range of Be/B ratios were measured at the beginning of the session to verify that there were no resolvable matrix effects on the RSF.

4.8.3 Third Session with Multicollection Using O_2^- Raster Analysis

We analyzed another suite of CO3 CAIs as well as CH/CBs and an FoB CAI. A primary $^{16}O_2^-$ primary beam current of 1-2 nA first produced a pre-sputtered 10 × 10 μm^2 rastered square, then produced a rastered area to 5 × 5 μm^2 for the analysis. Secondary ion intensities were measured with multiple electron multipliers (EMs) with a mass resolving power of ~2,500 in dynamic multi-collection mode (first collected $^{27}Al^{3+}$ and $^{28}Si^{3+}$ simultaneously for 5 sec, then ^{9}Be for 10 sec after one mass jump, and then ^{10}B and ^{11}B for 30 sec as the last step). A NIST 614 glass was used as a standard to determine the RSF and IMF correction factors.

4.9 IMS-1280 (UW-Madison) Measurements of Al-Mg Systematics

Analyses of Al-Mg isotope systematics were conducted using the Cameca IMS-1280 SIMS at UW-Madison using methods similar to those described in Kita et al. (2012) (Kita et al., 2012b). It was necessary to use the IMS-1280 for Al and Mg isotope measurements, rather than ASU's IMS-6f, because 1) fine-grained minerals within these CAIs require a smaller beam and 2) high-mass resolution coupled with multi-collection

results are not possible on the smaller radius SIMS. A primary $^{16}O^-$ beam with a total impact energy of 23 kV is used, with beam intensities ranging from ~30 pA to ~6 nA depending on the phase (measured phases included: spinel, melilite, pyroxene, and anorthite if present) and the spot size. The mass spectrometer was operated at a mass resolving power of ~2000 to resolve mass interferences (MgH^+ and $^{48}Ca^{++}$). The secondary ions $^{24}Mg^+$, $^{25}Mg^+$, $^{26}Mg^+$ and $^{27}Al^+$ were measured under two conditions, depending on the measured phase and necessary spot size; (1) simultaneously measuring the isotopes using four multi-collection faraday cup detectors (used to measure low Al/Mg phases: åkermanite-rich melilite, pyroxene, and spinel with spot size > 12μm) and (2) mono-collection electron multiplier detector (used to measure high Al/Mg phases: åkermanite-poor melilite and anorthite with spot size < 8 μm). In order to obtain high-precision results, we used the standard-sample bracketing technique to correct for magnesium isotope instrumental mass bias. The standards include melilite glass standards ($Åk_{15}$, $Åk_{25}$, $Åk_{65}$, $Åk_{75}$, $Åk_{65}$), natural pure spinel ($MgAl_2O_4$), pyroxene glass standards with differing Ti content (5-10 wt.% TiO_2), and anorthite glass standards (An_{59} MgO 0.1%, An_{100} MgO 0.1%, An_{100} MgO 1%). Excess ^{26}Mg was calculated using the equation $\delta^{26}Mg^* = \delta^{26}Mg - [(1 + \delta^{25}Mg/1000)^{1/\beta} - 1] \times 1000$ (e.g., (Davis et al., 2015)), the β value of 0.5128 (Davis et al. 2015) (Davis et al., 2015) was applied. Resulting data are shown in Table S9. The instrumental mass fractionation (IMF) was also measured using these standards.

4.10 Statistical Analysis

Boron counts are so low that the count rates were summed to give total counts for each isotope (integrated counts instead of the usual series of ratio measurements). All errors are 2σ and were calculated by adding in a quadratic way the internal errors of each spot (counting statistics), and the errors on RSF and IMF. All York regressions were calculated using IsoplotR (Vermeesch, 2018). After SIMS analysis sessions, we imaged the SIMS pits using the JEOL JXA-8530F electron microprobe at ASU to ensure that they were not on cracks or small inclusions. If they were, or if the B counts were not stable throughout an analysis, that data point was removed from the regression. If the B counts were constant/flat for at least 20 cycles but then became unstable, we calculated the $^{10}B/^{11}B$ and $^{9}Be/^{11}B$ ratios as well as counting statistics based on the stable portion of the analysis.

4.11 The Reclassification of Northwest Africa 5028

Northwest Africa (NWA) 5028 is a 2.45 kg meteorite and was originally classified as a CR2 chondrite (Weisberg et al., 2010; Harju et al., 2014). However, discrepancies between the petrology of the sample and known features of CR chondrites were noted during this study (including chondrule sizes, CAI abundance, and opaque mineralogy). To independently determine the classification of NWA 5028, we studied the petrology and chemical compositions of mineral phases in a polished mount (ASU1845) from the ASU Center for Meteorite Studies Meteorite Collection.

4.11.1 Analytical Methods

Backscattered electron (BSE) images of NWA 5028 ASU1845 were obtained with the JEOL-8530F electron probe microanalyzer (EPMA) at Arizona State University (ASU). Apparent chondrule diameters were obtained by measuring the major and minor axes of chondrules using a full thin section image with Adobe Photoshop®.

Major-element abundances were characterized quantitatively by the Cameca SX-100 EPMA at the University of Arizona. The polished and carbon-coated mount was analyzed with a focused beam as individual points and line scans, with operating conditions of 15kV and 20 nA, and a ZAF correction method (a Phi-Rho-Z correction technique). Only stoichiometric silicate analyses, and metal and sulfide analyses, with totals between 98.0–102.0 wt.% were retained. Standards and detection limits are listed in Tables S4.

4.11.2 Results

The maximum apparent diameters of the whole chondrules range from 0.25 to 3.52 mm (mean±2SE; 1.22±0.25 mm, 40 whole chondrules). Observed chondrule types include porphyritic olivine, porphyritic olivine-pyroxene, and barred olivine.

The sample also contains abundant CAIs, which range in maximum apparent diameters from 2.00 to 5.02 mm (e.g., Figure 4.27) and constitute ~6.5 vol.% of the sample.

Chondrule olivine ranges in composition from $Fa_{0.7\text{-}46.4}$ (18 analyses), with type I chondrules ($Fa_{0.7\text{-}1.3}$; 9 analyses), and type II chondrules ($Fa_{22.8\text{-}46.4}$; 9 analyses; Table S4). Type I chondrules (Figure 4.28) contain assemblages of Ni-poor (<10 wt.% Ni) and Ni-rich metal (>10 wt.% Ni), with abundant Ni-poor pyrrhotite (up to 0.25 wt.% Ni; Table

S4). Type II chondrules (Figure 4.28) contain minor amounts of Ni-rich metal, chromite, and rare Ni-bearing pyrrhotite (1.1 wt.% Ni). The Ni/Co ratio of metal in chondrules does not show a positive correlation (e.g., Ni-poor metal, 0.28-1.64 wt.% Co; Ni-rich metal, 0.15-1.50 wt.% Co; Figure 4.29).

4.11.3 Discussion

The compositions of individual minerals in, and petrology of, NWA 5028 are inconsistent with its original classification of CR2 chondrite and show that it is a reduced CV3 chondrite.

1) The mean chondrule size of NWA 5028 (1.22±0.25 mm; mean±2SE) is inconsistent with the mean chondrule size of 0.7 mm for the CR chondrites (e.g., (Kallemeyn et al., 1994; Friedrich et al., 2015; Schrader et al., 2015)). However, the mean chondrule size of NWA 5028 is consistent with that of CV chondrites (mean 0.9 mm) chondrites; (Rubin, 2010; Friedrich et al., 2015).

2) The size, type, and modal abundance of CAIs are inconsistent with those of CR chondrites. CR chondrites contain ~0.4 vol.% CAIs (Schrader et al., 2011), which are typically <0.5 mm in diameter (Aléon et al., 2002). In contrast, CV chondrites contain ~ 10 vol.% CAIs (Weisberg et al., 2006) with diameters typically >1 mm (Brearley & Jones, 1998).

3) The opaque mineralogy of type I and type II chondrules, and their compositions, in NWA 5028 are inconsistent with that in CR chondrites. In CR chondrites, type I chondrules contain abundant Ni-poor Fe,Ni metal and in rare cases minor sulfides (Schrader et al., 2015). Type II chondrules in CR chondrites contain ubiquitous sulfides and in very rare instances Fe,Ni metal which is usually Ni-rich. However, this is the opposite of that observed here for NWA 5028. In NWA 5028, type I chondrules contain Ni-poor and Ni-rich Fe,Ni metal and abundant sulfides (Figure 4.27), while its type II chondrules contain rare opaque minerals consisting of Ni-rich metal and rare sulfides (Figure 4.27) This is identical to the opaque mineralogy of reduced CV3 chondrites (Davidson et al., 2014).

The Co content of Fe,Ni metal is positively correlated in the CR chondrites, with low Co contents (<0.8 wt.%) in Ni-poor metal and high Co contents (up to 2 wt.%) in Ni-rich metal ((Schrader et al., 2015). There is no correlation between the Co and Ni content in Fe,Ni metal in NWA 5028 (Figure 4.28) indicating it is not a CR chondrite, but is consistent with that seen in reduced CV3 chondrites (Davidson et al., 2014). In addition, this Ni/Co association in metal is a sign of parent body thermal metamorphism (Kimura et al., 2008; Davidson et al., 2014) and is not observed in CR chondrites (Schrader et al., 2015).

4.11.4 Conclusion

The combination of the mineralogy and petrology of NWA 5028 shows that it is a reduced CV3 chondrite, and not a CR chondrite as originally classified.

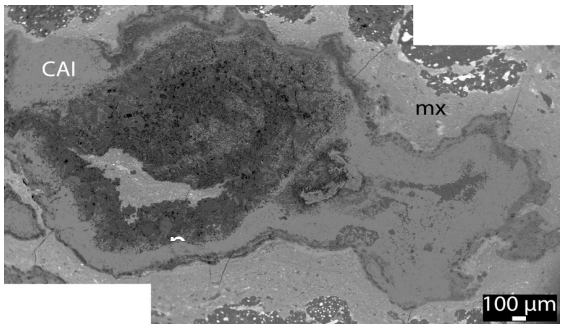


Figure 4.27. Mosaic BSE of portion of largest calcium-aluminum-rich inclusion (CAI) in NWA 5028 ASU1845. This CAI is much larger than those observed in CR chondrites. mx = matrix, mel = melilite, px = pyroxene.

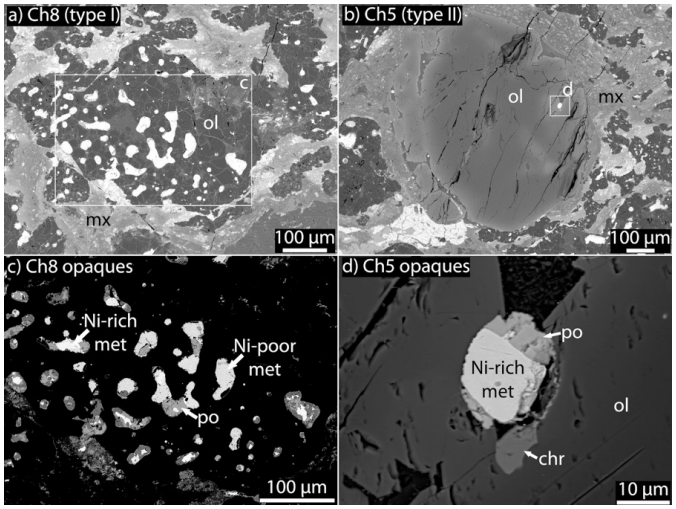


Figure 4.28. BSE images of a representative type I chondrule (a) and a type II chondrule (b) in NWA 5028 ASU 1845. Both porphyritic olivine (ol) chondrules. (c) The type I chondrule contains abundant Ni-poor metal (Ni-poor met), Ni-rich metal (Ni-poor met),

and pyrrhotite (po). The type II chondrule contains rare opaque minerals, which include Ni-rich metal, pyrrhotite, and chromite. The opaque mineral association is unlike that observed in CR chondrites (Schrader et al., 2015). mx = matrix.

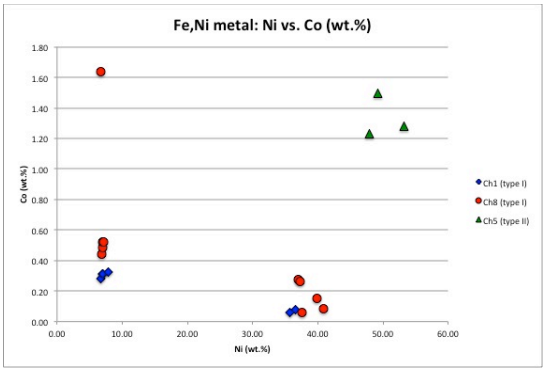


Figure 4.29. Ni vs. Co (wt.%) from Fe,Ni metal in type I and type II chondrules in NWA 5028 ASU1845. There is no correlation between Ni and Co, unlike that observed in metal from CR chondrites (Schrader et al., 2015).

CHAPTER 5

OXYGEN ISOTOPE VARIATIONS IN CV3 CAIs CORRELATED TO ^{26}Al AND ^{10}Be: IMPLICATIONS FOR SOLAR SYSTEM OXYGEN ISOTOPE RESERVOIRS

5.1 Introduction

Refractory calcium- and aluminum- rich inclusions (CAIs) are preserved within chondritic meteorites and they are the oldest dated objects in the Solar System (Amelin et al., 2002; Connelly et al., 2012). Because CAIs were the first solids to form in our solar nebula, they contain a wealth of information about events which took place in the early Solar System as well as the nature of the material from which the Solar System formed. CAIs have a wide variety of shapes, sizes, textures, mineralogy, bulk elemental abundances, and isotopic composition, so they preserve a view of the diverse conditions near the hot disk (<1300 K) of the Sun (MacPherson, 2013).

CAIs recorded the oxygen isotope reservoir in which they were originally formed and were subsequently processed. Interestingly, the oxygen isotopic compositions of CAIs span the whole range between the solar and planetary composition (MacPherson, 2013). While some CAIs have a homogeneous ^{16}O-rich composition in all minerals (Aléon et al., 2002; Simon et al., 2019), some CAIs range from near solar to planetary in individual samples; commonly in CAIs, spinel is ^{16}O-rich, melilite is ^{16}O-poor, and anorthite and pyroxene have a range of Δ^{17}O, although the details are very sample dependent (McKeegan et al., 1998; Aléon, 2016; Kawasaki et al., 2017; Aléon et al., 2018). Various models have been proposed to explain the variations in oxygen isotopic

compositions of phases in CAIs, including 1) evolution of the oxygen isotope composition of the nebular gas in the local environment where the igneous CAIs were crystallizing and processed (Yurimoto et al., 1998); 2) transport and processing of CAIs between ^{16}O-poor protoplanetary disk and ^{16}O-rich coronal gas located above the disk edge (Aléon, 2016; Kawasaki et al., 2018); 3) solid-state diffusion during nebular reheating of CAIs (Ryerson & McKeegan, 1994; Clayton & Mayeda, 1996); or 4) late isotopic exchange during parent-body secondary alteration (Wasson et al., 2001; Simon et al., 2019).

CAIs also attest to the former presence of short-lived radionuclides such as ^{26}Al and ^{10}Be in the solar nebula (half-lives of 0.7 and 1.4 Ma respectively; Norris et al., 1983; Korschinek et al., 2010). These SLRs are suggested to have been introduced and distributed uniformly in the solar nebula. The majority of normal CAIs recorded ^{26}Al/^{27}Al at or close to the canonical level (~5.2×10^{-5}; Jacobsen et al., 2008)), but some range down to about ~4×10^{-5} due to thermal processing ~0.25 Myr later (MacPherson et al., 2012b). These measurements suggest that initial ^{26}Al was likely distributed homogeneously in the CAI forming region (Villeneuve et al., 2009; Kita et al., 2013). Aluminum-26 was presumably produced by a nearby supernova or Wolf-Rayet star and inherited into the solar nebula (Wadhwa et al., 2007; Ouellette et al., 2009; Dauphas & Chaussidon, 2011; Dwarkadas et al., 2017). Beryllium-10, on the other hand, can only be produced by irradiation of high-energy particles interacting with gas and solids. The majority of CAIs had a uniform ^{10}Be/^{9}Be value of 7×10^{-4} (Chapter 4), so ^{10}Be was likely distributed uniformly in the CAI forming region. This suggests that ^{10}Be was inherited

from the molecular cloud (where it was produced by galactic cosmic ray-driven reactions in the gas; Chapter 4). Because both ^{26}Al and ^{10}Be were distributed uniformly in the CAI forming region, they can be used as chronometers as well as indicators of later alteration. In correlating these SLRs with oxygen isotopes in the same suite of CAIs, we are able to better understand the origin of oxygen isotope distributions recorded by CAIs, and therefore, the CAI formation environment, and processes in the protoplanetary disk.

5.2 Samples

The five CV3 CAIs considered in this study include *B4* (NWA 6991, $CV3_{ox}$), *Agave* (NWA 5028, $CV3_{red}$), *Cholla* (NWA 5028, $CV3_{red}$), *Saguaro* (NWA 5508, CV3), and *TS23* (Allende, $CV3_{ox}$). These samples have been previously described in detail (Chapter 4), so here we briefly describe the pertinent characteristics of each CAI. CAI *B4* (NWA 6991, $CV3_{ox}$) is a compact type A (CTA) inclusion (~10 mm in the longest dimension) predominately composed of coarse melilite grains (~$Åk_{4\text{-}61}$), along with fassaite, spinel, and minor anorthite; secondary alteration is only a minor component of *B4* (Bouvier et al., 2011; Bullock et al., 2014). This inclusion has an ancient absolute Pb-Pb age of 4567.94 ± 0.31 Ma (Bouvier et al., 2011), well-behaved ^{26}Al–^{26}Mg systematics corresponding to a near-canonical ^{26}Al/^{27}Al ratio (Wadhwa et al., 2014), and a ^{10}Be/^{9}Be ratio of $(6.8 \pm 2.8) \times 10^{-4}$ (Chapter 3).

CAI *Agave* (NWA 5028, $CV3_{red}$) is a type B2 inclusion (~5 mm across) dominated by fassaite, which encloses patches of melilite (~$Åk_{1\text{-}85}$) and anhedral spinel; only minimal alteration products are present. This inclusion has a $(^{10}Be/^{9}Be)_0$ ratio of

(11.6 ± 4.6) × 10^{-4} and a $^{26}Al/^{27}Al$ ratio of (5.01 ± 0.02) × 10^{-5} (Chapter 4). CAI *Cholla* (NWA 5028, $CV3_{red}$) is a fluffy type A (FTA) ~1 mm along the longest axis which contains anhedral spinel, typically <10 μm diameter, enclosed in melilite ($Åk_{4-18}$), the inclusion is surrounded by an irregular ~40 μm thick pyroxene rim. The only alteration found in the CAI is a patch of secondary anorthite. This inclusion has a $^{10}Be/^{9}Be$ ratio of (7.8 ± 6.6) × 10^{-4} and a $^{26}Al/^{27}Al$ ratio of (5.21 ± 0.28) × 10^{-5} (Chapter 4).

CAI *Saguaro* (NWA 5508, CV3) is a spherical type B2 inclusion (~18 mm diameter) composed predominately of melilite ($\sim Åk_{30-65}$), with fassaite, spinel, and anorthite. Saguaro includes minimal alteration products and recorded $^{10}Be/^{9}Be$ = (8.2 ± 2.0) × 10^{-4} (Chapter 4). CAI *TS23* (Allende, $CV3_{ox}$) is a type B1 inclusion (~10 mm in diameter) composed of melilite ($\sim Åk_{5-25}$), fassaite, pyroxene, and spinel; it includes some minor secondary anorthite. The $^{26}Al/^{27}Al$ in TS23 is estimated to be (4.4 ± 0.6) × 10^{-5} (Hutcheon, 1982), and it has a high $^{10}Be/^{9}Be$ = (6.1 ± 2.2) × 10^{-4} (Chapter 4).

5.3 Methods

5.3.1 Petrography and Mineralogy

The JEOL JXA-8530F EPMA at Arizona State University (ASU) was used to take back-scattered electron (BSE) and secondary electron (SE) images for characterization and SIMS preparation, and for mineral identification using EDS and WDS. The analytical conditions were: 20 kV, 20 nA, and the standards used for ZAF corrections include San Carlos Augite, Anorthite – Hakone, Orthoclase, Hornblende – Kakanui, rutile, Johnstown hypersthene, chromite, and Durango apatite.

4.3.2 Oxygen Isotopes

We used the CAMECA ims-1280 for *in-situ* oxygen isotope analyses at the WiscSIMS laboratory at UW-Madison. Cs^+ primary beam *in situ* oxygen isotope analyses of spinel, melilite, pyroxene, and anorthite in CAIs *Saguaro*, *Agave*, *B4*, and *TS23* were performed during one session, while *Cholla* analyses were completed during a separate session using a different configuration. For the first session, analytical conditions were similar to those reported using Faraday Cup FC-FC-FC configuration (Kita et al., 2010). The primary beam was focused to ~10 μm diameter at 0.6 nA. The secondary $^{16}O^-$ beam intensity was ~8×10^8 cps. We used a 10^{12} ohm resistor for the FC amplifier board for ^{17}O. The mass resolving power (MPR) was set to ~2200 for ^{16}O and ^{18}O using 2 detectors on the multi-collection array, and 5000 for ^{17}O using the axial electron multiplier (EM) detector. The correction for OH^- interference on ^{17}O was checked for each analysis and found to be negligibly small (<0.4%) except for a few cases. For the second session, analytical conditions were similar to those reported using FC-EM-EM (Nakashima et al., 2012). The focused primary beam was set to ~1 × 2 μm diameter and intensity of ~3pA. The secondary ions $^{16}O^-$, $^{17}O^-$, and $^{18}O^-$ were detected simultaneously by a Faraday cup ($^{16}O^-$), and electron multipliers ($^{17}O^-$ and $^{18}O^-$) on the multi-collection system. Intensities of $^{16}O^-$ were ~2×10^6 cps. The contribution of the tailing $^{16}OH^-$ interference to $^{17}O^-$ signal was corrected by the method (Heck et al., 2009), though the contribution was negligibly small (<0.04‰). For both sessions, San Carlos olivine was used as a standard and bracketed the unknown CAI analyses. Instrumental mass biases were corrected from the

analyses of pyroxene (TiO_2: 2%, 10%), melilite (åkermanitic and gehlenitic), anorthite, and spinel standards at the beginning of the session. The 2σ errors for $\Delta^{17}O$ (= $\delta^{17}O - 0.52 \times \delta^{18}O$) were typically ±0.5–1.0‰. After the SIMS session, SEM images were taken of the spot analyses; only a few visibly overlapped cracks, small inclusions, or were too close to previous oxygen primary analysis spots (this would force the analysis to be more ^{16}O-rich due to the composition of the primary beam); these were not considered in results interpretations.

5.4 Results

All oxygen isotope data collected for each of the five CAIs are shown in Figure 5.1 and summarized in Table 5.1 and S10. Data were collected *in situ* from multiple mineral phases within each inclusion. Some analyses overlapped cracks and are mentioned below; because this can affect the results these analyses were removed from interpretations. Data for all five inclusions plot slightly off the carbonaceous chondrite anhydrous mineral (CCAM) line (Clayton, 2003). The oxygen isotopic compositions of pyroxene and spinel of CAIs *Saguaro* and *B4* show a small degree (up to ~5‰) of mass-dependent fractionation and plot along a slope ~0.5 line.

5.4.1 NWA 5028 CAI *Agave*

We measured 4 spinel, 4 melilite, 5 fassaite, and 3 anorthite grains. Spinel and fassaite is ^{16}O-rich, melilite is ^{16}O-poor, and anorthite shows a range of $\Delta^{17}O$ from -20‰

to -4‰. All points are spread along the CCAM line with a slope ~9 (Figure 5.1 and 5.2, Tables 5.1 and S10).

5.4.2 NWA 5028 CAI *Cholla*

We measured 6 spinel, 7 melilite, and 6 fassaite grains. Five of these analyses were on cracks or too near a previous oxygen beam SIMS analysis, so the total number of data points plotted is 14. Spinel and all but one fassaite analysis (a fassaite grain with TiO_2 ~11 wt.% has $\Delta^{17}O$=-19) are ^{16}O-rich. The melilite ranges in $\Delta^{17}O$ from -24 to -7‰; this variation correlates to Åk content which ranges from 10 to 20 mol% (Figure 5.3). Most analyses are on the CCAM line except for 2 melilite data points which are to the left of the line. All analysis spots were approximately in the center of grains due to the fine-grained nature of the inclusion (Figure 5.1 and 5.2, Tables 5.1 and S10).

5.4.3 NWA 5508 CAI *Saguaro*

We measured 4 spinel, 4 melilite, 4 fassaite, and 5 anorthite grains. Spinel and pyroxene are ^{16}O-rich, melilite is ^{16}O-poor, and anorthite ranges in $\Delta^{17}O$ from -19 to -8‰. Most data points are slightly to the right of the CCAM line; spinel and pyroxene fall along slope 0.55, while anorthite and melilite fall along slope 0.93 (Figure 5.1 and 5.2, Tables 5.1 and S10).

5.4.4 NWA 6991 CAI *B4*

We measured 4 spinel, 4 melilite, 5 fassaite, and 3 anorthite grains. Spinel and pyroxene are ^{16}O-rich, anorthite is ^{16}O-poor, and melilite ranges in Δ^{17}O from -7 to -3‰. All data points are located to the right of the CCAM line; spinel and pyroxene fall along slope 0.62 while anorthite and melilite fall along slope 0.79 (Figure 5.1 and 5.2, Tables 5.1 and S10).

5.4.5 Allende CAI *TS23*

We only analyzed one spot of each spinel, melilite, fassaite, and anorthite. The reason for this is because the thin section was too damaged to proceed with additional SIMS analyses. So, these may not be a representative dataset. The data lies on the CCAM line; spinel and pyroxene are ^{16}O-rich while melilite and anorthite are ^{16}O-poor (Figure 5.1 and 5.2, Tables 5.1 and S10).

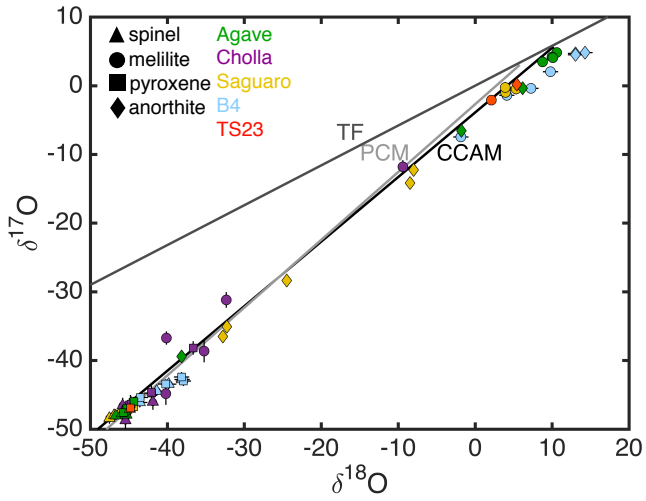


Figure 5.1. Oxygen isotope composition of 5 CAIs. CAIs *Agave* and *Cholla* are from NWA 5028 ($CV3_{red}$), CAI *Saguaro* is from NWA 5508 ($CV3_{red}$), CAI *B4* is from NWA

6991 ($CV3_{ox}$), and CAI *TS23* is from Allende ($CV3_{ox}$). The symbols indicate the mineral phase analyzed (spinel = triangle, melilite = circle, pyroxene = square, anorthite = diamond) and the colors represent the CAI (*Agave* = green, *Cholla* = purple, *Saguaro* = yellow, *B4* = blue, *TS23* = orange). TF=terrestrial fractionation line, PCM = primitive chondrite minerals line, CCAM = carbonaceous chondrite anhydrous mineral line.

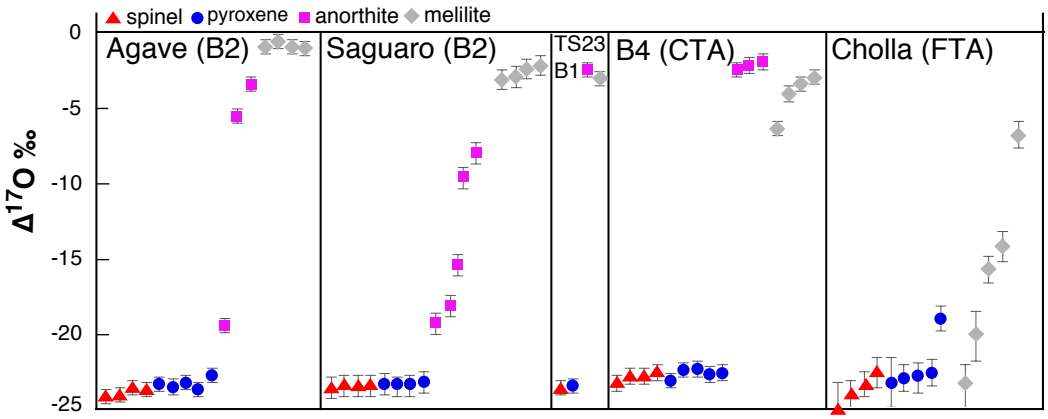


Figure 5.2. $\Delta^{17}O$ composition of 5 CAIs. Analyses are grouped by CAI and include spinel (red triangle), pyroxene (blue circle), anorthite (pink square), and melilite (gray diamond). CAIs *Agave* and *Cholla* are from NWA 5028 ($CV3_{red}$), CAI *Saguaro* is from NWA 5508 ($CV3_{red}$), CAI *B4* is from NWA 6991 ($CV3_{ox}$), and CAI *TS23* is from Allende ($CV3_{ox}$).

5.5 Discussion

Correlating oxygen isotope systematics with short-lived radionuclides ^{10}Be and ^{26}Al in a set of CV3 CAIs provides clues to the environment in which CAIs originated and evolved. In this chapter, we focus on better understanding the origin of oxygen isotope distributions in CAIs. All CAIs studied here have a ^{16}O-rich signature in the

early-formed spinel, which indicates that the reservoir in which the CAIs first formed was ^{16}O-rich (Figures 5.1 and 5.2; Kawasaki et al., 2017). But from that point on in their formation history, each CAI has a distinct story to tell.

5.5.1 Oxygen Isotope Distributions in CAI minerals

In comparing the oxygen isotope distribution in different CAI types (B2 CAIs, CTA CAI, FTA CAI and CAIs from other studies), we discuss the oxygen isotope reservoirs in which their minerals formed and evolved. Some CAIs appear to have been melted while others remained unprocessed condensates, as evidenced by textures and mineral compositions (i.e., melilite reverse zoning versus normal zoning respectively; (Simon et al., 1999; MacPherson, 2013)). The fine-grained fluffy type A, CAI *Cholla*, was, for the large part, un-melted and has a ^{16}O-rich signature. Only melilite in this CAI appears to have partially exchanged with a ^{16}O-poor reservoir, potentially because the oxygen diffusion rate in melilite is the fastest ((Ryerson & McKeegan, 1994). Other previously measured FTA CAIs have a similar oxygen isotope mineral variations except some have minerals with a larger range in Δ^{17}O (Fagan et al., 2004; Park et al., 2012; Kawasaki et al., 2017). The remaining CAIs measured in this work were equilibrated and melted to different degrees (Simon et al., 1999; MacPherson, 2013) and have a more dominant ^{16}O-poor signature.

Compact type As are composed of predominantly melilite but can additionally have spinel, pyroxene, and perovskite. Type Bs are composed of melilite, spinel, pyroxene, and anorthite in varying proportions depending on the sample. Type B1s have

a thick melilite mantle and an interior mixture of melilite, pyroxene, and anorthite (MacPherson, 2013). Type B2s are similar to B1s except they do not have a melilite mantle (so are less melilite-rich; Bullock et al., 2013). It has been hypothesized, using experiments (Mendybaev et al., 2006), that differing rates of molten CAI surface volatilization of Mg and Si during a melting event under reducing conditions could have caused the difference in type B1s and B2s. Experiments have also been conducted to determine the crystallization sequence from a melt. For a type B composition melt, it is determined that the sequence is: spinel (1550 °C) → melilite (1400 °C, Ak_{22}) → anorthite (1260 °C) → fassaite (1230 °C) (Stolper, 1982), with melilite becoming increasingly akermanitic with decreasing temperature. The different conditions under which the CTAs, Type B1s and Type B2s were formed and processed could have caused them to have distinct oxygen isotope distributions in their minerals.

The CTA CAI studied in this chapter, *B4* from NWA 6991, has ^{16}O-rich spinel and pyroxene but ^{16}O-poor melilite and anorthite. CTA CAIs studied previously have a range of oxygen isotope compositions. All have ^{16}O-rich spinel as well as melilite ranging to ^{16}O-poor, but the Δ^{17}O range of the melilite and pyroxene composition are variable (MacPherson et al., 2012a). The type B2 CAIs in this chapter (*Agave* and *Saguaro*) have ^{16}O-rich spinel and pyroxene, ^{16}O-poor melilite and anorthite which has a range in Δ^{17}O. Although the type B1 CAI studied here has only a few measurements, recorded ^{16}O-rich spinel and pyroxene, and ^{16}O-poor melilite and anorthite. We do not observe any correlation with these igneous CAI results and Åk or TiO_2, but it is possible that more analyses are necessary to reveal this. Type B2 CAIs had not been measured

until this work, but B1 CAIs from other studies have oxygen isotope compositions which vary between minerals. For example, B1 CAI *TS34* has ^{16}O-poor melilite, ^{16}O-rich melilite and anorthite, and pyroxene that ranges from Δ^{17}O of -3 to -23‰ (Kawasaki et al., 2018). Type B1 CAI, *USNM-3529-Z,* has ^{16}O-rich spinel, ^{16}O-poor melilite, anorthite ranging from Δ^{17}O of -5 to -7‰ and pyroxene ranging from Δ^{17}O of -15 to -24‰. Another type B1 CAI, *CGI-10,* has ^{16}O-rich spinel, fassaite, and anorthite while melilite is ^{16}O-poor (Fagan et al., 2004).

In comparing igneous CAI types across studies, there does not appear to be a trend between the CAI type or mineralogy and mineral oxygen isotope composition variations. Despite the differences, a commonality between igneous CAIs is that all spinel is ^{16}O-rich and all melilite has a ^{16}O-poor component.

5.5.2 Comparing Oxygen Isotopes of Adjacent CAIs

CAIs *Agave* and *Cholla* were found located within about 20 cm of each other in a slab of NWA 5028 ($CV3_{red}$). Because of the proximity of these two CAIs, we would expect them to have experienced nearly the same conditions on the parent body. With respect to oxygen isotopes, we would expect parent body fluids to have reacted with and introduced a ^{16}O-poor signature to the CAI by diffusion and/or dissolution and/or reprecipitation. We would also expect the thermal metamorphism on the parent body to have affected the CAIs similarly. Melilite with the fastest oxygen diffusion rate among CAI minerals, would more readily exchange with ^{16}O-poor material. In this scenario, we would also expect the finer grains with more surface area to be the most completely

altered (Fagan et al., 2004). CAI *Agave* is a large (~5 mm) igneous type B2 inclusion while *Cholla* is a smaller (~1 mm) fine-grained fluffy type A CAI (Chapter 3). Because of *Cholla's* fine-grained nature, we would expect it to be more ^{16}O-poor if it was aqueously altered (Fagan et al., 2004). We find, though, that igneous CAI *Agave* is more ^{16}O-poor (i.e., more minerals composing *Agave* are ^{16}O-poor) when compared to FTA *Cholla*. CAI *Agave* has ^{16}O-rich spinel and pyroxene but ^{16}O-poor melilite and anorthite ranging from ^{16}O-rich to ^{16}O-poor. CAI *Cholla* has ^{16}O-rich spinel and pyroxene and predominantly ^{16}O-rich melilite (Δ^{17}O from -24 to -16‰). Adjacent type B and FTA CAIs with differing oxygen isotope compositions have been measured previously (Fagan et al., 2004). Although the oxygen isotopes measured in the CAIs could have been minimally affected by alteration and processing on the CV parent body, we suggest that this was not the predominant mechanism causing oxygen isotope variations among the CAI minerals. Alteration in the nebula, however, remains a viable mechanism to produce oxygen isotope variations.

Another hint that parent body alteration was not the main process affecting oxygen isotope distribution is that CAI *Cholla* has oxygen isotope compositions correlated to melilite Åk content as well as fassaite TiO_2 content (Figure 5.3). Katayama et al., (2012) observed this in another $CV3_{red}$ fluffy CAI and suggests that melilite condensation proceeded with change in oxygen isotope composition of the gas. This melilite likely began condensing in a ^{16}O-poor reservoir and became continuously more ^{16}O-rich with time and decreasing gas pressure. So, the correlation between oxygen isotopic composition and åkermanite content may indicate that oxygen isotopes of the

solar nebula changed from ^{16}O-poor to ^{16}O-rich during melilite growth (Park et al., 2012). More analyses and profiles across melilite and pyroxene grains in *Cholla* and other FTAs would be helpful in constraining this astrophysical environment. Some studies find that pyroxene TiO_2 is correlated with $\Delta^{17}O$ in Type B CAIs (Aléon, 2016; Kawasaki et al., 2017); this demonstrates that oxygen isotopic composition of the blocky pyroxene crystals evolved during magmatic crystallization (Ti content will not vary as a function of aqueous alteration). Generally, isotope change from ^{16}O-poor to ^{16}O-rich is in direction of crystal growth (decreasing TiO_2 contents; Simon et al., 1999). We do not find this in our B2 CAIs, which could be due to fewer analyses possibly obscuring this trend, or perhaps our samples experienced higher temperatures/more aqueous alteration which could have erased these signatures.

5.5.3 Implications for Combined ^{10}Be–^{10}B, ^{26}Al–^{26}Mg and oxygen isotopes

Although SLRs ^{26}Al and ^{10}Be were likely inherited into the Solar System (Chapter 4), they provide clues about oxygen isotope reservoirs which existed in when the Solar System was forming and evolving. In correlating oxygen isotope compositions of different minerals to ^{10}Be and ^{26}Al in the same CAIs (Figures 5.4 and 5.5), we suggest that the initial reservoir in which CAIs formed was uniform with respect to oxygen and SLRs. This is due to the observation that the CAIs studied here all have ^{16}O-rich spinel, the first-formed (and slowest oxygen diffusivity) mineral and canonical ^{26}Al and ^{10}Be. So, these CAIs were initially formed in a reservoir with a uniform distribution of oxygen isotopes, ^{26}Al, and ^{10}Be. The later forming minerals, with faster oxygen diffusivities,

likely recorded other oxygen isotope signatures due to later processing. If the CAIs were equilibrated, melted, or aqueously altered to any degree, they would likely record the oxygen isotope composition of that environment. This processing did not likely occur on the CV parent body, as evidenced by adjacent CAIs. CAI processing more likely occurred in the nebula, where ^{16}O-rich and ^{16}O-poor materials were being mixed. The timescales of the mixing are unclear because it is difficult to compare diffusion parameters of O and Mg in CAI minerals (Yurimoto et al., 1989; Morioka et al., 1997; Sugiura et al., 2001; Chakraborty & Theimens, 2018).

Beryllium-10 correlated to oxygen isotope variations can be used to demonstrate that the later processing may not have occurred above the midplane. In addition to production in the molecular cloud (Chapter 4), ^{10}Be can also be produced in the solar nebula when solar energetic particles (SEPs) interact with the disk. Energetic protons are typically absorbed after 10^3 kg/m^2 (Umebayashi & Nakano, 1980) by the gas in the nebula. Due to the temperatures under which CAIs can form, they likely formed at the disk midplane from 0.1 – 1 AU and would be shielded from SEP irradiation by the overlying dense disk gas. It is possible, though, that CAIs can be transported above the disk plane to a region where they can be irradiated by SEPs, or where they can accrete irradiated gas/solids. An idea proposed (Aléon, 2016) based on oxygen isotope variations in a type B1 CAI is that CAIs crystallize in the ^{16}O-rich midplane, then are transported vertically by turbulence to a ^{16}O-poor reservoir (perhaps because it is located in an area exposed to protosolar and interstellar irradiation) where they undergo a partial melting event, likely short on the order of a few hours to 70 days (Connolly et al., 2006; Shahar &

Young, 2007) and are cooled back in the ^{16}O-rich disk plane. The CAI may go through this process multiple times and exist above the disk for an accumulated time of thousands of years. During their hypothesized short excursion to the outer disk, the CAI would not have been irradiated much due to the timescale (although multiple excursions would increase the exposure); at least ~1,000 years of irradiation with GeV particles at 1 AU would be necessary to raise the ^{10}Be level noticeably (Gounelle et al., 2001). The gas in this region, though, would likely contain variable abundances of ^{10}Be, although the abundance depends on exactly when and where the melting event took place, as well as how much this material mixed into the inner disk (the mixing timescale is likely on the order of years; (Jacquet, 2019)). If the CAI was melted above the disk, it would likely have incorporated some ^{10}Be-rich gas. However, all the CAIs measured in this study have the uniform ^{10}Be/^{9}Be value suggesting that they all inherited the same abundance of ^{10}Be (Figure 5.4; Chapter 4), which was not affected by later processing. More data and modeling is necessary to confirm this speculative scenario, but we suggest that if the CAI existed above the midplane of the disk, ^{10}Be would likely be affected. So, we do not favor the scenario of CAI transport above the disk midplane as a way to explain oxygen isotope distributions.

5.6. Conclusions

Correlating oxygen isotopes to ^{26}Al and ^{10}Be in a variety of types of CV3 CAIs allows us to make inferences about the origin of oxygen isotope distributions in CAIs. The initial reservoir in which CAIs formed was uniform with respect to oxygen isotopes (i.e., of CAI spinel), ^{10}Be, and ^{26}Al. Oxygen isotope variations in melilite, pyroxene, and anorthite likely occurred later and resulted from the CAIs being re-processed in different oxygen isotope reservoirs in the solar nebula.

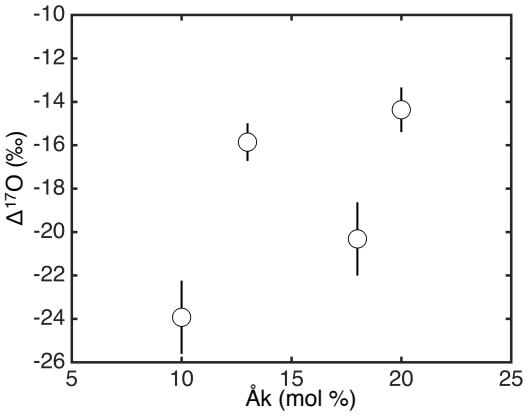


Figure 5.3 Δ^{17}O correlated to Åk content in fine-grained CAI *Cholla*.

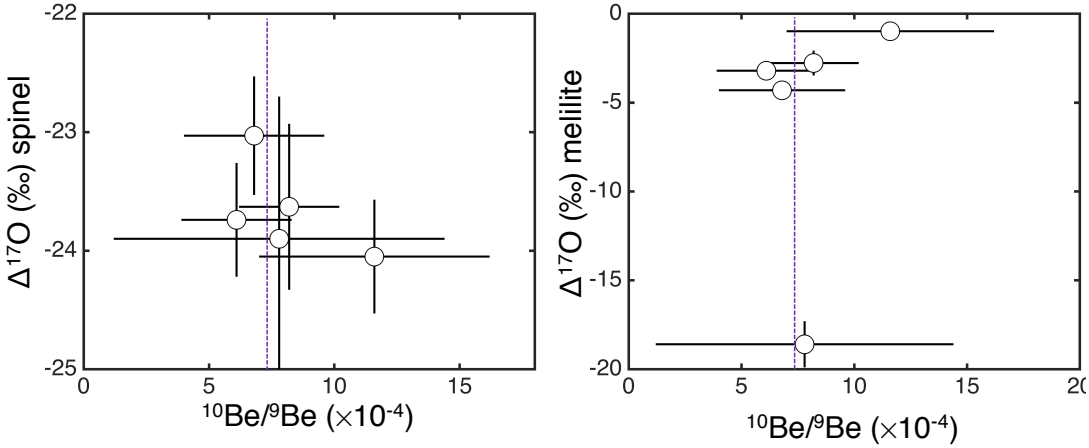


Figure 5.4. $\Delta^{17}O$ versus $^{10}Be/^{9}Be$ for spinel (left) and melilite (right). The purple vertical line indicates the uniform value of $^{10}Be/^{9}Be = 7 \times 10^{-4}$ (Chapter 3). If ^{10}Be is used as a chronometer, the time interval between the lowest $^{10}Be/^{9}Be$ and the uniform value is about 280,000 years.

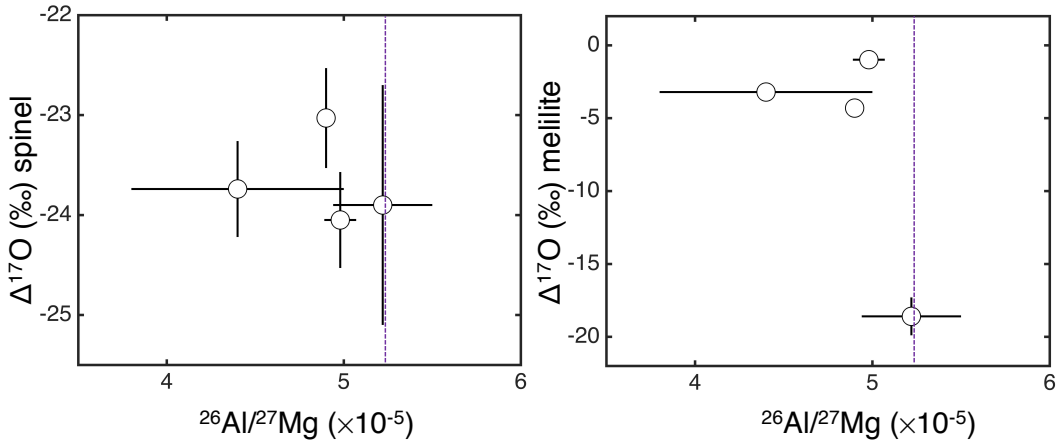


Figure 5.5. $\Delta^{17}O$ versus $^{26}Al/^{27}Mg$ for spinel (left) and melilite (right). The purple vertical line indicates the uniform value of $^{26}Al/^{27}Mg = 5.23 \times 10^{-4}$. If ^{26}Al is used as a chronometer, the time interval between the lowest $^{26}Al/^{27}Mg$ and the uniform value is about 150,000 years.

Table 5.1

Summary of oxygen isotope measurements and previous studies ^{26}Al and ^{10}Be

CAI	Phase	$\Delta^{17}O$ avg	$\Delta^{17}O$ 2SE	$\Delta^{17}O$ min	$\Delta^{17}O$ max	$^{26}Al/^{27}Al$ ($\times10^{-5}$)	$^{10}Be/^{9}Be$ ($\times10^{-4}$)
B4	spinel	-23.03	0.51	-23.45	-22.74	4.90±0.05[a]	6.7±2.2[c]
	mel	-4.31	0.51	-6.50	-3.06		
	px	-22.81	0.51	-23.28	-22.52		

	an	-2.32	0.51	-2.60	-2.08		
TS23	spinel	-23.74	0.48	-23.74	-23.74	4.40±0.60[b]	6.1±2.2[c]
	mel	-3.21	0.48	-3.21	-3.21		
	px	-23.63	0.48	-23.63	-23.63		
	an	-2.63	0.48	-2.63	-2.63		
Agave	spinel	-24.05	0.48	-24.37	-23.76	5.01±0.02[c]	11.6±4.6[c]
	mel	-0.99	0.48	-1.18	-0.68		
	px	-23.48	0.48	-23.82	-22.92		
	an	-9.60	0.48	-19.59	-3.57		
Saguaro	spinel	-23.63	0.70	-23.70	-23.58	N/A	8.1±1.5[c]
	mel	-2.78	0.70	-3.24	-2.29		
	px	-23.56	0.70	-23.69	-23.37		
	an	-14.25	0.70	-19.46	-8.11		
Cholla	spinel	-23.91	1.15	-25.10	-22.75	5.22±.27[c]	7.8±6.6[c]
	mel	-16.28	1.23	-23.93	-6.92		
	px	-22.29	1.06	-23.37	-19.12		

Note: * $\Delta^{17}O$ in per mil ‰

[a](Wadhwa et al., 2014)

[b](Hutcheon, 1982)

[c]Chapter 3

CHAPTER 6

SUMMARY AND FUTURE DIRECTIONS

6.1 Summary

The motivation of this dissertation was to determine the origin of the short-lived radionuclide (SLR) ^{10}Be in the Solar System. In answering this, we are able to better understand the astrophysical environment in which the Solar System formed. Calcium- and aluminum-rich inclusions (CAIs) are the first solids that formed in the Solar System in the hot (>1300 K) plane of the disk (MacPherson, 2013) so were able to record the existence of SLRs. The first study to infer the prior existence of ^{10}Be was nearly 20 years ago (McKeegan et al., 2000) and was accomplished by measuring an overabundance of ^{10}B correlated to ^{9}Be in a CAI; this allowed the determination of resolved initial ^{10}Be/^{9}Be ratio. Since then, over 30 CAIs have been measured, before the results published in this thesis (McKeegan et al., 2000; Sugiura et al., 2001; Marhas et al., 2002; MacPherson et al., 2003; Gounelle et al., 2006, 2013; Liu et al., 2010; Wielandt et al., 2012; Srinivasan & Chaussidon, 2013; Sossi et al., 2017; Mishra & Marhas, 2019).

Beryllium-10 is a unique short-lived radionuclide (SLR) because it can only be generated by irradiation reactions where a high-energy particle (GeV energies characteristic of solar energetic particles (SEPs) or Galactic cosmic rays (GCRs)) solar energetic particles or galactic cosmic rays (GCR)) spalls nuclei in gas and/or dust. The most common reaction is ^{16}O(p,x)^{10}Be. Most other SLRs, such as ^{26}Al (decays to ^{26}Mg with $t_{1/2}$ = 0.7 Ma), can be made by stellar nucleosynthesis in addition to irradiation. The

irradiation that takes place to produce ^{10}Be can occur in a number of astrophysical environments. There are three possible astrophysical settings in which the enhanced abundance of ^{10}Be in the early Solar System may have originated. One possible setting is the protosolar molecular cloud where ^{10}Be may have been produced by GCR irradiation (Gounelle et al., 2001; Desch et al., 2004; Tatischeff et al., 2014). A second setting is within the solar nebula, where irradiation of gas and/or refractory solids during an early active phase of the Sun may have produced ^{10}Be (McKeegan et al., 2000; Gounelle et al., 2001; Bricker & Caffee, 2010; Jacquet, 2019). A final setting is in a low-mass core-collapse supernova by neutrino reactions (Banerjee et al., 2016). These scenarios predict distinct spatial and temporal trends; determining how ^{10}Be is distributed among CAIs indicates where ^{10}Be originated. Inheritance of ^{10}Be (GCR irradiation of the molecular cloud and neutrino reactions in a supernova) would result in a uniform spatial distribution that would decrease in time as ^{10}Be decays. On the other hand, production of ^{10}Be from spallation of primarily gas in the solar nebula would result in large spatial and temporal variations of ^{10}Be (Jacquet, 2019). In order to distinguish between the astrophysical scenarios, the distribution of ^{10}Be in the Solar System must be understood.

It is important to measure many different types of CAIs from a variety of carbonaceous chondrites to determine how ^{10}Be was distributed. Most CAIs measured are from CV3 chondrites, which are known to have experienced varying degrees of aqueous alteration and thermal metamorphism on the CV parent body (Krot et al., 1998). Most CAIs yield a uniform ^{10}Be/^{9}Be $\sim 7 \times 10^{-4}$ (McKeegan et al., 2000; Sugiura et al., 2001; Marhas et al., 2002; MacPherson et al., 2003; Chaussidon, 2006; Liu et al., 2009, 2010;

Wielandt et al., 2012; Srinivasan & Chaussidon, 2013; Sossi et al., 2017; Mishra & Marhas, 2019), but there are clearly some CAIs that do not match this value (Gounelle et al., 2013; Sossi et al., 2017). This latter observation of a heterogeneous distribution of ^{10}Be, favoring a solar nebula irradiation origin. But before rejecting the inheritance origin, more evidence is needed. Most of the CAIs measured for ^{10}Be–^{10}B systematics were found in CV (Vigarano-type) carbonaceous chondrites because they are large (>500 μm) and generally coarse-grained (>20 μm). However, some CV3 chondrites, especially in the oxidized subgroup, are known to have undergone thermal metamorphism and aqueous alteration (Krot et al., 1998). These secondary processes could potentially alter the original ^{10}Be/^{9}Be CAI signature, so it is necessary to measure CAIs from more pristine meteorites.

Our basic approach to answering the question about the origin of ^{10}Be was to measure as many possible pristine CAIs from CV3 and non-CV3 chondrites for ^{10}Be–^{10}B and ^{26}Al–^{26}Mg isotope systematics. To accomplish this goal, we had to overcome a number of difficulties. The first issue we encountered was SIMS standardization. Because different elements ionize at different rates when the sample is sputtered with a primary ion SIMS beam, it is necessary to analyze standards along with the CAIs to correct for the Be/B ratio. It is important for the standard to be of similar composition to the unknown (i.e., matrix-matched) or else the correction factor may be incorrect. To this end, we synthesized melilite (solid solution between gehlinite, $Ca_2Al_2SiO_7$, and åkermanite, $Ca_2MgSi_2O_7$) composition glasses doped with Be and B. As detailed in

chapter 2, we determined that matrix matched standards are not necessary for accurate $^{10}Be/^{9}Be$ ratio results.

After analyzing CV3 CAIs with the ims-6f at ASU, we located CO3, CR2, and CH/CB CAIs to analyze. These CAIs, though, are significantly smaller and more fine-grained when compared to CV3 CAIs; this requires a SIMS primary ion analysis spot size of less than 20 μm. Because 20 μm is the smallest primary beam able to be calibrated for $^{10}Be–^{10}B$ measurement of the ims-6f, we needed to employ a larger radius SIMS. We were able to collaborate with researchers at UCLA to utilize their IMS-1290 equipped with the *Hyperion-II* primary ion source. This RF source allowed us to analyze a sample area ~5–10 um in size while using the same current as the ims-6f duoplasmatron source. This extra capability allowed us to expand our sample set from 12 CV3 CAIs to a total of 32 CAIs.

This large $^{10}Be–^{10}B$ dataset (correlated to $^{26}Al–^{26}Mg$ and oxygen data) allowed us to observe that the majority of CAIs have a single $^{10}Be/^{9}Be$ value, while only a few CAIs had values different than this. Because determining the distribution of ^{10}Be is vital to learning the origin of ^{10}Be, it was imperative to statistically analyze the data in a rigorous way and determine if the CAIs were part of a single population or not. It took some trial and error to settle on a proper statistical method for our case, but once we decided on using the p-value (i.e., reduced chi squared), we were able to test the null hypothesis that CAIs have a single ^{10}Be value.

The first step of this statistical analysis was to produce a self-consistent data set which included all previous $^{10}Be–^{10}B$ data. The main hurdle here was that not all studies

processed or reported data in the same way, making it difficult to compare across studies. So, we gathered literature data, in the rawest form possible, and re-processed it using the same methods. An important output from this re-processing was the MSWD (mean square weighted deviation), or reduced chi squared value. This parameter allowed us to statistically test the robust-ness and accuracy of the final $^{10}Be/^{9}Be$ value for a CAI. We found that 7 of the more than 30 CAI literature regressions were not robust, so we did not further consider them in interpretations. All of the 32 regressions produced in this work were robust.

Statistical analysis reveals that the majority of normal (n=42; i.e., no large isotopic anomalies or fractionations) CAIs with robust regressions have $^{10}Be/^{9}Be = (7.0 \pm 0.2) \times 10^{-4}$. The group of F(UN) CAIs (n=5) have resolvably lower $^{10}Be/^{9}Be$ while CH/CB CAIs and CV3 CAI *Lisa* have higher $^{10}Be/^{9}Be$. As detailed in chapter 4, we suggest that F(UN) CAIs initially had a $^{10}Be/^{9}Be \sim 7 \times 10^{-4}$, but the evaporation event which produced their observed fractionations (Mendybaev et al., 2013) caused B loss or Be–B system resetting. We suggest that CH/CB CAIs and *Lisa* also initially had a $^{10}Be/^{9}Be \sim 7 \times 10^{-4}$, but were later irradiated; this artificially increased the $^{10}Be/^{9}Be$ due to added spallogenic boron. The statistical analysis of a variety of CAIs reveal that $^{10}Be/^{9}Be$ was distributed uniformly in the CAI forming region.

A uniform distribution implies that well-mixed ^{10}Be was inherited by the Solar System from another astrophysical source. We do not conclude that ^{10}Be was produced in the solar nebula, by solar energetic particle irradiation, because a recent model (Jacquet, 2019) found that the $^{10}Be/^{9}Be$ value in this scenario would be highly variable both

spatially and temporally. We do not conclude that ^{10}Be was inherited from a low mass supernova because ^{26}Al and ^{10}Be are not correlated, which implies that ^{10}Be cannot also be generated in a supernova. We infer that the source of ^{10}Be is galactic cosmic ray irradiation in the protosolar molecular cloud. However, the level of ^{10}Be/^{9}Be we measure is significantly higher than the predicted background level of ^{10}Be in the molecular cloud region 4.56 Gyr ago ($<2 \times 10^{-4}$; (Tatischeff et al., 2014)).

To solve this conundrum, we modeled galactic cosmic ray (GCR) flux in the Milky Way galaxy. Because GCRs are generated by core-collapse supernovae from short-lived, massive stars, the GCR flux is proportional to the local, instantaneous SFR. We find that newly formed stars, on average, are surrounded by a SFR that is 3.7 times higher than the spatially averaged SFR in the galaxy at the same epoch; this is simply because most stars form together in stellar nurseries within giant molecular cloud complexes within spiral arms (Foyle et al., 2010). While the overall SFR in the galaxy may vary with time, and was likely 1.5 to 2 times higher 4.56 Gyr ago, we assume that the spatial inhomogeneity of the SFR was the same 4.56 Gyr as today. This implies that a typical star, forming in either epoch, experiences a GCR flux at its birth that is a factor of ~3.7 times higher than the average GCR flux in the galaxy. Multiplying all the factors determined above, we calculate that the measured ^{10}Be/^{9}Be = 7×10^{-4} value is highly probable for a star forming region 4.56 Gyr ago. The median ^{10}Be/^{9}Be value recorded by stars would be $(1.3 \times 10^{-4}) \times (3.7) = 4.8 \times 10^{-4}$, but 20% of stars should record $(1.3 \times 10^{-4}) \times (5.5) = 7.2 \times 10^{-4}$. So, ^{10}Be is likely distinct in star forming regions/protoplanetary disks because it is highly dependent on the specific star formation

rate of that area. The ^{10}Be abundances in meteorites probe the very local molecular cloud environment ~1 kpc and within 15 Ma (Yanasak et al., 2001) of Solar System formation and suggests that our Sun formed in a region with many other stars, with higher-than-average SFR.

The pursual of the origin of ^{10}Be in our Solar System revealed that, through the statistical analysis of many ^{10}Be and ^{26}Al measurements, SLRs in meteorites can be used as probes of the galactic environment in which our Solar System formed.

6.2 Future Directions and Implications

Through my isotopic measurements, statistical analysis, and astrophysical theorizing, I have identified future work that can be conducted to build off the work of previous research as well as this dissertation. The main improvements I suggest are: 1. expanding the sample set; 2. improving analytical uncertainties; 3. Experiments; and 4. modeling.

6.2.1 Expanding the Sample Set

In order to more confidently ascribe our data to the protosolar molecular cloud scenario for ^{10}Be production, it is desirable to measure more samples. Partially because more samples increase statistical reliability but also because specific types of samples are under-represented or could be important in constraining the origin of ^{10}Be.

Firstly, it would be beneficial to study more CAIs from non-CV3s, especially CH/CB CAIs and CAIs with fractionations and/or isotopic anomalies (FUN). Non-CV3

CAIs such as those from CR and CO chondrites, are important to measure because they are more likely to be pristine (underwent less thermal metamorphism and aqueous alteration than CV3 chondrites). We were able to measure 5 CR2 CAIs and 8 CO3 CAIs in this dissertation, but more data is needed to ensure that CAIs from all chondrite types can be considered a single ^{10}Be population. Although many CH/CB CAIs have been measured for ^{10}Be–^{10}B isotope systematics (25 from literature; Gounelle et al., 2013) and 5 in chapter 4), only three multi-CAI ^{10}Be/^{9}Be regressions could be made, due to the small size of the CAIs and a narrow spread of ^{9}Be/^{11}B in the data. Of these regressions (Gounelle et al., 2013), one has an MSWD>>1. The two statistically robust CH/CB CAI regressions (both multi-CAI isochrons) record ^{10}Be/^{9}Be slightly higher than the canonical value of ~7×10^{-4}, but due to the large errors it is difficult to determine if they are resolvably different from normal CAIs. If CH/CB CAIs are a distinct ^{10}Be population, their unique formation history is likely involved in the explanation.

Only 3 FUN, 3 PLAC, and 1 UN CAI ^{10}Be–^{10}B isotope regressions have been produced (Marhas et al., 2002; MacPherson et al., 2003; Liu et al., 2010; Wielandt et al., 2012). All but the UN CAI has low ^{10}Be/^{9}Be ~ 4.5×10^{-4}, but these F(UN) samples do not appear to be part of a single population. Measuring more of these samples would improve statistical reliability and enable us to better evaluate why we measure a lower ^{10}Be than normal CAIs. Analyzing FUN CAIs from non-CV3 chondrites would be useful as they are not as significantly overprinted by aqueous alteration or thermal metamorphism.

Some objects which have not been analyzed for ^{10}Be–^{10}B isotope systematics, and could be important, include: Al-rich chondrules, CAI rims, and CAI alteration minerals. Al-rich chondrules have a whole rock composition which is in between most chondrules and CAIs (Scott & Krot, 2013). Perhaps because they are aluminum-rich, they formed earlier, or in a different environment than most chondrules. Also being aluminum-rich, they may have a higher chance of hosting ^{10}Be (Srinivasan & Chaussidon, 2013). Some chondrules have been measured for Be and B isotopes, and variations in the $^{10}B/^{11}B$ ratio have been found (Chaussidon & Robert, 1995). Discovering the former presence of ^{10}Be in chondrules would give us another constraint on how ^{10}Be formed; since ^{10}Be was inherited, we would expect later forming chondrules to have less $^{10}Be/^{9}Be$ than CAIs, and this difference would indicate the time interval between the formation of these two solids.

CAI rims and CAI alteration minerals, if they have high $^{9}Be/^{11}B$ ratios, could indicate if later irradiation occurred and produced ^{10}Be. Because rims and alteration minerals are suggested to form after the main host CAI (MacPherson, 2013), they should have less ^{10}Be than normal CAIs, according to the model presented in this dissertation. If they have significant ^{10}Be, this could indicate that solar energetic particle irradiation in the disk is a more dominant process than we suggested.

6.2.2 Improving Analytical Uncertainties

To measure a wide spread in $^{9}Be/^{11}B$, necessary for producing a robust isochron and resolvable $^{10}Be/^{9}Be$ ratio, it is beneficial to locate areas in the CAI sample which have low B and high Be concentrations. But because the B concentration in CAIs is very

low, it is difficult to measure with statistical significance. In the analyses with the highest $^{9}Be/^{11}B$, [B] can be as low as 1 ppb, which equates to less than 1 count per second detected by the SIMS electron multipler. At this level, counting statistics are poor, so errors are large, up to 10% (1 sigma). In constructing an isochron, then, it is important to count B secondary ions at an analysis spot for as long as possible, to drive down counting statistics, and/or to analyze many sample areas so York regression slope errors are minimized. However, it is often difficult to count for an extended period of time because [B] and [Be] change due to mineral heterogeneity or sputtering into another phase, and it can be difficult to analyze many CAI regions when the CAI is small.

Through the research presented here, I have learned a few ways to minimize errors. In using the ims-1290, multicollection is possible and is beneficial because one can count multiple masses at the same time which lessens cycle time length and increases counting efficiency, allowing for more stable cycles. Multicollection allowed our precision to increase (by a few percent). We also found that analyzing with a raster instead of a spot increased precision slightly and allowed for a cleaner analysis; starting with a 10 μm × 10 μm raster presputter and then switching to a 5 μm × 5 μm analysis raster. Using an $^{16}O_2^-$ primary ion beam, instead of the usual $^{16}O^-$ beam, makes it possible to analyze with a lower current (~1 nA versus the usual ~10 – 20 nA). To ensure stable cycles, it is preferred to analyze samples with as much clean homogeneous melilite as possible and without intrusive spinel. Another way to improve precision would be to have standards with better-known [B] and [Be]. Some ^{10}Be–^{10}B standards range to 20% error in concentration (Jochum et al., 2011), and because these errors are quadratically added

into the unknown errors, the $^{10}Be/^{9}Be$ ratio errors are also increased. So, to make melilite composition glasses, with [Be] and [B] concentrations more comparable to the unknown and to measure these compositions more precisely, would be beneficial in minimizing $^{10}Be–^{10}B$ isotope systematic errors.

6.2.3 Experimental Studies to Test Be and B Behavior

Due to their trace abundances, the behavior of Be and B have not been well studied. Conducting experiments would be useful in constraining their behavior during evaporation, thermal metamorphism, or aqueous alteration. In chapter 4, we suggest that FUN CAIs have lower $^{10}Be/^{9}Be$ when compared to normal CAIs due to the evaporation event that produced the fractionations. We use evidence from an UN CAI to determine this, but we do not know exactly what would happen to B or Be during such an event. Due to boron's highly volatile nature (Lauretta & Lodders, 1997; Lodders, 2003), we would expect that some would escape during the evaporation event, while little beryllium would escape (it is also likely strongly bonded to oxygen as BeO). An experiment could show how much B and Be would be lost during vacuum evaporation, if any (as accomplished for major elements; Mendybaev, 2016). Perhaps it would only be lost from the very surface edge of a sample (Bullock et al., 2013).

Something else to consider is that during an evaporation or melting event, the $^{10}Be–^{10}B$ system could be reset. It is suggested that anorthite is most easily reset for $^{26}Al–^{26}Mg$ isotope systematics because when it is melted, the diffusion rate for Mg is fast and will set the system back to time 0 (Dauphas & Chaussidon, 2011). When $^{10}Be–^{10}B$ and

^{26}Al–^{26}Mg systems are correlated, it seems that Mg is reset in anorthite more easily than B in melilite (Sugiura et al., 2001). Diffusion experiments for Be and B in melilite would be extremely useful in determining how B behaves during melting events, either in the nebula or on the parent body.

With regards to aqueous alteration, it may be impossible to fully determine the behavior of B and Be, because we do not know the ion composition of the nebular or parent body fluid. But alteration experiments or modeling could confirm if ^{11}B prefers the tetrahedral coordination of water (Hervig et al., 2002), if so, we would expect B isotopes to be fractionated during this process.

6.2.4 Modeling

There exist models about the production of ^{10}Be for each astrophysical scenario explained in the dissertation (Gounelle et al., 2001; Desch et al., 2004; Bricker & Caffee, 2010; Tatischeff et al., 2014; Jacquet, 2019). Because they do not always predict the measured ^{10}Be/^{9}Be value and tend to over-emphasize particular data, more modeling is needed to prove or disprove our molecular cloud inheritance interpretation of the data. In addition, modeling is needed to determine the astrophysical scenario which produced the low FUN CAI ^{10}Be/^{9}Be ratio, as well as the scenario which produced CAIs with high ^{10}Be/^{9}Be ratios, potentially because of extra irradiation (this irradiation could occur in a number of distinct locations and times). In this dissertation, we only have enough information to speculate about the FUN CAIs and irradiated CAIs; a comprehensive model would test our predictions more robustly.

REFERENCES

Aléon, J. (2016). Oxygen isotopes in the early protoplanetary disk inferred from pyroxene in a classical type B CAI. *Earth and Planetary Science Letters*, *440*, 62–70.

Aléon, J., Krot, A. N., & McKeegan, K. D. (2002). Calcium-aluminum-rich inclusions and amoeboid olivine aggregates from the CR carbonaceous chondrites. *Meteoritics and Planetary Science*, *37*(12), 1729–1755.

Aléon, J., Marin-Carbonne, J., McKeegan, K. D., & El Goresy, A. (2018). O, Mg, and Si isotope distributions in the complex ultrarefractory CAI Efremovka 101.1: Assimilation of ultrarefractory, FUN, and regular CAI precursors. *Geochimica et Cosmochimica Acta*.

Amelin, Y., Krot, A. N., Hutcheon, I. D., & Ulyanov, A. A. (2002). Lead Isotopic Ages of Chondrules and Calcium-Aluminum-Rich Inclusions. *Science*, *297*, 1678–1683.

Banerjee, P., Heger, A., Haxton, W. C., & Qian, Y. (2016). Evidence from stable isotopes and 10Be for solar system formation triggered by a low-mass supernova. *Nature Communications*, *7*, 1–6.

Bouvier, A., Brennecka, G. A., & Wadhwa, M. (2011). Absolute chronology of the first solids in the Solar System (abstract#9054). *LPSC: Formation of the First Solids in the Solar System*.

Brearley, A. J., & Jones, R. H. (1998). Chondritic meteorites. *Reviews in Mineralogy and Geochemistry*, *36*(1), 3.1-3398.

Bricker, G. E., & Caffee, M. W. (2010). Solar wind implantation model for 10Be in calcium–aluminum inclusions. *The Astrophysical Journal*, *725*(1), 443–449.

Bullock, E. S., Bouvier, A., Wadhwa, M., MacPherson, G. J., & Kita, N. T. (2014). Mineralogy and Petrology of an unusual large Type A CAI from NWA 6991 (abstract #1919). *45th Lunar and Planetary Science Conference*.

Bullock, E. S., Knight, K. B., Richter, F. M., Kita, N. T., Ushikubo, T., MacPherson, G. J., … Mendybaev, R. A. (2013). Mg and Si isotopic fractionation patterns in types B1 and B2 CAIs: Implications for formation under different nebular conditions. *Meteoritics and Planetary Science*, *48*(8), 1440–1458.

Bullock, E. S., Macpherson, G. J., Nagashima, K., Krot, A. N., Petaev, M. I., Jacobsen, S. B., & Ulyanov, A. A. (2012). Forsterite-bearing type B refractory inclusions from CV3 chondrites: From aggregates to volatilized melt droplets. *Meteoritics and Planetary Science*, *47*(12), 2128–2147.

Chakraborty, S., & Theimens, M. H. (2018). Mineral formation and growth with anomalous oxygen isotopic composition on siliceous dust surfaces (abstract #2866). *49th Lunar and Planetary Science Conference*.

Chaussidon, M. (2006). Li and B isotopic variations in an Allende CAI : Evidence for the in situ decay of short-lived 10 Be and for the possible presence of the short-lived nuclide 7 Be in the early solar system. *Geochemica Cosmochemica Acta*, *70*, 224–245.

Chaussidon, M., & Robert, F. (1995). Nucleosynthesis of 11B-rich boron in pre-solar cloud recorded in meteoritic chondrules. *Nature*, *374*, 337–339.

Clayton, R. N. (2003). Oxygen Isotopes in Meteorites. *Treatise on Geochemistry*, *1–9*, 1–14.

Clayton, R. N., & Mayeda, T. K. (1996). Oxygen isotope studies of achondrites. *Geochim. Cosmochim. Acta*, *60*(11), 1999–2017.

Coath, C. D., Steele, R. C. J., & Lunnon, W. F. (2013). Statistical bias in isotope ratios. *Journal of Analytical Atomic Spectrometry*, *28*(1), 52–58.

Connelly, J. N., Bizzarro, M., Krot, A. N., Nordlund, A., Wielandt, D., & Ivanova, M. A. (2012). The Absolute Chronology and Thermal Processing of Solids in the Solar Protoplanetary Disk. *Science (New York, N.Y.)*, *338*(6107), 651–655.

Connolly, H. C. J., Desch, S. J., Ash Richard, D., & Jones, R. H. (2006). Transient Heating Events in the Protoplanetary Nebula. *Meteorites and the Early Solar System II*, 383–397.

Dauphas, N., & Chaussidon, M. (2011). A Perspective from Extinct Radionuclides on a Young Stellar Object: The Sun and Its Accretion Disk. *Annual Review of Earth and Planetary Sciences*, *39*(1), 351–386.

Davidson, J., Schrader, D. L., Alexander, C. M. O. D., Lauretta, D. S., Busemann, H., Franchi, I. A., … Verchovsky, A. (2014). Petrography, stable isotope compositions, microRaman spectroscopy, and presolar components of Roberts Massif 04133: A reduced CV3 carbonaceous chondrite. *Meteoritics and Planetary Science*, *49*(12), 2133–2151.

Davidson, J., Schrader, D. L., Alexander, C. M. O., Nittler, L. R., & Bowden, R. (2019). Re-examining thermal metamorphism of the Renazzo-like (CR) carbonaceous chondrites: Insights from pristine Miller Range 090657 and shock-heated Graves Nunataks 06100. *Geochimica et Cosmochimica Acta*, *267*, 240–256.

Davis, A. M., & McKeegan, K. D. (2014). Treatise on Geochemistry: Short-Lived Radionuclides and Early Solar System Chronology. In A. M. Davis (Ed.), *Treatise on Geochemistry* (Vol. 1). Elsevier.

Davis, A. M., Richter, F. M., Mendybaev, R. A., Janney, P. E., Wadhwa, M., & McKeegan, K. D. (2015). Isotopic mass fractionation laws for magnesium and their effects on 26Al–26Mg systematics in solar system materials. *Geochimica et Cosmochimica Acta*, *158*, 245–261.

De Hoog, J. C. M., Monteleone, B. D., Savov, I. P., Marschall, H. R., & Zack, T. (2017). Matrix effects in B isotope analysis of silicate minerals by SIMS. *Goldschmidt Conference*.

Defouilloy, C., Nakashima, D., Joswiak, D. J., Brownlee, D. E., Tenner, T. J., & Kita, N. T. (2017). Origin of crystalline silicates from Comet 81P/Wild 2: Combined study on their oxygen isotopes and mineral chemistry. *Earth and Planetary Science Letters*, *465*, 145–154.

Desch, S. J., Connolly, Jr., H. C., & Srinivasan, G. (2004). An interstellar origin for the beryllium 10 in calcium-rich, aluminum-rich inclusions. *The Astrophysical Journal*, *602*(1), 528–542.

Desch, S. J., Kalyaan, A., & Alexander, C. M. O. (2018). The Effect of Jupiter's Formation on the Distribution of Refractory Elements and Inclusions in Meteorites. *The Astrophysical Journal Supplement Series*, *238*, 31.

Dunham, E. T., Wadhwa, M., & Desch, S. J. (2017). Beryllium-boron systematics of two distinctive CAIs from CV3 chondrites: the relatively pristine CAI B4 from NWA 6991 and the FUN CAI CMS-1 from Allende (abstract # 1507). *LPSC*.

Dunham, E. T., Wadhwa, M., Desch, S. J., & Hervig, R. L. (2020). Best practices for determination of initial 10Be/9Be in early Solar System materials by SIMS. *Geostandards and Geoanalytical Research*, *submitted*.

Dwarkadas, V. V, Dauphas, N., Meyer, B., Boyajian, P., & Bojazi, M. (2017). Triggered Star Formation inside the Shell of a Wolf – Rayet Bubble as the Origin of the Solar System. *The Astrophysical Journal*, *851*(2), 147.

Everett, J. E., & Zweibel, E. G. (2011). The interaction of cosmic rays with diffuse clouds. *Astrophysical Journal*, *739*(2).

Fagan, T. J., Krot, A. N., Keil, K., & Yurimoto, H. (2004). Oxygen isotopic alteration in Ca-Al-rich inclusions from Efremovka: Nebular or parent body setting? *Meteoritics & Planetary Science*, *39*(8), 1257–1272.

Foyle, K., Rix, H. W., Walter, F., & Leroy, A. K. (2010). Arm and interarm star formation in spiral galaxies. *Astrophysical Journal*, *725*(1), 534–541.

Friedrich, J. M., Weisberg, M. K., Ebel, D. S., Biltz, A. E., Corbett, B. M., Iotzov, I. V., … Wolman, M. D. (2015). Chondrule size and related physical properties: A compilation and evaluation of current data across all meteorite groups. *Chemie Der Erde - Geochemistry*, *75*(4), 419–443.

Frisch, P. C., Bzowski, M., Grün, E., Izmodenov, V., Krüger, H., Linsky, J. L., … Wood, B. E. (2009). The galactic environment of the sun: Interstellar material inside and outside of the heliosphere. In P. C. Frisch, M. Bzowski, E. Grun, V. Izmodenov, & H. Kruger (Eds.), *Space Science Reviews* (Vol. 146, pp. 235–273).

Fujimoto, Y., Chevance, M., Haydon, D. T., Krumholz, M. R., & Kruijssen, J. M. D. (2019). A fundamental test for stellar feedback recipes in galaxy simulations. *Monthly Notices of the Royal Astronomical Society*, *487*(2), 1717–1728.

Fukuda, K., Fuijya, W., Hiyagon, H., Makino, Y., Sugiura, N., Takahata, N., … Sano, Y. (2018). Beryllium-boron relative sensitivity factors for melilitic glasses measured with a NanoSIMS ion microprobe. *Geochemical Journal*, *52*, 1–8.

Fukuda, K., Hiyagon, H., Fujiya, W., Takahata, N., Kagoshima, T., & Sano, Y. (2019). Origin of the Short-lived Radionuclide 10 Be and Its Implications for the Astronomical Setting of CAI Formation in the Solar Protoplanetary Disk. *The Astrophysical Journal*, *886*(34), 11pp.

Gangjian, W., Jingxian, W., Ying, L., Ting, K., Zhongyuan, R., Jinlong, M., & Yigang, X. (2013). Measurement on high-precision boron isotope of silicate materials by a single column purification method and MC-ICP-MS. *Journal of Analytical Atomic Spectrometry*, *28*(4), 606–612.

Garvie, L. A. J., Knauth, P., & Morris, M. A. (2017). Sedimentary laminations in the Isheyevo (CH/CBb) carbonaceous chondrite formed by gentle impact-plume sweep-up. *Icarus*, *292*, 36–47.

Gnaser, H., & Hutcheon, I. D. (1987). Velocity-dependent isotope fraactionation in secondary ion emission. *Physical Review B*, *35*, 877–879.

Gounelle, M., Chaussidon, M., & Rollion-Bard, C. (2013). Variable and extreme irradiation conditions in the early solar system inferred from the initial abundance of 10Be in Isheyevo CAIs. *The Astrophysical Journal*, *763*(2), L33.

Gounelle, M., Shu, F. H., Shang, H., Glassgold, a. E., Rehm, K. E., & Lee, T. (2001). Extinct Radioactivities and Protosolar Cosmic Rays: Self-Shielding and Light Elements. *The Astrophysical Journal*, *548*(2), 1051–1070.

Gounelle, M., Shu, F. H., Shang, H., Glassgold, A. E., Rehm, K. E., & Lee, T. (2006). The Irradiation Origin of Beryllium Radioisotopes and Other Short-lived Radionuclides. *The Astrophysical Journal*, *640*(2), 1163–1170.

Gregory, T., Luu, T.-H., Coath, C. D., Russell, S. S., & Elliott, T. (2020). Primordial formation of major silicates in a protoplanetary disc with homogeneous 26 Al/ 27 Al. *Science Advances*, *6*(11), 1–8.

Harju, E. R., Rubin, A. E., Ahn, I., Choi, B. G., Ziegler, K., & Wasson, J. T. (2014). Progressive aqueous alteration of CR carbonaceous chondrites. *Geochimica et Cosmochimica Acta*, *139*, 267–292.

Heck, P. ., Gyngard, F., Ott, U., Meier, M., Vila, J. N., Amari, S., … Wieler, R. (2009). Interstellar residence times of presolar SiC dust grains from the murchison carbonaceous meteorite. *Astrophysical Journal*, *698*(2), 1155–1164.

Hertwig, A. T., Kimura, M., Ushikubo, T., Defouilloy, C., & Kita, N. T. (2019). The 26Al-26Mg systematics of FeO-rich chondrules from Acfer 094: Two chondrule generations distinct in age and oxygen isotope ratios. *Geochemica Cosmochemica Acta*, *253*, 111–126.

Hervig, R. L., Mazdab, F. K., Williams, P., Guan, Y., Huss, G. R., & Leshin, L. A. (2006). Useful ion yields for Cameca IMS 3f and 6f SIMS: Limits on quantitative analysis. *Chemical Geology*, *227*(1–2), 83–99.

Hervig, R. L., Moore, G. M., Williams, L. B., Peacock, S. M., Holloway, J. R., & Roggensack, K. (2002). Isotopic and elemental partitioning of boron between hydrous fluid and silicate melt. *American Mineralogist*, *87*(5–6), 769–774.

Howard, K. T., Alexander, C. M. O. D., Schrader, D. L., & Dyl, K. A. (2015). Classification of hydrous meteorites (CR, CM and C2 ungrouped) by phyllosilicate fraction: PSD-XRD modal mineralogy and planetesimal environments. *Geochimica et Cosmochimica Acta*, *149*, 206–222.

Hutcheon, I. D. (1982). Ion Probe Magnesium Isotopic Measurements of Allende Inclusions. *American Chemical Society, ACS Symposium Series*, *176*, 94–128.

Ihinger, P. D., Hervig, R. L., & McMillan, P. M. (1994). Analytical methods for volatiles in glasses. In M. Carroll & J. R. Holloway (Eds.), *Reviews in Mineralogy* (Vol. 30, pp. 67–121).

Ivanova, M. A. (2016). Ca–Al-rich inclusions in carbonaceous chondrites: the oldest solar system objects. *Geochemistry International*, *54*(5), 387–402.

Jacobsen, B., Yin, Q., Moynier, F., Amelin, Y., Krot, A. N., Nagashima, K., … Palme, H. (2008). 26Al–26Mg and 207Pb–206Pb systematics of Allende CAIs: Canonical solar initial 26Al/27Al ratio reinstated. *Earth and Planetary Science Letters*, *272*(1–2), 353–364.

Jacquet, E. (2019). On beryllium-10 production in gaseous protoplanetary disks and implications on the astrophysical setting of refractory inclusions. *Astronomy & Astrophysics*, *624*, A131.

Jilly-Rehak, C. E., Huss, G. R., Nagashima, K., & Schrader, D. L. (2018). Low-temperature aqueous alteration on the CR chondrite parent body: Implications from in situ oxygen-isotope analyses. *Geochimica et Cosmochimica Acta*, *222*, 230–252.

Jochum, K. P., Weis, U., Stoll, B., Kuzmin, D., Yang, Q., Raczek, I., … Enzweiler, J. (2011). Determination of reference values for NIST SRM 610-617 glasses following ISO guidelines. *Geostandards and Geoanalytical Research*, *35*, 397–429.

Jochum, K. P., Willbold, M., Raczek, I., Stoll, B., & Herwig, K. (2005). Chemical Characterisation of the USGS Reference Glasses GSA-1G, GSC-1G, GSD-1G, GSE-1G, BCR-2G, BHVO-2G and BIR-1G Using EPMA, ID-TIMS, ID-ICP-MS and LA-ICP-MS. *Geostandards and Geoanalytical Research*, *29*(3), 285–302.

Kallemeyn, G. W., Rubin, A. E., & Wasson, J. T. (1994). The compositional classification of chondrites: VII. The R chondrite group. *Geochimica et Cosmochimica Acta*, *58*(13), 2873–2888.

Kawasaki, N., Itoh, S., Sakamoto, N., & Yurimoto, H. (2017). Chronological study of oxygen isotope composition for the solar protoplanetary disk recorded in a fluffy Type A CAI from Vigarano. *Geochimica et Cosmochimica Acta*, *201*, 83–102.

Kawasaki, N., Simon, S. B., Grossman, L., Sakamoto, N., & Yurimoto, H. (2018). Crystal growth and disequilibrium distribution of oxygen isotopes in an igneous Ca-Al-rich inclusion from the Allende carbonaceous chondrite. *Geochimica et Cosmochimica Acta*, *221*, 318–341.

Kimura, M., Grossman, J. N., & Weisberg, M. K. (2008). Fe-Ni metal in primitive chondrites: Indicators of classification and metamorphic conditions for ordinary and CO chondrites. *Meteoritics and Planetary Science*, *43*(7), 1161–1177.

Kita, N. T., Nagahara, H., Tachibana, S., Tomomura, S., Spicuzza, M. J., Fournelle, J. H., & Valley, J. W. (2010). High precision SIMS oxygen three isotope study of chondrules in LL3 chondrites: Role of ambient gas during chondrule formation. *Geochimica et Cosmochimica Acta*, *74*(22), 6610–6635.

Kita, N. T., Ushikubo, T., Knight, K. B., Mendybaev, R. A., Davis, A. M., Richter, F. M., & Fournelle, J. H. (2012a). Internal 26Al–26Mg isotope systematics of a Type B CAI: Remelting of refractory precursor solids. *Geochimica et Cosmochimica Acta*, *86*, 37–51.

Kita, N. T., Ushikubo, T., Knight, K. B., Mendybaev, R. A., Davis, A. M., Richter, F. M., & Fournelle, J. H. (2012b). Internal 26Al–26Mg isotope systematics of a Type B CAI: Remelting of refractory precursor solids. *Geochimica et Cosmochimica Acta*, *86*, 37–51.

Kita, N. T., Yin, Q., MacPherson, G. J., Ushikubo, T., Jacobsen, B., Nagashima, K., … Jacobsen, S. B. (2013). Al-Mg isotope systematics of the first solids in the early solar system. *Meteoritics & Planetary Science*, *48*(8), 1383–1400.

Korschinek, G., Bergmaier, A., Faestermann, T., Gerstmann, U. C., Knie, K., Rugel, G., … Remmert, A. (2010). A new value for the half-life of 10Be by Heavy-Ion Elastic Recoil Detection and liquid scintillation counting. *Nuclear Instruments and Methods in Physics Research, Section B: Beam Interactions with Materials and Atoms*, *268*(2), 187–191.

Krot, A. N., Nagashima, K., Bizzarro, M., Huss, G. R., Davis, A. M., Meyer, B. S., & Ulyanov, A. A. (2008a). Multiple Generations of Refractory Inclusions in the Metal-Rich Carbonaceous Chondrites Acfer 182/214 and Isheyevo. *The Astrophysical Journal*, *672*(1), 713–721.

Krot, A. N., Nagashima, K., Bizzarro, M., Huss, G. R., Davis, A. M., Meyer, B. S., & Ulyanov, A. A. (2008b). Multiple Generations of Refractory Inclusions in the Metal-Rich Carbonaceous Chondrites Acfer 182/214 and Isheyevo. *The Astrophysical Journal*, *672*(1), 713–721.

Krot, A. N., Nagashima, K., Wasserburg, G. J., Huss, G. R., Papanastassiou, D., Davis, A. M., … Bizzarro, M. (2014). Calcium-aluminum-rich inclusions with fractionation and unknown nuclear effects (FUN CAIs): I . Mineralogy , petrology , and oxygen isotopic compositions. *Geochimica et Cosmochimica Acta*, *145*, 206–247.

Krot, A. N., Peaev, M., Scott, E., Choi, B.-G., Zolensky, M., & Keil, K. (1998). Progresive alteration in CV3 chondrites : more evidence for asteroidal alteration. *Meteoritics & Planetary Science*, *1085*(33), 1065–1085.

Kuffmeier, M., Mogensen, T. F., Haugbølle, T., Bizzarro, M., & Nordlund, Åke. (2016). Tracking the distribution of 26Al and 60Fe during the early phases of star and disk evolution. *The Astrophysical Journal*, *826*(1), 22.

Lauretta, D. S., & Lodders, K. (1997). The cosmochemical behavior of beryllium and boron. *Earth and Planetary Science Letters*, *146*(1–2), 315–327.

Leya, I., Lange, H. J., Neumann, S., Wieler, R., & Michel, R. (2000). The production of cosmogenic nuclides in stony meteoroids by galactic cosmic-ray particles. *Meteoritics & Planetary Science*, *35*(2), 259–286.

Liu, M.-C., McKeegan, K. D., Goswami, J. N., Marhas, K. K., Sahijpal, S., Ireland, T. R., & Davis, A. M. (2009). Isotopic records in CM hibonites: Implications for timescales of mixing of isotope reservoirs in the solar nebula. *Geochimica et Cosmochimica Acta*, *73*(17), 5051–5079.

Liu, M.-C., Mckeegan, K. D., Harrison, T. M., & Jarzebinski, G. (2018). International Journal of Mass Spectrometry The Hyperion-II radio-frequency oxygen ion source on the UCLA ims 1290 ion microprobe : Beam characterization and applications in geochemistry and cosmochemistry. *International Journal of Mass Spectrometry*, *424*, 1–9.

Liu, M.-C., Nittler, L. R., Alexander, C. M. O., & Lee, T. (2010). Be and early solar system irradiation. *The Astrophysical Journal*, *719*(1), L99–L103.

Lodders, K. (2003). Solar System Abundances and Condensation Temperatures of the Elements. *The Astrophysical Journal*, *591*(2), 1220–1247.

Ludwig, K. R. (1988). Isoplot for MS-DOS: A plotting and regression program for radiogenic-isotope data, for IBM-PC compatible computers. *United States Geological Survey*, *88–557*, 1–37.

MacPherson, G. ., Nagashima, K., Ivanova, M. A., & Krot, A. N. (2012a). Primary reverse oxygen-isotope evolution of pyroxene in compact type A CAIs from the Efremovka and NWA-3118 CV3 chondrites: Insights into the interal CAI mixing lines (abstract#2415). *43rd Lunar and Planetary Science Conference*.

MacPherson, G. J. (2013). Calcium-Aluminum-Rich Inclusions in Chondritic Meteorites. In *Treatise on Geochemistry: Second Edition* (2nd ed., pp. 139–179). Elsevier.

MacPherson, G. J., Bullock, E. S., Tenner, T. J., Nakashima, D., Kita, N. T., Ivanova, M. A., … Jacobsen, S. B. (2017). High precision Al–Mg systematics of forsterite-bearing Type B CAIs from CV3 chondrites. *Geochimica et Cosmochimica Acta*, *201*, 65–82.

MacPherson, G. J., Huss, G. R., & Davis, A. M. (2003). Extinct 10Be in Type A calcium-aluminum-rich inclusions from CV chondrites. *Geochimica et Cosmochimica Acta*, *67*(17), 3165–3179.

MacPherson, G. J., Kita, N. T., Ushikubo, T., Bullock, E. S., & Davis, A. M. (2012b). Well-resolved variations in the formation ages for Ca-Al-rich inclusions in the early Solar System. *Earth and Planetary Science Letters*, *331–332*, 43–54.

Makide, K., Nagashima, K., Krot, A. N., Huss, G. R., Hutcheon, I. D., & Bischoff, A. (2009). Oxygen- and magnesium-isotope compositions of calcium-aluminum-rich inclusions from CR2 carbonaceous chondrites. *Geochimica et Cosmochimica Acta*, *73*(17), 5018–5050.

Marhas, K. K., Goswami, J. N., & Davis, A. M. (2002). Short-lived nuclides in hibonite grains from Murchison: evidence for solar system evolution. *Science (New York, N.Y.)*, *298*(5601), 2182–2185.

Marschall, H. R., & Monteleone, B. D. (2014). *Boron Isotope Analysis of Silicate Glass with Very Low Boron Concentrations by Secondary Ion Mass Spectrometry*. 1–16.

McKeegan, K. D., Chaussidon, M., & Robert, F. (2000). Incorporation of Short-Lived 10Be in a Calcium-Aluminum-Rich Inclusion from the Allende Meteorite. *Science (New York, N.Y.)*, *289*, 1334–1337.

McKeegan, K. D., Leshin, L. A., Russell, S. S., & MacPherson, G. J. (1998). Oxygen isotope abundances in calcium- aluminum-rich inclusions for ordinary chondrites: Implications for nebular heterogeneity. *Science (New York, N.Y.)*, *280*(5362), 414–418.

Mendybaev, R. A. (2016). Thermal and chemical evolution in the early solar system as recorded by FUN CAIs: Part II – Lab evaporation of potential CMS-1 precursor material. *Geochimica et Cosmochimica Acta*.

Mendybaev, R. A., Richter, F. M., & Davis, A. M. (2006). Crystallization of melilite from CMAS-liquids and the formation of the melilite mantle of Type B1 CAIs: Experimental simulations. *Geochimica et Cosmochimica Acta*, *70*(10), 2622–2642.

Mendybaev, R. A., Richter, F. M., Georg, R. B., Janney, P. E., Spicuzza, M. J., Davis, A. M., & Valley, J. W. (2013). Experimental evaporation of Mg- and Si-rich melts: Implications for the origin and evolution of FUN CAIs. *Geochimica et Cosmochimica Acta*, *123*, 368–384.

Mendybaev, R. A., Williams, C. D., Spicuzza, M. J., Richter, F. M., Valley, J. W., Fedkin, A. V., & Wadhwa, M. (2017). Thermal and chemical evolution in the early solar system as recorded by FUN CAIs: Part II – Lab evaporation of potential CMS-1 precursor material. *Geochimica et Cosmochimica Acta*, *201*, 49–64.

Mishra, R. K., & Marhas, K. K. (2019). Meteoritic evidence of a late superflare as source of 7Be in the early Solar System. *Nature Astronomy*, *41550*.

Morioka, M., Kamata, Y., & Nagasawa, H. (1997). Diffusion in single crystals of melilite: III. Divalent cations in gehlenite. *Geochimica et Cosmochimica Acta*, *61*(5), 1009–1016.

Moskalenko, I. V., & Mashnik, S. G. (2003). Evaluation of Production Cross Sections of Li, Be, B in CR. *The 28th International Cosmic Ray Conference*, 1–14.

Nakashima, D., Ushikubo, T., Joswiak, D. J., Brownlee, D. E., Matrajt, G., Weisberg, M. K., … Kita, N. T. (2012). Oxygen isotopes in crystalline silicates of comet Wild 2: A comparison of oxygen isotope systematics between wild 2 particles and chondritic materials. *Earth and Planetary Science Letters*, *357–358*, 355–365.

Nittler, & Dauphas. (2006). Meteorites and the Chemical Evolution of the Milky Way. *Meteorites and the Early Solar System II*, 127–146.

Nittler, L. R., Stroud, R. M., Trigo-Rodríguez, J. M., De Gregorio, B. T., Alexander, C. M. O., Davidson, J., … Tanbakouei, S. (2019). A cometary building block in a primitive asteroidal meteorite. *Nature Astronomy*, *3*, 659–666.

Noh, H.-R., & Scalo, J. (1990). History of the Milky Way star formation rate from the white dwarf luminosity function. *The Astrophysical Journal*, *352*(1980), 605.

Norris, T. L., Gancarz, A. J., Rokop, D. J., & Thomas, K. W. (1983). Half-life of 26Al. *Journal of Geochemical Research*, *88*, 331–333.

Ottolini, L., Camara, F., Hawthorne, F. C., & Stirling, J. (2002). SIMS matrix effects in the analysis of light elements in silicate minerals: Comparison with SREF and EMPA data. *American Mineralogist*, *87*(10), 1477–1485.

Ouellette, N., Desch, S. J., Bizzarro, M., Boss, A. P., Ciesla, F., & Meyer, B. (2009). Injection mechanisms of short-lived radionuclides and their homogenization. *Geochimica et Cosmochimica Acta*, *73*(17), 4946–4962.

Park, C., Nagashima, K., Krot, A. N., Huss, G. R., Davis, A. M., & Bizzarro, M. (2017). Calcium-aluminum-rich inclusions with fractionation and unidentified nuclear effects (FUN CAIs): II . Heterogeneities of magnesium isotopes and 26 Al in the early Solar System inferred from in situ high-precision magnesium-isotope measurem. *Geochimica et Cosmochimica Acta*, *201*, 6–24.

Park, C., Wakaki, S., Sakamoto, N., Kobayashi, S., & Yurimoto, H. (2012). Oxygen isotopic composition of the solar nebula gas inferred from high-precision isotope imaging of melilite crystals in an Allende CAI. *Meteoritics and Planetary Science*, *47*(12), 2070–2083.

Podosek, F. A., Zinner, E. K., Macpherson, G. J., Lundberg, L. L., Brannon, J. C., & Fahey, A. J. (1991). Correlated study of initial 87Sr86Sr and AlMg isotopic systematics and petrologic properties in a suite of refractory inclusions from the Allende meteorite. *Geochimica et Cosmochimica Acta*, *55*(4), 1083–1110.

Render, J., Ebert, S., Burkhardt, C., Kleine, T., & Brennecka, G. A. (2019). Titanium isotopic evidence for a shared genetic heritage of refractory inclusions from different carbonaceous chondrites. *Geochimica et Cosmochimica Acta*, *254*, 40–53.

Rocha-Pinto, H. J., Maciel, W. J., Scalo, J., & Flynn, C. (2000a). Chemical enrichment and star formation in the Milky Way disk; I. Sample description and chromospheric age-metallicity relation. *Astronomy & Astrophysics*, *10*, 1–20.

Rocha-Pinto, H. J., Scalo, J., Maciel, W. J., & Flynn, C. (2000b). An Intermittent Star Formation History in a "Normal" Disk Galaxy: The Milky Way. *ApJ*, *531*(2), L115–L118.

Rosner, M., Wiedenbeck, M., & Ludwig, T. (2008). Composition-induced variation in SIMS IMF during boron isotope ratio measurements of silicate glasses. *Geostandards and Geoanalytical Research*, *32*, 27–38.

Rubin, A. E. (2010). Physical properties of chondrules in different chondrite groups: Implications for multiple melting events in dusty environments. *Geochimica et Cosmochimica Acta*, *74*(16), 4807–4828.

Rubin, A. E., Trigo-Rodríguez, J. M., Huber, H., & Wasson, J. T. (2007). Progressive aqueous alteration of CM carbonaceous chondrites. *Geochimica et Cosmochimica Acta*, *71*, 2361–2382.

Russell, S. S., Huss, G. R., Fahey, A. J., Greenwood, R. C., Hutchison, R., & Wasserburg, G. J. (1998). An isotopic and petrologic study of calcium-aluminum-rich inclusions from CO3 meteorites. *Geochemica Cosmochemica Acta*, *62*(4), 689–714.

Ryerson, F. J., & McKeegan, K. D. (1994). Determination of oxygen self-diffusion in akermanite, anorthite, diopside, and spinel: Implications for oxygen isotopic anomalies and the thermal histories of Ca-Al-rich inclusions. *Geochimica et Cosmochimica Acta*, *58*(17), 3713–3734.

Schrader, D. L., Connolly, H. C., Lauretta, D. S., Zega, T. J., Davidson, J., & Domanik, K. J. (2015). The formation and alteration of the Renazzo-like carbonaceous chondrites III: Toward understanding the genesis of ferromagnesian chondrules. *Meteoritics and Planetary Science*, *50*(1), 15–50.

Schrader, D. L., Davidson, J., Greenwood, R. C., Franchi, I. A., & Gibson, J. M. (2014). A water-ice rich minor body from the early Solar System: The CR chondrite parent asteroid. *Earth and Planetary Science Letters*, *407*, 48–60.

Schrader, D. L., Franchi, I. . A., Connolly, H. C., Greenwood, R. C., Lauretta, D. S., & Gibson, J. M. (2011). The formation and alteration of the Renazzo-like carbonaceous chondrites I: Implications of bulk-oxygen isotopic composition. *Geochimica et Cosmochimica Acta*, *75*(1), 308–325.

Schrader, D. L., Nagashima, K., Krot, A. N., Ogliore, R. C., Yin, Q. Z., Amelin, Y., … Kaltenbach, A. (2017). Distribution of26Al in the CR chondrite chondrule-forming region of the protoplanetary disk. *Geochimica et Cosmochimica Acta*, *201*, 275–302.

Scott, E. R. D., & Krot, A. N. (2013). Chondrites and Their Components. In *Treatise on Geochemistry: Second Edition* (2nd ed., Vol. 1). Elsevier Ltd.

Seifried, D., Walch, S., Girichidis, P., Naab, T., Wunsch, R., Klessen, R. S., … Clark, P. (2017). SILCC-Zoom: the dynamic and chemical evolution of molecular clouds. *Monthly Notices of the Royal Astronomical Society*, *472*(4), 4797–4818.

Shahar, A., & Young, E. D. (2007). Astrophysics of CAI formation as revealed by silicon isotope LA-MC-ICPMS of an igneous CAI. *Earth and Planetary Science Letters*, *257*(3–4), 497–510.

Shollenberger, Q. R., Borg, L. E., Render, J., Ebert, S., Bischoff, A., Russell, S. S., & Brennecka, G. A. (2018). Isotopic coherence of refractory inclusions from CV and CK meteorites: Evidence from multiple isotope systems. *Geochimica et Cosmochimica Acta*, *228*, 62–80.

Simon, S. B., Davis, A. M., & Grossman, L. (1999). Origin of compact type A refractory inclusions from CV3 carbonaceous chondrites. *Geochimica et Cosmochimica Acta*, *63*(7/8), 1233–1248.

Simon, S. B., & Grossman, L. (2015). Refractory inclusions in the pristine carbonaceous chondrites DOM 08004 and DOM 08006. *Meteoritics & Planetary Science*, *1049*(6), 1032–1049.

Simon, S. B., Krot, A. N., & Nagashima, K. (2019). Oxygen and Al-Mg isotopic compositions of grossite-bearing refractory inclusions from CO3 chondrites. *Meteoritics & Planetary Science*, *54*, 1362–1378.

Simon, S. B., Krot, A. N., Nagashima, K., Kööp, L., & Davis, A. M. (2018). Condensate refractory inclusions from the CO3.00 chondrite Dominion Range 08006: Petrography, mineral chemistry, and isotopic compositions. *Geochimica et Cosmochimica Acta*.

Sossi, P. A., Moynier, F., Chaussidon, M., Villeneuve, J., Kato, C., & Gounelle, M. (2017). Early Solar System irradiation quantified by linked vanadium and beryllium isotope variations in meteorites. *Nature Astronomy*, *1*, 0055.

Srinivasan, G., & Chaussidon, M. (2013). Constraints on 10Be and 41Ca distribution in the early solar system from 26Al and 10Be studies of Efremovka CAIs. *Earth and Planetary Science Letters*, *374*, 11–23.

Srinivasan, G., Huss, G. R., & Wasserburg, G. J. (2000). A petrographic, chemical, and isotopic study of calcium-aluminum-rich inclusions and aluminum-rich chondrules from the Axtell (CV3) chondrite. *Meteoritics and Planetary Science*, *35*(6), 1333–1354.

Stolper, E. (1982). Crystallization sequences of Ca-Al-rich inclusions from Allende: An experimental study. *Geochimica et Cosmochimica Acta*, *46*(11), 2159–2180.

Stone, E. C., Cummings, A. C., McDonald, F. B., Heikkila, B. C., Lal, N., & Webber, W. R. (2013). Voyager 1 observes low-energy Galactic cosmic rays in a region of depleted heliospheric ions. *Science (New York, N.Y.)*, *341*, 150–153.

Sugiura, N., Shuzou, Y., & Ulyanov, A. (2001). Beryllium-boron and aluminum-magnesium chronology of calcium-aluminum-rich inclusions in CV chondrites. *Meteoritics and Planetary Science*, *1408*, 1397–1408.

Tang, H., & Dauphas, N. (2015). Low 60Fe abundance in Semarkina and Sahara 99555. *The Astrophysical Journal*, *802*, 22.

Tatischeff, V., Duprat, J., & De Sereville, N. (2014). Light-element nucleosynthesis in a molecular cloud interacting with a supernova remnant and the origin of beryllium-10 in the protosolar nebula. *The Astrophysical Journal*, *796*, 124–144.

Telus, M., Huss, G. R., Ogliore, R. C., Nagashima, K., & Tachibana, S. (2013). Recalculation of data for short-lived radionuclide systems using less-biased ratio estimation. *Meteoritics & Planetary Science*, *2030*(12), 2013–2030.

Thrane, K., Nagashima, K., Krot, A. N., & Bizzarro, M. (2008). Discovery of a New FUN CAI from a CV Carbonaceous Chondrite: Evidence for Multistage Thermal Processing in the Protoplanetary Disk. *Astrophysical Journal*, *680*, L141–L144.

Umebayashi, T., & Nakano, T. (1980). Recombination of ions and electrons on grains and the ionization degree in dense interstellar clouds. *Astronomical Society of Japan*, *32*, 405–421.

Ushikubo, T., Tenner, T. J., Hiyagon, H., & Kita, N. (2017). A long duration of the 16O-rich reservoir in the solar nebula , as recorded in fine-grained refractory inclusions from the least metamorphosed carbonaceous chondrites. *Geochimica et Cosmochimica Acta*, *201*, 103–122.

Vermeesch, P. (2018). IsoplotR: A free and open toolbox for geochronology. *Geoscience Frontiers*, *9*(5), 1479–1493.

Villeneuve, J., Chaussidon, M., & Libourel, G. (2009). Homogeneous distribution of 26Al in the solar system from the Mg isotopic composition of chondrules. *Science (New York, N.Y.)*, *325*(5943), 985–988.

Wadhwa, M., Amelin, Y., Davis, a. M., Lugmair, G. W., Meyer, B., Gounelle, M., & Desch, S. J. (2007). From dust to planetesimals: implications for the solar protoplanetary disk from short-lived radionuclides in meteorites. *Protostars and Planets V*, (1), 835–848.

Wadhwa, M., Kita, N. T., Bullock, E. S., MacPherson, G. J., & Bouvier, A. (2014). High precision Al-Mg isotope systematics for an almost pristine refractory inclusion: implications for the absolute age of the solar system (abstract #2698). *45th Lunar and Planetary Science Conference*.

Wasson, J. T., Yurimoto, H., & Russell, S. S. (2001). 16O-rich melilite in CO3.0 chondrites: Possible formation of common, 16O-poor melilite by aqueous alteration. *Geochimica et Cosmochimica Acta*, *65*(24), 4539–4549.

Weisberg, M. K., McCoy, T. J., & Krot, A. N. (2006). Systematics and Evaluation of Meteorite Classification. *Meteorites and the Early Solar System II*, 19–52.

Weisberg, M. K., Smith, C., Benedix, G., Herd, C. D. K., Righter, K., Haack, H., … Grossman, J. N. (2010). The meteoritical bulletin, No. 97. *Meteoritics and Planetary Science*, *45*(3), 449–493.

Wendt, I., & Carl, C. (1991). The statistical distribution of the mean squared weighted deviation. *Chemical Geology: Isotope Geoscience Section*, *86*(4), 275–285.

Wielandt, D., Nagashima, K., Krot, A. N., Huss, G. R., Ivanova, M. A., & Bizzarro, M. (2012). Be in the early Solar System. *The Astrophysical Journal*, *748*(2), L25.

Williams, C. D., Ushikubo, T., Bullock, E. S., Janney, P. E., Hines, R. R., Kita, N. T., … Wadhwa, M. (2017). Thermal and chemical evolution in the early solar system as recorded by FUN CAIs: Part I – Petrology, mineral chemistry, and isotopic composition of Allende FUN CAI CMS-1. *Geochimica et Cosmochimica Acta*, *201*, 25–48.

Williams, L. B., Hervig, R. L., Wieser, M. E., & Hutcheon, I. (2001). *The influence of organic matter on the boron isotope geochemistry of the gulf coast sedimentary basin , USA*.

Yanasak, N. E., Wiedenbeck, M. E., Mewaldt, R. A., Davis, A. J., Cummings, A. C., George, J. S., … Israel, M. H. (2001). Measurements of the secondary radionuclides 10Be, 26Al, 36Cl, 54Mn, and 14C and implications for the galactic cosmic-ray age. *The Astrophysical Journal*, *563*, 768–792.

York, D. (1966). Least-squares fitting of a straight line. *Canadian Journal of Physics*, *44*, 1079–1086.

York, D., Evensen, N. M., Martínez, M. L., & De Basabe Delgado, J. (2004). Unified equations for the slope, intercept, and standard errors of the best straight line. *American Journal of Physics*, *72*(3), 367.

Young, E. D. (2016). Bayes' Theorem and Early Solar Short-Lived Radionuclides: the Case for an Unexceptional Origin for the Solar System. *The Astrophysical Journal*, *826*(2), 129.

Yurimoto, H., Ito, M., & Nagasawa, H. (1998). Oxygen Isotope Exchange Between Refractory Inclusion in Allende and Solar Nebula Gas. *Science*, *282*, 1874–1877.

Yurimoto, H., Morioka, M., & Nagasawa, H. (1989). Diffusion in single crystals of melilite: I. Oxygen. *Geochimica et Cosmochimica Acta*, *53*(9), 2387–2394.

Zapartas, E., Mink, S. E., Dyk, S. D., Fox, O. D., Smith, N., Bostroem, K. A., … Ryder, S. (2017). Predicting the Presence of Companions for Stripped-envelope Supernovae: The Case of the Broad-lined Type Ic SN 2002ap. *The Astrophysical Journal*, *842*(2), 125.

Zhai, M., Nakamuar, E., Shaw, D. M., & Nakano, T. (1996). Boron isotopes in meteorites and lunar rocks. *Geochim Cosmochim Acta*, *60*(23), 4877–4881.

Zhang, Y., Ni, H., & Chen, Y. (2010). Diffusion data in silicate melts. *Reviews in Mineralogy and Geochemistry*, *72*, 311–408.

APPENDIX A

LONG TABLES

Table S1

Chapter 3: Representative CR2 CAI Mineralogy

CAI	mineral	K_2O	Al_2O_3	Na_2O	TiO_2	CaO	SiO_2	MgO	Cr_2O_3	FeO	TOTAL	Ak
Creosote	melilite	0.01	26.08	0.00	0.00	40.18	28.66	4.38	0.05	0.22	99.6	31
Creosote	melilite	0.00	29.41	0.03	0.02	40.69	25.33	2.72	0.00	0.01	98.2	18
Creosote	anorthite	0.03	36.39	0.07	0.19	19.47	42.24	0.16	-0.01	0.96	99.5	
Creosote	anorthite	0.02	36.69	0.04	0.05	21.17	41.84	0.14	-0.01	0.03	100.0	
Creosote	anorthite	0.02	36.35	0.07	0.27	19.32	42.44	0.23	-0.02	0.93	99.6	
Creosote	anorthite - rim	0.03	36.81	0.02	0.02	21.15	41.87	0.26	-0.01	0.16	100.3	
Creosote	hibonite	0.00	82.93	0.00	6.45	8.40	-0.02	3.31	0.08	0.01	101.2	
Creosote	pyroxene - interior	0.00	24.19	0.02	18.42	24.57	27.49	4.36	0.05	0.02	99.1	
Creosote	pyroxene - rim	0.00	3.41	0.02	0.44	25.53	51.85	16.54	0.05	0.29	98.1	
Dalea	melilite	0.00	33.89	0.00	0.02	40.73	23.68	1.37	0.00	0.17	99.8	8
Dalea	melilite	0.00	29.42	0.01	0.02	40.90	26.13	2.93	0.01	0.25	99.7	20
Dalea	pyroxene	0.00	1.27	0.00	0.08	25.41	54.46	18.57	0.01	0.30	100.1	
Dalea	spinel	0.01	69.44	0.00	0.16	0.39	0.33	27.77	0.27	0.36	98.7	
Dalea	anorthite	0.00	37.01	0.02	0.05	20.29	42.49	0.15	0.00	0.26	100.3	
Dalea2	pyroxene	0.00	5.11	0.00	3.19	22.60	49.99	17.63	0.65	0.69	99.9	
Dalea2	spinel	0.00	68.03	0.00	1.08	0.04	0.07	27.30	0.90	1.45	98.9	
Dalea2	anorthite	0.01	36.78	0.10	0.11	20.04	42.70	0.18	0.02	0.31	100.2	
Yucca	melilite	0.02	28.54	0.00	0.02	40.30	27.34	3.57	-0.02	0.16	99.9	21
Yucca	melilite	0.04	27.32	0.02	0.02	40.35	27.67	3.92	-0.01	0.02	99.4	26
Yucca	pyroxene - interior	0.00	20.05	0.00	6.61	24.70	38.95	9.08	0.04	0.01	99.5	
Yucca	pyroxene - rim	0.00	1.49	0.09	0.10	22.87	52.61	17.75	0.31	1.66	97.0	
Yucca	spinel	0.00	70.38	0.00	0.43	0.09	0.39	28.10	0.18	0.31	99.9	
Yucca	anorthite - rim	0.02	27.12	0.05	0.23	20.73	44.04	5.11	0.16	1.85	99.3	
Rosewood	melilite	nm	34.25	nm	0.03	40.99	22.84	0.59	nm	1.1	99.8	3
Rosewood	melilite	nm	33.54	nm	0.01	41.01	23.44	1.04	nm	0.6	99.6	6
Sonoran	melilite	nm	30.7	nm	0.03	39.85	25.21	2.56	nm	1.44	99.8	15
Sonoran	melilite	nm	30.9	nm	0.05	39.36	25.64	2.29	nm	1.42	99.7	14
Palo Verde	melilite	nm	27.48	nm	0.02	41.25	27.09	3.22	nm	0.74	99.8	21
Palo Verde	melilite	nm	26.57	nm	0.12	40.73	27.94	3.43	nm	1.03	99.8	23
Cereus	melilite	nm	30.93	nm	0.19	41.66	25.04	1.99	nm	nm	99.8	12
Cereus	melilite	nm	33.71	nm	0.08	41.8	23.24	1.03	nm	0.10	100.0	6
Hibiscus	melilite	nm	26	nm	0.13	40.05	26.99	3.16	nm	3.14	99.5	22

Hibiscus	melilite	nm	26.79	nm	0.18	40.43	27.31	3.43	nm	1.51	99.7	23

Notes: all abundances in wt. %, nm = not measured

Table S2

Chapter 3: ^{10}Be–^{10}B Isotope Systematics Data for five CR2 CAIs

Sample spot	$^{9}Be/^{11}B$	2 SE	$^{10}B/^{11}B$	2 SE	Error Correlation Factor	[Be] ppm	[B] ppm	Al_2O_3 wt. %	Åk content (mol %)
Creosote-1	19.2	0.7	0.257	0.011	0.12	0.89	0.07	25.2	30
Creosote-2	23.9	0.9	0.256	0.013	0.21	0.97	0.06	24.5	32
Creosote-3	23.9	1.0	0.258	0.015	0.46	0.67	0.04	25.9	28
Creosote-5	10.2	0.4	0.260	0.009	0.34	0.52	0.08	30.0	16
Creosote-6	14.0	0.5	0.258	0.010	0.08	0.78	0.08	28.2	21
Creosote-7	17.3	0.6	0.259	0.010	0.21	0.98	0.08	28.9	19
Creosote-8	34.3	1.4	0.268	0.015	0.11	0.65	0.03	25.4	29
Creosote-9	19.4	0.7	0.264	0.008	0.25	0.78	0.06	26.5	26
Yucca-1	10.4	0.4	0.255	0.009	0.06	0.38	0.05	25.4	30
Yucca-2	10.6	0.4	0.253	0.009	0.00	0.51	0.04	28.1	21
Yucca-3	20.9	0.8	0.258	0.011	0.05	0.53	0.02	25.2	31
Yucca-4	45.7	1.8	0.281	0.015	0.46	0.48	0.02	27.6	24
Yucca-5	45.9	1.8	0.288	0.015	0.46	0.36	0.05	27.4	23
Dalea-1_1	123.1	6.3	0.331	0.026	0.38	1.44	0.02	29.7	19
Dalea-1_2	52.2	2.0	0.283	0.012	0.36	1.34	0.04	29.7	19
Dalea-2	10.0	0.3	0.253	0.005	0.13	1.01	0.15	31.8	12
Dalea-3	16.2	0.5	0.258	0.006	0.18	2.33	0.22	18.2	36
Dalea-4	0.4	0.0	0.245	0.001	0.15	2.35	8.71	18.2	37
Cereus-1	0.7	0.0	0.251	0.001	0.00	1.06	2.41	30.4	14
Cereus-2	4.1	0.0	0.255	0.004	0.14	0.97	0.36	32.1	12
Cereus-3	0.6	0.0	0.250	0.002	0.00	0.87	2.14	33.2	13
Cereus-5	5.0	0.1	0.255	0.004	0.00	1.22	0.36	32.1	11
Cereus-7	1.5	0.0	0.251	0.002	0.00	1.05	1.05	32.2	10
PaloVerde-1_1	0.1	0.0	0.246	0.001	0.00	0.57	11.84	27.3	23
PaloVerde-1_2	6.4	0.3	0.248	0.010	0.59	0.63	0.15	27.3	23
PaloVerde-2	8.0	0.4	0.263	0.009	0.22	0.62	0.12	28.5	19
PaloVerde-4	5.5	0.2	0.252	0.008	0.27	0.52	0.14	29.1	18
PaloVerde-5	7.2	0.4	0.248	0.008	0.13	0.38	0.08	28.4	20

Notes: Each spot is associated with a number in analysis order, if a number is missing, the pit was located on a crack or the counts were unstable; these analyses were eliminated from the final regression. When the analysis number is indicated as #1, #2, etc., the analysis was broken up into multiple parts because the counts show that phases with distinct Be and B isotopic compositions were analyzed.

Table S3

Chapter 3: ^{26}Al–^{26}Mg Isotope Systematics Data for three CR2 CAIs

sample spots	$^{27}Al/^{24}Mg$	2 SE	$\delta^{26}Mg$*	2 SE	Error Correlation Factor
Creosote_an-1	620	36	210.4	14.3	0.81
Creosote_an-2	420	27	140.3	10.9	0.79
Creosote_an-3	424	58	139.9	22.8	0.87
Creosote_an-rim-4	1324	91	408.7	61.5	0.41
Creosote_mel-1	6.2	0.1	2.0	0.3	0.00
Creosote_mel-2	6.7	0.1	2.1	0.3	0.00
Creosote_mel-3	5.9	0.1	1.9	0.3	0.00
Creosote_mel-4	8.1	0.1	2.8	0.3	0.00
Creosote_mel-5	3.6	0.0	1.0	0.3	0.00
Creosote_mel-6	17.5	0.2	6.3	0.4	0.00
Creosote_mel-7	7.3	0.1	2.5	0.3	0.00
Creosote_px-rim-1	0.43	0.02	0.12	0.18	0.00
Creosote_px-rim-2	0.17	0.00	0.04	0.19	0.00
Creosote_px-rim-3	0.14	0.00	0.00	0.20	0.00
Creosote_px-rim-4	0.55	0.01	0.16	0.18	0.00
Creosote_px-rim-5	0.29	0.00	-0.02	0.18	0.00
Creosote_px-6	0.28	0.02	0.13	0.17	0.00
Creosote_px-7	0.28	0.01	0.04	0.18	0.00
Creosote_sp-1	2.64	0.03	0.87	0.15	0.00
Creosote_sp-2	2.58	0.03	0.73	0.15	0.00
Creosote_sp-3	2.72	0.03	0.69	0.16	0.00

Yucca_an-1	833	43	2.6	12.3	0.31
Yucca_an-2	147	27	0.0	7.9	0.05
Yucca_an-3	832	49	10.1	27.3	0.32
Yucca_an-4	812	38	3.2	16.3	0.40
Yucca_mel-1	9.0	0.1	3.0	0.3	0.00
Yucca_mel-2	6.9	0.2	2.4	0.2	0.00
Yucca_mel-3	7.7	0.1	2.5	0.2	0.00
Yucca_mel-4	7.2	0.1	2.1	0.3	0.00
Yucca_mel-5	8.2	0.1	2.7	0.4	0.00
Yucca_px-1	2.14	0.02	0.58	0.22	0.00
Yucca_px-2	1.80	0.02	0.63	0.22	0.00
Yucca_px-3	2.30	0.03	0.72	0.22	0.00
Yucca_sp-1	2.58	0.03	0.86	0.16	0.00
Yucca_sp-2	2.58	0.03	1.05	0.16	0.00
Yucca_sp-3	2.58	0.03	1.07	0.16	0.00
Yucca_sp-4	2.58	0.03	0.86	0.16	0.00
Dalea_mel-1	5.5	0.4	1.8	0.4	0.00
Dalea_mel-2	9.4	0.3	2.7	0.4	0.00
Dalea_mel-3	12.9	0.4	4.6	0.5	0.00
Dalea_px-1	0.28	0.02	0.13	0.17	0.00
Dalea_px-2	0.28	0.01	0.04	0.18	0.00

Notes: Each spot name is associated with the mineral phase analyzed and the number in analysis order. If a number is missing, the pit was located on a crack or the counts were unstable; these analyses were eliminated from the final regression.

Table S4

Chapter 4: Olivine (top), Metal, and Sulfide (bottom, wt. %) Composition of Chondrules in NWA 5028.

Meteorite	NWA 5028	NWA 5028	NWA 5028	NWA 5028	NWA 5028	NWA 5028	NWA 5028	NWA 5028	NWA 5028	NWA 5028	NWA 5028	NWA 5028	NWA 5028	NWA 5028	NWA 5028	NWA 5028	NWA 5028	NWA 5028	NWA 5028
Area	Ch1	Ch1	Ch1	Ch8	Ch8	Ch8	Ch8	Ch8	Ch8	Ch8	Ch5	Ch5	Ch5	Ch5	Ch5	Ch5	Ch5	Ch5	Ch5
Ch. Type	I	I	I	I	I	I	I	I	I	I	II	II	II	II	II	II	II	II	II
Grain	G1	G1	G3	G1	G1	G2	G3	G4	G4	G1	G1	G1	G1	G1	G1	G2	G2	G2	G2
Analysis #	4	5	7	27	28	29	42	43	44	17	18	19	20	21	22	24	25	26	
MgO	56.2	56.0	56.7	56.8	56.5	56.5	56.9	56.7	56.6	28.1	32.0	35.7	37.0	39.8	25.4	29.0	30.0	25.1	
Na_2O	bdl	bdl	bdl	bdl	bdl	bdl	bdl	bdl	bdl	bdl	bdl	bdl	bdl	bdl	bdl	0.2	bdl	bdl	
SiO_2	42.1	42.1	42.3	42.1	42.2	42.4	42.3	42.4	42.4	35.5	36.3	36.9	37.4	38.2	34.5	35.7	36.0	35.0	
Al_2O_3	0.22	0.28	0.16	0.08	0.11	bdl	bdl	0.09	0.11	0.05	bdl	0.05	0.06	0.06	0.09	0.30	bdl	0.05	
CaO	0.53	0.49	0.46	0.30	0.28	0.22	0.25	0.24	0.24	0.24	0.17	0.17	0.15	0.14	0.24	0.30	0.17	0.25	
FeO	0.81	0.68	0.86	0.93	0.99	1.35	0.98	0.98	1.16	35.3	30.8	26.7	24.7	21.0	38.5	32.2	33.0	38.8	
MnO	bdl	bdl	bdl	bdl	bdl	0.13	0.10	0.09	bdl	0.46	0.30	0.29	0.29	0.19	0.42	0.28	0.38	0.45	
K_2O	bdl	bdl	bdl	bdl	bdl	bdl	bdl	bdl	bdl	bdl	bdl	bdl	bdl	bdl	bdl	bdl	bdl	bdl	
TiO_2	0.12	0.12	0.07	0.05	bdl	bdl	bdl	bdl	bdl	bdl	bdl	bdl	bdl	bdl	bdl	bdl	bdl	bdl	
Cr_2O_3	0.28	0.23	0.31	0.39	0.36	0.41	0.39	0.39	0.38	0.41	0.41	0.40	0.36	0.31	0.31	1.51	0.27	0.30	
NiO	bdl	bdl	bdl	bdl	bdl	bdl	bdl	bdl	bdl	bdl	bdl	bdl	bdl	bdl	bdl	bdl	bdl	bdl	
Total	100.3	99.9	101.0	100.7	100.6	101.2	101.0	101.0	101.1	100.0	99.9	100.4	100.0	99.7	99.6	99.7	99.9	100.0	
Cations based on 4 oxygens																			
Mg	1.970	1.968	1.975	1.985	1.976	1.970	1.980	1.974	1.971	1.165	1.298	1.414	1.455	1.540	1.080	1.196	1.233	1.063	
Na	bdl	bdl	bdl	bdl	bdl	bdl	bdl	bdl	bdl	bdl	bdl	bdl	bdl	bdl	bdl	0.009	bdl	bdl	
Si	0.989	0.992	0.989	0.986	0.990	0.991	0.989	0.992	0.991	0.989	0.987	0.982	0.987	0.992	0.984	0.987	0.990	0.992	
Al	0.006	0.008	0.004	0.002	0.003	bdl	bdl	0.002	0.003	0.002	bdl	0.002	0.002	0.002	0.003	0.010	bdl	0.002	
Ca	0.013	0.012	0.011	0.007	0.007	0.006	0.006	0.006	0.006	0.007	0.005	0.005	0.004	0.004	0.007	0.009	0.005	0.008	
Fe	0.016	0.013	0.017	0.018	0.019	0.026	0.019	0.019	0.023	0.823	0.700	0.594	0.546	0.455	0.917	0.744	0.760	0.921	
Mn	bdl	bdl	bdl	bdl	bdl	0.003	0.002	0.002	bdl	0.011	0.007	0.007	0.006	0.004	0.010	0.007	0.009	0.011	
K	bdl	bdl	bdl	bdl	bdl	bdl	bdl	bdl	bdl	bdl	bdl	bdl	bdl	bdl	bdl	bdl	bdl	bdl	
Ti	0.002	0.002	0.001	0.001	bdl	bdl	bdl	bdl	bdl	bdl	bdl	bdl	bdl	bdl	bdl	bdl	bdl	bdl	
Cr	0.005	0.004	0.006	0.007	0.007	0.008	0.007	0.007	0.007	0.009	0.009	0.008	0.008	0.006	0.007	0.033	0.006	0.007	
Ni	bdl	bdl	bdl	bdl	bdl	bdl	bdl	bdl	bdl	bdl	bdl	bdl	bdl	bdl	bdl	bdl	bdl	bdl	
Cations	3.002	3.000	3.003	3.007	3.002	3.003	3.004	3.002	3.000	3.005	3.006	3.011	3.007	3.003	3.009	2.994	3.004	3.003	
Fa	0.8	0.7	0.8	0.9	1.0	1.3	1.0	1.0	1.1	41.4	35.1	29.6	27.3	22.8	45.9	38.4	38.1	46.4	
Fo	99.2	99.3	99.2	99.1	99.0	98.7	99.0	99.0	98.9	58.6	64.9	70.4	72.7	77.2	54.1	61.6	61.9	53.6	
Fe/Mn	-	-	-	-	-	10.2	9.4	10.9	-	75.8	101.7	90.7	85.7	110.1	90.6	113.6	86.7	85.7	

Ch = chondrule; I = type I chondrule; II = type II chondrule; G = grain; bdl = below detection limit.
Standards and detection limits (in wt.%): albite for Na (0.03), diopside for Si (0.02), Mg (0.04), and Ca (0.01), anorthite for Al (0.02), orthoclase for K (0.02), rhodonite for Mn (0.05), rutile for Ti (0.02), fayalite for Fe (0.07), chromite for Cr (0.02), and nickel metal for Ni (0.07).

Meteorite	NWA 5028	NWA 5028	NWA 5028	NWA 5028	NWA 5028	NWA 5028	NWA 5028	NWA 5028	NWA 5028	NWA 5028	NWA 5028	NWA 5028	NWA 5028	NWA 5028	NWA 5028	NWA 5028	NWA 5028	NWA 5028	NWA 5028	NWA 5028	NWA 5028	NWA 5028	NWA 5028	NWA 5028	NWA 5028	NWA 5028	NWA 5028
Chondrule	Ch1	Ch1	Ch1	Ch1	Ch1	Ch1	Ch1	Ch8	Ch8	Ch8	Ch8	Ch8	Ch8	Ch8	Ch8	Ch8	Ch8	Ch8	Ch5	Ch5	Ch5	Ch1	Ch8	Ch8	Ch8	Ch5
Ch. Type	I	I	I	I	I	I	I	I	I	I	I	I	I	I	I	I	I	I	I	II	II	I	I	I	I	II
Assemblage	OA1	OA1	OA1	OA1	OA1	OA1	OA1	OA3	OA1	OA1	OA2	OA2	OA3	OA3	OA2	OA3	OA2	OA1	OA1	OA1	OA1	OA1	OA2	OA3	OA1	
Analysis #	12	10	11	2	9	8	1	40	30	31	32	35	38	39	36	37	34	13	15	14	3	33	41	16		
	Ni-poor metal	Ni-poor metal	Ni-poor metal	Ni-poor metal	Ni-poor metal	Ni-rich metal	Ni-rich metal	Ni-poor metal	Ni-poor metal	Ni-poor metal	Ni-poor metal	Ni-poor metal	Ni-rich metal	Ni-rich metal	Ni-rich metal	Ni-rich metal	Ni-rich metal	Ni-rich metal	Ni-rich metal	Ni-rich metal	po	po	po	po		
Mg	bdl	bdl	bdl	bdl	bdl	bdl	bdl	0.05	bdl	bdl	bdl	bdl	bdl	bdl	bdl	bdl	bdl	bdl	bdl	bdl	bdl	0.05	0.06	bdl		
Si	0.06	bdl	0.04	0.18	0.09	0.09	0.07	0.05	0.07	0.04	0.03	0.05	0.02	0.03	0.03	0.02	0.02	0.02	bdl	0.02	0.19	0.07	0.06	0.07		
Ca	0.00	0.01	0.00	0.00	0.00	0.00	0.00	0.73	0.02	0.02	0.04	0.03	0.01	0.03	0.04	0.02	0.03	0.02	0.03	0.01	0.01	0.07	0.07	0.06		
Fe	90.3	90.8	90.5	90.3	90.1	62.2	62.7	88.3	90.8	91.5	91.0	91.2	61.2	61.3	59.7	58.4	57.1	49.6	48.2	45.2	62.1	62.4	62.8	61.2		
Cr	0.86	0.80	0.78	0.74	0.78	0.70	0.12	0.66	0.66	0.40	0.48	0.58	0.63	0.27	0.49	0.52	0.40	0.09	0.02	0.03	1.47	0.60	0.84	0.03		
Ni	6.7	7.0	7.1	7.1	7.8	35.7	36.6	6.7	6.8	7.0	7.0	7.1	37.0	37.3	37.6	39.9	40.9	47.9	49.2	53.2	bdl	bdl	0.2	1.1		
S	0.05	0.06	0.05	0.06	0.05	0.05	bdl	0.04	0.04	bdl	0.03	0.03	bdl	0.06	0.03	0.03	0.07	bdl	bdl	bdl	34.47	35.09	35.30	36.51		
P	bdl	0.03	0.04	bdl	0.05	bdl	bdl	0.31	0.14	bdl	bdl	0.08	bdl	bdl	bdl	bdl	bdl	bdl	bdl	bdl	bdl	bdl	bdl	bdl		
Co	0.28	0.31	0.31	0.31	0.32	bdl	bdl	1.64	0.44	0.49	0.52	0.52	0.28	0.26	bdl	0.15	bdl	1.23	1.50	1.28	bdl	bdl	bdl	bdl		
Cu	bdl	bdl	bdl	bdl	bdl	bdl	0.2	bdl	bdl	bdl	bdl	bdl	bdl	0.1	0.1	0.1	0.2	0.2	0.2	0.3	bdl	bdl	bdl	bdl		
Total	98.3	99.0	98.7	98.7	99.2	98.7	99.6	98.4	99.0	99.5	99.1	99.6	99.1	99.4	98.1	99.1	98.7	99.1	99.1	100.0	98.3	98.3	99.4	99.0		

Ch = chondrule; I = type I chondrule; II = type II chondrule; OA = opaque assemblage; bdl = below detection limit.
Standards and detection limits (in wt.%): diopside for Si (0.01) and Ca (0.02), spinel for Mg (0.03) and Al (0.02), indium phosphide for P (0.02), manganese metal for Mn (0.03), rutile for Ti (0.02), chalcopyrite for Fe (0.11), S (0.02), and Cu (0.12), chromium metal for Cr (0.03), nickel metal for Ni (0.16), and cobalt metal for Co (0.09).
Al, Mg, and Ti are always bdl.

Table S5

Chapter 4: Summary of CAI Classifications

Chondrite	Sample	CAI name	longest axis	Ak range	CAI characterization
CO3	DaG 005	Bascom	720 μm	9-18	Irregular shape, melilite nodules enclosing spinel clumps, minimal alteration in cracks
CO3	DaG 005	Mitchell	330 μm	5-6	Irregular rounded shape, predominately melilite with concentrations of sp, hibonite, and perovskite in the interior, thin pyroxene rim
CO3	DaG 027	Krafft	640 μm	22-34	Rounded shape, coarse melilite with spinel clumps and pyroxene rim
CO3	DaG 027	Anning	830 μm	8-13	Rounded shape, some coarse melilite, most melilite encloses spinel, hibonite, and perovskite
CO3	DaG 027	Jemmison	300 μm	12-15	Fragmented diamond shape, coarse melilite surrounding large rounded spinel, multi-mineralic rim
CO3	DaG 027	Goeppert	340 μm	7-10	Elongate rounded shape, melilite surrounding spinel clumps, fragmented, faulted pyroxene rim
CO3	NWA 7892	Mesquite	5 mm	5	Rounded shape, interior composed of melilite with some calcite and hibonite, mantle composted of hibonite and spinel, complete multi-mineralic rim composed of melilite, spinel, and hibonite
CO3	DOM 08006	31-2	3 mm	grossite	Irregular shape resembling a condensate, concentric layers of hibonite, grossite, melilite, pyroxene and Fe-rich phases from core to rim
CH/CB	Isheyevo	Tereshkova	290 μm	5-17	Round shape, melilite enclosing round hibonite grains, some interspersed perovskite chains
CH/CB	Isheyevo	Tharp	180 μm	5-17	Rounded fragment shape, mostly melilite with many cracks/grain boundaries, euhedral spinel throughout, some perovskite and a partial rim
CH/CB	Isheyevo	Bell	120 μm	5-17	Round fragmented shape, melilite enclosing grossite laths
CH/CB	Isheyevo	Meitner	180 μm	5-17	Round fragmented shape, fractured melilite enclosing grains of rounded spinel and perovskite, partial rim
CH/CB	Isheyevo	Rubin	150 μm	5-17	Fragmented composed of melilite and large spinel (~10 μm) with thick px rim on one edge

CV3ox	Allende	CMS-1	5 mm	35-41	FUN, irregularly-shaped aggregate of nodules composed of melilite, pyroxene, spinel, and anorthite
CV3ox	NWA 6991	B4	10 mm	15-36	CTA, predominately composed of coarse melilite grains, along with fassaite, spinel, and minor anorthite; secondary alteration is only a minor component of B4 (Bouvier et al., 2011; Bullock et al., 2014).
CV3ox	NWA 6991	Lisa	3 mm	26-43	B1; melilite and fassaite (up to 1 mm with TiO_2 6-12 wt.%) poikilitically enclose small euhedral spinel, 800 μm mantle of melilite (Ak_{15-51} mol%), rim of spinel embedded with perovskite overlain by Al-bearing diopside (Shollenberger et al., 2018)
CV3ox	Allende	TS68	2.3 mm	26	CTA, rounded shape and contains large (up to 700 μm) stubby melilite crystals and coarse fassaite, euhedral spinel is heterogeneously distributed through the sample, lightly altered and contains fremdlinge (FeNi-metal, Pt-metal alloys, V-rich magnetite, sulfides, and phosphates)
CV3ox	Allende	TS23	10 mm	23	B, rounded shape with monomineralic melilite mantle surrounding a core with melilite laths, blocky fassaite, and interstitial anorthite as well as ubiquitous spinel
CV3red	Vigarano	FoB 3137-2	6 mm	71-87	FoB, rounded shape with nodular segments, outer zones which are forsterite-free but melilite-rich and an interior forsterite region enclosed in diopside and melilite
CV3red	Leoville	ZT4	5.2 mm	12	CTA, irregular rounded shape with distinct nodules, consists predominately of porous melilite, margins are perovskite-rich, spinel-pyroxene rim
CV3red	NWA 5028	Cholla	1 mm	7-39	FTA, contains anhedral spinel, typically 10 μm diameter, enclosed in melilite, the inclusion main is surrounded by an irregular ~40 μm thick pyroxene rim. The only alteration found in the CAI is a patch of secondary anorthite
CV3red	Leoville	ZT1	6.3 mm	31	B, irregular and fragmented shape, mantle is predominately melilite and core is composed of melilite enclosing sections of pyroxene and anorthite, spinel dispersed throughout and tends to clump in pallasade bodies, partial rim

CV3red	NWA 5028	Agave	5 mm	1-85	B2, dominated by fassaite, which encloses patches of melilite and anhedral spinel; only minimal alteration products are present
CV3red	NWA 5508	Saguaro	18 mm	9-35	B2, spherical inclusion composed predominately of melilite with fassaite, spinel, and anorthite. Spinel is often distributed as rounded palisade bodies surrounding melilite, fassaite, and spinel (Simon et al., 1999). Saguaro includes minimal alteration products
CV3an	NWA 7891	ZT7	3.3 mm	21-24	CTA, rounded shape consisting of predominately melilite enclosing spinel (often connected in a line) and symplectic perovskite, some alteration near the rim

Table S6

Chapter 4: Calibration Details of SIMS Sessions

Session start date	IMS	Beam Conditions	Samples analyzed	Standards used	RSF average	IMF average	MRP
7/1/15	6f	10 nA	NWA 5028 CAI Agave	IMt, NIST 610	2.32±0.12	1.051±0.005	1200
11/4/15	6f	15-20 nA	NWA 5028 CAI Agave, Allende CAI TS68	IMt, NIST 610	2.37±0.12	1.031±0.012	1000
12/7/15	6f	20-25 nA	NWA 5028 CAI Cholla	IMt, NIST 610	2.10±0.11	1.027±0.003	1000
2/2/16	6f	18-21 nA	Axtell CAI AX4, Allende CAI TS23	IMt, NIST 610	2.48±0.12	1.038±0.005	700
5/6/16	6f	18-25 nA	Axtell CAI AX30	IMt, NIST 610	2.30±0.11	1.022±0.011	1000
12/6/16	6f	10-20 nA	NWA 6991 B4, Allende CAI CMS-1	IMt, NIST 610	2.27±0.11	1.030±0.012	1300
4/17/17	6f	15-25nA	NWA 5508 CAI Saguaro	IMt, melilite glasses	1.95±0.20	1.066±0.004	1300
5/1/17	1290	10 nA	Allende CAI CMS-1	NIST 614, melilite glasses	2.21±0.16	1.050±0.014	2500
6/7/17	6f	20-23 nA	Leoville CAI ZT1	IMt, NIST 610,614 melilite glasses	2.19±0.22	1.040±0.007	1500
6/19/17	6f	20 nA	Leoville CAI ZT1, ALHA 77307 CAI 60-1	IMt, NIST 610 melilite glasses	2.17±0.02	1.044±0.022	1500
8/16/17	6f	16-20 nA	Leoville CAI ZT4	IMt, NIST 610, GS-1G glasses, melilite glasses	2.15±0.22	1.029±0.019	1500

10/16/17	6f	20-24 nA	NWA 7891 CAI ZT7	IMt, NIST 610 melilite glasses	2.33±0.23	1.037±0.004	1400
10/30/17	1290	10 nA	5 CO3 CAIs (DOM 08006 CAIs, DOM 08004 CAIs, ALHA 77307 CAIs), Allende CAI CMS-1	NIST 614, melilite glasses	2.44±0.02	1.037±0.002	2500
3/1/18	6f	19-25 nA	NWA 6991 CAI Lisa	IMt, NIST 610, melilite glasses	2.43±0.02	1.039±0.004	1400
7/16/18	1290	3-10 nA	8 CR2 CAIs (LAP 02342, Shişr 033, NWA 801, MIL 090657) NWA 7892 CAI Mesquite	NIST 614	3.04±0.10	1.037±0.002	2500
2/19/19	1290	5-10 nA	6 CO3 CAIs (DaG 027, DaG 005), NWA 6991 CAI Lisa, NWA 5028 CAI Cholla, 2 Isheyevo CAIs	NIST 614	3.44±0.22	1.049±0.004	2500
3/25/19	1290	1.5-2.0 nA	4 Isheyevo CAIs, Vigarano FoB 3137 re-measure	NIST 614	3.49±0.16	1.049±0.005	2500
6/13/19	6f	20-50 nA	Allende CAIs TS23, TS68	NIST 610	2.30±0.10	1.038±0.008	1550

Table S7

Chapter 4: ^{10}Be–^{10}B Data for 25 CAIs

Chondrite-type	Meteorite	CAI SIMS spot	$^{9}Be/^{11}B$	1 SE	$^{10}B/^{11}B$	1 SE	r[1]	[Be] ppm[2]	[B] ppm[2]	Al_2O_3[3]	Åk[4]	SiO_2[3]
CO3	DaG 027	Krafft_1-1	52.67	2.15	0.31	0.01	0.43	0.42	0.01	26	27	26
CO3	DaG 027	Krafft_1-2	34.14	1.46	0.27	0.01	0.40	0.32	0.01	26	27	26
CO3	DaG 027	Krafft_2	4.57	0.21	0.28	0.02	0.38	0.01	0.00	79	NA - hib	1
CO3	DaG 027	Krafft_3	45.89	2.04	0.31	0.02	0.36	0.26	0.01	24	34	27
CO3	DaG 027	Krafft_4	71.54	3.12	0.36	0.02	0.30	0.43	0.01	28	22	24
CO3	DaG 027	Krafft_5	19.59	0.75	0.27	0.01	0.27	0.13	0.01	28	22	23
CO3	DaG 027	Anning_1	49.01	1.91	0.28	0.01	0.19	0.29	0.01	31	13	22
CO3	DaG 027	Anning_2	52.06	2.03	0.29	0.01	0.20	0.28	0.01	32	10	22
CO3	DaG 027	Anning_3-1	92.73	4.66	0.33	0.02	0.34	0.30	0.00	32	11	22
CO3	DaG 027	Anning_3-2	6.43	0.23	0.26	0.01	0.20	0.21	0.05	32	11	22
CO3	DaG 027	Anning_4	92.87	4.31	0.35	0.02	0.52	0.26	0.00	31	13	22
CO3	DaG 027	Anning_5	16.58	0.62	0.25	0.01	0.26	0.09	0.01	33	8	22
CO3	DaG 027	Jemmison_1	41.55	1.61	0.27	0.01	0.37	0.18	0.01	31	12	22
CO3	DaG 027	Jemmison_2-1	96.57	4.09	0.32	0.02	0.38	0.43	0.01	31	13	22
CO3	DaG 027	Jemmison_2-2	24.16	0.95	0.28	0.01	0.00	0.28	0.02	31	13	22
CO3	DaG 027	Jemmison_3	84.21	3.25	0.33	0.01	0.32	0.40	0.01	30	15	22
CO3	DaG 027	Jemmison_4	7.45	0.28	0.26	0.01	0.09	0.02	0.00	30	14	22
CO3	DaG 027	Goeppert_2	5.28	0.19	0.26	0.01	0.17	0.11	0.03	32	7	21
CO3	DaG 027	Goeppert_3	46.00	1.86	0.29	0.01	0.41	0.17	0.01	70	NA-sp	NA
CO3	DaG 027	Goeppert_4	43.68	1.71	0.28	0.01	0.17	0.22	0.01	33	10	21
CO3	DaG 005	Bascom_3	20.48	0.74	0.27	0.01	0.11	0.11	0.01	31	11	23
CO3	DaG 005	Bascom_4	153.40	7.75	0.38	0.03	0.47	0.39	0.00	31	14	22
CO3	DaG 005	Bascom_6	28.57	1.20	0.27	0.01	0.53	0.32	0.02	32	9	22
CO3	DaG 005	Bascom_7	9.86	0.34	0.26	0.00	0.00	0.73	0.11	29	18	24
CO3	DaG 005	Mitchell_1	11.95	0.52	0.26	0.01	0.27	0.04	0.00	35	5	20
CO3	DaG 005	Mitchell_2	16.01	0.71	0.27	0.01	0.00	0.11	0.01	34	6	21
CO3	DaG 005	Mitchell_3	55.33	2.47	0.30	0.01	0.43	0.20	0.01	34	5	21

CO3.0	NWA 7892	Mesquite_1	34.21	0.89	0.27	0.01	0.38	0.55	0.02	34	5	22
CO3.0	NWA 7892	Mesquite_2	7.35	0.14	0.25	0.01	0.60	0.30	0.06	34	5	22
CO3.0	NWA 7892	Mesquite_3	6.77	0.15	0.25	0.01	0.01	0.26	0.06	34	5	22
CO3.0	NWA 7892	Mesquite_4	16.42	0.30	0.27	0.01	0.23	0.48	0.04	34	5	22
CO3.0	NWA 7892	Mesquite_5	13.80	0.24	0.26	0.00	0.13	0.64	0.07	34	5	22
CO3.0	NWA 7892	Mesquite_6	1.25	0.03	0.25	0.01	0.10	0.01	0.01	34	5	22
CO3.0	DOM 08006	31-2_3	3.71	0.03	0.25	0.00	0.39	0.27	0.11	78	NA	1
CO3.0	DOM 08006	31-2_4	4.40	0.06	0.25	0.01	0.00	0.22	0.07	78	NA	1
CO3.0	DOM 08006	31-2_5	2.66	0.02	0.25	0.00	0.00	0.55	0.31	78	NA	1
CO3.0	DOM 08006	31-2_6-1	8.86	0.08	0.26	0.00	0.08	0.26	0.04	78	NA	1
CO3.0	DOM 08006	31-2_6-2	8.02	0.06	0.26	0.00	0.00	0.26	0.05	78	NA	1
CO3.0	DOM 08006	31-2_7	1.53	0.01	0.25	0.00	0.06	0.45	0.12	78	NA	1
CO3.0	DOM 08006	31-2_8	5.48	0.04	0.25	0.00	0.17	0.34	0.34	78	NA	1
CO3.0	DOM 08006	31-2_9	22.70	0.34	0.28	0.01	-0.01	0.36	0.02	78	NA	1
CO3.0	DOM 08006	31-2_11	3.25	0.04	0.26	0.01	0.12	0.16	0.07	78	NA	1
CH/CB	Isheyevo	Burnell_1	60.62	1.84	0.29	0.01	0.05	0.28	0.01	34	6	
CH/CB	Isheyevo	Burnell_2	48.44	1.71	0.30	0.02	0.33	0.21	0.01	34	6	
CH/CB	Isheyevo	Meitner_1	25.69	1.17	0.25	0.02	0.16	0.13	0.01	34	7	
CH/CB	Isheyevo	Meitner_2	7.53	0.22	0.26	0.01	0.02	0.16	0.03	34	7	
CH/CB	Isheyevo	Meitner_3	28.86	0.94	0.27	0.01	0.33	0.28	0.01	34	7	
CH/CB	Isheyevo	Meitner_4	8.63	0.26	0.25	0.01	0.09	0.15	0.03	34	7	
CH/CB	Isheyevo	Rubin_1	5.64	0.14	0.24	0.00	0.23	0.73	0.19	30	17	
CH/CB	Isheyevo	Rubin_4-1	6.93	0.18	0.25	0.01	0.64	0.75	0.16	30	17	
CH/CB	Isheyevo	Rubin_4-2	11.85	0.34	0.26	0.01	0.30	0.58	0.07	30	17	
CH/CB	Isheyevo	Tharp_1	39.01	1.52	0.29	0.01	0.39	0.22	0.01	33	9	
CH/CB	Isheyevo	Tharp_2-1	60.90	2.73	0.31	0.02	0.19	0.22	0.01	33	9	
CH/CB	Isheyevo	Tharp_2-2	28.31	1.34	0.28	0.02	0.36	0.22	0.01	33	9	
CH/CB	Isheyevo	Tharp_3	64.37	3.04	0.33	0.02	0.45	0.28	0.01	33	9	
CH/CB	Isheyevo	Tereshkova_2	13.85	0.51	0.25	0.01	0.30	0.08	0.01	34	5	
CH/CB	Isheyevo	Tereshkova_3-1	30.01	1.24	0.26	0.01	0.00	0.11	0.01	34	5	
CH/CB	Isheyevo	Tereshkova_3-2	21.83	0.85	0.24	0.01	0.41	0.10	0.01	34	5	
CV3ox	Vigarano	FoB3137_2	16.10	0.40	0.26	0.00	0.16	0.55	0.05	14	71	
CV3ox	Vigarano	FoB3137_3	23.27	0.59	0.27	0.00	0.19	0.81	0.05	14	71	
CV3ox	Vigarano	FoB3137_4	11.43	0.29	0.26	0.00	0.26	0.67	0.09	14	71	
CV3ox	Vigarano	FoB3137_5	9.54	0.23	0.25	0.00	0.27	0.55	0.09	14	71	

CV3ox	Vigarano	FoB3137_6	4.82	0.12	0.26	0.00	0.29	0.69	0.21	14	71	
CV3ox	Vigarano	FoB3137_7	9.83	0.24	0.26	0.00	0.24	0.52	0.08	14	71	
CV3ox	Vigarano	FoB3137_8	2.81	0.07	0.25	0.00	0.01	0.49	0.26	14	71	
CV3ox	Vigarano	FoB3137_10	0.28	0.01	0.25	0.00	0.25	0.17	0.92	4	87	
CV3ox	Vigarano	FoB3137_12	1.61	0.04	0.25	0.00	0.15	0.18	0.17	4	87	
CV3ox	Vigarano	FoB3137_12	4.56	0.11	0.26	0.00	0.11	0.44	0.14	14	71	
CV3ox	Allende	CMS1-6f_1	4.99	0.55	0.25	0.00	0.25	0.60	0.21		35	30
CV3ox	Allende	CMS1-6f_4	3.92	0.44	0.25	0.00	0.34	0.58	0.46		35	30
CV3ox	Allende	CMS1-6f_6	1.08	0.12	0.25	0.00	0.12	0.55	0.90		36	30
CV3ox	Allende	CMS1-6f_7	2.81	0.32	0.24	0.01	0.53	0.03	0.02		NA	px
CV3ox	Allende	CMS1-1290(1)_1	8.93	0.16	0.27	0.01	0.09	0.69	0.14		41	30
CV3ox	Allende	CMS1-1290(1)_3	26.55	0.74	0.25	0.01	0.41	0.99	0.07		41	30
CV3ox	Allende	CMS1-1290(1)_4	84.54	4.01	0.28	0.02	0.43	0.90	0.02		41	30
CV3ox	Allende	CMS1-1290(1)_5	2.46	0.06	0.24	0.01	0.06	0.07	0.04		41	30
CV3ox	Allende	CMS1-1290(1)_7	9.49	0.11	0.25	0.01	0.28	0.82	0.13		41	30
CV3ox	Allende	CMS1-1290(1)_10	7.29	0.07	0.26	0.00	0.02	1.05	0.21	24	41	30
CV3ox	Allende	CMS1-1290(2)_12	46.10	0.03	0.25	0.01	0.37	0.42	0.01	24	41	30
CV3ox	Allende	CMS1-1290(2)_13	12.01	0.06	0.25	0.00	-0.01	0.50	0.06	24	41	30
CV3ox	Allende	CMS1-1290(2)_14	1.21	0.02	0.25	0.00	0.06	0.47	0.58	24	41	30
CV3ox	Allende	CMS1-1290(2)_15	12.70	0.08	0.25	0.01	-0.20	0.59	0.07	24	41	30
CV3ox	Allende	CMS1-1290(2)_16	2.89	0.06	0.25	0.00	0.14	0.64	0.33	24	41	30
CV3ox	Allende	CMS1-1290(2)_17	2.98	0.04	0.25	0.00	0.00	0.70	0.35	24	41	30
CV3ox	Allende	CMS1-1290(2)_18	3.33	0.01	0.25	0.00	0.17	0.46	0.21	24	41	30
CV3ox	Allende	CMS1-1290(2)_19	13.40	0.34	0.25	0.01	0.13	0.41	0.05	24	41	30
CV3	NWA 5508	Saguaro_8	2.56	0.14	0.24	0.00	0.53	0.61	0.23		10	23
CV3	NWA 5508	Saguaro_9	3.33	0.18	0.24	0.00	0.73	0.46	0.16		9	24
CV3	NWA 5508	Saguaro_10	6.71	0.45	0.25	0.00	0.32	0.57	0.14		35	30
CV3	NWA 5508	Saguaro_12	0.47	0.03	0.24	0.00	0.28	0.61	0.20		26	28
CV3	NWA 5508	Saguaro_13	70.74	4.82	0.30	0.01	0.71	0.83	0.04		27	28

CV3	NWA 5508	Saguaro_ 16	2.47	0.14	0.24	0.00	0.61	0.59	0.22		31	29
CV3	NWA 5508	Saguaro_ 17	3.33	0.21	0.24	0.00	0.49	0.57	0.13		25	27
CV3	NWA 5508	Saguaro_ 20	4.69	0.25	0.24	0.00	0.47	0.87	0.27		25	28
CV3	NWA 5508	Saguaro_ 21	57.67	4.39	0.28	0.01	0.70	0.79	0.01		35	30
CV3red	Leoville	ZT1_2	9.66	1.14	0.27	0.01	0.74	0.77	0.09	24	31	29
CV3red	Leoville	ZT1_4	10.97	1.54	0.26	0.01	0.60	0.71	0.07	24	31	29
CV3red	Leoville	ZT1_6	3.95	0.53	0.25	0.01	0.50	0.34	0.01	24	31	29
CV3red	Leoville	ZT1_7	17.06	2.36	0.26	0.01	0.45	0.37	0.11	24	31	29
CV3red	Leoville	ZT1_8	34.69	4.58	0.29	0.02	0.59	1.34	0.09	24	31	29
CV3red	Leoville	ZT1_9	85.47	9.47	0.33	0.02	0.76	0.52	0.01	24	31	29
CV3red	Leoville	ZT1_10	15.27	1.70	0.26	0.01	0.69	0.44	0.01	24	31	29
CV3red	Leoville	ZT1_11	11.66	1.36	0.27	0.01	0.08	0.40	0.03	24	31	29
CV3red	Leoville	ZT1_12	11.66	2.72	0.27	0.02	0.08	0.45	0.04	24	31	29
CV3red	Leoville	ZT4_3	15.77	1.80	0.24	0.01	0.53	matri x		31	12	25
CV3red	Leoville	ZT4_4	12.75	1.40	0.25	0.01	0.48	1.62	0.26	31	12	25
CV3red	Leoville	ZT4_5	8.13	0.90	0.25	0.01	0.04	2.44	0.60	31	12	25
CV3red	Leoville	ZT4_6	21.68	2.79	0.25	0.01	0.34	0.94	0.09	31	12	25
CV3red	Leoville	ZT4_7	6.61	0.68	0.24	0.00	0.33	1.22	0.37	31	12	25
CV3red	Leoville	ZT4_8	612.6 1	77.36	0.65	0.05	0.81	2.45	0.01	31	12	25
CV3red	Leoville	ZT4_9	36.78	3.76	0.27	0.00	0.48	2.95	0.16	31	12	25
CV3red	Leoville	ZT4_10	42.54	5.25	0.27	0.02	0.67	1.42	0.07	31	12	25
CV3red	Leoville	ZT4_11	271.6 6	33.67	0.46	0.04	0.76	0.66	0.01	31	12	25
CV3an	NWA 7891	ZT7_1	116.2 1	13.08	0.30	0.02	0.65	0.96	0.02	34	24	29
CV3an	NWA 7891	ZT7_3	65.04	10.47	0.30	0.04	0.60	0.43	0.02	41	21	30
CV3an	NWA 7891	ZT7_4	17.48	1.84	0.27	0.01	0.35	0.24	0.01	41	22	30
CV3an	NWA 7891	ZT7_5	70.47	13.76	0.24	0.05	0.59	0.72	0.07	37	23	29
CV3an	NWA 7891	ZT7_6	31.28	3.63	0.26	0.02	0.83	0.23	0.01	35	24	29
CV3an	NWA 7891	ZT7_7	1.53	0.15	0.25	0.00	0.48	0.43	0.02	40	23	30
CV3an	NWA 7891	ZT7_8	49.73	8.39	0.25	0.03	0.71	0.69	0.80	32	24	28
CV3ox	NWA 7891	Lisa(6f)_1	24.43	0.70	0.31	0.01	0.70	0.56	0.02	25	28	28
CV3ox	NWA 7891	Lisa(6f)_4	3.91	0.11	0.25	0.01	0.34	0.35	0.19	25	28	28
CV3ox	NWA 7891	Lisa(6f)_5	10.80	0.49	0.28	0.01	0.56	0.46	0.09	25	28	28
CV3ox	NWA 7891	Lisa(6f)_6	11.98	0.43	0.28	0.01	0.62	0.47	0.09	25	28	28
CV3ox	NWA 7891	Lisa(6f)_7	21.20	0.76	0.30	0.01	0.80	0.48	0.05	25	28	28
CV3ox	NWA 7891	Lisa(6f)_8	8.68	0.27	0.26	0.01	0.45	0.70	0.18	25	28	28

CV3ox	NWA 7891	Lisa(6f)_9	2.48	0.12	0.26	0.00	0.42	0.51	0.45	25	28	28
CV3ox	NWA 7891	Lisa(1290)_1	15.21	0.46	0.29	0.01	0.19	0.18	0.02	23	38	27
CV3ox	NWA 7891	Lisa(1290)_3	1.72	0.04	0.25	0.00	0.20	0.14	0.13	26	28	26
CV3ox	NWA 7891	Lisa(1290)_4	17.29	0.55	0.28	0.01	0.40	0.25	0.02	24	34	27
CV3ox	NWA 7891	Lisa(1290)_5	12.89	0.35	0.28	0.01	0.33	0.26	0.03	26	26	25
CV3ox	NWA 7891	Lisa(1290)_6	15.27	0.42	0.28	0.01	0.35	0.36	0.03	21	43	28
CV3ox	NWA 7891	Lisa(1290)_7	6.36	0.16	0.26	0.00	-0.06	0.35	0.08	24	35	27
CV3ox	NWA 7891	Lisa(1290)_8	15.54	0.45	0.27	0.01	0.38	0.27	0.03	24	32	26
CV3red	NWA 5028	Agave_2	9.39	0.51	0.26	0.01	0.48	2.14	0.29	15	15	34
CV3red	NWA 5028	Agave_6	5.07	0.26	0.25	0.00	0.62		1.77	24	24	29
CV3red	NWA 5028	Agave_9	4.05	0.63	0.25	0.00	0.48	2.38	0.74	6	6	40
CV3red	NWA 5028	Agave_10	0.73	0.06	0.24	0.00	0.42	0.11	0.19	6	6	40
CV3red	NWA 5028	Agave_13	1.00	0.05	0.25	0.00	0.36	0.14	0.18	26	26	28
CV3red	NWA 5028	Agave_11	51.99	4.08	0.30	0.01	0.78	0.89	0.02	30	30	26
CV3red	NWA 5028	Cholla(1290)_1-1	15.03	0.54	0.26	0.01	0.17	0.37	0.04	33	7	
CV3red	NWA 5028	Cholla(1290)_1-2	8.55	0.30	0.26	0.01	0.25	0.12	0.02	27	39	
CV3red	NWA 5028	Cholla(1290)_2	1.55	0.05	0.25	0.00	0.09	0.72	0.70	32	11	
CV3red	NWA 5028	Cholla(1290)_3	10.63	0.37	0.26	0.00	0.26	0.41	0.06	69	NA - sp	0
CV3ox	NWA 6991	B4_3	0.59	0.06	0.24	0.00	0.35	0.53	1.46		25	27
CV3ox	NWA 6991	B4_4-1	24.14	2.78	0.26	0.01	0.54	0.92	0.06		36	30
CV3ox	NWA 6991	B4_4-2	42.71	4.77	0.27	0.01	0.54	0.84	0.03		36	30
CV3ox	NWA 6991	B4_5	58.92	6.97	0.28	0.01	0.73	0.85	0.02		36	30
CV3ox	NWA 6991	B4_7	0.64	0.07	0.24	0.00	0.39	0.78	1.96		30	29
CV3ox	NWA 6991	B4_8	1.19	0.13	0.25	0.00	0.36	0.57	0.77		15	25
CV3ox	NWA 6991	B4_11	19.68	2.19	0.25	0.01	0.77	0.58	0.05		30	29
CV3ox	NWA 6991	B4_12	23.54	2.62	0.26	0.01	0.76	0.49	0.03		32	29
CV3ox	Allende	TS68_1	18.95	0.41	0.27	0.01	0.75	0.43	0.03	26	26	25
CV3ox	Allende	TS68_2-1	6.06	0.12	0.27	0.01	0.44	0.41	0.10	26	26	25
CV3ox	Allende	TS68_2-2	2.86	0.04	0.26	0.00	0.48	0.41	0.22	26	26	25
CV3ox	Allende	TS68_3	84.16	3.58	0.29	0.02	0.80	0.35	0.01	26	26	25
CV3ox	Allende	TS68_4	4.10	0.12	0.25	0.01	0.69	0.41	0.15	26	26	25
CV3ox	Allende	TS68_5	61.55	1.67	0.29	0.01	0.75	0.38	0.01	26	26	25
CV3ox	Allende	TS68_7	61.24	1.71	0.30	0.01	0.80	0.50	0.01	26	26	25
CV3ox	Allende	TS23_1	5.41	0.08	0.26	0.00	0.40	0.26	0.07	27	23	23

CV3ox	Allende	TS23_2	2.52	0.05	0.24	0.01	0.23	0.27	0.16	27	23	23
CV3ox	Allende	TS23_3-1	29.58	1.51	0.27	0.02	0.66	0.28	0.01	27	23	23
CV3ox	Allende	TS23_3-2	4.22	0.07	0.25	0.01	0.64	0.28	0.10	27	23	23
CV3ox	Allende	TS23_4	201.08	14.92	0.39	0.04	0.69	0.32	0.00	27	23	23
CV3ox	Allende	TS23_5	13.82	0.55	0.26	0.01	0.54	0.22	0.02	27	23	23
CV3ox	Allende	TS23_6	57.60	2.33	0.28	0.02	0.76	0.31	0.01	27	23	23
CV3ox	Allende	TS23_7	76.13	2.85	0.29	0.01	0.78	0.45	0.01	27	23	23
CV3ox	Allende	TS23_8	11.89	0.46	0.26	0.01	0.76	0.28	0.04	27	23	23

Note: These measurements were only conducted in melilite; each line represents a single analysis spot. The standard errors are 2σ calculated by combining counting statistics and uncertainties of RSF and IMF. Only the most stable counts during these analyses were included in the counting statistics – because ^{28}Si was measured at the end of each analysis, often these analyses have inaccurate [B] and [Be].

[1]r is the correlation coefficient

[2]Abundances in ug/g

[3]wt. %

[4]mol %

(1,2) Two analyses at the same location

Table S8

Chapter 4: ^{10}Be–^{10}B Extra Results for 4 CO3 CAIs

Chondrite CAI analysis	^{9}Be/^{11}B	^{9}Be/^{11}B SE	^{10}B/^{11}B	^{10}B/^{11}B SE	[Be]	[B]
ALHA77307_60-1_1	1.619	0.009	0.2505	0.0014	0.370	0.342
ALHA77307_60-1_2	1.360	0.008	0.2498	0.0014	0.344	0.379
ALHA77307_60-1_3	2.923	0.026	0.2470	0.0035	0.338	0.173
ALHA77307_60-1_4	1.622	0.013	0.2545	0.0028	0.280	0.258
ALHA77307_60-1_5	0.821	0.005	0.2494	0.0013	0.263	0.479
ALHA77307_60-1_6	0.318	0.002	0.2490	0.0014	0.256	1.208

ALHA77307_60-1_7	0.431	0.002	0.2490	0.0009	0.293	1.018
ALHA77307_60-1_8	0.506	0.003	0.2484	0.0012	0.266	0.787
ALHA77307_60-1_9	0.221	0.002	0.2508	0.0011	0.357	2.421
ALHA77307_60-1_11	0.499	0.003	0.2482	0.0014	0.410	1.231
ALHA77307_43-1_1	8.845	0.072	0.2510	0.0032	0.487	0.082
ALHA77307_43-1_2	4.506	0.032	0.2487	0.0023	0.396	0.132
ALHA77307_43-1_3	0.813	0.005	0.2507	0.0010	0.415	0.765
DOM08004_16-1_1	0.526	0.003	0.2492	0.0009	0.070	0.198
DOM08004_16-1_3	0.568	0.004	0.2477	0.0017	0.087	0.229
DOM08004_16-1_4	0.278	0.002	0.2455	0.0011	0.071	0.384
DOM08004_16-1_6-1	0.396	0.005	0.2438	0.0030	0.080	0.301
DOM08004_16-1_6-2	0.428	0.003	0.2488	0.0010	0.088	0.309
DOM08004_16-1_8	1.634	0.015	0.2450	0.0031	0.073	0.067
DOM08004_26-1_1	0.675	0.004	0.2499	0.0005	0.109	0.241
DOM08004_26-1_2	0.228	0.001	0.2517	0.0005	0.089	0.584
DOM08004_26-1_3	1.153	0.008	0.2521	0.0012	0.107	0.140
DOM08004_26-1_4	0.389	0.003	0.2528	0.0012	0.075	0.289
DOM08004_26-1_5	0.752	0.005	0.2514	0.0010	0.084	0.167

Note: Abundances in ug/g

Table S9

Chapter 4: ^{26}Al–^{26}Mg Results for 2 CAIs from NWA 5028 ($CV3_{red}$)

Sample spots	phase	$^{27}Al/^{24}Mg$	1 SE	$\delta^{26}Mg$*	1 SE
Agave_1	melilite	0.515	0.003	0.380	0.122
Agave_2	melilite	1.071	0.005	0.305	0.122
Agave_3	melilite	1.779	0.009	0.834	0.122
Agave_4	melilite	1.430	0.007	0.429	0.115
Agave_5	melilite	1.635	0.008	0.570	0.115
Agave_6	melilite	2.690	0.013	0.844	0.115
Agave_7	melilite	2.433	0.012	1.006	0.115
Agave_8	melilite	2.579	0.013	0.887	0.115
Agave_9	melilite	2.642	0.013	1.296	0.121
Agave_10	melilite	0.448	0.002	0.206	0.115
Agave_11	spinel	2.566	0.013	0.794	0.123

Agave_12	pyroxene	1.028	0.005	0.178	0.078
Agave_13	pyroxene	0.577	0.003	-0.188	0.073
Agave_14	pyroxene	1.125	0.006	0.291	0.068
Agave_15	pyroxene	0.566	0.003	-0.050	0.083
Agave_16	pyroxene	1.285	0.006	-0.034	0.086
Agave_17	pyroxene	1.461	0.007	0.342	0.082
Agave_18	pyroxene	1.016	0.005	0.291	0.089
Agave_19	pyroxene	0.576	0.003	-0.069	0.072
Agave_20	pyroxene	1.152	0.006	0.010	0.078
Agave_21	anorthite	316.383	2.037	108.856	1.783
Agave_22	anorthite	334.735	2.014	118.890	2.397
Agave_23	anorthite	369.298	2.159	131.044	1.535
Agave_24	anorthite	389.442	2.236	137.318	1.975
Agave_25	anorthite	493.242	2.541	174.561	1.650
Agave_26	anorthite	1837.798	9.507	657.289	4.544
Agave_27	anorthite	369.720	4.388	133.694	3.032
Cholla_1	melilite	6.212	0.038	1.792	0.530
Cholla_2	melilite	12.643	0.094	5.062	1.298
Cholla_3	melilite	9.094	0.051	3.120	0.778
Cholla_4	melilite	11.781	0.063	3.984	0.622
Cholla_5	melilite	13.616	0.073	4.415	0.590
Cholla_6	melilite	13.823	0.142	3.864	0.633
Cholla_7	melilite	27.092	0.166	10.666	1.126
Cholla_8	melilite	13.697	0.079	5.346	0.607
Cholla_9	melilite	14.190	0.074	5.658	0.634
Cholla_10	melilite	27.128	0.144	10.142	0.572
Cholla_11	melilite	34.827	0.178	13.590	0.620
Cholla_12	melilite	39.600	0.222	14.815	
Cholla_13	spinel	2.575	0.013	0.972	0.123
Cholla_14	spinel	2.534	0.013	0.858	0.123
Cholla_15	pyroxene	0.647	0.009	0.288	0.113
Cholla_16	pyroxene	2.860	0.015	0.856	0.128
Cholla_17	pyroxene	1.900	0.010	0.787	0.113
Cholla_18	pyroxene	0.770	0.010	0.140	0.078

Note: These measurements were conducted in melilite, spinel, pyroxene, or anorthite as indicated. The standard errors are calculated by combining counting statistics and uncertainties of the standards.

Table S10

Chapter 5: Oxygen Isotope Data for 5 CAIs

CAI analysis	$\delta^{18}O$	$\delta^{18}O$ 2SE	$\delta^{17}O$	$\delta^{17}O$ 2SE	$\Delta^{17}O$	$\Delta^{17}O$ 2SE
B4_sp1	-39.82	0.99	-43.45	0.71	-22.74	0.51
B4_sp2	-38.08	0.99	-42.77	0.71	-22.96	0.51
B4_sp3	-41.39	0.99	-44.47	0.71	-22.95	0.51
B4_sp4	-43.59	0.99	-46.11	0.71	-23.45	0.51
B4_mel1	9.80	0.99	2.03	0.71	-3.06	0.51
B4_mel2	7.25	0.99	-0.39	0.71	-4.16	0.51
B4_mel3	-1.85	0.99	-7.46	0.71	-6.50	0.51
B4_mel4	4.12	0.99	-1.40	0.71	-3.54	0.51
B4_px1	-37.91	0.99	-43.00	0.71	-23.28	0.51
B4_px2	-38.15	0.99	-42.40	0.71	-22.57	0.51
B4_px3	-40.21	0.99	-43.43	0.71	-22.52	0.51
B4_px4	-42.04	0.99	-44.75	0.71	-22.89	0.51
B4_px5	-43.52	0.99	-45.39	0.71	-22.76	0.51
B4_an1	14.28	0.99	4.82	0.71	-2.60	0.51
B4_an2	13.05	0.99	4.70	0.71	-2.08	0.51
B4_an3	13.04	0.99	4.50	0.71	-2.29	0.51
TS23_sp1	-44.86	0.42	-47.07	0.58	-23.74	0.48
TS23_mel1	2.11	0.42	-2.11	0.58	-3.21	0.48
TS23_px1	-44.78	0.42	-46.92	0.58	-23.63	0.48
TS23_an1	5.41	0.42	0.18	0.58	-2.63	0.48
Agave_sp1	-45.32	0.42	-47.93	0.58	-24.37	0.48
Agave_sp2	-45.62	0.42	-47.94	0.58	-24.22	0.48
Agave_sp3	-46.71	0.42	-48.05	0.58	-23.76	0.48
Agave_sp4	-45.91	0.42	-47.74	0.58	-23.87	0.48
Agave_mel1	8.76	0.42	3.46	0.58	-1.10	0.48
Agave_mel2	10.61	0.42	4.84	0.58	-0.68	0.48
Agave_mel3	9.99	0.42	4.19	0.58	-1.01	0.48
Agave_mel4	10.10	0.42	4.07	0.58	-1.18	0.48
Agave_px1	-45.39	0.42	-47.14	0.58	-23.54	0.48
Agave_px2	-45.36	0.42	-47.27	0.58	-23.68	0.48
Agave_px3	-45.26	0.42	-46.97	0.58	-23.43	0.48
Agave_px4	-45.69	0.42	-47.58	0.58	-23.82	0.48
Agave_px5	-44.34	0.42	-45.98	0.58	-22.92	0.48
Agave_an1	-38.15	0.42	-39.42	0.58	-19.59	0.48
Agave_an2	6.18	0.42	-0.36	0.58	-3.57	0.48

Agave_an3	-1.79	0.42	-6.57	0.58	-5.64	0.48
Saguaro_sp1	-47.53	0.42	-48.42	0.79	-23.70	0.70
Saguaro_sp2	-46.92	0.42	-47.97	0.79	-23.58	0.70
Saguaro_sp3	-45.94	0.42	-47.52	0.79	-23.63	0.70
Saguaro_sp4	-46.13	0.42	-47.61	0.79	-23.62	0.70
Saguaro_mel1	3.98	0.42	-0.47	0.79	-2.54	0.70
Saguaro_mel2	3.95	0.42	-0.98	0.79	-3.03	0.70
Saguaro_mel3	3.91	0.42	-0.26	0.79	-2.29	0.70
Saguaro_mel4	5.33	0.42	-0.47	0.79	-3.24	0.70
Saguaro_px1	-45.35	0.42	-47.11	0.79	-23.52	0.70
Saguaro_px2	-45.14	0.42	-47.16	0.79	-23.69	0.70
Saguaro_px3	-44.38	0.42	-46.74	0.79	-23.66	0.70
Saguaro_px4	-45.44	0.42	-47.00	0.79	-23.37	0.70
Saguaro_an1	-24.48	0.42	-28.36	0.79	-15.63	0.70
Saguaro_an2	-32.26	0.42	-35.08	0.79	-18.30	0.70
Saguaro_an3	-8.00	0.42	-12.27	0.79	-8.11	0.70
Saguaro_an4	-8.45	0.42	-14.16	0.79	-9.77	0.70
Saguaro_an5	-32.79	0.42	-36.51	0.79	-19.46	0.70
Cholla_sp2	-45.44	0.36	-48.73	1.64	-25.10	1.69
Cholla_sp4	-45.05	0.54	-46.95	0.97	-23.52	0.87
Cholla_sp5	-41.88	0.56	-46.04	1.14	-24.27	1.03
Cholla_sp6	-45.80	0.56	-46.57	1.14	-22.75	1.03
Cholla_mel1	-35.22	0.36	-38.63	1.64	-20.32	1.69
Cholla_mel2	-40.19	0.36	-44.82	1.64	-23.93	1.69
Cholla_mel3	-40.12	0.54	-36.73	0.97	-15.86	0.87
Cholla_mel4	-9.40	0.54	-11.80	0.97	-6.92	0.87
Cholla_mel6	-32.34	0.56	-31.18	1.14	-14.37	1.03
Cholla_px1	-44.79	0.36	-46.67	1.64	-23.37	1.69
Cholla_px3	-44.93	0.54	-46.46	0.97	-23.09	0.87
Cholla_px4	-36.64	0.54	-38.17	0.97	-19.12	0.87
Cholla_px5	-42.07	0.54	-44.63	0.97	-22.75	0.87
Cholla_px7	-44.71	0.56	-46.36	1.14	-23.11	1.03

APPENDIX B

PREVIOUS PUBLICATION/STATEMENT OF CO-AUTHORS

A manuscript version of Chapter 2 has been accepted for publication in *Geostandards and Geoanalytical Research.* Chapters 3 through 5 are manuscripts in work that will be submitted to Nature Astronomy, Proceedings of the National Academy of Sciences, and Geochimica et Cosmochimica Acta respectively.

Chapter 2 co-authors are: Meenakshi Wadhwa, Richard Hervig and Steven Desch.

Chapter 3 co-authors are: Meenakshi Wadhwa, Steven Desch, Ming-Chang Liu, Jemma Davidson, Devin Schrader, Noriko Kita, Kohei Fukuda, Andreas Hertwig.

Chapter 4 co-authors are: Meenakshi Wadhwa, Steven Desch, Ming-Chang Liu, Richard Hervig, Steven Simon, Noriko Kita, Celine Defouilloy, Devin Schrader, and Yusuke Fujimoto.

Chapter 5 co-authors are: Meenakshi Wadhwa, Steven Desch, Steven Simon, Noriko Kita, and Celine Defouilloy.